HUMBOLDT-UNIVERSITÄT ZU BERLIN

The Permian-Triassic boundary in the NW-Iranian Transcaucasus and in Central Iran: Petrographic and geochemical investigations aimed at an improved characterization of the environmental shift around the time of the major mass extinction

Dissertation
zur Erlangung des akademischen Grades
doctor rerum naturalium
(Dr. rer. nat.)
im Fach: Chemie Spezialisierung: Mineralogie
eingereicht an der
Mathematisch-Naturwissenschaftlichen Fakultät
der Humboldt-Universität zu Berlin
von

Diplom-Geologin Lucyna Leda

Präsidentin der Humboldt-Universität zu Berlin
Prof. Dr.-Ing. Dr. Sabine Kunst
Dekan der Mathematisch-Naturwissenschaftlichen Fakultät
Prof. Dr. Elmar Kulke
Gutachter / innen:
1. Prof. Dr. Franziska Emmerling
2. Prof. Dr. Wolfgang Kiessling
3. Prof. Dr. Wolf Uwe Reimold

Tag der mündlichen Prüfung: 18.12.2019

für Natur MUSEUM FÜR NATURKUNDE BERLIN

Leibniz Gemeinschaft

Hiermit versichere ich, dass ich die vorliegende Arbeit selbstständig verfasst und keine anderen als die angegebenen Hilfsmittel benutzt habe. Die Stellen der Arbeit, die anderen Werken wörtlich oder inhaltlich entnommen sind, wurden durch entsprechende Angaben der Quellen kenntlich gemacht.

Diese Arbeit hat in gleicher oder ähnlicher Form noch keiner Prüfungsbehörde vorgelegen.

Lucyna Leda, Zamarte, den 27 März 2019

ACKNOWLEDGMENTS

First and foremost, I am grateful to PD Dr. Dieter Korn (Berlin) who supervised this thesis and whose inspirational thinking stimulated various aspects of this project. He supported me with advice, constructive discussion, comments, and suggestions during the course of this work. I also want to thank him for his invaluable assistance in the field, where I profited from his extensive knowledge of the Permian-Triassic geology. His time and work invested in this task are much appreciated.

Special thanks are also due to Prof. Wolf Uwe Reimold (formerly Museum für Naturkunde Berlin, now University of Brasilia, DF, Brasil), who co-promoted this thesis. He introduced me to impact geology, helped with his broad petrographical and mineralogical knowledge, and provided necessary literature about the marine and continental P-Tr boundary sections. He supported me many times with advice. I would like to thank him for providing access to the necessary laboratory equipment. His constructive criticism helped to improve content and English of the manuscript.

Dr. Ulrich Struck (Berlin) is gratefully acknowledged for his help and advice during my work in the stable isotope laboratory, and for introducing me to isotope analytics of C and N and for providing access to the necessary laboratory equipment.

I wish to thank my close colleague Dr. Martin Schobben (Utrecht). His stimulating discussions and constructive critical review significantly improved my thesis.

I thank Dr. Christoph Korte (Kopenhagen) for sharing his isotopic experience, and support with advice and practical help.

I am indebted to Dr. Abbas Ghaderi (Ferdowsi University of Mashhad, Iran) and Dr. Vachik Hairapetian (Islamic Azad University, Esfahan, Iran) for their assistance in the field in Iran and for their constructive comments on the sedimentology, and palaeoenvironment of the studied carbonates.

I am particularly indebted to Prof. Ali Reza Ashouri (Ferdowsi University of Mashhad) for providing the permission to carry out the field work and export the samples, to the Aras Free Zone Office, and to Adel Najafzadeh for the support of the field work in the Julfa region. And I want to thank the Islamic Azad University (Esfahan, Iran) for support of the field work in the Baghuk Mountain.

Acknowledgements are also extended to Ewgenija Kuhl and Marianne Falk (both Berlin), who helped me with every technical problem during the laboratory work. I wish to thank Kirsten Born (Berlin), who carried out the SEM-EDX and CL analysis of carbonates, and Cordelia Lange (TU Berlin), who carried out XRD analysis of shale samples. I would like to express my gratitude also to Sylvia Salzmann, Markus Brinkmann, Hans-Rudolf Knöfler, Christian Beck, Katharina Böhm, Lisa Schlegelmilch, Carina Klein, and Marianne Falk (all in Berlin), who

helped me to process all rock samples. Thanks are also due to Amir Akbari and Sadegh Zamani (Esfahan) for their assistance in the field.

Financial support for this study was provided by the Deutsche Forschungsgemeinschaft and is gratefully acknowledged. This is a contribution to the research project “The Permian-Triassic boundary and the Early Triassic in Transcaucasian pelagic sections” funded by the DFG (projects Ko1829/12-1, Ko1829/12-2 and Ko2011/8-1).

Finally, I wish to thank my family for their enduring mental support and trust.

Contents

KURZFASSUNG

Einige der am besten aufgeschlossenen marinen Perm/Trias-Grenzprofile können in Nordwest- und Zentral-Iran studiert werden. Sie gehören zu den wichtigsten Orten, an denen die dramatische Faunenveränderung pelagischer Organismen zwischen dem Paläozoikum und dem Mesozoikum untersucht werden kann. Die marinen Ablagerungen in Nordwest-und Zentral-Iran bieten eine einzigartige Gelegenheit, ununterbrochene, sehr fossilreiche Schichten in einer Karbonat- und Tonstein-dominierten Fazies zu studieren; sie stellen die notwendige Verbindung zu den gut untersuchten chinesischen P/Tr-Grenzprofilen dar. Diese Arbeit stellt quantitative sedimentologische Untersuchungen im Bereich von Petrographie, Geochemie und Geochemie stabiler Isotopen der lithologischen Abfolge vor, um mögliche ökologische Gründe aufzudecken, die für das Aussterbeereignis und seine nachfolgende Erholung verantwortlich gewesen sein könnten.

Perm/Trias-Grenzprofile in den Regionen von Julfa (NW-Iran) und Abadeh (Zentral-Iran) zeigen eine Abfolge von drei charakteristischen Gesteinseinheiten, (1) den *Paratirolites* Limestone mit dem end-permischen Massensterbehorizont an seiner Oberkante, (2) den „Boundary Clay" und (3) die untertriassische Elikah-Formation mit der nach Conodonten definierten Perm/Trias-Grenze an seiner Basis. Die Karbonatmikrofazies zeigt eine zeitliche Veränderung in den Profilen bei Julfa; innerhalb des *Paratirolites* Limestone ist eine zunehmende Anzahl von Intraklasten, Fe-Mn-Krusten und biogenen Verkrustungen erkennbar. Ein Rückgang der Karbonat-Akkumulation findet im oberen Abschnitt der Gesteinseinheit statt; an der Oberkante, direkt vor dem vollständigen Erlöschen der Karbonatproduktion, befindet sich ein sponge packstone. Die Abfolge im „Boundary Clay" und der weitgehend untertriassischen Elikah-Formation unterscheidet sich in den beiden Regionen; dünne Horizonte von sponge packstone sind in der Region von Julfa charakteristisch, während "calcite fans", wahrscheinlich anorganischen Ursprungs, in der Region von Abadeh vorkommen. Die Karbonatproduktion wurde mit der Ablagerung von mikrobiellen Karbonaten an der Basis der Elikah-Formation bei Julfa in Gang gesetzt; es überwiegen dicht laminierter bindstone, floatstone mit spärlichen Calcitsphären und oncoid wackestone/floatstone. Die in den Profilen von Baghuk (Abadeh-Region) vorkommenden Mikrobialite sind vielfältig; es gibt groß-und kleinskalige, arboreszierende Mikrobialit-Ansammlungen mit auffälliger Morphologie und innerer Struktur. Die häufigsten Mesostrukturtypen von Mikrobialiten in den Baghuk-Profilen sind Dendrolithe, Stromatolithe und Leiolithe.

In den Regionen von Julfa (NW-Iran) und Abadeh (Zentral-Iran) deutet eine deutliche und weltweit nachvollziehbare negative Kohlenstoffisotopenexkursion auf große Störungen des Kohlenstoffkreislaufs an der Perm/Trias-Grenze hin. Die neuen Daten erlauben die Bewertung der Ursachen der großen negativen Veränderung im jüngsten Perm. Es zeigt auch, dass der negative $\delta^{13}C$-Trend „erster Ordnung""vom Perm in die Trias durch primäre positive und negative Ereignisse („Exkursionen zweiter Ordnung") überlagert wird. Die $\delta^{13}C_{carb}$ Entwicklung der meisten Profile zeigt keine plötzliche starke Schwankung; der Trend ist kontinuierlich und zeigt eine progressive Abnahme über die P/Tr-Grenze hinweg. Die rasche Exkursion des $\delta^{13}C$

unterhalb des Aussterbehorizonts im obersten Bereich des *Paratirolites* Limestone wird durch eine stratigraphische Kondensation, die ein Defizit der Karbonatproduktion/Akkumulation und/oder eine schnelle geochemische Veränderung in Richtung Karbonatuntersättigung spiegelt, verstärkt. Dies deutet darauf hin, dass ein lang andauernder Mechanismus, wie etwa die thermische Metamorphose von Sedimenten reich an organischem Material, möglicherweise verursacht durch ausgedehnte Lavaströme des sibirischen Trap-Vulkanismus und/oder verstärkte Verwitterung auf den Kontinenten, die negative Perm/Trias-$\delta^{13}C$-Exkursion verursacht haben könnte. Der Übergang vom Paläozoikum ins Mesozoikum ist durch Veränderungen der stabilen Stickstoffisotopenzusammensetzung gekennzeichnet. Der Massenstickstoff-Isotopenrekord in den Profilen der Julfa-Region zeigt Störungen des regionalen Stickstoffkreislaufs an der Perm/Trias-Grenze. Die $\delta^{15}N_{bulk}$-Werte zeigen keinen Trend unterhalb des Aussterbehorizonts. Ähnlich sind die $\delta^{15}N_{bulk}$-Werte oberhalb der P/Tr-Grenze heterogen; die $\delta^{15}N_{bulk}$-Werte zeigen keinen Trend und keine Streuung, was auf eine Kombination verschiedener Prozesse (Stickstofffixierung und einen Gleichgewichtszustand zwischen Nitratassimilation, N_2-Fixierung und Denitrifikation) hinweist (die sogenannte “normale Meeresproduktion”). Innerhalb des mergeligen „Boundary Clay”, der Einheit zwischen dem Aussterbehorizont und der P/Tr-Grenze, zeigen die $\delta^{15}N_{bulk}$-Werte ein Plateau. Es wurde ein niedriger $CaCO_3$-Gehalt gemessen und es kommt zu einer Erhöhung des Tonmineralgehaltes. Es ist wahrscheinlich, dass die $\delta^{15}N_{bulk}$-Werte innerhalb des „Boundary Clay” durch frühe Diagenese beeinflusst wurden und verstärkte Nitrifikations-Denitrifikations-Wechselwirkungen während der Remineralisierung organischer Materie im Sediment widerspiegeln. Die relativ hohe Menge an Gesamtstickstoff im „Boundary Clay” könnte das Ergebnis der Absorption und des Zurückhaltens von Ammonium (NH_4+) in Tonmineralen sein. Es ist anzunehmen, dass das Ammonium nicht vom Land stammt, sondern dass es vom Meeressediment über anaerobe Oxidation von organischem Kohlenstoff in einem Prozess namens “dissimilatory nitrate reduction to ammonium” (DNRA) gelangt ist.

ABSTRACT

Some of the best-exposed marine Permian-Triassic (P-Tr) boundary successions can be accessed in NW and Central Iran. They are among the most important localities in which the dramatic faunal change of pelagic organisms across the boundary between the Palaeozoic and Mesozoic can be studied. The marine sections in NW and Central Iran provide an unique opportunity to study uninterrupted, highly fossiliferous successions in a carbonate- and claystone-dominated facies and represent the necessary link to the well-investigated Chinese P-Tr boundary sections. This thesis presents quantitative sedimentological studies in the field with petrographic, geochemical, and stable isotope investigations of the lithological succession to detect possible ecological reasons, which might have been agents for the extinction event and its subsequent recovery.

Permian-Triassic boundary sections in the Julfa (NW Iran) and Abadeh (Central Iran) regions display a succession of three characteristic rock units, (1) the *Paratirolites* Limestone with the end-Permian mass extinction horizon at its top, (2) the "Boundary Clay", and (3) the Early Triassic Elikah Formation with the conodont-defined Permian-Triassic boundary at its base. The carbonate microfacies reveals a change, in the sections near Julfa, within the *Paratirolites* Limestone with an increasing number of intraclasts, Fe-Mn crusts, and biogenic encrustation. A decline in carbonate accumulation occurs towards the top of the unit with a sponge packstone in the sections, and finally resulting in a complete demise of the carbonate factory. The succession of the 'Boundary Clay' differs in the two regions; thin horizons of sponge packstone are present in the Julfa region and 'calcite fans' of probably inorganic origin in the Abadeh Region. The skeletal carbonate factory of the Late Permian was restored with the deposition of microbial carbonates at the base of the Elikah Formation at Julfa, where densely laminated bindstone, floatstone with sparry calcite spheres, and oncoid wackestone/floatstone predominate. At Baghuk Mountain (Abadeh region), the occurrence of the microbialites is diverse including large- and small-scale, arborescent microbialite buildups with conspicuous morphology and internal structure. The most common mesostructure types of microbialites in the Baghuk Mountain area are dendrolites, stromatolites, and leiolites.

In the Julfa (NW Iran) and Abadeh (Central Iran) regions, a prominent and globally traceable negative carbon isotope excursion indicates major perturbations of the carbon cycle around the Permian-Triassic boundary. The new data allow the evaluation of the causes of the major negative shift in the latest Permian. It also shows that the ''first-order'' negative $\delta^{13}C$ trend from the Permian into the Triassic is superimposed by primary positive and negative events (''second-order'' excursions). The $\delta^{13}C_{carb}$ isotope record of most of the sections does not show any sudden strong variation; the trend is continuous and shows a progressive decrease across the P-Tr boundary. However, the sudden $\delta^{13}C$ decrease below the extinction horizon in the uppermost *Paratirolites* Limestone is triggered by stratigraphic condensation that mirrors a deficit of the carbonate production/accumulation and/or a rapid geochemical change towards carbonate undersaturation. Our new data show clearly that the ''first-order'' negative carbon isotope trend before extinction horizon is gradual, suggesting that a longer lasting mechanism, such

as thermal metamorphism of organic-rich sediments, possibly caused by extensive lava flows and dykes of the Siberian Trap volcanism, and/or enhanced weathering on the continents may have caused the negative Permian-Triassic $\delta^{13}C$ excursion.The Palaeozoic-Mesozoic transition is marked by changes in the stable nitrogen isotope composition. The bulk nitrogen isotope record in the sections of the Julfa region indicates perturbations of the regional nitrogen cycle around the Permian-Triassic boundary. The $\delta^{15}N_{bulk}$ values do not show any trend below the extinction horizon. Similarily, above the P-Tr boundary the $\delta^{15}N_{bulk}$ values are heterogeneous, do not show any trend, and scatter, rather pointing to mixing of different processes (nitrogen fixation and an equilibrium state between nitrate assimilation, N_2 fixation, and denitrification) (the so-called 'normal marine production'). Within the marly "Boundary Clay", the unit between the extinction horizon and the P-Tr boundary, the $\delta^{15}N_{bulk}$ values shows a plateau, low $CaCO_3$ content was measured, and increase in clay mineral content occurs. It is probable that $\delta^{15}N_{bulk}$ values within the "Boundary Clay"may have been affected by early diagenesis and may reflect intensified nitrification-denitrification interactions during organic matter remineralization within the sediment. The relatively high amount of total nitrogen in the "Boundary Clay" may be the result from absorption and retention of ammonium (NH_4^+) within clay minerals. It may be hypothesized that the ammonium is not land-derived, but instead originated in marine sediment via anaerobic oxidation of organic carbon in a process called "dissimilatory nitrate reduction to ammonium" (DNRA).

LISTS OF FIGURES AND TABLES

boundary of the Ali Bashi 1 section in the Julfa region.

Fig. 13. Carbonate microfacies of the upper part of the Julfa Beds. a – Grey, peloidal, laminated wackestone with ostracods and foraminifera. A large, vertical burrow is partially filled with micrite and sparite, forming a geopetal fabric. Ali Bashi 1, -19.95 m. b – Details of a peloidal, laminated wackestone, showing a biogenic component of foraminifera (f) within micritic and sparry peloidal matrix. Ali Bashi 1, -19.95 m. c – Reddish-brown, burrowed bioclastic packstone with fine-grained biodetritus of ostracods (o), echinoderms (e), brachiopods (br), radiolarian, foraminifera. Ali Bashi 1, -21.55 m. d – Fine-bioclastic, marly micritic matrix of a burrowed bioclastic packstone with a brachiopod (br) and ostracods (o) shells. Ali Bashi 1, -21.55 m.

Fig. 14. Carbonate microfacies of the Ali Bashi Formation. a – Reddish-brown, a marly, burrowed, bioclastic wackestone with brachiopods (br), echinoderms, ostracods and an nautiloid shell (n). Ali Bashi 1, -5.70 m. b – An orthocone nautiloid (n) shell embedded in a marly, burrowed matrix. The shell has been infilled with pelagic micrite with disarticulated ostracod shells (o). The shell is broken and the septa are filled by calcite. Ali Bashi 1, -5.70 m. c – Red, argillaceous, burrowed lime mudstone with ostracods (o) and foraminifera (f) within a bine-grained matrix. Ali Bashi 1, -6.90 m. d – Light green, peloidal lime mudstone with skeletal components of ostracods and foraminifera. Ali Bashi 1, -10.85 m.

Fig. 15. Carbonate microfacies of the lower part of the *Paratirolites* Limestone. a – Red, nodular, burrowed, bioclastic lime mudstone. Biogenic encrustations (be); microborings on/inside a brachiopod (br) shell and an ammonoid (a) conch. Ali Bashi 1, -0.75 m. b – Red, nodular, burrowed, bioclastic wackestone with ammonoids (a). Ali Bashi 1, -0.90m. c – Biogenic encrustation (be) around a micrite clast. Ali Bashi 1, -1.50 m. d – Red, nodular, burrowed, bioclastic lime mudstone with single ostracods (o). Ammonoid (a) conch dissolved and deformed. Ali Bashi 1, -1.77 m. e – Peloidal packstone with components of dasycladacean (d) green algae and foraminifera (f). Aras Valley, -2.20 m. f – Burrowed, bioclastic wackestone with ostracod shells (o) and gastropods (g). Ali Bashi 1, -2.65 m. g – Pelagic burrowed wackestone with bivalve filaments (bf), ammonoid (a), foraminifera (f) and radiolaria (r). Ali Bashi 1, -2.95 m. h – Red, burrowed bioclastic wackestone with ostracods (o) and foraminifera (f). Ali Bashi 1, -0.65 m.

Fig. 16. Carbonate microfacies of the P-Tr boundary beds at Aras Valley section. a – Red, nodular, burrowed, bioclastic wackestone with ostracods, foraminifera, radiolaria and echinoderms. -0.70 m. b – Partly micritized echinoderm plate with boring traces. -0.45 m. c – An example of foraminifera (*Frondina*? sp.) from the burrowed, bioclastic wackestone. -0.45 m. d – Top of the uppermost 4–5-cm-thick bed of the *Paratirolites* Limestone (=extinction horizon) with sponge spicules and ammonoids. e – Spherulites of aragonite pseudomorphs in a strongly burrowed and fractured lime mudstone. Aras Valley, +1.65 m. f – Gastropod packstone. +2.35 m. g – Floatstone with sparry calcite spheres; spheres are occluded by rhombic dolomite crystals. +4.30 m. h – Honey-colored, zonar, rhombic dolomite crystals. +4.30 m.

Fig. 17. Carbonate microfacies of the upper part of the *Paratirolites* Limestone. a – Top of the uppermost 4–5-cm-thick bed of the *Paratirolites* Limestone (=extinction horizon with sponge spicules). The chambers of the ammonoid (a) conch have been partially filled with matrix rich in sponge (s) skeletons and pure marly micrite, as well as with sparry cement. The marly, bioclastic matrix contains small radiolaria, gastropods (g), and micrite pebbles. Stylolite seams and micro-fractures are common. Ali Bashi 1, -0 m. b – Top of the uppermost 4–5-cm-thick bed of the *Paratirolites* Limestone (=extinction horizon). Light-grey lime mudstone with single ostracods. Baghuk Mountain A, -0 m. c – Red, nodular, burrowed, bioclastic lime mudstone; microborings (mb) in a bivalve shell. Ali Bashi 1, -0.35 m. d – Red, nodular, burrowed, bioclastic lime mudstone. Endolithozoan crusts (ec). Ali Bashi 4, extinction horizon. e – Ammonoid preservation: the upper and lower surface of the conch are completely truncated by dissolution. The section is longitudinal to the plane of the coiling. The lines of the junction of septa and the shell walls and septa are well preserved. After dissolution, the chambers were filled with muddy sediment, which have later recrystallized to microspar and pseudospar. The matrix is a bioclastic wackestone. Aras Valley, -1.10 m. f – Hardground intraclasts ('subsolution clasts'). Fe–Mn crusts with biogenic encrustation (be) by foraminifera around the micrite clasts. Ali Bashi 1, -0.75 m. g – Red, nodular, burrowed bioclastic lime mudstone with subrounded limestone clasts and single bellerophontid (g). The matrix is red-colored due to Fe-oxides, and is partially neomorphosed to microspar. The pebbles are fossil-rich and contain fine-grained biodetritus of radiolaria, benthic foraminifera, and ostracods. Clasts are surrounded by circumgranular crusts and biogenic encrustation. Ali Bashi 1, extinction horizon. h – Burrowed fossiliferous lime mudstone with radiolaria, ostracods, echinoderms (e) and ammonoids (a). Ali Bashi 1, -0.35 m.

Fig. 18. Carbonate microfacies of the 'Sponge Spike', all from topmost 2 cm of the *Paratirolites* Limestone (=extinction horizon). a – Sponge packstone with small vug-like cavities with geopetal infill; micro-fractures. The marly matrix is rich in crystal silt-filled and spar-filled interparticle cavities. Ammonoid (a) conch with well-preserved shell walls and septa; chambers infilled with micrite and blocky calcite cement. Ali Bashi 4. b – Enlarged view of the top part of a. Sponge packstone. Siliceous sponge skeletons were dissolved and replaced by calcite. Irregular forms predominate. The matrix is marly micrite. Ali Bashi 1. c – Micrite pebbles (mp) of the micrite-clast wackestone underlying the sponge packstone horizon; the clasts have been reworked and transported to the sponge packstone horizon. Matrix is rich in vugs filled with calcite cement. Micro-cracks and fractures give a breccia-like appearance. Ali Bashi 1. d – Enlarged view of the top part of c. Sponge network without rigid skeletons. Ali Bashi 1.

Fig. 19. Carbonate microfacies of the uppermost 4–5-cm-thick bed of the *Paratirolites* Limestone. a – Contact between the marly matrix rich in crystal silt-filled and spar-filled interparticle cavities and the 'sponge spike'. Ali Bashi 4. b – Marly matrix rich in crystal silt-filled and spar-filled interparticle cavities. Ali Bashi 4. c – Micrite clast and micrite-filled burrows. Ali Bashi 1. d – Ammonite preservation. The shell has been infilled with micritic matrix, micrite peloids, and after breakage and dissolution the shell and septa were later filled by sparry calcite. Ali Bashi 1.

Fig. 20. Carbonate microfacies of the Aras Member. a – Horizons of sponge lime mudstone within a marly siltstone. Ali Bashi 1, +0.45 m. b – Burrowed and bioturbated ostracod-sponge lime mudstone. Ali Bashi 1, +0.75 m. c – Abundant rhombic crystals (microspar) floating in matrix. Ali Bashi 1, +0.40 m. d – Foraminifera tests (f) within the microspar matrix. Ali Bashi 1, +0.75 m. e – Echinoderm remains (e). Ali Bashi 1, +0.28 m. f – A recrystallized ostracod shell (o). Ali Bashi 1, +1.29 m. g – Triaxon-like sponge remains (s) on an etched bedding surface of a marly interval in the 'Boundary Clay'. Ali Bashi 1, +0.85 m. h – Sicilified ostracod shells (o) on an etched bedding surface of a marly interval in the 'Boundary Clay'. Ali Bashi 1, +0.85 m.

Fig. 21. Carbonate microfacies of the *Claraia* Beds at Zal. a – Sponge gastropod wackestone, +0.42 m. b – Bellerophontid wackestone. The bellerophontids (g) are poorly preserved and deformed. The shell has been dissolved and the chambers are filled with sediment and calcite spar, +0.43 m. c – Laminated bindstone with algal/microbial mat, +2.45 m. d – Bioclastic wackestone with high-spired gastropods (g), +1.90 m. e – Horizon with sparry calcite spheres of the seafloor cement crusts, +4.05 m. f – Oncoid floatstone. The nucleus is a recrystallized bellerophontid (g); its cortex is laminated, with crenulated micritic and sparry laminae. The inhomogeneous matrix contains filaments of black organic matter, pyrite and dolomite crystals, as well as clay seams, +7.15 m. g – Spherical, laminated (sl) oncoids as well as non-laminated, micritic oncoids with sparry spots, +10.05 m. h – Micrite and sparite lamina couplets of the oncoid cortex, +7.15 m.

Fig. 22. Carbonate microfacies of the *Claraia* Beds. a – Bellerophontid wackestone with marly and burrowed matrix. A well-preserved bellerophontid (g) conch is filled with crystal silt. Ali Bashi 1, +1.25 m. b – Yellow-brown, burrowed bioclastic wackestone with skeletal components of ostracods, gastropods, spirobids and foraminifera. Ali Bashi 1 +1.61 m. c – The gastropods (g) are poorly preserved. The shell has been dissolved and the chambers are filled with sediment and calcite spar. Ali Bashi 1, +1.61 m. d – Irregular, diffuse lamination and bindstone, and small, sparry calcite spheres of a bindstone. Ali Bashi 1, +2.20 m. e – Marly wackestone with dense micrite and with small sparry calcite spheres. Ali Bashi 1, +3.01 m. f – Wackestone with sparry calcite spheres of the seafloor cement crusts. Ali Bashi 1, +3.65 m. g – Sparry calcite spheres with traces of borings (eb), biogenic encrustation (be), and dense micrite envelope. Ali Bashi 1, +4.15 m. h – Oncoid wackestone/floatstone. Ali Bashi N, +7.10 m.

Fig. 23. SEM-EDX characteristics of the floatstone with sparry calcite spheres at Zal (at +5.90 m). a – EDX image of an Fe-rich phyllosilicate crystal. A cross in pink in the centre of the crystal shows a place, where an EDS analysis was obtained. b – EDX spectrum of a crystal in a. c – EDX image of a celestine crystal. A cross in pink in the centre of the crystal shows a place, where the EDX measurement was taken. d – EDX spectrum of a celestine crystal in c.

Fig. 24. Non-metric multidimensional scaling (NMDS) of the microfacies data from the Ali Bashi 1 section. a – Scatter plot for each thin section of the *Paratirolites* Limestone, Aras Member and the base of the Elikah Formation. b – Position of the centroids for the subunits.

Fig. 25. The correlation of the conodont schemes by Kozur (2005, 2007), Shen and Mei (2010) and Ghaderi et al. (2014) with the ammonoid stratigraphy by Shevyrev (1965) and Korn et al. (2016). Triassic (Tr.), Griesbachian (Gr.),Wuchiapingian (Wu.).

Fig. 26. Characteristic Late Permian–Early Triassic conodonts from the Julfa region (from Ghaderi et al. 2014); all scale bars are 100 μm. All specimens are stored in the collection of the Ferdowsi University of Mashhad. a – *Clarkina orientalis* (Barskov and Koroleva, 1970); FUM#1J192.1; Upper Julfa Beds (*Vedioceras* Beds), Ali Bashi 1 section. b – *Clarkina subcarinata* Sweet, 1973; FUM#4J142.8; Zal Member (Ali Bashi Formation), Ali Bashi 4 section. c – *Clarkina changxingensis* Wang and Wang, 1981; FUM#4J153.1; Zal Member (Ali Bashi Formation), Ali Bashi 4 section. d – *Clarkina bachmanni* Kozur, 2004; FUM#AJ185.23; *Paratirolites* Limestone (Ali Bashi Formation), Aras Valley section. e – *Clarkina nodosa* Kozur, 2004; FUM#G249.16; *Paratirolites* Limestone (Ali Bashi Formation), Ali Bashi M section. f – *Clarkina yini* Mei, 1998; FUM#AJ192.4; *Paratirolites* Limestone (Ali Bashi Formation), Aras Valley section. g – *Clarkina abadehensis* Kozur, 2004; FUM#1J248.9; *Paratirolites* Limestone (Ali Bashi Formation), Ali Bashi 1 section. h – *Clarkina hauschkei* Kozur, 2004, FUM#1J249D.9; *Paratirolites* Limestone (Ali Bashi Formation), Ali Bashi 1 section. i – *Hindeodus eurypyge* Nicoll, Metcalfe and Wang, 2002, FUM#1J255.7 (cusp broken); Zal Member (Ali Bashi Formation), Ali Bashi 1 section. j – *Hindeodus typicalis* Sweet, 1970, FUM#G233.5; *Paratirolites* Limestone (Ali Bashi Formation), Ali Bashi M section. k – *Hindeodus typicalis* Sweet, 1970, FUM#4J200.56; *Paratirolites* Limestone (Ali Bashi Formation), Ali Bashi 4 section. l – *Hindeodus julfensis* Sweet, 1973, FUM#1J198.4; Zal Member (Ali Bashi Formation), Ali Bashi 4 section. m – *Hindeodus praeparvus* Kozur, 1996, FUM#G274.6 (cusp broken); Aras Member (Elikah Formation), Ali Bashi M section. n – *Hindeodus changxingensis* Wang, 1995, FUM#4J201.6 (cusp broken); Aras Member (Elikah Formation), Ali Bashi 4 section. o – *Merrillina ultima* Kozur, 2004, FUM#AJ204.13; Aras Member (Elikah Formation), Aras Valley Section. p – *Hindeodus parvus* Kozur and Pjatakova, 1976, FUM#4J213.1; Elikah Formation; Ali Bashi 4 section.

Fig. 27. Columnar sections of the *Paratirolites* Limestone in the Aras Valley, Ali Bashi 4, Ali Bashi 1 and Zal sections, with their ammonoid zonation. From Korn et al. (2016, Fig. 5).

Fig. 28. Characteristic Changhsingian ammonoids from the Julfa region (Ghaderi et al. 2014, Fig. 7); scale bars equal to 5 mm. All specimens stored in the collection of the Museum für Naturkunde, Berlin. a – *Phisonites triangulus* (Shevyrev 1965) from the Aras Valley section, specimen MB.C.22703. b – *Iranites transcaucasius* (Shevyrev 1965) from the Aras Valley section, specimen MB.C.22704. c – *Dzhulfites nodosus* (Shevyrev 1965) from the Aras Valley section, specimen MB.C.22705. d – *Shevyrevites nodosus* (Shevyrev 1965) from the Aras Valley section, specimen MB.C.22706. e – *Paratirolites trapezoidalis* (Shevyrev 1965) from the Ali Bashi 4 section, specimen MB.C.22707. f – *Stoyanowites dieneri* (Stoyanow 1910) from the Aras Valley section, specimen MB.C.22708. g – *Paratirolites vediensis* (Shevyrev 1965) from the Ali Bashi N section, specimen MB.C.22709. h – *Abichites stoyanowi* (Kiparisova 1947) from the Ali Bashi N section, specimen MB.C.22715. i – *Arasella minuta* (Zakharov 1983)

from the Ali Bashi N section, specimen MB.C.22711.

Fig. 29. Two parallel sections of the uppermost 5 m of the Hambast at Baghuk Mountain (section C is 100 m west of section 1). The sections have been aligned at the extinction horizon (top of the sections). The middle correlation line refers to a dark red index horizon in the lower half of the Hambast Formation, the lower correlation line refers to the index horizon rich in the ammonoid genus *Shevyrevites*.

Fig. 30. Slab of a marly limestone within the lower part of the 'Boundary Clay' with many small ammonoids. Baghuk Mountain, C section.

Fig. 31. Two parallel sections across the 'Boundary Clay' and the base of the Shahreza Formation at Baghuk Mountain (section A is 600 m south-west of section C). All sections have been aligned at the extinction horizon (base of the sections). The upper correlation line refers to the top of the 'Boundary Clay'.

Fig. 32. Composite log with carbonate microfacies characteristics of the Permian–Triassic boundary in the Baghuk Mountain sections.

Fig. 33. Carbonate microfacies of the 'Boundary Clay' at Baghuk Mountain. a – Marly nodules with sponge remains and single ostracods embedded in marly siltstone. Baghuk Mountain, A section, +0.02 m. b – Hematite coated *Frutexites (*Fr*)* and algae segments (a) within microsparitic matrix. Baghuk Mountain, A section, +0.40 m. c – Single ostracod shells (o) and bellerophontid gastropod remains (g) embedded in marly siltstone, Baghuk Mountain, A section, +0.40 m. d – Irregular masses of calcified tubes of microfossils. Baghuk Mountain, A section, +0.69 m.

Fig. 34. A scheme for the conodont zones of NW Iran, central Iran (Abadeh section) and South China (Meishan section). A correlation based on conodont zones between NW Iran and central Iran follows Ghaderi et al. (2014). A correlation between South China and the P-Tr interval in Iran can only be achieved, with great confidence, for the thick lined conodont zones and the extinction horizon (red line). Modified after Schobben (2014; PhD thesis).

Fig. 35. Combined litho- and biostratigraphy scheme for the P-Tr sections of the Julfa region (from Schobben 2014, PhD thesis). Conodont zonation as in Ghaderi et al. (2014) and Schobben et al. (2016). Radiometric and calculated datums for the Meishan P-Tr GSSP section for the Wu-Ch of Shen et al. (2011) as well as the P-Tr boundary and the extinction horizon (South China) of Burgess et al. (2014). Lithology and conodont zones are according to reports by Korte et al. (2004b) for the Abadeh section and Yuan et al. (2014) for the Meishan section. Conodont zones NW Iran, Abadeh and Meishan are numbered according to Fig. 34.

Fig. 36. A scheme for the conodont zones of NW Iran, central Iran (Abadeh section) and South China (Meishan section) (from Schobben 2014, PhD thesis). The correlation based on conodont zones between NW Iran and central Iran follows Ghaderi et al. (2014). The correlation between

South China and the P-Tr interval in Iran can only be achieved, with great confidence, for the thick lined conodont zones and the extinction horizon (red line).

Fig. 37. Morphological classification of microbial build-ups at Baghuk Mountain based on macro- and mesostructural features. Not to scale.

Fig. 38. Field photographs of in situ microbialite occurences in the Baghuk Mountain area (photographs of V. Hairapetian). a – 'Calcite fan' layer in the 'Boundary Clay' showing digitate, upward-growing branches growing together during botryoidal growth. b – A giant domal dendrolite. It shows massive, plano-convex, low relief and lenticular general morphology. Its upper surface is rough and mammillated. In the longitudinal view, sparitic mesoclots within a micritic matrix are observed. Seen in cross-section these mesoclots are composed of digitate columns of laminated nature, growing in vertical and horizontal direction. The columns are laterally linked and are separated by a red, weathered, impure micritic matrix. c – A conical, columnar thrombolite mound with a hemispheroidal macrostructure and clotted mesofabric. d – Small-scale microbial structures on the bedding plane of platy limestones of the Shahreza Formation. C section, +13.80 m.

Fig. 39. Details of in situ microbialites from the Shahreza Formation. a – Field photographs of in situ microbialites. C section, +13.60 m (photograph of V. Hairapetian). b – Scanned polished slab of knobby micropeloidal thrombolite/ precipitated cement. C section +13.85 m. c – Scanned thin section of an arborescent thrombolite with fan-shaped crystals. C section, +13.85 m. d – Rod-like crystals of a knobby micropeloidal thrombolite. C section +13.80 m. e – A framework of fenestral packstone/bindstone with porostromate microfossils, consisting of cyanobacteria and algae with spar-filled fenestral voids. C section, +18.65 m. f – Scanned thin section of a digitate dendrolite showing lobate margins. C section, +18.80 m. g – Bush-like, vertically erect, radial fabric of a dendrolite. C section, +18.80 m. h –Microphotograph of a dendrolite showing internal structure composed of acicular crystals. C section, +18.80 m.

Fig. 40. Field images of limestone outcrop of the Shahreza Formation at C section (photographs by V. Hairapetian). a – Thin, platy limestone beds of the Shahreza Formation. b – Branching, dendroid-like, knobby microbialites at +13.80 m. c – A horizon with abundant microbialites at +13.60 m. d – Club-shaped microbialite with 'holdfast' on the upper bedding plane and inverted conical microbialite on the lower bedding plane.

Fig. 41. Field photographs of the Early Triassic coalescent microbialites (float specimens) (photographs by V. Hairapetian). a – Dark-grey, flower-shaped, sparry calcite microbialite developed in the pale brown micritic matrix, containing filaments, bivalve shell fragments, ammonoids, and high-spired gastropods. The microbialite is capped by a micritic film. b – Kidney-shaped microbialite characterized by irregular, partly concentric structure, where micrite and sparite alternate. c – Concave, flower-shaped microbialite embedded in the fenestral, filament-rich micritic matrix. d – Dark-grey, ovoidal, lenticular sparry calcite microbialite developed in the pale brown micritic matrix, containing abundant filaments (probably sponge spicule remains).

The microbialite is filled by an argillaceous micrite.

Fig. 42. Field photographs of the Early Triassic microbialites (float specimens) (photographs by V. Hairapetian). a – Bedding plane of platy limestone with closely packed small microbial structures. b – Kidney-shaped microbialite formed by amalgamation of two single ovoidal specimes and/or coalescent sponge with a dermal surface. c – Dark-grey, ovoidal, sparry calcite microbialite. Note the mineralization in the centre of the structure within the micritic matrix. d – Leaf-like, lobated microbialite with sparry calcite on the rims. Partly stromatolitic seen in a cross-section.

Fig. 43. Details of the Early Triassic microbialites from float material. a – Field photograph of an ovoidal microbialite with a large calcite crystals in their interior (photograph by V. Hairapetian). b – Scanned thin-section of an ovoidal microbialite in picture a showing an inverted conical (club-shaped) microbialite with dendrolitic and aphanitic microstructure embedded in a micritic matrix containing filaments. c – Detail of microbialite in b showing bundles of rod-like calcite crystals. d – Small cuspate to vermiform microfenestrae within the matrix.

Fig. 44. Field photographs of the 'Boundary Clay' and the Shahreza Formation at Baghuk Mountain (photographs by V. Hairapetian). a – Outcrop of shales and clays of the 'Boundary Clay'. b – 'Calcite fan' layer at C section. c – Dome-shaped buildups containing the 'Calcite fan'at K section. d – Enlarged view of white rectangle in c showing a botryoidal fan.

Fig. 45. Microphotographs of the 'Calcite fan'. a – Scanned thin-section showing fanning aragonite pseudomorphs with irregular margins, enclosed in grey-colored micrite matrix with mesh of filaments. Internal lamination disturbed by stylolites. Baghuk Mountain, C section, +1.30 m. b – Sparry calcite-filled void with a dense bushy micrite crust. Baghuk Mountain, C section, +1.30 m. c – Scanned thin-section showing calcite fans with botryoidal, upward-branching crystals. Baghuk Mountain, C section, +0.80 m. d – Crystals with blades with broad, flattened terminations. Aggrading neomorphism produced calcite crystal mosaic of inequigranular fabric. Baghuk Mountain C section, +0.80 m.

Fig. 46. SEM-EDX characteristics of the 'Calcite fan'. a – Backscattered electron image (SEM-BSE) of cubic magnetite crystals within the 'calcite fan' botryoids. b –Secondary electron (SEM-SE) image of magnetite crystals; crosses show a place where measurements were taken and numbers 1 and 2 are spectrum numbers. c – EDX spectrum of a point 1 in b showing that analyzed crystal is a magntetite, not pyrite. d – EDX spectrum of a point 2 in b (magntetite). Baghuk Mountain, C section, +1.30 m.

Fig. 47. Elemental distribution maps illustrating differences in composition betwen 'calcite fan' crystals and surrounding matrix. Baghuk Mountain, C section, +1.30 m.

Fig. 48. Plain light images of the 'calcite fan' crystals and surrounding matrix in a, c, e, g and with corresponding optical cold-cathode cathodoluminescence images in b, d, f, h. Baghuk Mountain, C section, +1.30 m.

Fig. 49. Microphotographs of a peloidal bindstone. a – Scanned thin-section showing alternating couplets of micritic and peloidal layers. Peloidal clotted and grumous micrite of a thrombolite with small sparite-filled cavities. Baghuk Mountain, A section, +2.20 m. b –Bundles of close-packed micrite threads in a partly dolomitized microsparitic matrix – Baghuk Mountain, C section, +2.43 m. c – Sparry calcite spheres and dense micrite of Baghuk Mountain, C section, +2.45 m. d – Bushy micrite with poorly defined margin and locally showing transition to a microsparite. Baghuk Mountain, C section, +2.20m.

Fig. 50. Details of in situ microbialites from the Shahreza Formation. a – Scanned polished slab of a club-shaped hybrid stromatolite. C section, + 8.55 m. b – Details of a stromatolitic lamination – alternation of a dense micrite layers with sparry calcite layers with fan-shaped crystals. C section, + 8.55 m. c – Bindstone/boundstone on a bivalve shells that acted as substrate for growth of microbial, micritic and microsparitic crusts. C section, + 8.70 m. d – Micritic microbial crust on skeletal elements of an ammonoid and of a bivalve. Note abundant gastropod (g) shells in the matrix. C section, + 13.95 m. e – Benthic microbial communities (BMC). C section, + 9.35 m. f – Scanned thin section of a microbial packstone showing irregular, columnar and spherical, peloidal, microsparitic bodies. C section, + 9.30 m. g – Micritic, microbial ooids. C section, + 9.30 m. h – Fenestral voids with irregular roofs filled with a sparry calcite. C section, + 9.30 m.

Fig. 51. Scanned polished slab of a mushroom-shaped hybrid microbialite. This microbialite is characterized by a thick sparitic, partly laminated ‘holdfast’ and is covered by a sparitic ‘lid’. Internal structure is composed of alternating layers of sparry calcite and mud-to silt-sized material. The sparitic ‘lid’ is cracked. This microbialite can be classified as hybrid microbialite, where stromatolitic lamination is preserved in the centre of the specimen, whereas its walls and edges are made of leiolite (structureless sparry calcite of the walls). The hybrid microbialite is enclosed in a burrowed, partly recrystallized lime mudstone with remains of sponge spicules.

Fig. 52. Bindstones/cement crust from float specimens at Baghuk Mountain. a – Scanned polished slab of a digitate, isopachous crust on an ammonoid shell. b – Scanned thin section showing isopachous, fibrous crust. c – Skeletal stromatolite composed of tiny filaments that are probably sponge spicule remains or algal threads. d – Scanned polished slab showing biolaminated structures as well as micritic and sparitic crust on a bivalve shell.

Fig. 53. Hybrid microbialites from the Baghuk Mountain float specimens. a – Scanned polished slab of an hybrid microbialite showing sparitic ‘lid’ and small stromatolitic columns. b – Scanned polished slab of a hybrid microbialite. It is characterized by a stromatolitic lamination in the centre, lobate margins of dendritic spar and spartic ‘lid’ in the uppermost part of the specimen. c – Scanned thin-section of a club-shaped microbialite with dendritic calcite crystals on the edges, embedded in a fenestral wackestone. d – Scanned thin-section of a club-shaped microbialite with microfabric made of granular calcite crystals.

Fig. 54. Lithology and bulk carbonate carbon isotope values of the P-Tr boundary sections at

Aras Valley (20 m below, 5 m above the extinction horizon). Conodont zone sare numbered according to the conodont zonation after Ghaderi et al. (2014) in the Fig. 34.

Fig. 55. Lithology and bulk carbonate carbon isotope values of the P-Tr boundary sections at Ali Bashi 1 (20 m below, 5 m above the extinction horizon). Conodont zones are numbered according to the conodont zonation after Ghaderi et al. (2014) in the Fig. 34.

Fig. 56. Lithology and bulk carbonate carbon isotope values of the P-Tr boundary sections at Ali Bashi 4 (20 m below, 5 m above the extinction horizon). Conodont zones are numbered according to the conodont zonation after Ghaderi et al. (2014) in the Fig. 34.

Fig. 57. Lithology and bulk carbonate carbon isotope values of the P-Tr boundary sections at Zal (20 m below, 5 m above the extinction horizon). Conodont zones are numbered according to the conodont zonation after Ghaderi et al. (2014) in the Fig. 34.

Fig. 58. Lithology and bulk carbonate carbon isotope values of the P-Tr boundary sections at Baghuk Mountain, composed of section 1 (10 m below the extinction horizon) and section C (15 m above the extinction horizon). Conodont zones are numbered according to the conodont zonation after Ghaderi et al. (2014) in the Fig. 34.

Fig. 59. Lithology and bulk carbonate carbon isotope values of the P-Tr boundary sections at Aras Valley, Ali Bashi 1, and Zal (5 m below, 5 m above the extinction horizon). Conodont zones are numbered according to the conodont zonation after Ghaderi et al. (2014) in the Fig. 34.

Fig. 60. Box-and-Whiskers diagram of bulk carbonate carbon isotope values of the P-Tr boundary sections from NW and Central Iran subdivided into conodont-based stratigraphic intervals. AB1 (Ali Bashi 1), AB4 (Ali Bashi 4), AV (Aras Valley), BGK1 (Baghuk Mountain 1), BGKA (Baghuk Mountain A), BGKB2 (Baghuk Mountain B2), BMC (Baghuk Mountain C), BMJ (Baghuk Mountain J), Aba (Abadeh), ZL (Zal).

Fig. 61. Stratigraphic median $\delta^{13}C_{carb}$ values of the P-Tr boundary sections from NW and Central Iran subdivided into conodont-based stratigraphic intervals.

Fig. 62. Lithology and bulk nitrogen isotope values of the P-Tr boundary sections at Ali Bashi 1 (20 m below, 5 m above the extinction horizon).

Fig. 63. Chemostratigraphy of the P-Tr interval at Ali Bashi 1 section. TN (total nitrogen), TOC (total organic carbon). Conodont zones are numbered as follows: 1 - *C. changxingensis*, 2 - *C. bachmanni*, 3 - *C. nodosa*, 4 - *C. yini*, 5 - *C. abadehensis*, 6 - *C. hauschkei*, 7 - *Hindeodus praeparvus–H. changxingensis*, 8 - *Merrilina ultima–Stepanovites* ?*mostleri*, 9 - *Hindeodus parvus*, 10 - *H. lobota*, 11 - *Isarcica staeschei* zone.

Fig. 64. Chemostratigraphy of the P-Tr interval at Zal section. TN (total nitrogen), TOC (total

organic carbon). Conodont zones are numbered as follows: 1 - *C. changxingensis*, 2 - *C. bachmanni*, 3 - *C. nodosa*, 4 - *C. yini*, 5 - *C. abadehensis*, 6 - *C. hauschkei*, 7 - *Hindeodus praeparvus–H. changxingensis*, 8 - *Merrilina ultima–Stepanovites* ?*mostleri*, 9 - *Hindeodus parvus*, 10 - *H. lobota* zone.

Fig. 65. Nitrogen and bulk carbonate carbon isotopic compositions, and their relations to TN and TOC contents at Ali Bashi 1 section.

Fig. 66. Nitrogen and bulk carbonate carbon isotopic compositions, and their relations to TN and TOC contents at Zal section. Dashed line represents a C/N ratio of 6.6 for original organic matter in sediments (Redfield value).

Fig. 67. Bulk carbonate carbon, and bulk nitrogen isotopic compositions, and calcium carbonate content, and a diagram showing presence of clay minerals in marly/silty samples around the extinction horizon in the Ali Bashi 1 section. Conodont zones are numbered as follows: 1 - *C. changxingensis*, 2 - *C. bachmanni*, 3 - *C. nodosa*, 4 - *C. yini*, 5 - *C. abadehensis*, 6 - *C. hauschkei*, 7 - *Hindeodus praeparvus–H. changxingensis*, 8 - *Merrilina ultima–Stepanovites* ?*mostleri*, 9 - *Hindeodus parvus*, 10 - *H. lobota*, 11 - *Isarcica staeschei* zone.

Fig. 68. Fossil frequency changes around the extinction horizon coupled with calcium carbonate content at Ali Bashi 1. i. Conodont zones are numbered as follows: 1 - *C. changxingensis*, 2 - *C. bachmanni*, 3 - *C. nodosa*, 4 - *C. yini*, 5 - *C. abadehensis*, 6 - *C. hauschkei*, 7 - *Hindeodus praeparvus–H. changxingensis*, 8 - *Merrilina ultima–Stepanovites* ?*mostleri*, 9 - *Hindeodus parvus*, 10 - *H. lobota*, 11 - *Isarcica staeschei* zone.

Fig. 69. Bulk carbonate carbon, and bulk nitrogen isotopic compositions, and calcium carbonate content around the extinction horizon in the Zal section. Conodont zones are numbered as follows: 1 - *C. changxingensis*, 2 - *C. bachmanni*, 3 - *C. nodosa*, 4 - *C. yini*, 5 - *C. abadehensis*, 6 - *C. hauschkei*, 7 - *Hindeodus praeparvus–H. changxingensis*, 8 - *Merrilina ultima–Stepanovites* ?*mostleri*, 9 - *Hindeodus parvus*, 10 - *H. lobota* zone.

Fig. 70. Cross section of a specimen of *Paratirolites* sp. from Baghuk Mountain, MB.C.22215; 92.0. Note the different states of preservation of shell walls and septa: a -recrystallized but rather well preserved shell wall and septa preferably in the mid-dorsal portion of the ammonoid conch; b - dissolved shell wall but sharp demarcation of the ammonoid's internal mould from the sediment at the lower side of the ammonoid conch; c -dissolved shell wall and nearly continuous transition from the ammonoid's internal mould towards the sediment on the upper side of the ammonoid conch.

Fig. 71. Cross-plots of $\delta^{13}C_{carb}$ and $\delta^{18}O_{carb}$ for Ali Bashi 1 section. a - for an interval of 25 m (20 m below, 5 m above the extinction horizon); b - for the *Paratirolites* Limestone; c - for the Aras Member, d - for the *Claraia* Beds; r - correlation coefficient.

Table 1. Lithological and stratigraphic subdivision of the P–Tr boundary sections in the Ali

Bashi Mountains (units, unit names, lithology, fauna, and thickness after Stepanov et al. 1969).

Table 2. Lithological and stratigraphic subdivision of the P–Tr boundary sections in Central Iran (units, unit names, lithology, fauna, and thickness after Taraz et al. 1981; stages after Kozur 2005).

Table 3. Detailed facies description of the investigated Permian and Triassic beds in the Ali Bashi 1 section.

Table 4. Detailed facies description of the investigated Permian beds in the Ali Bashi 4 section.

Table 5. Detailed facies description of the investigated Triassic beds in the Ali Bashi N section.

Table 6. Detailed facies description of the investigated Permian and Triassic beds in the Aras Valley section.

Table 7. Detailed facies description of the investigated Permian and Triassic beds in the Zal section.

Table 8. Detailed facies description of the investigated Permian and Triassic beds in the Baghuk Mountain sections.

Table 9. References for the P-Tr boundary sections and regions in Iran with investigated microbialite structures and direct precipitates from seawater.

Table 10. Approximate estimates of typical ranges of sedimentary bulk $\delta^{15}N$ values in relation to the respective governing processes affecting the marine nitrogen cycle and their typical marine environments (modified after Struck 2012 and Cremonese et al. 2013).

Table 11. Average $\delta^{15}N$ values of different substrates.

Table 12. Correlation coefficients for entire investigated sections and for each lithostratigraphic unit. EF = Elikah Formation, BC = 'Boundary Clay', PL = *Paratirolites* Limestone, n = number of samples.

1 INTRODUCTION

The end-Permian mass extinction event and the Permian-Triassic boundary

The end-Permian mass extinction (EPME) just prior to the conodont-defined Permian-Triassic boundary was one of the *Big Five* mass extinction events in Earth history; it was the most severe diversity crisis of marine and terrestrial biota in the Phanerozoic. The end-Permian mass extinction resulted in extinction of more than 90 % of marine species, about 70 % of terrestrial vertebrate species, and about 90 % of plant life (Erwin 1994, 2001, 2006; Hallam and Wignall 1997; Knoll et al. 2007). Particularly the tropical and reef-building organisms and the warm water biota were affected, marking the beginning of the 'metazoan reef gap' and 'chert gap', respectively (Hallam and Wignall 1997; Kozur 1998; Racki 1999; Knoll et al. 2007; Foster and Twitchett 2014). The highly diversified Late Permian reef communities with brachiopods, fusulinid foraminifers, corals and crinoids were replaced in Earliest Triassic time by the poorly diversed marine communities dominated by microbes, ostracods, gastropods and disaster taxa (Chen et al. 2010; Chen and Benton 2012). The recovery of marine life began rapidly within the first 2 Ma of the Triassic for ammonoids and conodonts (Chen and Benton 2012, and references therein). The end-Permian mass extinction was a physiological crisis affecting carbonate-secreting organisms with a poorly buffered respiratory system (Caldeira and Wickett 2003; Pörtner et al. 2005; Knoll et al. 2007). According to Knoll et al. (1996, 2007), the animals with siliceous and phosphatic skeletons were more likely to survive the mass extinction event compared to taxa with calcitic skeletons (see also Clapham and Payne 2011). In addition, the P-Tr marine mass extinction caused a great change in dominance from non-motile to motile animals (Bambach et al. 2002).

As a consequence of the end-Permian extinction, marine ecosystems underwent a profound reorganization. The Late Permian tropical skeletal carbonate factories with foraminifers and algae as carbonate producers were replaced in the Early Triassic by micritic, biotically-induced and abiotic carbonate factories, which are predominantly characterized by the abundance of grains and micrite formed by microbes (Baud 1997; Leven 1998; Chen et al. 2010; Chen and Benton 2012; Pietsch et al. 2016). In the aftermath of the EPME, carbonate platforms experienced a gradual transition from heterozoan- to photozoan-dominated communities, which are interpreted as biased towards primary productivity of probable phototrophic cyanobacteria, archaea, green-sulfur bacteria and chemoautotroph-dominated ecosystems (Grice et al. 2005; Xie et al. 2005, 2007a, 2007b, 2010; Cao et al. 2009; Luo et al. 2013; Heindel et al. 2014; Shen et al. 2015). Microbial carbonates became dominant and grew mostly as layers and small buildups in low-latitude shallow shelf settings (localities in South China, Vietnam, Southern Turkey, Iran, Eastern Arabia, Japan, Italy), in low-latitude deep shelf (Hungary, Oman, Armenia) and in high latitude shallow shelf (Greenland, Madagascar, Tibet) environments (Kershaw et al. 2002, 2007, 2011; 2012; Baud et al. 1997, 2005a 2005b, 2007; Sano and Nakashima 1997; Lehrmann et al. 1998, 2001; Lehrmann 1999; Wignall and Twitchett 2002; Maurer et al. 2009; Richoz et al. 2010). Microbialites and inorganic carbonate crystal fans represent space- and time-specific, environmentally induced carbonates (Riding 1997, 2000; Ezaki et al. 2008). The causes for the

rapid colonization of the microbial communities in marine settings after the EPME are still a matter of discussion. The possible hypotheses comprise ecological relaxation after the mass extinction caused by diminution of predation and competition (Vermeij 1977; Schubert and Bottjer 1992; Riding and Liang 2005; Yang et al. 2011) and geochemical seawater and atmosphere changes (Grotzinger and Knoll 1995; Kidder and Worsley 2004; Kershaw et al. 2002, 2007, 2015).

On land the extinction event was marked by a loss of many vertebrate species and major vegetation changes (Looy et al. 1999; Ward et al. 2005). In the Late Permian, diminution of woody vegetation dramatically affected terrestrial ecosystems. In the semi-arid, equatorial areas, the stable gymnosperm-dominated floras were replaced by rapidly growing, early successional communities dominated by lycopods and ferns (Hermann et al. 2011). Peat forests became extinct during the Permian-Triassic transition in the northern and southern humid climatic zones of Pangaea (Looy et al. 1999). In the Permian-Triassic terrestrial strata of the Karoo Basin, South Africa, abrupt and gradual extinction particularly among the dicynodont therapsids and carnivorous gorgonopsians occurred through the end-Permian mass extinction (Ward et al. 2005; Brusatte et al. 2010).

The timing of the crisis is relatively well established. Jin et al. (2000) placed the end-Permian mass extinction horizon in the Meishan section between Bed 24e (lime mudstone) and the base of Bed 25 (white ash clay) based on the last occurrence of major benthos, and decline in abundance and diversity of fossil fragments. The first occurrence datum (FAD) of the conodont *Hindeodus parvus* between bed 27c and bed 27b at section D of Meishan has been proposed as the biostratigraphic P-T boundary (Jin et al. 2000). U-Pb dating with ID TIMS of zircon crystals from five volcanic ash beds from the Global Stratotype Section and Point for the Permian-Triassic boundary at Meishan, China, by Burgess et al. (2014) defined an age model for the extinction. The 'extinction horizon' (base bed 25 at Meishan) is 251.941± 0.037 Ma, the extinction event is possibly confined to an interval of 60 ± 48 kyr, and and coincided with a $\delta^{13}C$ excursion of -5 ‰ that is estimated to have lasted for around 20 kyr (Shen et al. 2011a; Burgess et al. 2014).

Several scenarios have been proposed as possible causes for the most dramatic demise of life, including extensive Siberian Trap volcanism (e.g., Saunders and Reichow 2009; Svensen et al. 2009) acting as a trigger mechanism for many cascading, devastating environmental events such as rapid temperature changes (Joachimski et al. 2012; Schobben et al. 2014), marine anoxia (e.g., Algeo et al 2011a,b; Brennecka et al. 2011), photic zone euxinia with poisonous H_2S (e.g., Kump et al. 2005; Riccardi et al. 2006, 2007; Grice et al. 2007, Meyer et al. 2008), strong terrestrial weathering (Algeo and Twitchet 2010; Algeo et al. 2011), and enhanced carbon dioxide concentration (hypercapnia) together with related ocean acidification (e.g., Knoll et al. 1996, 2007; Fraiser and Bottjer 2007) and abrupt blooms of methane-producing microbes (Renne et al. 1995; Berner 2002; Rothman et al. 2014). The synergistic effects of global warming (enhanced ocean uptake of CO_2 with climate driven enhanced vertical water column stratification and subsequent seawater deoxygenation) are referred to as the 'deadly trio' (Bijma et al.

2013). Ocean acidification has been mentioned to be responsible for the reef crisis and thus for a decline in carbonate production across the Permian-Triassic boundary (Clapham and Payne 2011; Kiessling and Simpson 2011). Additionally, it has been hypothetised that fluctuations in reactive iron supply at short time intervals (10 ka) could have spawned large-scale euxinic regions hazardous for many eukaryotic life forms (Schobben et al. 2015, 2017).

Some scenarios have linked extraterrestrial perperators to the mass extinction (Kajiwara et al. 1994; Kaiho et al. 2001, 2006a, 2006b; Newton et al. 2004; Bottrell and Newton 2006). The large bolide impact hypothesis has triggered numerous and occasionally contentious debates, with the widely debated alleged existence of the large "Bedout" impact structure on the Ontong Plateau and evidence of impact evidence in the form of planar deformation features at Antarctic and Australian sites. These were variably judged by the scientific community (e.g., Becker et al. 2004; Glikson 2004; Retallack et al. 1998; Langenhorst et al. 2005). Supposed shocked quartz grains found at sites in Australia appear to be falsely identifed (Renne et al. 2004). Globally recorded isotope characteristics ostensibly diagnostic for an impact, platinum group element enrichment and a sulphur isotope excursion, can also be related to volcanism and marine anoxia, respectively (Koeberl et al. 2002, 2004). It is safe to say at this time that there is no evidence in favour of this extinction mechanism, with respect to the P-Tr boundary, that has not remained highly controversial. On the other hand, some have inferred from the confirmed relationship between the considerable Cretaceous-Paleogene mass extinction and bolide impact that the even greater extent of the P-Tr boundary extinction and its equally very short duration could only be the result of an even larger impact event (Chapman 2005).

Extensive chemostratigraphic investigations have been conducted for numerous marine and continental P-Tr boundary sections. Isotope profiles across the boundary show significant changes. The P-Tr boundary interval is marked by long-term (0.5-1.0 Ma) perturbations in the global carbon cycle, visible in a globally prominent negative carbon isotope excursion (Baud et al. 1989; Oberhänsli et al.1989) observed in marine carbonates (e.g., Chen et al. 1984; Holser and Magaritz 1987; Magaritz et al. 1988; Holser et al. 1989; Baud et al. 1989; Heydari et al. 2000b; Dolenec et al. 2001; Musashi et al. 2001; Twitchett et al. 2001; Korte et al. 2004a; Korte et al. 2004b; Korte et al. 2004c; Payne et al. 2004; Korte and Kozur 2005a, 2010; Riccardi et al. 2007; Xie et al. 2007a) and marine organic matter (e.g., Wang et al. 1994; Wignall et al. 1998; Hansen et al. 2000; Krull et al. 2000; Musashi et al. 2001; de Wit et al. 2002; Thomas et al. 2004; Visscher et al. 2004; Sandler et al. 2006; Fenton et al. 2007; Riccardi et al. 2007; Fio et al. 2010; Luo et al. 2011) and in both shallow-marine as well as deep-marine environments (for a review, see Korte and Kozur 2010). This $\delta^{13}C$ feature has been documented in non-marine P-Tr boundary sections (e.g., Hansen et al. 2000; Krull and Retallack 2000; de Wit et al. 2002; Peng et al. 2005; Retallack et al. 2005; Coney et al. 2007; Retallack and Jahren 2008) and lacustrine carbonates (Korte and Kozur 2005b). All these observations suggest that the P-Tr negative carbon isotope excursion is global in scale, enabling its use for stratigraphic correlations (Korte and Kozur 2005a; Grasby and Beauchamp 2008; Kraus et al. 2009; Cao et al. 2010; Hermann et al. 2010; Richoz et al. 2010) and identifying palaeoenvironmental changes.

The carbon isotope perturbation associated with the EPME has been reported in detail for biostratigraphically well-characterized sections in China, such as the Global Boundary Stratotype Section and Point (GSSP) for the base of the Triassic at Meishan (Chen et al. 1984, 1991; Jin et al. 2000; Yin et al. 2001; Cao et al. 2002, 2009). The Iranian P-Tr boundary sections also represent biostratigraphically complete and well-defined successions with higher sedimentation rates compared to Meishan. Moreover, the sedimentary environment of the Iranian sections is interpreted to have been an open ocean, pelagic palaeoenvironment (Stepanov et al. 1969; Teichert et al. 1973; Kozur, 2004, 2005, 2007b; Shen and Mei 2010), therefore representing a detailed record of palaeoenvironmental changes across the Palaeozoic-Mesozoic transition. Carbon isotope records for several Iranian sections have already been published (Baud et al. 1989; Korte et al. 2004a; Korte et al. 2004b; Korte et al. 2004c; Korte and Kozur 2005a; Horacek et al. 2007; Korte et al. 2010; Richoz et al. 2010) and chemostratigraphic characteristics of these successions suggest a general carbon isotope trend for the P-Tr boundary (Korte and Kozur 2010). This "first-order" $\delta^{13}C$ trend (sensu Schobben et al. 2016) has been attributed to Siberian Trap volcanism and related metamorphism of organic-rich deposits (Retallack and Krull 2006; Svensen et al. 2009; Sobolev et al. 2011), erosion of organic matter from continents (Holser and Magaritz 1987) and a reduction in marine primary productivity (Rampino and Caldeira, 2005). Superimposed fluctuations around the "first-order" carbon isotope trend are referred to as "second-order excursions" that represent short (~ 2-20 kyr) stratigraphic intervals including individual lithological horizons (e.g., Richoz et al. 2010; Schobben et al. 2016). Those short-term $\delta^{13}C$ excursions (e.g., at Meishan, South China) have been attributed to massive CH_4 release from methane clathrate dissociation (Berner 2002; Benton and Twitchett 2003) or rapid expansion of methanogens (Rothman et al. 2014).

The Palaeozoic-Mesozoic transition is marked by changes in the stable nitrogen isotope composition (Luo et al. 2011; Saitoh et al. 2014). Algeo et al. (2007) analyzed $\delta^{15}N$ values of Late Permian to Early Triassic marine rocks at Guryul Ravine in Kashmir (India) and pointed out a negative $\delta^{15}N$ anomaly around the extinction horizon. The $\delta^{15}N$ values of bulk marine organic matter were also reported from several Chinese P-Tr boundary sections (Cao et al. 2009; Luo et al. 2011). Cao et al. (2009) revealed a progressive $\delta^{15}N$ decline in the Changhsingian (Late Permian) at Meishan and a negative $\delta^{15}N$ shift around the PTB suggesting increased nitrogen fixation in the ocean. Algeo et al. (2012) and Knies et al. (2013) carried out nitrogen isotopic analysis of Late Permian to Early Triassic clastic successions in Arctic Canada. They documented relatively high $\delta^{15}N$ values for the Late Permian implying denitrification. A negative $\delta^{15}N$ shift across the extinction horizon is apparently well correlated on a global scale.

P-Tr boundary sections in NW and Central Iran

The discovery history of Permian-Triassic (P-Tr) boundary sections in NW Iran sections is tightly connected to the two neighbouring towns of Dzhulfa (or Culfa; Nakhichevan Province, Azerbaijan) and Julfa (or Jolfa; East Azerbaijan Province, Iran), located on the northern and southern banks of the Araxes (Aras) River in the southern Transcaucasian region (Ruzhencev and Sarytcheva 1965; Teichert et al. 1973; Rostovtsev and Azaryan 1973) (Fig. 1) Time-equiv-

alent occurrences in the vicinity of the town of Abadeh (Central Iran) have since gained increasing interest; these sections have provided eminently important material (Taraz 1969, 1971, 1973; Bando 1979, 1981; Taraz et al. 1981). The sedimentary successions in Iran allow documention of the most severe mass extinction event in the Phanerozoic in great detail (Ghaderi et al. 2014a, 2014b; Leda et al. 2014; Schobben et al. 2014). The P-Tr boundary sections in Iran had a palaeogeographic position at 252 Ma in the central Tethys near the equator (Golonka 2000). They provide a great opportunity to study biostratigraphically complete, fossiliferous successions in a carbonate-dominated facies and complement the much more intensely investigated South Chinese sections. The global (Chinese) Wuchiapingian and Changxingian stages are, in the Tethyan region, often named Dzhulfian and Dorashamian, respectively. The latter two are named after the town of Dzhulfa and the railway station at Dorasham, both north of the Araxes River in the province of Nakhichevan, Azerbaijan.

Most of the P-Tr boundary sections in the Transcaucasian region (Armenia, Azerbaijan), NW Iran and Central Iran display a characteristic rock succession composed of carbonates (the latest Permian *Paratirolites* Limestone and the Triassic Elikah Formation) with the intercalated so-called 'Boundary Clay', which is the base of the Elikah Formation) (Kozur 2004; Korte and Kozur 2005). An abrupt lithological change from nodular limestones of the *Paratirolites* Limestone to clays and shales of the Elikah Formation marks the end-Permian mass extinction horizon (EPME) (e.g., Kozur 2007; Korte and Kozur 2010.) At the extinction horizon (EH) a significant change in the frequency of fossils occurs, and that change is contemporaneous with a rapid drop of carbonate content from more than 90% to less than 30% (Ghaderi et al. 2014). At this horizon, all corals and brachiopods disappear and substantial decreases in conodont abundances are observed (Korn et al. 2016). However, ostracods, foraminifera and sponge spicules remain abundant (Kozur 2007; Leda et al. 2014). For ammonoids, two extinction pulses may exist at Julfa (1.4 and 2.5 m below the Aras Member), whereas only one pulse is evident at Baghuk (2.4 m below the 'Boundary Clay') (Kiessling et al. 2018). There is a pronounced trend toward smaller body size of ammonoids, expressed by reduction in the number of notches in the regional *Paratirolites kittli* ammonoid zone. There is, however, no indication of an extinction pulse at the boundary between *Paratirolites* Limestone and Aras Member at Julfa (Kiessling et al. 2018). The first appearance datum (FAD) of the conodont *Hindeodus parvus* has been proposed as the biostratigraphic P-T boundary. The conodont-defined Permian-Triassic boundary has, in studied sections in Iran, a position near the top of the 'Boundary Clay' at the base of the carbonatic portion of the Elikah Formation (e.g., Kozur 2004, 2007). A detailed lithostratigraphic and sedimentological analysis of the P-Tr boundary beds of NW and Central Iran has been carried out already (Heydari et al. 2000, 2003, 2008; Kozur 2007; Leda et al. 2014). For instance, a subdivision of the *Paratirolites* Limestone based on characteristics in lithology or microfacies was achieved for both regions (Leda et al. 2014).

In the following I present petrographical and sedimentological results for five parallel sections in the Julfa area and compare them with those for three newly discovered sections in the Baghuk Mountain area near Abadeh in Central Iran.

Goals

The main goal of my thesis is the investigation of the P-Tr biotic crisis and its aftermath through the documentation of the P-Tr boundary in fossiliferous sections of northwestern and Central Iran. The fundamental questions to be addressed are:

• Do the Iranian sections show a continuous lithological record across the P-Tr boundary and can significant lithological marker beds, such as the Boundary Clay, event horizons, etc. be correlated with other sections in the Tethyan region?

• Is there a gradual or punctuated succession of faunas and can biological and physical trends and events be correlated?

• What has produced the seawater isotope ($\delta^{13}C$, $\delta^{15}N$) signals at the P-Tr boundary and in the Early Triassic?

• Can temperature changes, ocean anoxia, strong volcanism or other factors be related to the Late Permian biotic crisis?

This interdisciplinary study integrates detailed sedimentological studies in the field with petrographic and geochemical - including stable isotope - investigations. The results will show how changes in these properties correspond to the faunal evolutionary patterns and will provide a better understanding of the nature and causes of the P-Tr boundary events in the Palaeotethys.

Sedimentological investigation of the sections in the field concentrated on the recognition of features indicative of subaerial exposure, such as desiccation cracks, peritidal fenestrae, calcretes etc., particularly in the vicinity of the P-Tr boundary. Thin section analysis was used for carbonate microfacies determination and to examine the microfossil content, but also to assess the diagenetic history of the sediments. X-ray diffraction analyses of the sediments allowed to determine their mineralogical compositions, helped to identify ash layers and with the deciphering of changes in the composition of the siliciclastic influx into the shallow marine environment.

High-stratigraphic-resolution carbon isotope values ($\delta^{13}C_{carb}$) for bulk rock carbonate samples served to infer palaeoclimatic and palaeoenvironmental processes, which may be related to the biological crisis. This work also helped to document and to explain changes in the rock succession and the environment. $\delta^{13}C_{carb}$ was measured because it is one of the most important tracers for the stratigraphic location of the P-Tr mass extinction event and the P-Tr boundary (e.g., Payne et al. 2004; Korte et al. 2005a; Korte and Kozur 2010). The excellent outcrop conditions allowed for the production of a carbonate isotope curve at an extremely detailed resolution. Nitrogen isotopes of decalcified samples and nitrogen isotopes of bulk rock samples, together with detailed knowledge of the local depositional and diagenetic environment, held great promise to reveal at least semi-quantitatively temporal variations of marine nitrogen cycle processes across the P-Tr boundary, and to identify ocean anoxic events.

All investigations in this project were aimed at figuring out possible reasons for the Permian-Triassic crisis and paleoenvironmental development thereafter. The sections in NW and Central Iran provide, because of their excellent outcrop conditions and their rich inventory of sedimentological and palaeontological features, an important basis for future discussions.

Figure 1 Geographic position of the Permian-Triassic boundary sections in the regions of Julfa and at Baghuk Mountain.

2 LOCALITIES, PALAEOGEOGRAPHY AND HISTORICAL BACKGROUND

2.1 Julfa area

Figure 2 Outcrop of the Permian–Triassic boundary beds at Aras Valley. Thickness of the *Paratirolites* Limestone is 4.60 m.

Outcrops of Late Permian to Early Triassic successions are known from north and south of the Aras (Araxes) River in the vicinity of Dzhulfa (Nakhichevan; Azerbaijan) and Julfa (East Azerbaijan, Iran) (Fig. 1). These sections expose sedimentary rocks of the outer shelf (Mohtat Aghai et al. 2005; Kozur 2007) and enable a detailed investigation of the Late Permian stratigraphy and the Palaeozoic-Mesozoic transition. Five fossil-rich pelagic P-Tr boundary sections were investigated with respect to their sedimentology and carbonate microfacies:

(1) Aras Valley (39.015° N, 45.434° E): This section is situated about 19 km WNW of the towns of Dzhulfa and Julfa. The outcrop is exposed on the south side of a small hill immediately west of the Aras (Araxes) River, which here coincides with the political boundary between Iran and the province of Nakhichevan (Azerbaijan) (Fig. 2). The Aras Valley section has a position approximately two kilometres west of the Dorasham II section of Ruzhencev et al. (1965).

(2–4) Kuh-e-Ali Bashi (= Ali Bashi Mountains), 9 km west of Julfa (Fig. 3): P-Tr boundary beds crop out in many parallel sections (Teichert et al. (1973) over an extent of about 1.5 km. Three sections were sampled: the Ali Bashi 1 (38.940° N, 45.520° E) and Ali Bashi 4 sections (38.942° N, 45.516° E) of Teichert et al. (1973), and a new one that has a position approximately five hundred metres south-east of the Ali Bashi 1 section (Ali Bashi N section; 38.941° N, 45.516° E).

(5) Zal: This section is situated 22 km SSW of Julfa and 2.2 km NNW of the village of Zal (38.733° N, 45.580° E).

Palaeogeographically the studied sections are situated on the Sanandaj-Sirjan Terrane that belonged, during the latest Permian, to the Cimmerian microcontinent (Scotese and Langford 1995; Golonka 2000; Stampfli and Borel 2002, 2004; Torsvik and Cocks 2004). The Cimmerian terranes migrated from southern Gondwanan paleolatitudes in the Early Permian to subequatorial paleolatitudes by the Middle Permian to the Early Triassic (Muttoni et al. 2009a, 2009b). The Julfa region had a position on the NNE part of the Sanandaj-Sirjan Terrane close to the Palaeotethys.

P-Tr boundary sections in Transcaucasia have been known for a long time; already Abich (1878) described a number of invertebrate fossils, which he considered to be of Early Carboniferous age, from the Araxes Gorge near Dzhulfa in Armenia (now belonging to the Nakhichevan province of Azerbaijan). Additional pioneering studies were reported by Frech and Arthaber (1900), who coined the term 'Djulfa-Schichten' for these fossiliferous strata. Subsequently, Stoyanow (1910) subdivided the Araxes section into 15 lithological units; he described the first ammonoids from the latest Permian *Paratirolites* Limestone. A full examination of the classic section near the Dorasham railway station, about 17 km WNW of Dzhulfa, was provided by Arakelyan et al. (1965) and Ruzhencev et al. (1965). These articles were published in the voluminous monograph edited by Ruzhencev and Sarytcheva (1965), which contains a detailed report of the Dorasham section including descriptions of the fossil content. Rostovtsev and Azaryan (1973) reexamined the rocks across the P-Tr boundary at the Araxes River. Kozur et al. (1980) described the conodont succession of the Dorasham II and Sovetashen sections (the latter in Armenia), which were recommended as stratotypes for the P-Tr boundary by Kotlyar et al. (1993). A more detailed description of the Triassic lithological succession in the Dorasham section was provided by Zakharov (1992). Above the *Paratirolites* Limestone follow almost two metres of latest Permian argillites with a few marly limestone intercalations. The P-Tr boundary is marked by a first, light-green limestone of 8 cm thickness carrying the bivalve *Claraia* (Zakharov 1992). Similar horizons occur commonly in the overlying 2.5 m of the Elikah Formation.

The NW Iranian P-Tr boundary sections in the Ali Bashi Mountains (Kuh-e-Ali Bashi) west of Julfa and near the town of Zal possess a relatively young research history. Sections in the Ali Bashi Mountains were discovered in the 1960s and were described by Stepanov et al. (1969). These authors demonstrated that the succession closely resembles that of Dorasham, which is located only eight kilometres towards the north. The Kuh-e-Ali Bashi section was subdivided

into units A to H by Stepanov et al. (1969), of which units C to G are of special interest with respect to the P-Tr boundary (Table 1). An additional but somewhat problematic description of sections in the Ali Bashi Mountains was provided by Teichert et al. (1973), who gave a detailed historical outline of the research history of these sections. The correlation of their localities 1 and 4 has recently been a matter of intense debate (e.g., Sweet and Mei 1999; Kozur 2004; Baud 2008; Henderson et al. 2008; Leda et al. 2014) because of misinterpretation of 'Locality 4' by Teichert et al. (1973) (see Discussion in Leda et al. 2014). Biostratigraphic data (e.g., Kozur 2004, 2005, 2007; Mette and Mohtat-Aghai 2004; Richoz et al. 2010; Shen and Mei 2010) and chemostratigraphic characteristics (Holser and Magaritz 1987; Baud et al. 1989; Korte et al. 2004a; Korte and Kozur 2005a; Kakuwa and Matsumoto 2006; Richoz 2006; Horacek et al. 2007; Richoz et al. 2010) were published in the last 25 years for the Ali Bashi sections and led to a significantly increased knowledge about these sections. Recently, a revision of brachiopod, conodont and ammonoid stratigraphy from the section near Julfa was done by Ghaderi et al. (2014a, 2014b) and Korn et al. (2016). Schobben et al. (2014, 2015, 2016, 2017) presented the systematics with respect to bulk carbonate carbon, bulk carbonate oxygen, carbonate associated sulphate (CAS), chromium-reducible sulphide (CRS), oxygen isotopes from diagenetically resistant conodont apatite, and oxygen isotopes from low Mg-calcite of well-preserved brachiopods for the Kuh-e-Ali Bashi 1 and Zal sections (both NW Iran) that led to considerable improvement of the geochemical knowledge about these sections.

Table 1 Lithological and stratigraphic subdivision of the P–Tr boundary sections in the Ali Bashi Mountains (units, unit names, lithology, fauna, and thickness after Stepanov et al. 1969).

Unit	Stage	Unit name	Lithology	Fauna	Thickness (m)
H	Induan	upper part of the Elikah Formation	platy limestone	bivalves (*Claraia*), ceratitid ammonoids	200
G		lower part of the Elikah Formation	thin-bedded limestone dark-purple to violet shales		280
F	Changhsingian	*Paratirolites* Limestone	red, cliff-forming limestone	ceratitid ammonoids, corals, brachiopods	3.60
E		Permian-Eotriassic Transition Beds	purple-red shale with thin intercalations of limestone and marl	brachiopods and ammonoids	17.60
C-D	Wuchiapingian	Julfa Beds	limestone, marl, and shales	brachiopods, ammonoids (*Araxoceras*, *Vedioceras*)	33.30
B	Capitanian (?)	Khachik Beds	dark-grey bedded limestone with abundant occurrence of black chert nodules	brachiopods, corals, bryozoans, fusulinids	168
A	Capitanian (?)	Gnishik Beds	dark-grey, bedded limestone	brachiopods, corals, bryozoans, fusulinids	308

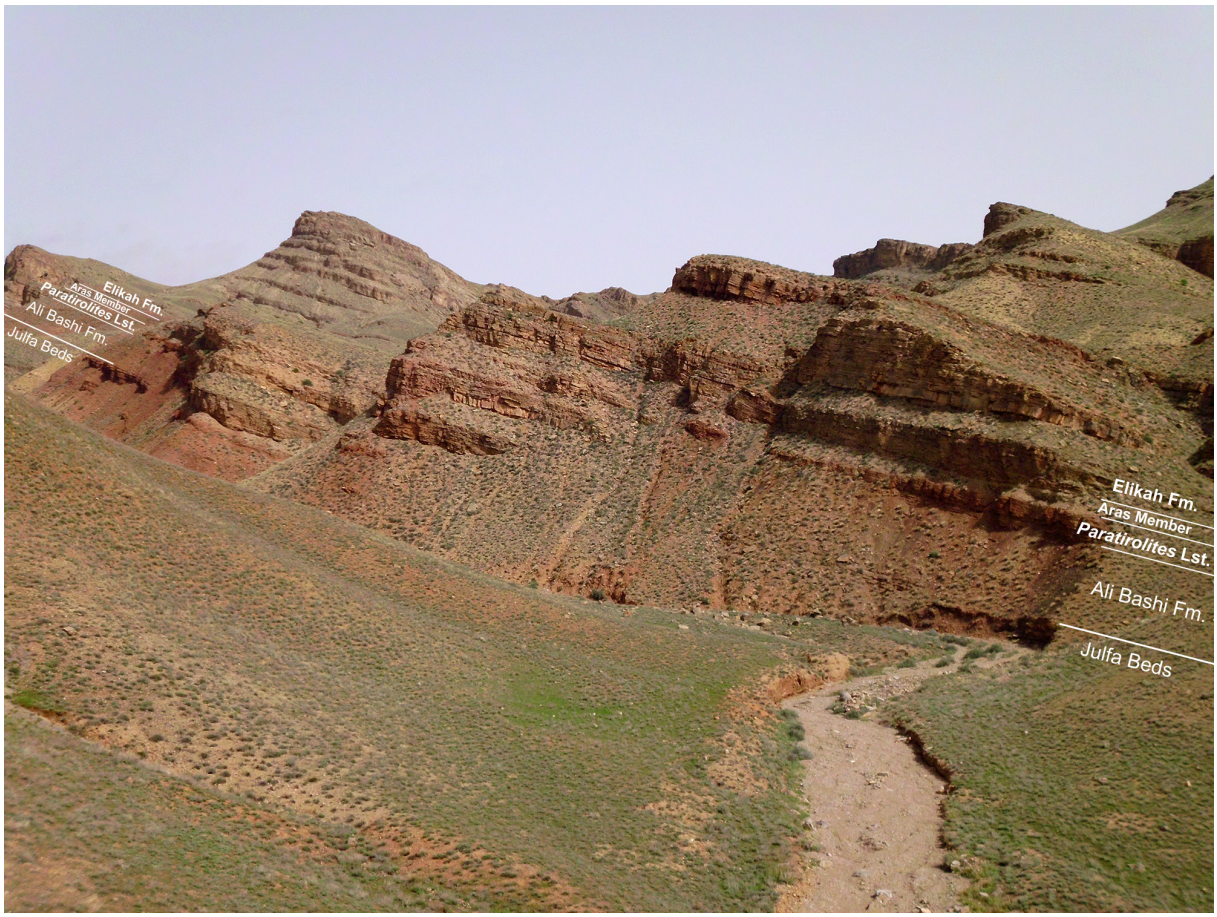

Figure 3 The Permian–Triassic boundary sections in the Ali Bashi Mountains, NW Iran. Thickness of the *Paratirolites* Limestone is 4.15 m.

2.2 Baghuk Mountain

Outcrops of Late Permian to Early Triassic successions are also known from Central Iran, in the vicinity of Abadeh in Esfahan province (Fig. 1). Three fossil-rich pelagic P-Tr boundary sections were investigated at Baghuk Mountain with respect to their sedimentology and carbonate microfacies. Three parallel sections in the Baghuk Mountain range (Fig. 4) were studied in the Shahreza-Abadeh area, 50 km NNW of Abadeh and 140 km SSE of Esfahan. These sections have the following geographic positions: section A (31.563° N, 52.438° E), section 1 (31.567° N, 52.444° E) and section C (31.567° N, 52.443° E). Section A is situated 600 m southwest of the C section that, in turn, was sampled in greater detail.

Palaeogeographically, the studied sections are situated on the Sanandaj-Sirjan Terrane that belonged, during the latest Permian, to the Cimmerian microcontinent (Scotese and Langford 1995; Golonka 2000; Stampfli and Borel 2002, 2004; Torsvik and Cocks 2004). The Baghuk Mountain region is situated on the SSW part of the Neotethyan shelf (Fig. 5). However, there exist other palaeogeographic reconstructions, which represent a different division of the Cim-

merian microcontinent (e.g., Sengör 1990; Ruban et al. 2007a, 2007b). According to Ruban et al. (2007a, 2007b), NW Iran, Central Iran, and the Sanandaj-Sirjan terrane are separate tectonic units that were apparently adjacent to each other. The Shahreza-Abadeh region was located in a latitudinal position near the equator (about 0° for Shahreza and about 10° for Abadeh) (Sengör 1990; Ruban et al. 2007a, 2007b; Muttoni et al. 2009a, 2009b).

Permian-Triassic (P-Tr) boundary sections in the vicinity of Esfahan have been known for less than 50 years (Taraz 1969, 1971, 1973) but have become very important for the study of the most severe extinction event in the Phanerozoic (Bando 1979, 1981; Taraz et al. 1981) (Table 2). In the pioneering studies, the ammonoid content of these sections was described (Taraz 1969, 1971, 1973; Bando 1979, 1981; Taraz et al. 1981). Particularly the sections at Kuh-e-Hambast (60 km southeast of Abadeh) and Shahreza (14.5 km NNE of Shahreza) have been studied intensely in more recent times, e.g., for their sedimentology, geochemistry and stable isotopes (Baud et al. 1997; Besse et al. 1998; Gallet et al. 2000; Partoazar 2002; Yazdi and Shirani 2002; Kozur 2004, 2005, 2007; Horacek et al. 2007; Richoz et al. 2010; Heydari et al. 2013). Korte et al. (2004b) published a rather detailed $\delta^{13}C_{carb}$ curve for the Kuh-e-Hambast section. Liu et al. (2013) demonstrated the carbon and strontium isotopic chemostratigraphy for the Abadeh section. The conodont stratigraphy of section VI in the Hambast Range was outlined by Kozur (2005, 2007), Richoz et al. (2010), and Shen and Mei (2010). In these articles it was shown that the latest Permian and earliest Triassic successions are very similar to the classical sections near Dzhulfa and Julfa. The rock interval containing the *Clarkina bachmanni* to *C. hauschkei* zones (i.e., the time-equivalent of the *Paratirolites* Limestone) has a thickness of 3.65 m. According to Kozur (2007), this interval ends with a significant sea-level fall. The overlying 'Boundary Clay' is about 0.7 m thick and is overlain by 'stromatolite-bearing limestone' (equivalent to the 'Colonial limestones' of Taraz et al. 1981 and 'Calcite Fans' of Heydari et al. 2003, 2008) and then by basal Triassic platy limestone beds.

Most of the P-Tr boundary sections in Central Iran feature continuous rock successions; any evidence for a sedimention gap is lacking. The sections in the Hambast Range and the sections at Baghuk Mountain are almost exclusively built up of carbonates with thin shaly intercalations. Occurrences of microbialites and inorganic precipitates in the Early Triassic successions of northern and central Iran have been known for a long time. A first description of microbial structures in the Hambast section was published by Taraz et al. (1981). They reported massive and stratified algal biolithite ('Colonial limestones') in the first few centimetres of the Early Triassic limestone and designated them as thrombolite and planar stromatolite. Baghbani (1993) introduced the term 'Thrombolite Zone' for the 'stromatolite-thrombolite' unit of Taraz et al. (1981). Baud et al. (1972) and Stampfli et al. (1976) reported laminated microbialites in the lowermost part of the Elikah Formation in the basal Triassic in the Elburz Range of northern Iran. Later, the working group of E. Heydari (Jackson State University, Jackson, USA) described and discussed various types of microbial deposits from the Hambast and Shahreza sections in detail (Heydari et al. 2000, 2001, 2003, 2013). These authors focused mainly on the lithology of the 'Boundary Clay' and the 'calcite fans' occurring in this unit. More recently, the microbial deposits in NW Iran (Julfa area) and in the Shahreza-Abadeh area were restudied by Richoz

(2006), Baud et al. (2007), Horacek et al. (2007), Richoz et al. (2010) and Leda et al. (2014). Hampe et al. (2013) reported on Late Permian fish assemblages from Baghuk Mountain.

Table 2 Lithological and stratigraphic subdivision of the P–Tr boundary sections in Central Iran (units, unit names, lithology, fauna, and thickness after Taraz et al. 1981; stages after Kozur 2005).

Unit	Stage	Unit name	Lithology	Fauna	Thickness (m)
A	Brahmanian (Induan) Dorashamian	Elikah Formation	grey platy lime mudstone with calcite fan and grainstone layer	*Claraia*	190
7	Dorashamian, Dzhulfian	Hambast Formation	red nodular limestone	ammonoids, conodonts	18
6	Dzhulfian		light-grey thin-bedded, argillaceous lime mudstone	ammonoids	16
5	Dzhulfian	Abadeh Formation	dark grey, thick-bedded, skeletal limestone	fusulinids, foraminifera, bryozoans, and green algae	56

Figure 4 Outcrop of the Permian–Triassic boundary beds at Baghuk Mountain. Thickness of the 'Boundary Clay' is about 2.00 m.

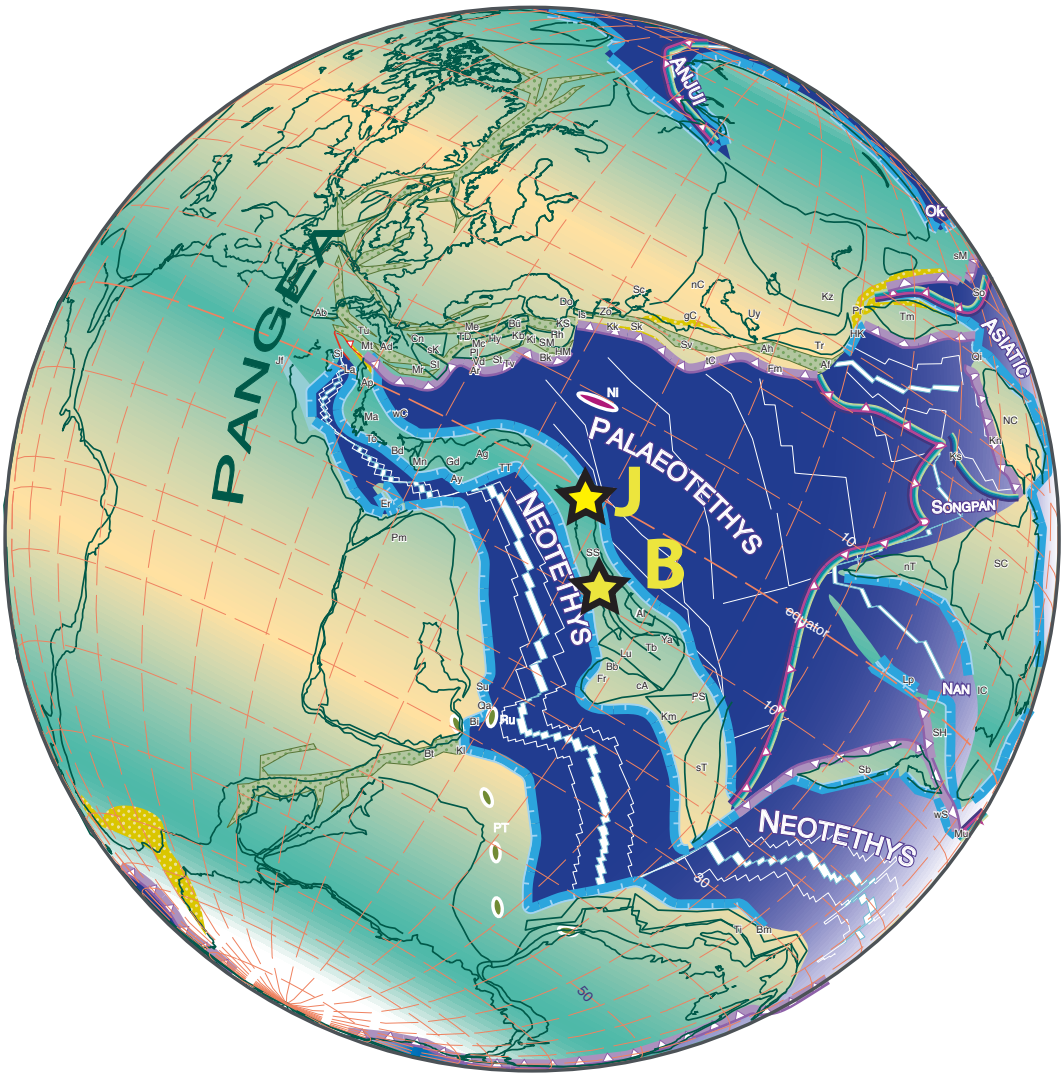

Figure 5 Palaeogeographic position of the P–Tr boundary sections described here, after Stampfli and Borel (2002, 2004). J Julfa region, B Baghuk Mountain.

3 MATERIALS AND METHODS

3.1 Field work and processing of rock samples

Samples used in this study were collected from the rock succession around the P-Tr boundary in the five NW Iranian and three Central Iranian sections during field excursions in 2010, 2011 and 2012. The sections were densely sampled on a bed-by-bed basis with respect to lithology and sedimentary content. Rock samples of one to three kilograms each were predominantly limestone and marly limestone; only a few samples were taken from shales. All samples were processed in the micropalaeontological and mineralogical laboratory of the Museum für Naturkunde Berlin.

The most conspicuous horizon in the study interval in the sections near Julfa is the top surface of the *Paratirolites* Limestone (the top of the Hambast Formation in the Baghuk Mountain sections) with its sharp contact to the Aras Member (= 'Boundary Clay' in the Baghuk Mountain sections). This bedding surface marks the P-Tr extinction horizon and was used here as the reference horizon for measuring the studied sections; it marks the 0 m level of the sections. In the following, the positions of samples are either prefixed with a - sign (beginning at the top of the sample) or a + sign (beginning at the base of the sample), depending on the distance (in m) below or above the reference horizon.

The P-Tr boundary sections were sampled as follows:

• Aras Valley section – a portion from 19.95 m below (upper part of the Julfa Formation and the Ali Bashi Formation including the *Paratirolites* Limestone) and 5.40 m above (Aras Member and the lower part of the *Claraia* Beds) the extinction horizon; in total 98 samples.

• Ali Bashi 1 section – the intervals from 21.55 m below (upper part of the Julfa Beds and the entire Ali Bashi Formation) to 4.50 m above (Aras Member and *Claraia* Beds, both Elikah Formation) the extinction horizon; in total 120 samples.

• Ali Bashi 4 section – only a 0.45 m thick interval below (the uppermost *Paratirolites* Limestone) and 1.70 m above, the extinction horizon (Aras Member and the lower part of the *Claraia* Beds) was sampled in great detail; in total 37 samples.

• Zal section – samples were taken over an interval of 35.50 m; from 21.00 m below (upper part of the Julfa Formation and the complete Ali Bashi Formation including the *Paratirolites* Limestone) to 14.50 m above (Aras Member and overlying carbonate rocks of the Elikah Formation) the extinction horizon; in total 55 samples.

• Baghuk Mountain section 1 – intervals from 9.90 m below (the middle and the upper part of the Hambast Formation) to the extinction horizon; in total 48 samples.

• Baghuk Mountain section A – intervals from extinction horizon (the uppermost part of the Hambast Formation) to 2.47 m above ('Boundary Clay', and overlying carbonate rocks, both Shahreza Formation) the extinction horizon; in total 24 samples.

• Baghuk Mountain section C – intervals from 0.02 m above (the 'Boundary Clay' and the lower part of the Hambast Formation) to 18.85 m above ('Boundary Clay', and overlying carbonate rocks, both Shahreza Formation) the extinction horizon; in total 76 samples.

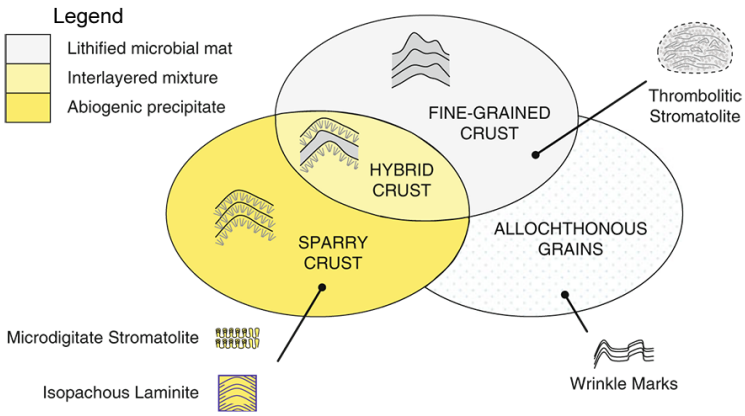

Figure 6 Sketch representig how sparry and fine-grained crust, as well as incorporated allochthonous grains, contribute to the formation of hybrid crust, thrombolitic stromatolite, other macrolayered authigenic carbonate crusts, and wrinkle marks. After Riding (2011).

3.2 Analytical procedures

Thin sections

Thin sections and polished slabs were prepared from more than 140 samples for the systematic study of fossil content, of non-skeletal grains, and sedimentary structures. In addition, more than 90 polished slabs were prepared for the study of the morphology of the microbialites. Thin sections and polished slabs were prepared in the mineralogical lab (by Sylvia Saltzmann and Hans-Rudolf Knöfler). Detailed petrographic analysis was carried out with a polarizing microscope of the type Zeiss Axioskop 40 equipped with a digital camera (Zeiss AxioCam MRc5) working with Axio Vision LE software.

Abundance of biogens, abundance of non-skeletal grains, presence of specific depositional and diagenetic fabrics, presence of discontinuity surfaces, and presence of syndepositional and postdepositional features were recorded by semi-quantitative area counting and comparison with the charts of Bacelle and Bosellini (1965). The investigated limestone samples are fossiliferous but the grain size is usually small. I used additionally an area counting method, as the

small grains (e.g., foraminifera or sponge spicules occurring in low percentages of less than 10 % according to point-counting measurements) could be potentially excluded using comparison charts only. The estimations were made using an appropriate magnification corresponding to the component size. I used multistage quantitative variables and introduced a five-stage scale for relative frequency of grain categories: absent (= 0), single (= 1), rare (= 2), medium (= 3), and abundant (= 4). Presence of specific depositional and diagenetic fabrics, presence of discontinuity surfaces, and presence of syndepositional and postdepositional features were coded as simple presence or absence attributes (i.e., 1 or 0). The degree of bioturbation was obtained semi-quantitatively, using visual estimation. I distinguished between three levels of bioturbation: low (slightly bioturbated, burrow diameter small to minute, discrete trace fossils, bedding distinct), moderate (moderately bioturbated, burrows isolated and locally overlapping, bedding boundaries sharp) and high (burrows overlap, burrows well-defined, high trace density, bedding boundaries indistinct). Identified facies were compared with Standard Microfacies Types (SMF) and with Ramp Microfacies Types (RMF) (e.g., Burchette and Wright 1992; Wilson 1975; Flügel 2004). Depositional environments of the carbonate facies are discussed based on their petrographic characteristics (Flügel 2004). The Standard Facies Zone model (FZ) established by Wilson (1975) and modified by Schlager (2002) was used to obtain the depositional area of the distinguished microfacies. Concerning nomenclature, this work follows the definitions and descriptions of microbial limestones after Shapiro (2000), who used different categories to describe the microbial fabric (mega-, macro-, meso-, and microstructural). I used the term microbialite (Burne and Moore, 1987) as an overall term for all microbial carbonates. However, in the detailed description of the microbial deposits I used a classification of Riding (2000, 2008) for describing abiogenic, microbial and hybrid carbonate crusts (Fig. 6). Furthermore, I applied the stromatolite classification of Logan et al. (1964).

Non-metric multidimensional scaling (NMDS)

For statistical analysis, nearly all features (frequency of biogens, frequency of non-skeletal grains, presence of specific depositional and diagenetic fabric, presence of discontinuity surfaces, presence of syndepositional and postdepositional features) recognized in the thin sections from the Ali Bashi 1 section were quantified. I analysed these data with the method of non-metric multidimensional scaling (NMDS), using the Bray Curtis dissimilarity algorithm (Faith et al. 1987). This method enables tracing similarities and dissimilarities based on distance between single points.

Scanning electron microscopy coupled with X-ray detection system (SEM-EDX)

I investigated polished, uncovered thin sections and cut slabs for their surface properties and chemical composition in the mineralogical lab of the Museum für Naturkunde (with assistance from Kirsten Born). Scanning electron microscopy (SEM) combined with an energy dispersive X-ray detection system (EDX) was achieved using a JEOL JSM-6610LV scanning microscope with LaB6-Cathode coupled with a Quantax 800 EDX-System Bruker AXS spectrometer. The thin sections and slab samples were prepared by mounting them on a SEM stub. This stub was

subsequently placed into a sample holder of the SEM, upon which the whole sample chamber is evacuated. When the required pressure was reached, an electron beam of 60 nA is emitted from a tungsten filament operating under a 15 kV acceleration voltage. The measurements took place in low vacuum.

Cathodoluminescence (CL)

I investigated carbon-covered, polished thin sections for cathodoluminescence (CL) analysis in the mineralogical lab of the Museum für Naturkunde Berlin (with assistance from Kirsten Born). The CL analysis was done with a Lumic polarizing microscope and a HC3-LM Hot Cathode instrument. Operating conditions were 14-18 kVa accelerating voltage and 0.04-0.3 mA beam current. Photomicrographs were taken using a Kappa colour camera.

X-ray diffraction (XRD)

Whole-rock sample powders were placed into aluminum holders and scanned by X-ray diffraction (XRD) using a PW 1729 diffractometer at the Technical University Berlin (with assistance from Cordelia Lange). Samples were scanned from 4-70° 2θ at a rate of 1°/min, at a step size of 0.2° 2θ using Cu Kα radiation and a graphite monochromator. The X' Pert HighScore software package was used for phase identification. Semi-quantitative results were obtained using quantitative analysis software; χ^2 values for the analyses ranged from 2.63 to 3.54.

Carbon and oxygen isotope analyses on bulk rock samples

Samples for the isotope work were taken from fresh surfaces of marly or micritic carbonate rocks using a micro-drill. Cracks, veins and stylolites were avoided. Small portions of the powdered bulk-rock samples (100-400 µg) were placed into 10 ml vials that were sealed with rubber septum lids. After flushing for 6 min with helium and adding H_3PO_4, the thus generated CO_2 was measured for $\delta^{13}C$ and $\delta^{18}O$ on a Thermo Finnigan GASBENCH II linked online to a Thermo Finnigan DELTA V mass spectrometer at the Museum für Naturkunde in Berlin (analyses by Ulrich Struck). The isotope values were calibrated against the Vienna Pee Dee Belemnite (VPDB) and are reported in conventional δ notation. The reproducibility (1σ) of replicated standards (Pfeil STD; Solnhofen Limestone) was better than 0.1 ‰ for both $\delta^{13}C$ and $\delta^{18}O$.

Carbon and nitrogen isotope analyses on bulk-rock and decalcified samples

About 50 g of the rock sample were ground with a mechanic agate mill (Retsch RS 100) at the Museum für Naturkunde Berlin. To acquire a homogeneous grain size, the ground samples were sieved with a 160 µm mesh. Residual 2 g of a sample powder (carbonate, marl and shale) were decalcified using 2M hydrochloric acid, followed by a repeated neutralisation treatment with distilled water, centrifugation and decantation. The samples were dried at 40 ºC for a week. About 50 mg of each of these samples were packed into silver capsules (C_{org}). The $\delta^{15}N$ isotope measurements were carried out on 100-130 mg of untreated sediment wrapped in tin-foil cups. Stable isotope analysis ($\delta^{13}C_{org}$, $\delta^{15}N$) and concentration measure-

ments of nitrogen and carbon were performed simultaneously with a Thermo Finnigan Delta V mass spectrometer, coupled to a Thermo Flash EA 1112 elemental analyzer via a Thermo Finnigan Conflo III-interface. Measurements were done in the stable isotope laboratory of the Museum für Naturkunde Berlin by Ulrich Struck. The reference gas was pure (N_2) nitrogen. The external reproducibility was tested with an internal standard (peptone) after every 5 measurements. Standard deviations for repeated measurements of the lab standard (peptone) were generally better than 0.15 per mil (‰) for nitrogen and carbon, respectively. Standard deviations of concentration measurements of replicates of the lab standard were <3% of the concentration analyzed. The isotope values were calibrated against VPDB and are reported in conventional delta notation ($\delta^{13}C$ / $\delta^{15}N$) relative to atmospheric nitrogen (Mariotti 1983) and VPDB (Vienna PeeDee Belemnite standard). The Thermo Flash EA 1112 elemental analyzer analyzes total carbon and nitrogen in solid samples. The analytical method is based on the complete and instantaneous oxidation of the sample by ”flash combustion“, which converts all organic and inorganic substances into combustion products. The resulting combustion gases are passed through a reduction furnace and swept into the chromatographic column by the carrier gas (helium). The gases were separated in the column and detected by isotope ratio mass spectrometry, which gives an output signal proportional to the concentration of the individual components of the mixture. The samples were loaded into the automatic autosampler. When the autosampler was triggered, the samples were introduced into the combustion reactor, which was maintained at around 1050°C. The sample container melted and the tin promoted a violent reaction (flash combustion) in a temporary enriched atmosphere of oxygen. The combustion products (N_2, NO_x, CO_2, H_2O, SO_2 and SO_3) were carried by a constant flow of carrier gas (helium), passed through an oxidation catalyst of chromium oxide (CrO) kept at 1050°C inside the reaction combustion tube. Furthermore, to ensure complete oxidation, a 5 cm layer of silver coated cobalt oxide was placed at the bottom of the combustion tube. The catalyst also retained interfering substances, produced during the combustion of halogenated compounds. The mixture of combustion products and water was passed through a second tube known as the reduction reactor, which contained metallic copper kept at 650°C. The excess oxygen was removed in the reaction reactor and at this temperature, the nitrogen oxides coming from the combustion tube were reduced to elemental nitrogen, which together with carbon dioxide and water passed trough the H_2O absorbent filter.

4 LITHOSTRATIGRAPHY, BIOSTRATIGRAPHY AND CARBONATE MICROFACIES

4.1 Julfa area

4.1.1 Macroscopic petrography

The transition from the Paleozoic into the Mesozoic is, in the regions of Transcaucasia (Araxes Gorge and its vicinity in Armenia, Azerbaijan, and NW Iran) and Central Iran (Shahreza-Abadeh area), represented by complete successions of sedimentary rocks. The Kuh-e-Ali Bashi 1 section of Teichert et al. (1973) displays a complete P-Tr transition of fossil-rich carbonates and marls and can serve as a standard for all lithostratigraphic P-Tr boundary sections in NW Iran. It is composed, in ascending order, of the following rock units (Stepanov et al. 1969) (Table 1):

(1) Julfa Formation (Julfa Beds sensu Stepanov et al. 1969), 33 m thick; Wuchiapingian in age (Fig. 7). It consists of grey to red shales with nodular limestone and marl intercalations. The macrofauna consists of brachiopods (particularly common at the base of the formation), ammonoids (*Araxoceras* in the lower part, *Vedioceras* in the upper part of the formation), and nautiloids as well as rugose and tabulate corals.

(2) Ali Bashi Formation (16 m thick), composed of two members; both are Changhsingian in age:

(a) Shaly unit at the base (Zal Member sensu Ghaderi et al. 2014), 12 m thick; it is composed of dark-grey shales at the base turning violet-reddish towards the top. Marly and nodular limestone packages are alternating; they are grey at the base of the member and red to pink at the top. The member is only occasionally rich in macrofossils, of which ammonoids, nautiloids and small brachiopods are the most common.

(b) The *Paratirolites* Limestone is the uppermost of the Permian carbonate formations; it is typically developed in the Julfa area, but similar sedimentary rocks occur in Central Iran. It represents an about four to five metre thick unit (Aras Valley: 4.60 m, Ali Bashi N: 4.50 m, Ali Bashi 4: 4.15 m, Ali Bashi 1: 4.15 m, Zal: 5.10 m) of red, nodular, marly limestone composed of beds with 5-30 cm thickness (Fig. 8). The unit was named after the occurrence of the ceratitic ammonoid genus *Paratirolites*, which together with some closely related genera serves as index fossil. The $CaCO_3$ content of this unit in the Ali Bashi 1 section ranges from 80 to 96 wt % (Ghaderi et al. 2014). All sections in the vicinity of Julfa show similar internal organisation of this rock unit; a rather precise lithostratigraphic correlation based on the alternation of more marly or compact beds can be achieved (Fig. 8).

Three classes of fossils can be listed for the *Paratirolites* Limestone:- Macrofossils include cephalopods (ammonoids and much more rarely coiled and straight nautiloids), brachiopods,

rugose corals, fish remains and echinoderm ossicles.- Microfossil assemblages found in the residue of rock processed with formic acid are mainly composed of conodonts (up to 1000 platform elements per 1 kg rock sample), actinopterygian teeth (up to 1000 specimens per kg), shark teeth and scales, foraminifera, etc.- In thin sections, ostracods, echinoderms, radiolaria, foraminifera, bivalves and gastropods are the most abundant fossils.

In the field, the *Paratirolites* Limestone appears as a uniform rock unit. However, detailed petrographic studies of the Ali Bashi section 1 demonstrated that two subunits need to be separated based on microfacies character:

- The lower part (3.85 m) is a red, marly, nodular, burrowed and poorly sorted bioclastic lime mudstone and wackestone with echinoderms, ostracods, bivalves, foraminifera and calcispheres; nautiloid and ammonoid conchs occur occasionally. The marly matrix is well bioturbated and the micrite is often recrystallized to microspar. Sutured and non-sutured stylolite seams give a breccia-like appearance of the lime mudstones. The *Paratirolites Limestone* begins at the base with some rather compact beds of 10-30 cm thickness, which are separated by red shale horizons of similar thickness. The shale intervals, which become much less prominent higher in the section, occasionally contain limestone nodules. From 1.90 to 2.00 m below the top of the unit, a conspicuous limestone bed occurs that differs in its much lighter colour and denser matrix from the other beds of the *Paratirolites* Limestone. This horizon represents a lithological reference horizon in all studied sections around Julfa (Fig. 8); its position is always near the middle of the *Paratirolites* Limestone. In terms of microfacies, however, this horizon does not differ from the overlying and underlying beds of the *Paratirolites* Limestone. In the Ali Bashi 1 section it is a burrowed bioclastic wackestone with foraminifera, ostracods, echinoderms and bivalves. In the Zal section it occurs as fractured fossiliferous lime mudstone with bivalves, gastropods, ostracods and echinoderm remains. In contrast, in the Aras Valley this horizon is a foraminifer-algae packstone (Leda et al. 2014, fig. 6c). Skeletal grains are loosely packed and well-preserved lagenid foraminifera tests and algae segments. Abundant peloids and cortoids occur as aggregates and are embedded in a clotted micritic and sparry peloidal matrix. This conspicuous foraminifer-algae packstone horizon occurs within a bioclastic lime mudstone with ammonoids, radiolaria, echinoderms, foraminifera and ostracods.

- The upper part (0.30 m) of the *Paratirolites* Limestone is a red, marly, nodular, burrowed and poorly sorted bioclastic wackestone and packstone with sponges, radiolarians, ammonoids, ostracods and benthic foraminifera. The marly, microbioclastic matrix contains carbonate nodules. Isolated nodules exhibit occasionally black ferruginous and manganese coating and are preserved as hardground clasts. The matrix-nodule contact is marked by dark clay seams (single or swarms). Scoured and sutured discontinuity surfaces are impregnated with iron and manganese oxides and covered by mm-thick, ferruginous microstromatolite crusts. Microbial Fe-Mn crusts grow upward on these hardgrounds as well as perpendicular to the wall of dissolved components. Agglutinated foraminifera encrust micrite clasts and fossils. Occasionally occurring ammonoid conchs have been filled by sparry calcite cement and sponge spicules (Fig. 17a).

The top of the *Paratirolites* Limestone is marked by the cessation of limestone beds and is conformably overlain by a unit consisting dominantly of clay, called here the Aras Member (formerly 'Boundary Clay') (Kozur 2004; Korte and Kozur 2005; Ghaderi et al. 2014). The top surface of the *Paratirolites* Limestone with its sharp contact to the overlying Aras Member marks the end-Permian mass extinction horizon (EH) and is referred as the extinction horizon (e.g., Korte and Kozur 2005; Kozur 2004; Leda et al. 2014; Fig. 19).

(3) Elikah Formation (more than 170 m thick in the Ali Bashi 1 section), containing the P-Tr boundary. The Elikah Formation is the lowermost Triassic carbonate formation and has a total thickness of about 360 m (Stepanov et al. 1969). It is composed of two very different units:(a) Aras Member (sensu Ghaderi et al. 2014; formerly Boundary Clay). It has a thickness of 0.60 m (Zal), 1.18 m (Ali Bashi 1), and 3.30 m (Aras Valley). It is of latest Changhsingian age (Ghaderi et al. 2014).

The Aras Member is a red claystone with marly nodules and a few thin, light-green horizons (Fig. 9). In the Zal section the base of the Aras Member is marked by red and green shale. The Aras Member is poor in macrofossils. A few thin (up to 10 cm) horizons of nodular limestone within this unit are sponge wackestones and burrowed ostracod lime mudstones. Scanning electron microscopy in combination with energy-dispersive X-ray spectroscopy (SEM-EDX) showed that major elements occurring in the matrix are Ca, Si, Sr, Al, K and Mg (Fig. 10); they are contained in fine-grained mosaics of calcium carbonate and phyllosilicate minerals. Single, larger grains within the matrix are irregular or rhombic calcite crystals with Fe-rich zones (Fig. 11). There is no evidence of dolomitisation.

(b) Carbonate unit of the Elikah Formation (*Claraia* Beds sensu Ghaderi et al. 2014). The lower part of this unit (0.80 m thick at Ali Bashi 1) is composed of yellow-grey, marly, thin-bedded limestone beds of 3-15 cm thickness, interbedded with green and red marly shales (Fig. 9). Lithologically, this limestone unit resembles the *Paratirolites* Limestone, with a high marl content and nodular fabric. The lower part of the unit is overlain by light-grey, thick-bedded limestone beds that are intercalated with grey shales and occur in beds of up to 35 cm thickness. These limestone beds are slightly bioturbated and, in most cases, highly recrystallized. Microfacies studies show that the limestone of the *Claraia* Beds is a densely laminated bindstone, wackestone with calcite sparry spheres and oncoid floatstone. The basal part of the *Claraia* Beds is marked by the FAD (first appearance datum) of *H. parvus*.

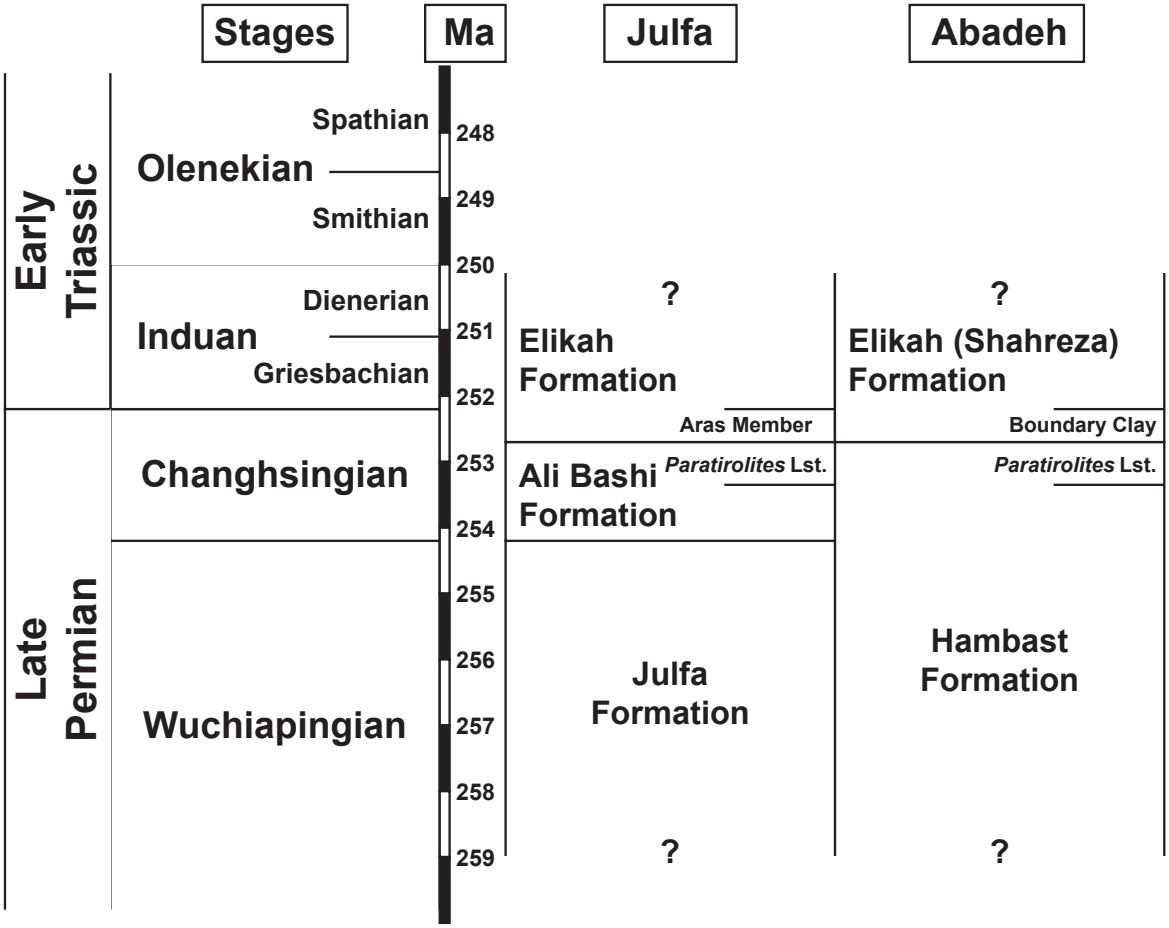

Figure 7 Timescale for the Late Permian and Early Triassic with lithostratigraphic units of the investigated areas (geochronological data from Schobben et al. 2014).

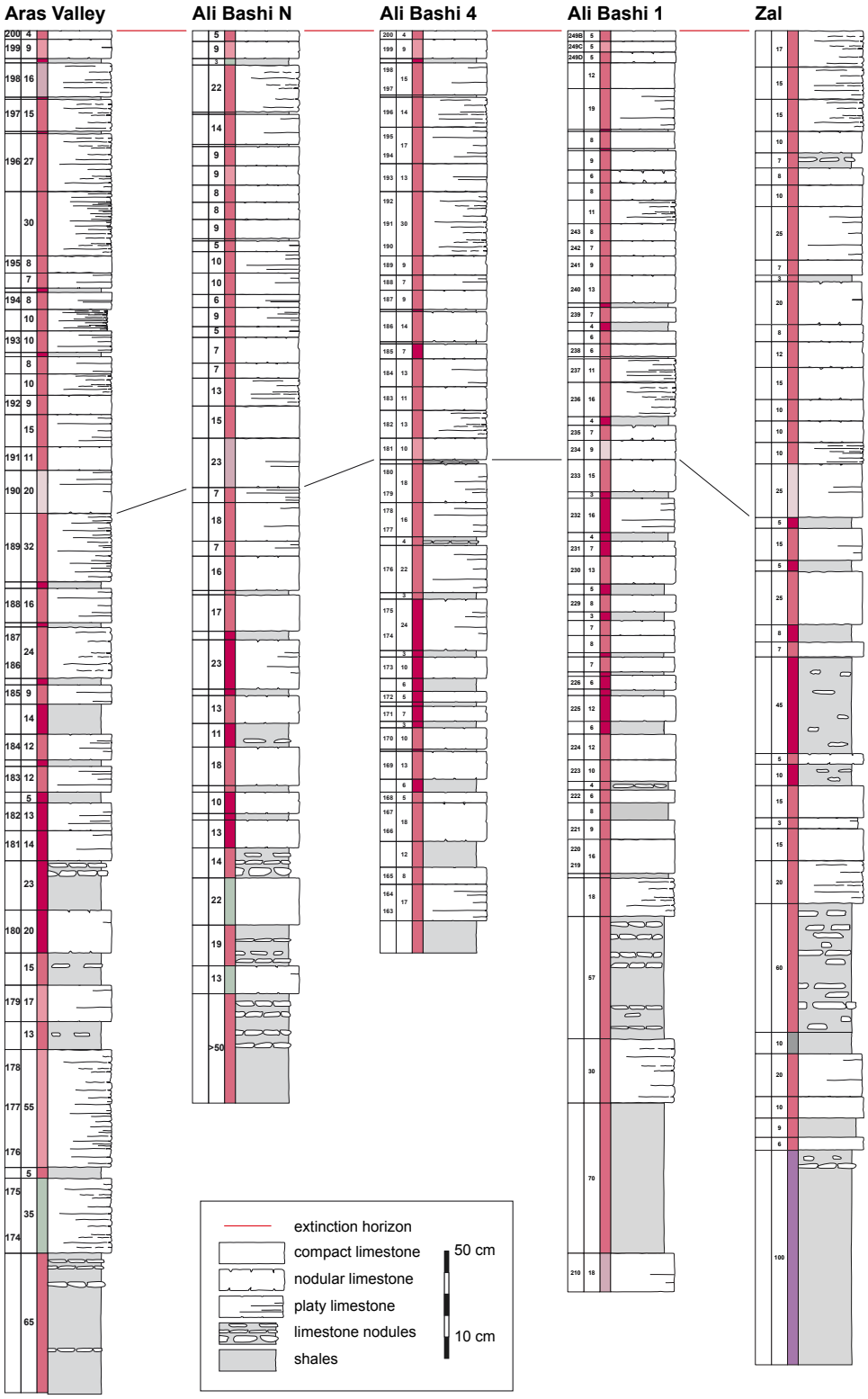

Figure 8 Five parallel sections of the *Paratirolites* Limestone in the Julfa region. All sections have been aligned at the extinction horizon (top of the sections; red line). The lower correlation line refers to the light pink lithological reference horizon in the middle of the *Paratirolites* Limestone. Columns left of the lithology logs refer to sample numbers, thicknesses (cm scale), and rock colour.

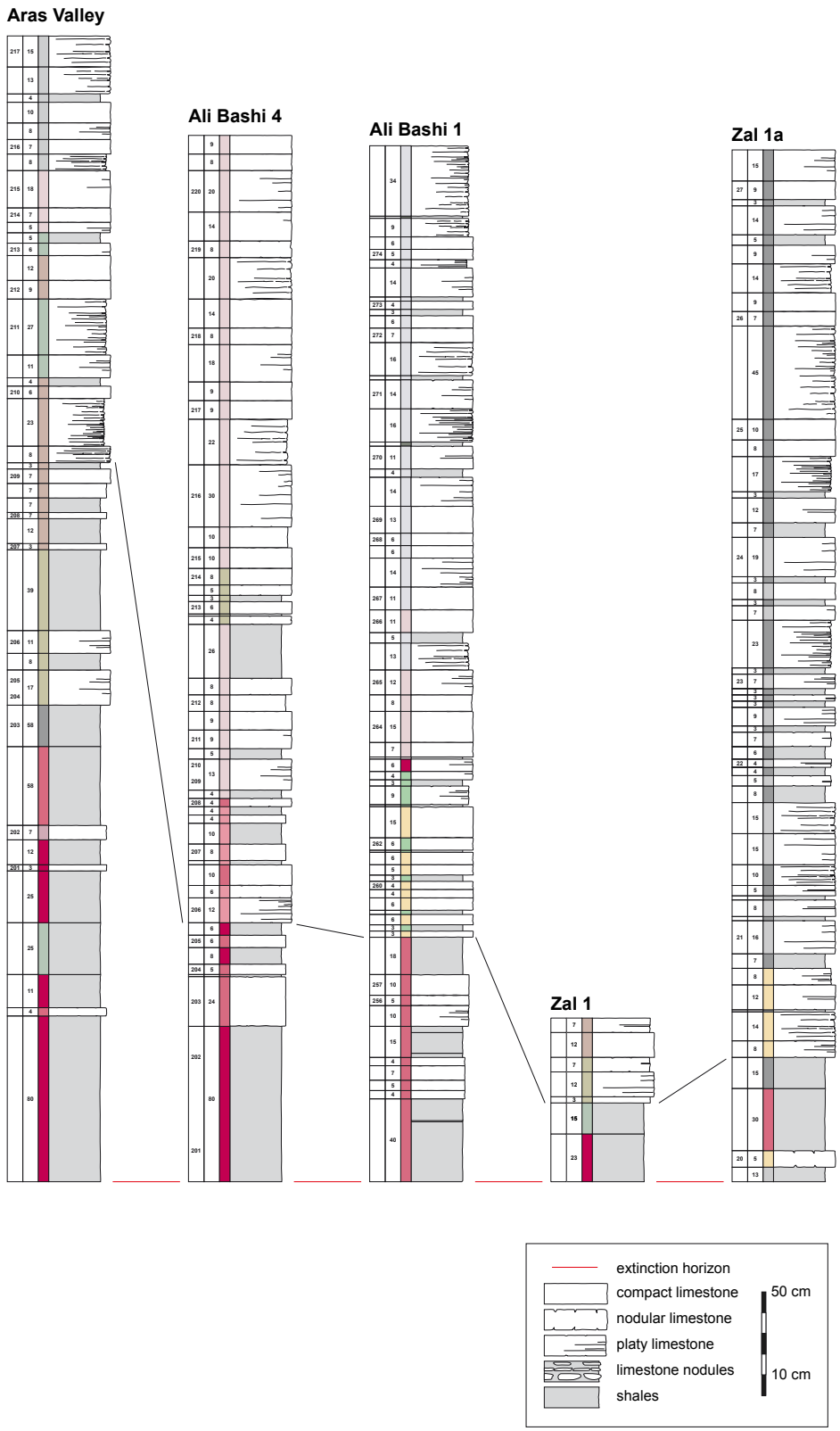

Figure 9 Five parallel sections across the Aras Member and the base of the Elikah Formation in the Julfa region. All sections have been aligned at the extinction horizon (base of the sections). The upper correlation line refers to the top of the Aras Member.

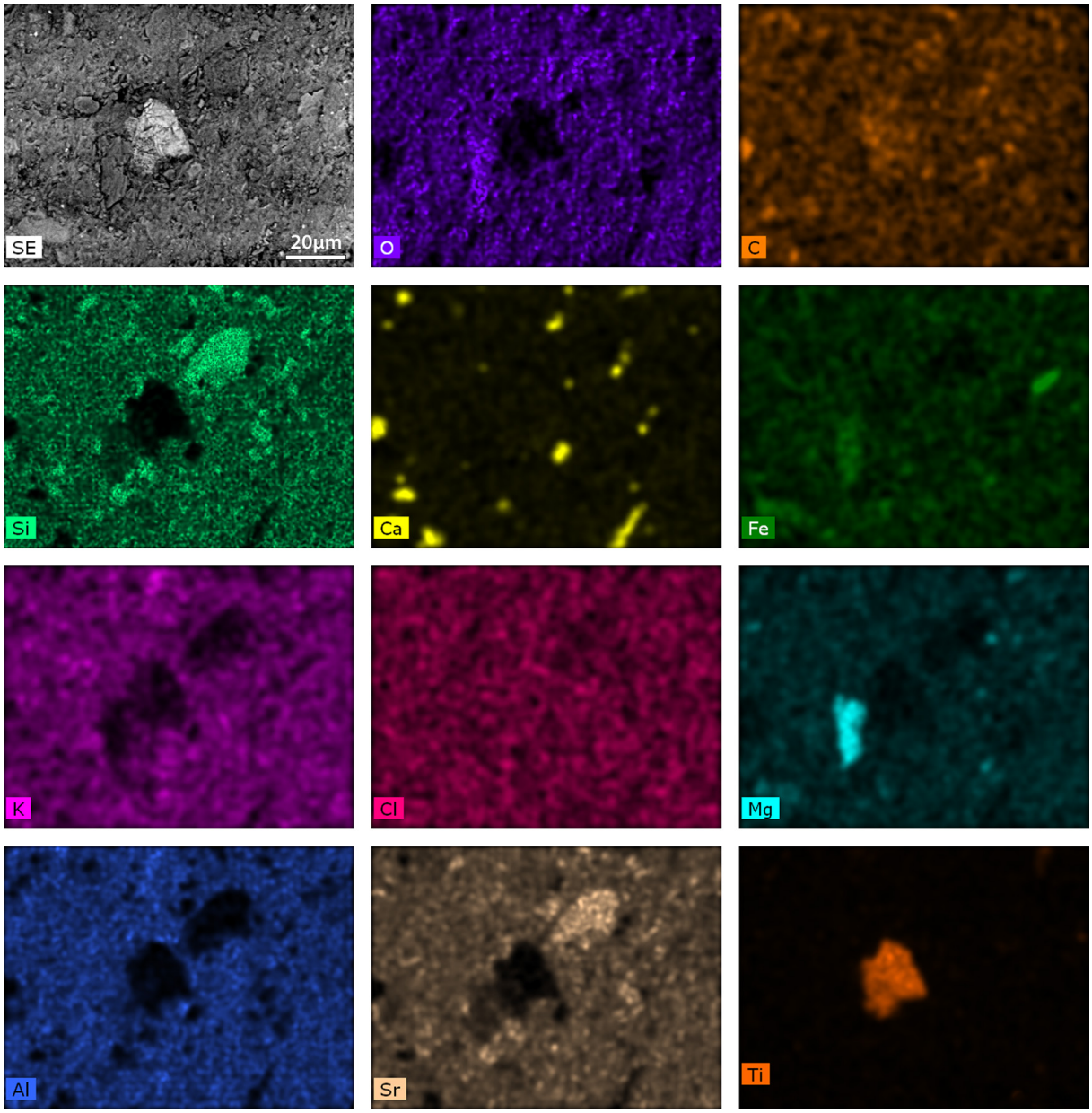

Figure 10 Results of an EDX element mapping of a burrowed and bioturbated ostracod-sponge lime mudstone showing that major elements occurring in the matrix are Ca, Si, Sr, Al, K, Mg. They are incorporated in fine-grained mosaics of calcium carbonate and phyllosilicate minerals. The large crystal in the centre is an accessory mineral that contains Ti. Ali Bashi1, +0.75 m.

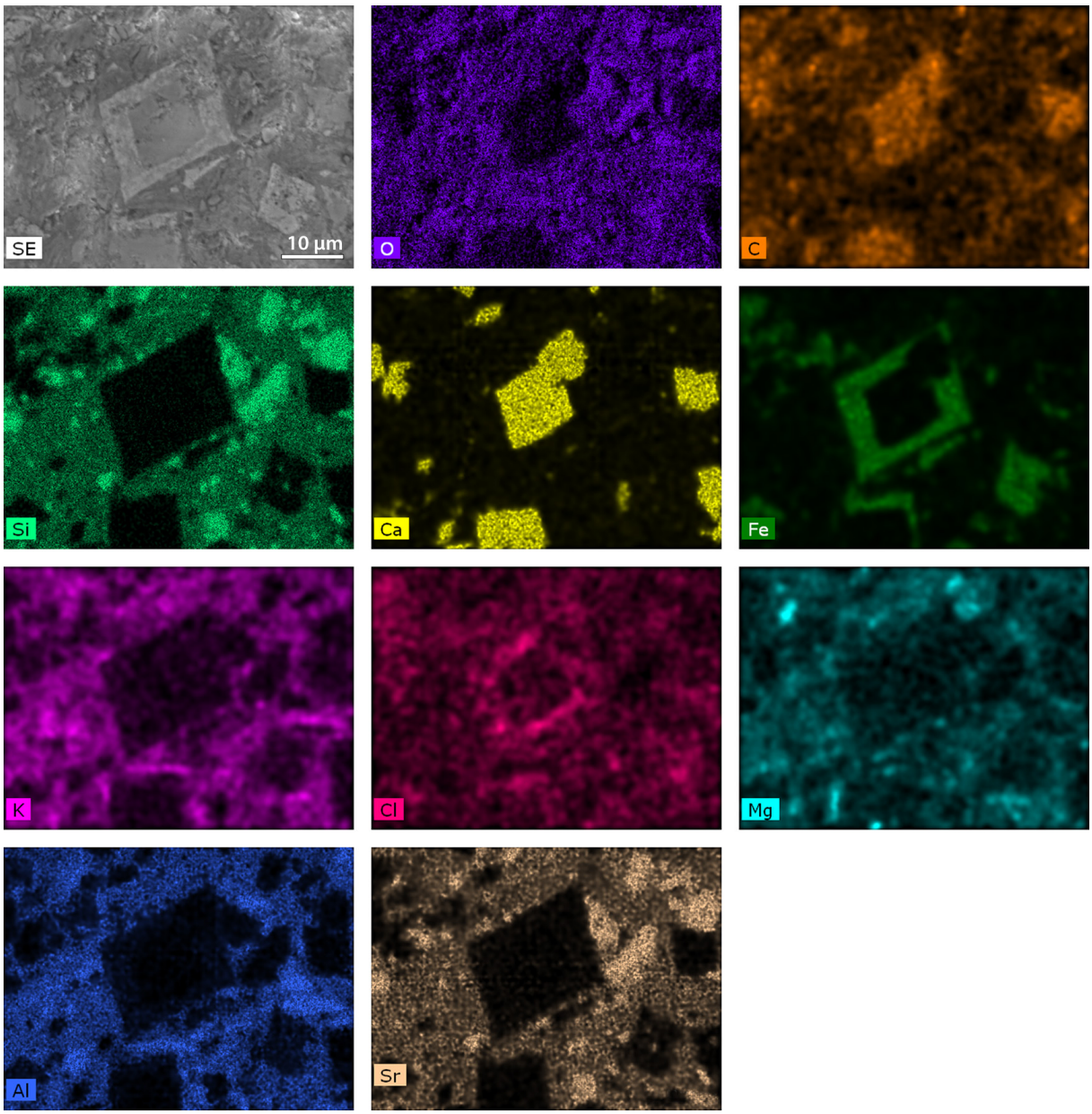

Figure 11 Results of an EDX element mapping of a marly limestone showing rhombic calcite crystals that possess an Fe-rich rims. The matrix contains, besides Ca, also Si, Sr, Al, K, Mg. Ali Bashi1, +1.29 m.

Figure 12 Composite log with carbonate microfacies characteristics across the Permian–Triassic boundary of the Ali Bashi 1 section in the Julfa region.

4.1.2 Carbonate microfacies

Petrographic investigation of carbonate allows distinguishing between several microfacies types according to fabrics and bioclast occurrences. I present below a detailed depiction of only a few microfacies types, which I studied most intensively because of their interesting features. A complete facies list and description of microfacies from all sections are included in Tables 3, 4, 5, 6, 7, and their distribution pattern is given in Fig. 12.

Red, burrowed, bioclastic packstone

This microfacies type is characterized by densely packed microfossils (e.g., Fig. 13c) and occurs in the Julfa Formation. Skeletal grains are small and comprise shell debris, ostracods, echinoderms, foraminifera, radiolaria, and brachiopods scattered within a dense, strongly burrowed matrix (Fig. 13d).

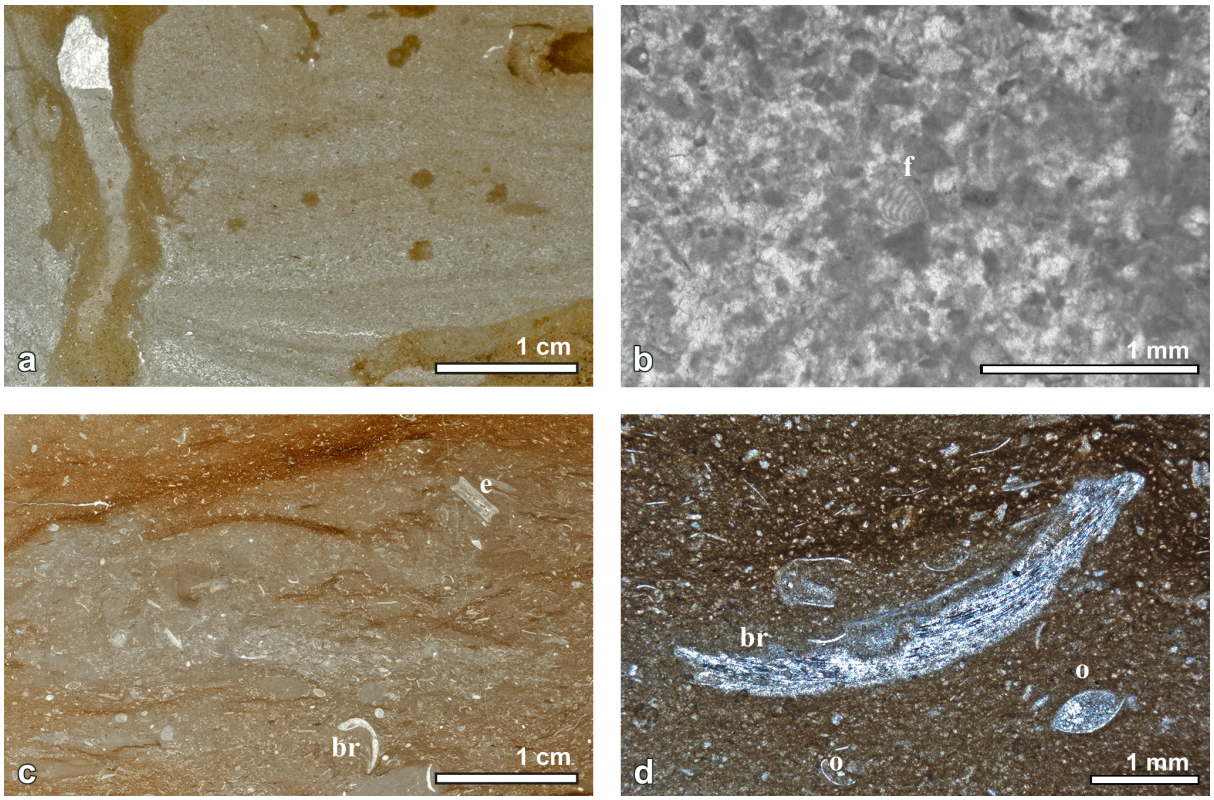

Figure 13 Carbonate microfacies of the upper part of the Julfa Beds. a – Grey, peloidal, laminated wackestone with ostracods and foraminifera. A large, vertical burrow is partially filled with micrite and sparite, forming a geopetal fabric. Ali Bashi 1, -19.95 m. b – Details of a peloidal, laminated wackestone, showing a biogenic component of foraminifera (f) within micritic and sparry peloidal matrix. Ali Bashi 1, -19.95 m. c – Reddish-brown, burrowed bioclastic packstone with fine-grained biodetritus of ostracods (o), echinoderms (e), brachiopods (br), radiolarian, foraminifera. Ali Bashi 1, -21.55 m. d – Fine-bioclastic, marly micritic matrix of a burrowed bioclastic packstone with a brachiopod (br) and ostracods (o) shells. Ali Bashi 1, -21.55 m.

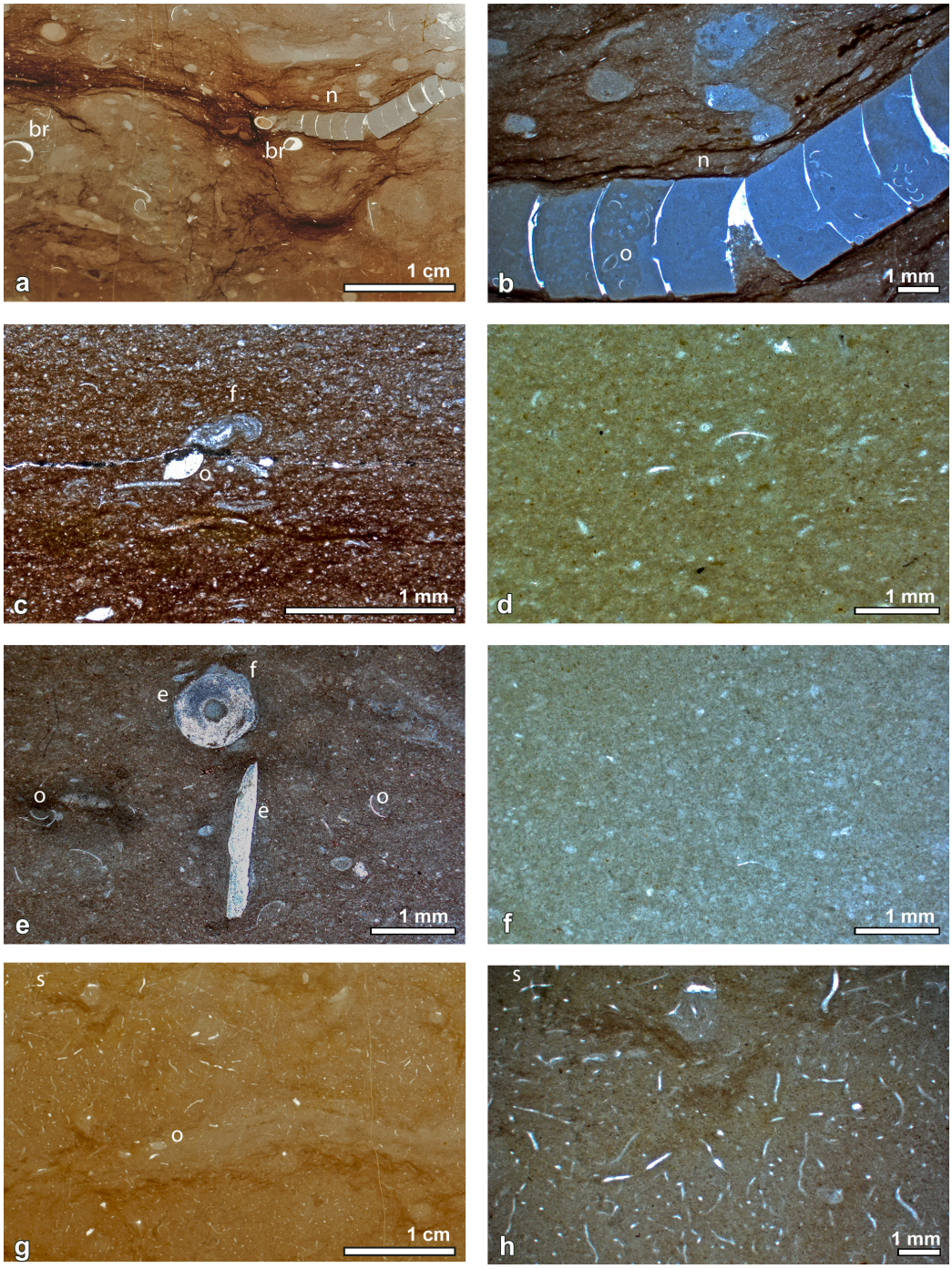

Figure 14 Carbonate microfacies of the Ali Bashi Formation. a – Reddish-brown, a marly, burrowed, bioclastic wackestone with brachiopods (br), echinoderms, ostracods and an nautiloid shell (n). Ali Bashi 1, -5.70 m. b – An orthocone nautiloid (n) shell embedded in a marly, burrowed matrix. The shell has been infilled with pelagic micrite with disarticulated ostracod shells (o). The shell is broken and the septa are filled by calcite. Ali Bashi 1, -5.70 m. c – Red, argillaceous, burrowed lime mudstone with ostracods (o) and foraminifera (f) within a bine-grained matrix. Ali Bashi 1, -6.90 m. d – Light green, peloidal lime mudstone with skeletal components of ostracods and foraminifera. Ali Bashi 1, -10.85 m.

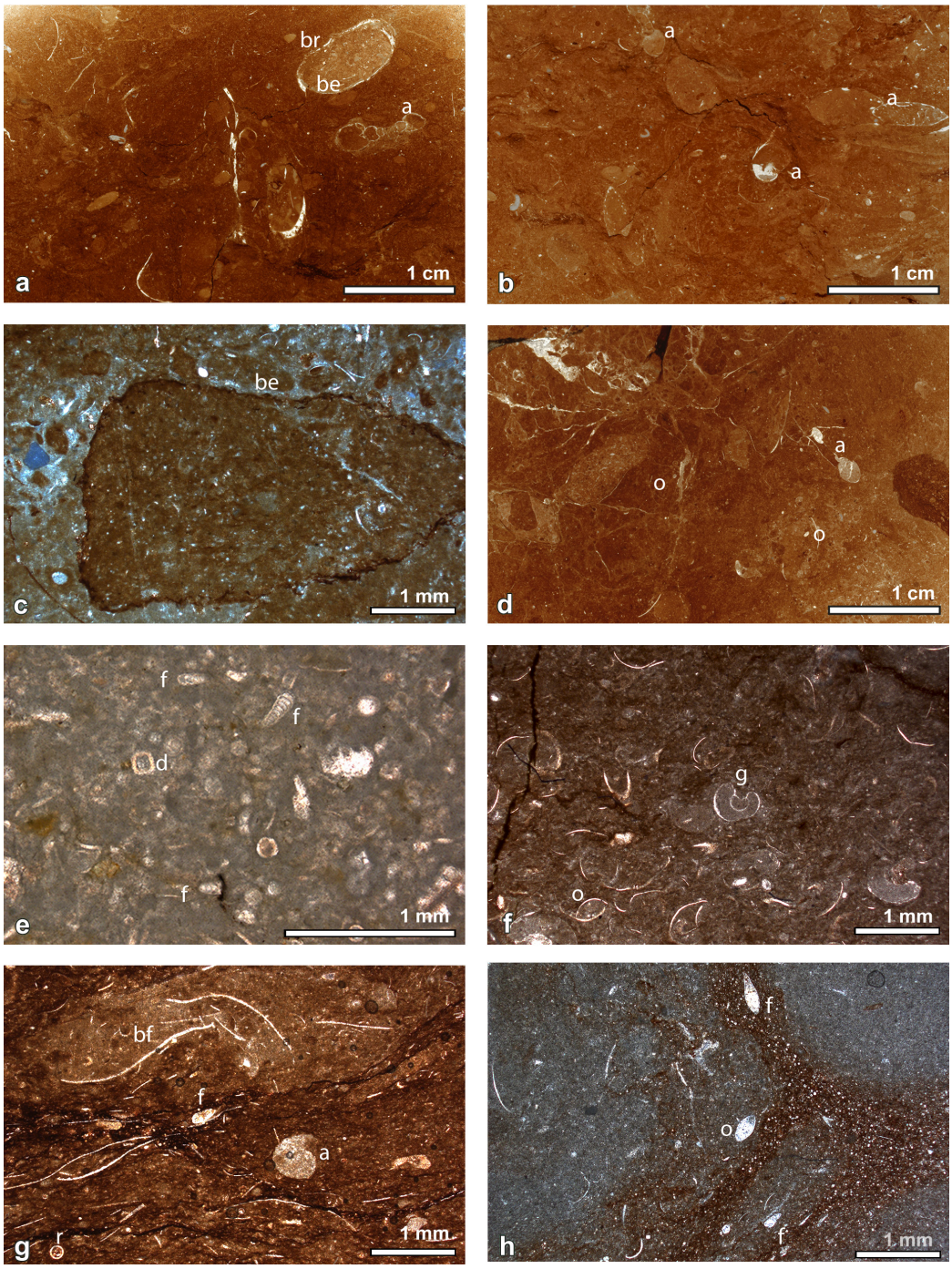

Figure 15 Carbonate microfacies of the lower part of the *Paratirolites* Limestone. a – Red, nodular, burrowed, bioclastic lime mudstone. Biogenic encrustations (be); microborings on/inside a brachiopod (br) shell and an ammonoid (a) conch. Ali Bashi 1, -0.75 m. b – Red, nodular, burrowed, bioclastic wackestone with ammonoids (a). Ali Bashi 1, -0.90m. c – Biogenic encrustation (be) around a micrite clast. Ali Bashi 1, -1.50 m. d – Red, nodular, burrowed, bioclastic lime mudstone with single ostracods (o). Ammonoid (a) conch dissolved and deformed. Ali Bashi 1, -1.77 m. e – Peloidal packstone with components of dasycladacean (d) green algae and foraminifera (f). Aras Valley, -2.20 m. f – Burrowed, bioclastic wackestone with ostracod shells (o) and gastropods (g). Ali Bashi 1, -2.65 m. g – Pelagic burrowed wackestone with bivalve filaments (bf), ammonoid (a), foraminifera (f) and radiolaria (r). Ali Bashi 1, -2.95 m. h – Red, burrowed bioclastic wackestone with ostracods (o) and foraminifera (f). Ali Bashi 1, -0.65 m.

Peloidal, laminated wackestone

The characteristic feature of this microfacies type is subtle lamination, and inhomogeneous, mottled matrix with an occurrence of biogenic components of algae, ostracods and shell debris. Sparry and micritic peloids are abundant (Fig. 13a, b).

Burrowed sponge spicule wackestone

It is characterized by abundant, loosely packed sponge spicule remains embedded in a marly, burrowed micritic matrix (Fig. 14g, h). Ostracods, echinoderms, gastropods and shell debris are also present. Geopetal fillings occur within non-skeletal voids.

Red, nodular, burrowed, bioclastic lime mudstone and wackestone

This microfacies contains echinoderm remains, foraminifera, ostracods, radiolaria, bivalves, gastropods, and ammonoids (Figs. 15a-d, 16a-c). The characteristic feature of this microfacies is the occurrence of partly rounded limestone nodules embedded in a muddy, fine-bioclastic, marly matrix (Fig. 17g). The limestone nodules and the marly matrix are cut by systems of cracks and subtle fractures, which give them a breccia-like appearance (Fig. 17d). The composition of the nodules closely resembles the surrounding matrix. The boundaries between the nodules are often marked by irregular and anastomosing pressure solution seams; stylolitization produces a stylonodular fabric. The surface of micrite clasts is occasionally impregnated with Fe-Mn oxides. Also chambers of foraminiferal tests and ammonoid conchs are filled with Fe-Mn oxides. Hematite-filled sponge (?) perforation occurs on a brachiopod shell. Biogenic encrustation by attached agglutinated foraminifera and/or calcimicrobes and microborings are common. Calcareous encrustations are less than a millimeter in thickness; they grow upward from bivalve shells and on/inside micrite clasts (Figs. 15a, 17c, d). Geopetal structures occur within ammonoid conchs as well as in synsedimentary, interskeletal cavities (Fig. 17a). Few subsolution clasts (i.e., hardground intraclasts) indicate repeated phases of erosion, impregnation/ encrustation and accretion (Fig. 17e). Early lithification of carbonate mud was followed by exhumation of the lithified parts by weak currents, later erosion and encrustation at the surface. The radiolarians are poorly preserved; their original opaline silica has been replaced by calcite (mould preservation) and the margins of the tests appear ragged.

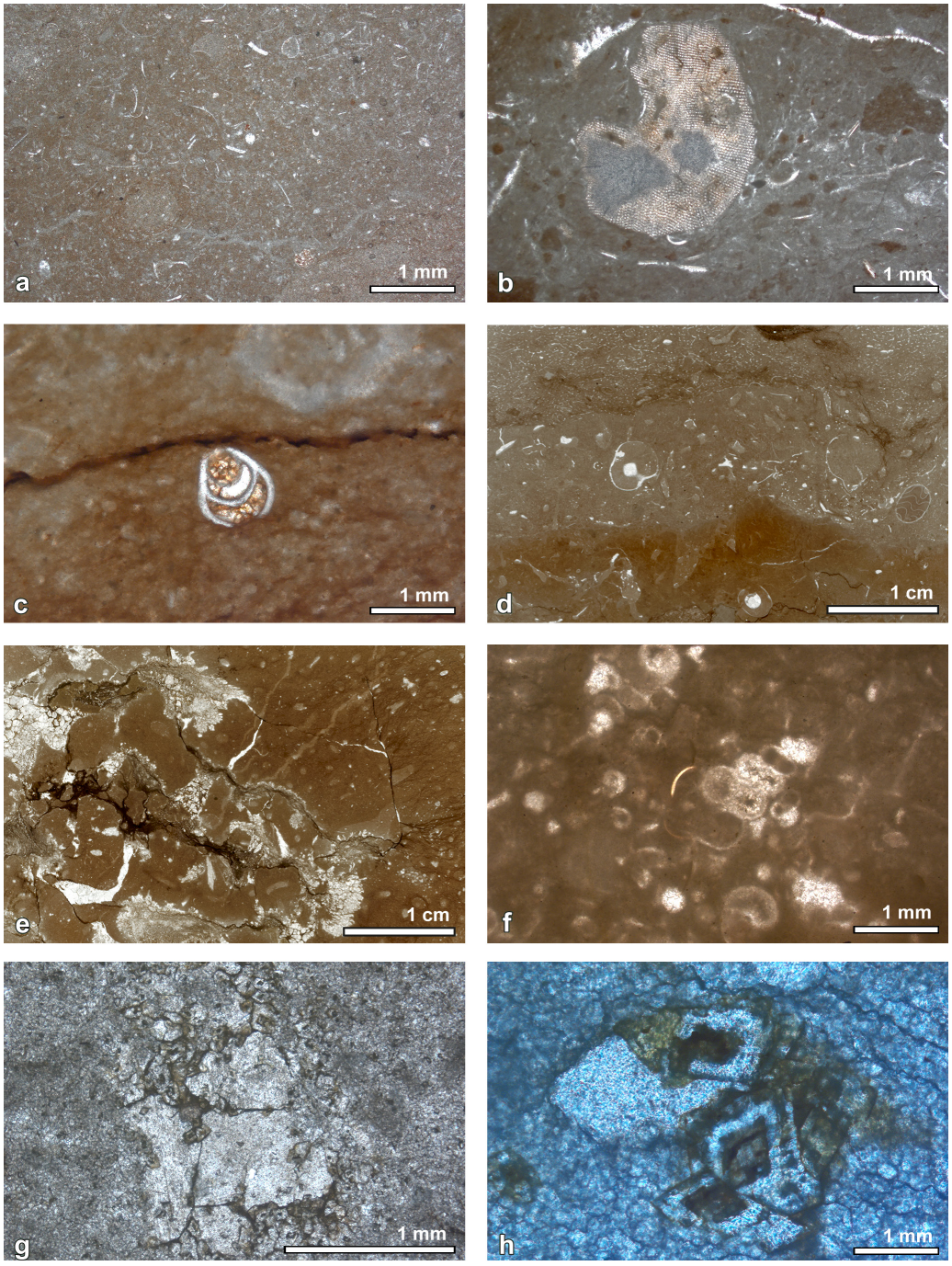

Figure 16 Carbonate microfacies of the P-Tr boundary beds at Aras Valley section. a – Red, nodular, burrowed, bioclastic wackestone with ostracods, foraminifera, radiolaria and echinoderms. -0.70 m. b – Partly micritized echinoderm plate with boring traces. -0.45 m. c – An example of foraminifera (*Frondina*? sp.) from the burrowed, bioclastic wackestone. -0.45 m. d – Top of the uppermost 4–5-cm-thick bed of the *Paratirolites* Limestone (=extinction horizon) with sponge spicules and ammonoids. e – Spherulites of aragonite pseudomorphs in a strongly burrowed and fractured lime mudstone. Aras Valley, +1.65 m. f – Gastropod packstone. +2.35 m. g – Floatstone with sparry calcite spheres; spheres are occluded by rhombic dolomite crystals. +4.30 m. h – Honey-colored, zonar, rhombic dolomite crystals. +4.30 m.

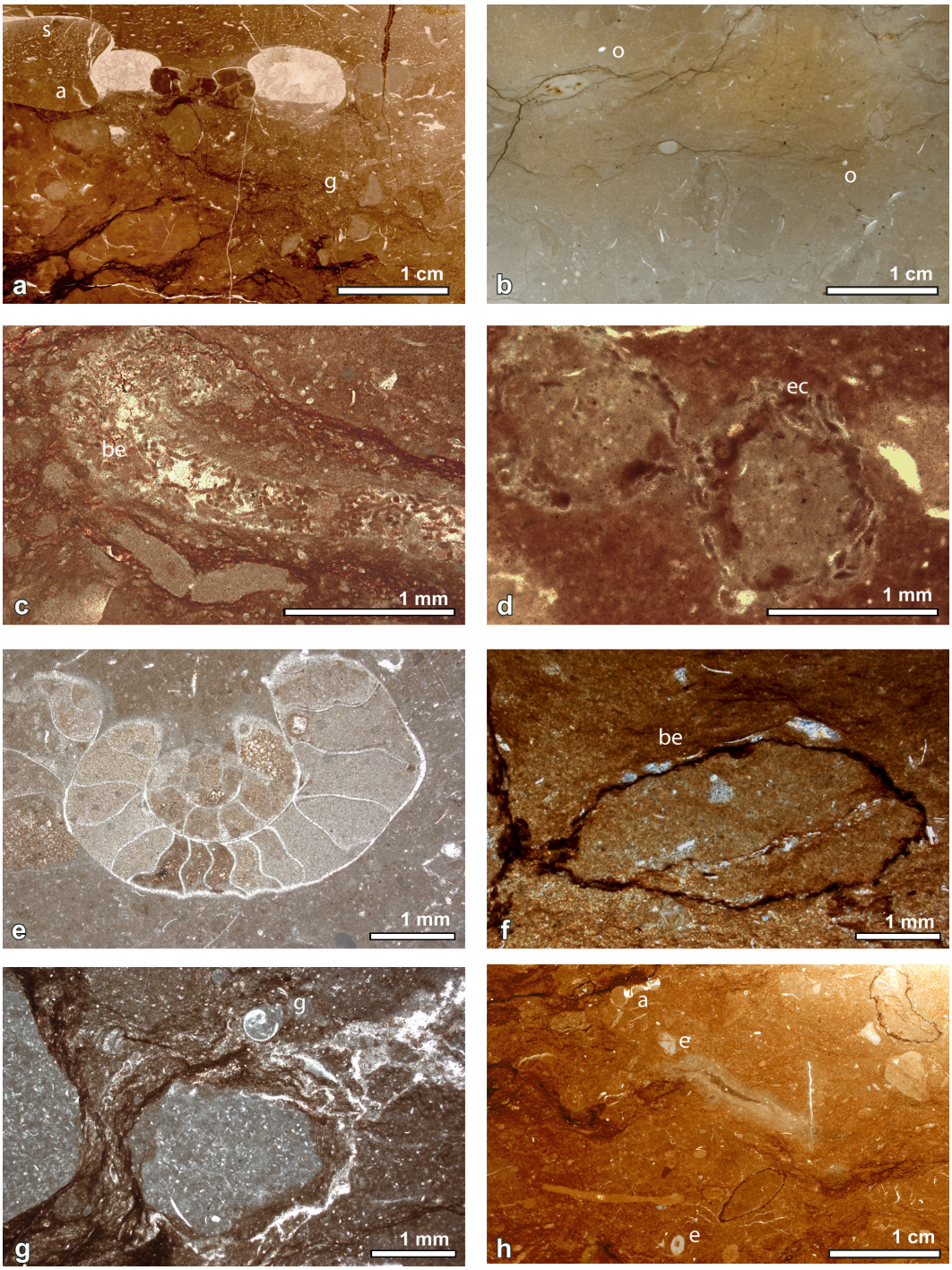

Figure 17 Carbonate microfacies of the upper part of the *Paratirolites* Limestone. a – Top of the uppermost 4–5-cm-thick bed of the *Paratirolites* Limestone (=extinction horizon with sponge spicules). The chambers of the ammonoid (a) conch have been partially filled with matrix rich in sponge (s) skeletons and pure marly micrite, as well as with sparry cement. The marly, bioclastic matrix contains small radiolaria, gastropods (g), and micrite pebbles. Stylolite seams and micro-fractures are common. Ali Bashi 1, -0 m. b – Top of the upper 4–5-cm-thick bed of the *Paratirolites* Limestone (=extinction horizon). Light-grey lime mudstone with single ostracods. Baghuk Mountain A, -0 m. c – Red, nodular, burrowed, bioclastic lime mudstone; microborings (mb) in a bivalve shell. Ali Bashi 1, -0.35 m. d – Red, nodular, burrowed, bioclastic lime mudstone. Endolithozoan crusts (ec). Ali Bashi 4, extinction horizon. e – Ammonoid preservation: the upper and lower surface of the

conch are completely truncated by dissolution. The section is longitudinal to the plane of the coiling. The lines of the junction of septa and the shell walls and septa are well preserved. After dissolution, the chambers were filled with muddy sediment, which have later recrystallized to microspar and pseudospar. The matrix is a bioclastic wackestone. Aras Valley, -1.10 m. f – Hardground intraclasts ('subsolution clasts'). Fe–Mn crusts with biogenic encrustation (be) by foraminifera around the micrite clasts. Ali Bashi 1, -0.75 m. g – Red, nodular, burrowed bioclastic lime mudstone with subrounded limestone clasts and single bellerophontid (g). The matrix is red-colored due to Fe-oxides, and is partially neomorphosed to microspar. The pebbles are fossil-rich and contain fine-grained biodetritus of radiolaria, benthic foraminifera, and ostracods. Clasts are surrounded by circumgranular crusts and biogenic encrustation. Ali Bashi 1, extinction horizon. h – Burrowed fossiliferous lime mudstone with radiolaria, ostracods, echinoderms (e) and ammonoids (a). Ali Bashi 1, -0.35 m.

Micrite-clast wackestone

Abundant micrite clasts occur in the lower part of the uppermost 4- to 5-cm-thick bed of the *Paratirolites* Limestone (Fig. 18c, 19c, d). The millimetre-sized micrite clasts are lithified, fine-grained carbonate mud pebbles, which have been embedded in a soft, marly matrix. Circumgranular crusts around the clasts as well as biogenic encrustations by attached agglutinated foraminifera and/or calcimicrobes are common. The clasts are cut by systems of cracks and subtle fractures (Fig. 19d). Point and tangential contacts of the pebbles are caused by compaction. Some clasts appear plastically deformed and redeposited; they can be considered as plasticlasts. They represent pieces of semi-lithified sediment, which has been reworked synsedimentary. The micrite-clast wackestone is overlain by a horizon filled with sponge remains. The boundary between the poorly sorted, marly micrite-clast wackestone facies and the overlying sponge packstone is not sharp. It is characterized by an occurrence of a 1.5-cm-thick horizon of marly matrix rich in crystal silt-filled and spar-filled interparticle cavities. The cavities are irregular in shape. Geopetal structures as well as mould peloids within these cavities are very common (Fig.19b). The cavities appear to be relics of burrows. Occasionally, ammonoid remains are present (Fig. 19a, b, d).

Sponge packstone ('Sponge Spike')

A conspicuous accumulation of sponge remains occurs at the uppermost part of the topmost 4- to 5-cm-thick bed of the *Paratirolites* Limestone, marking the extinction horizon in all sections between the Aras Valley, and the Ali Bashi Mountains (Fig. 12). Thin sections show an about two centimetre thick horizon of sponge packstone with more or less articulated skeletons of siliceous sponges, which are embedded in a widely occurring micritic matrix (Figs. 17a, 18a-d, 16d). Various spicule morphologies occur; predominant are irregular desmas, but also tetraxons and monaxons are present. The amorphous silica of the sponges is completely replaced by calcite, so that they are preserved as calcite pseudomorphs (Fig. 18a, b). Late cementation of roofed cavities within the sponge network caused geopetal infill. Rigid skeletons are not recognizable in the thin sections and a preferred orientation of the spicules cannot be seen (Fig. 18a d). Evidence of a benthic microbial community, and shallow water organisms (e.g., calcareous

algae) are lacking in this horizon. Thin sections give an impression that this material rather resembles spiculite (loosely accumulated siliceous spicules) than a sponge (A. Pisera, Warsaw, personal communication). Loose spicules float in the sediment, and were partially transported, and deposited with sediment. Because of poor preservation, identification of the sponge remains was not possible; the absence of suitable cross sections of the spicules made geometric reconstructions impossible. The sponges probably belong to the order Lithistida (J. Wendt, Tübingen, personal communication), most probably Megaclons (desmas of Pleromidae/Megamorina; A. Pisera, Warsaw, personal communication). The siliceous spicules are recognizable in the field only with a hand lens. Any single silica spicule remained in the acid residue from the carbonate dissolving process. Sponge remains are occasionally abundant in marly nodules and marly siltstone horizons within the Aras Member; such horizons exist 0.40, 0.75 and 0.85 m above the base of the Aras Member in the Ali Bashi 1 section (Fig. 20a, b, d, g) and 0.74 m above the base of the Aras Member in the Zal section (Fig. 21a). They do not show any preferred arrangement and are embedded in a mottled marly matrix. In the uppermost of the three horizons they occur together with disarticulated thin-shelled ostracods (Fig. 20h).

Argillaceous, non-fossiliferous, fractured lime mudstone

Lime mudstone with single, vertical microcracks filled with calcite cement. Abundant stylolite seams form a stylobedded structure. This microfacies type occurs only in the Zal section, 0.20 m above the reference horizon.

Bioturbated ostracod sponge lime mudstone

The ostracods are represented by disarticulated valves and complete tests, which are replaced by coarse calcite cement and/or filled with micrite (Fig. 20f). Some ostracods are silicified (Fig. 20h). Fractures and single calcite veins disrupt the heterolithic siltstone/limestone bedding. Radiolarian and echinoderm remains occur occasionally (Fig. 20e).

Bellerophontid wackestone

Red-brown and yellow-grey, marly, nodular, burrowed wackestone with bellerophontids, sponges, ostracods, gastropods and moulds of foraminifera. The marly micrite matrix contains micrite clasts. The bellerophontids are poorly preserved (Figs. 21a, b, 22a, b).

Bioclastic wackestone with diverse fossils

Light grey and yellow-brown lime mudstone and wackestone contain high-spired gastropods, ostracods, microconchid molluscs, algae, foraminifera, bivalves, and single radial ooids (Figs. 22b, c, 21d, 16f). The matrix and grains are partly recrystallized to dolomitic microsparite with amber-colored rhombic dolomite crystals of inequigranular, spotted fabric.

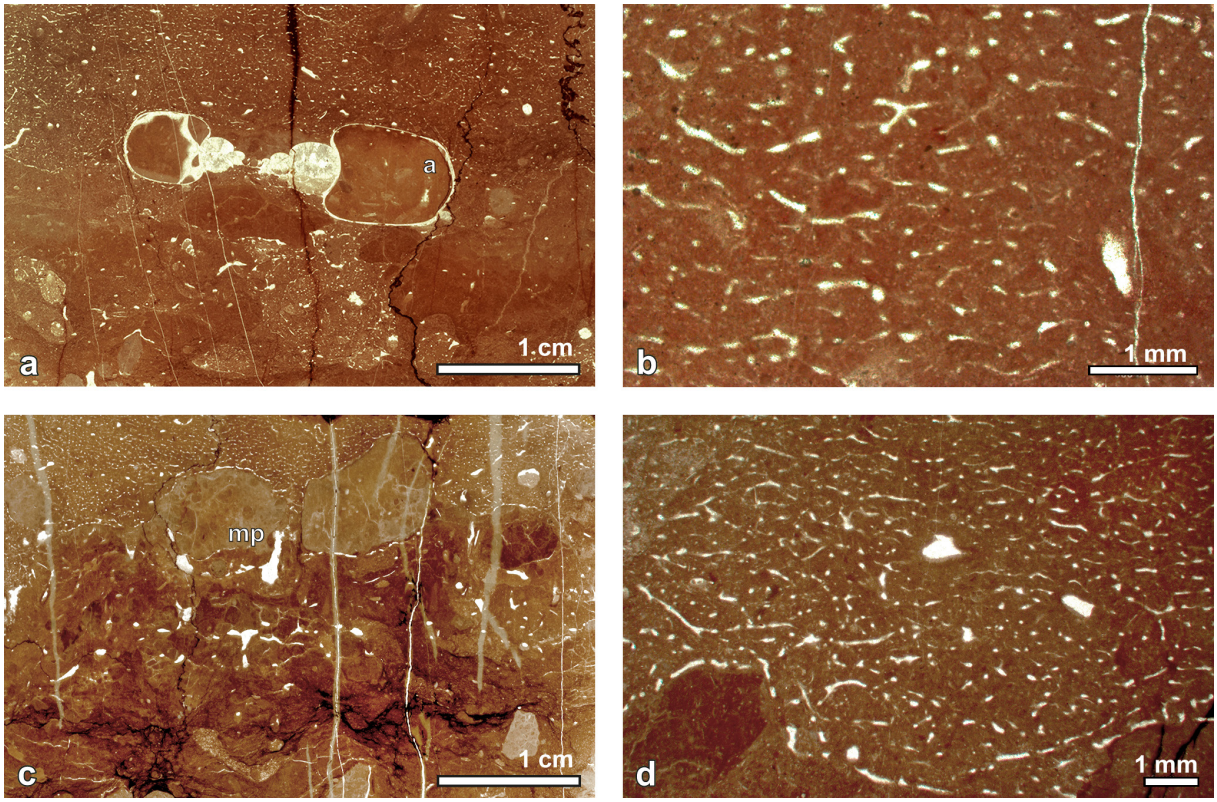

Figure 18 Carbonate microfacies of the 'Sponge Spike', all from topmost 2 cm of the *Paratirolites* Limestone (= extinction horizon). a – Sponge packstone with small vug-like cavities with geopetal infill; micro-fractures. The marly matrix is rich in crystal silt-filled and spar-filled interparticle cavities. Ammonoid (a) conch with well-preserved shell walls and septa; chambers infilled with micrite and blocky calcite cement. Ali Bashi 4. b – Enlarged view of the top part of a. Sponge packstone. Siliceous sponge skeletons were dissolved and replaced by calcite. Irregular forms predominate. The matrix is marly micrite. Ali Bashi 1. c – Micrite pebbles (mp) of the micrite-clast wackestone underlying the sponge packstone horizon; the clasts have been reworked and transported to the sponge packstone horizon. Matrix is rich in vugs filled with calcite cement. Micro-cracks and fractures give a breccia-like appearance. Ali Bashi 1. d – Enlarged view of the top part of c. Sponge network without rigid skeletons. Ali Bashi 1.

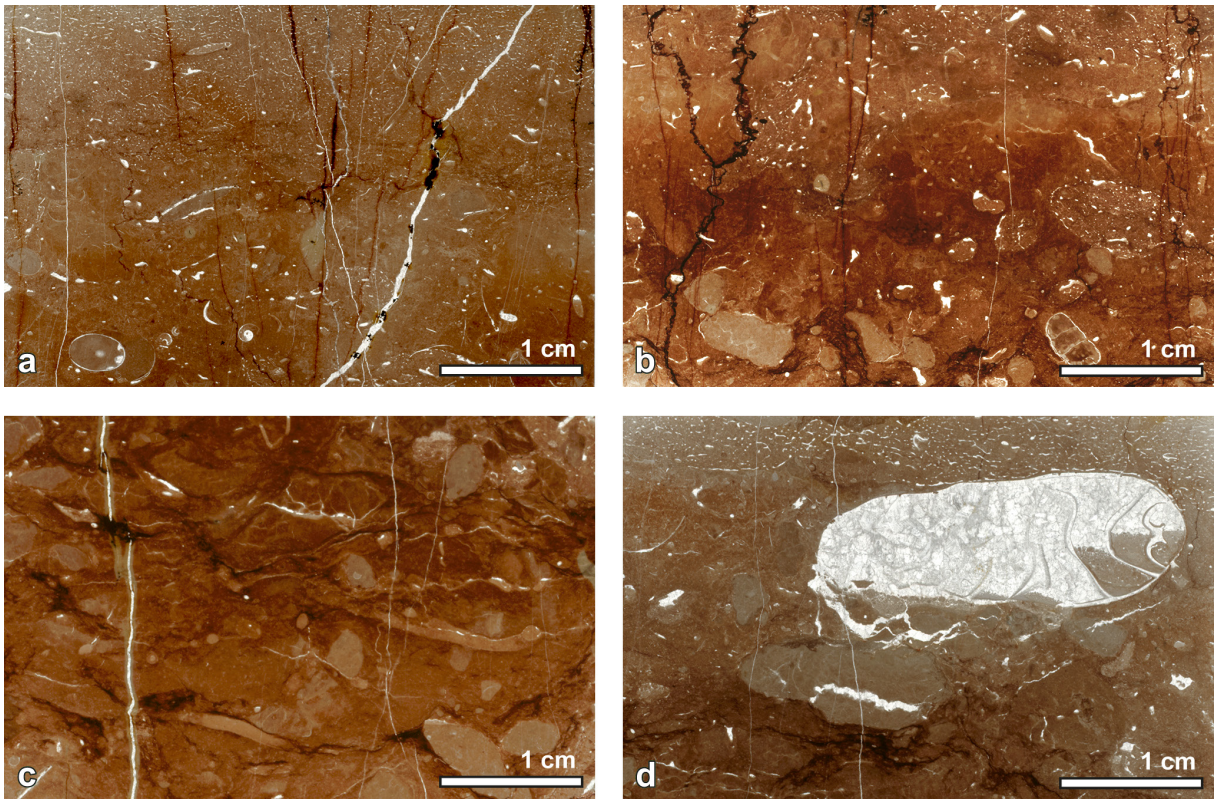

Figure 19 Carbonate microfacies of the uppermost 4–5-cm-thick bed of the *Paratirolites* Limestone. a – Contact between the marly matrix rich in crystal silt-filled and spar-filled interparticle cavities and the 'sponge spike'. Ali Bashi 4. b – Marly matrix rich in crystal silt-filled and spar-filled interparticle cavities. Ali Bashi 4. c – Micrite clast and micrite-filled burrows. Ali Bashi 1. d – Ammonite preservation. The shell has been infilled with micritic matrix, micrite peloids, and after breakage and dissolution the shell and septa were later filled by sparry calcite. Ali Bashi 1.

Densely laminated bindstone

This microfacies type comprises fine-grained, agglutinated carbonate with ostracods, bivalves, gastropods, foraminifera and algae. This microfacies marks the replacement of the Permian skeletal carbonate factory by the Triassic microbial carbonate factory at +2.01 m in Ali Bashi section 1, at +2.24 m in the Zal section, and at +1.90 m in the Baghuk Mountain sections. This microfacies type is characterized by microbial sedimentary structures, consisting of alternating couplets of fine, dark, micritic and coarser, light sparry and peloidal layers forming a laminated, planar and crenulated fabric (Fig. 22d). Small sparry spheres form occasionally a fenestral clotted packstone fabric. The sparry spheres appear to be former cavities that probably formed after the decay of organic matter and subsequently were filled with cement. In the Zal section the horizontally crinkle-laminated microbial carbonates are fine-grained agglutinated stromatolites. The microstructure comprises dark, dense and clotted micrite and light, sparry layers (Fig.

21c). In the Ali Bashi and Aras Valley sections, the organo-sedimentary deposits are controlled by benthic microbial communities; they are poorly structured thrombolites and cryptic microbialites, but discontinuous micrite laminae also occur. This microfacies represents microbially mediated calcareous structures (Burne and Moore 1987; Riding 2000). The lamination is related to the trapping and binding activity of microbes and algae and to autochthonous precipitation of calcium carbonate. I postulate that clotted micritic laminae precipitated within the microbial mat. Neither erosional discontinuities below and above the densely laminated bindstone, nor evidence of subaerial exposure within this unit was detected. Large-scale features of microbial limestones, e.g., biostromal buildups, were not found in the field. The classification of the microbialites was based only on microstructure observed under the microscope.

Floatstone with sparry calcite spheres

Another distinct character of the platy limestone beds in the lower part of the Elikah Formation is the common occurrence of irregular and roughly circular spheres up to 20 mm in size (Fig. 21e). They are filled with equant calcite spar and occasionally with celestine crystals (Fig. 23c, d). Horizons rich in these spheres begin in the Ali Bashi section 1 at about +3.15 m and extend to the top of the studied lithological section at +4.50 m. In the Zal section, the interval rich in sparry calcite spheres has a thickness of 2.05 m (between +4.80 to +6.85 m). It is overlain by an about 4.65-m-thick oncoid-bearing limestone. The limestone beds containing sparry calcite spheres are normal-graded and bedded with parallel wave and crinkled lamination. Horizontal stylolitic seams create a pseudo-laminated texture. The boundaries between spar-rich and spar-poor layers are erosional. The coarse-grained sparry spheres are closely spaced, irregular in shape, crushed and bound together; they form cement crusts at μm to mm scales (Figs. 22f, 16g). They display traces of borings; microborers (mainly foraminifera) may be responsible for the formation of dense micrite envelopes around the grains (cortoids; Fig. 22g). At the edges of the calcite crystals, small, brownish, honey-colored, euhedral and anhedral, rhombic dolomite crystals occur (Fig. 16f). The sparry spheres are partly micritized and embedded in honey-colored, clotted and peloidal micrite matrix. The irregular sparry calcite spheres may represent crinoid remains, of which previous outlines and surface ornamentation have largely vanished. In this case, the dense accumulation of crinoids may be allochthonous and could represent storm-induced deposits. Coarse-grained, crinoid-dominated beds may represent proximal tempestite deposits. The lack of original structures caused by diagenetic alteration may point to an inorganic origin of these structures, where calcite and celestine crystals grew directly on the seafloor, as postulated by Horacek et al. (2007) and Richoz et al. (2010). Floatstone with calcite spar-filled voids may have formed carbonate seafloor cement crusts of equant calcite. Brownish, honey-coloured dolomitic spots reflect diagenetic overprint and formed probably during a later emersion phase under arid or semi-arid conditions.

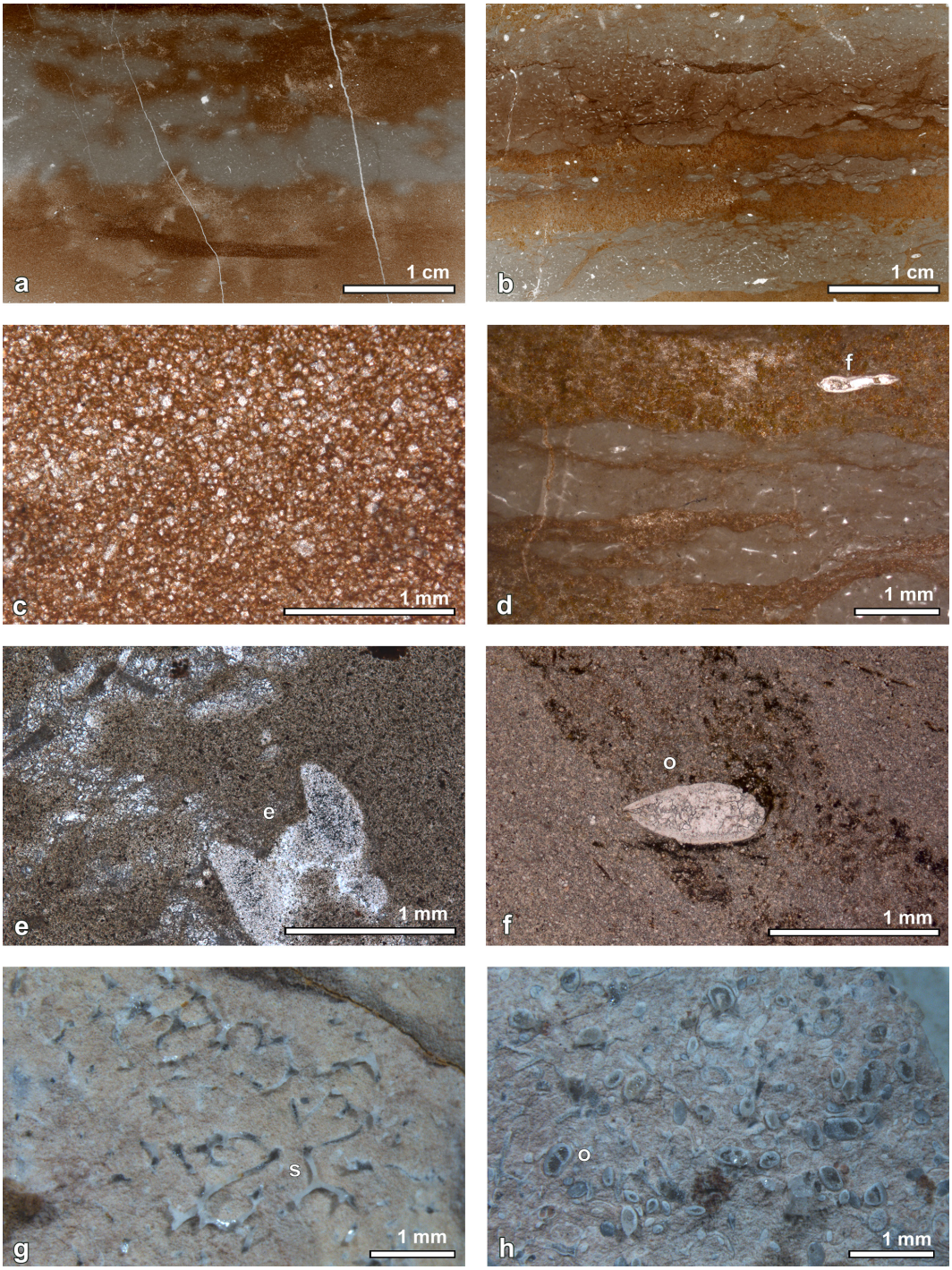

Figure 20 Carbonate microfacies of the Aras Member. a – Horizons of sponge lime mudstone within a marly siltstone. Ali Bashi 1, +0.45 m. b – Burrowed and bioturbated ostracod-sponge lime mudstone. Ali Bashi 1, +0.75 m. c – Abundant rhombic crystals (microspar) floating in matrix. Ali Bashi 1, +0.40 m. d – Foraminifera tests (f) within the microspar matrix. Ali Bashi 1, +0.75 m. e – Echinoderm remains (e). Ali Bashi 1, +0.28 m. f – A recrystallized ostracod shell (o). Ali Bashi 1, +1.29 m. g – Triaxon-like sponge remains (s) on an etched bedding surface of a marly interval in the Aras Member. Ali Bashi 1, +0.85 m. h – Sicilified ostracod shells (o) on an etched bedding surface of a marly interval in the Aras Member. Ali Bashi 1, +0.85 m.

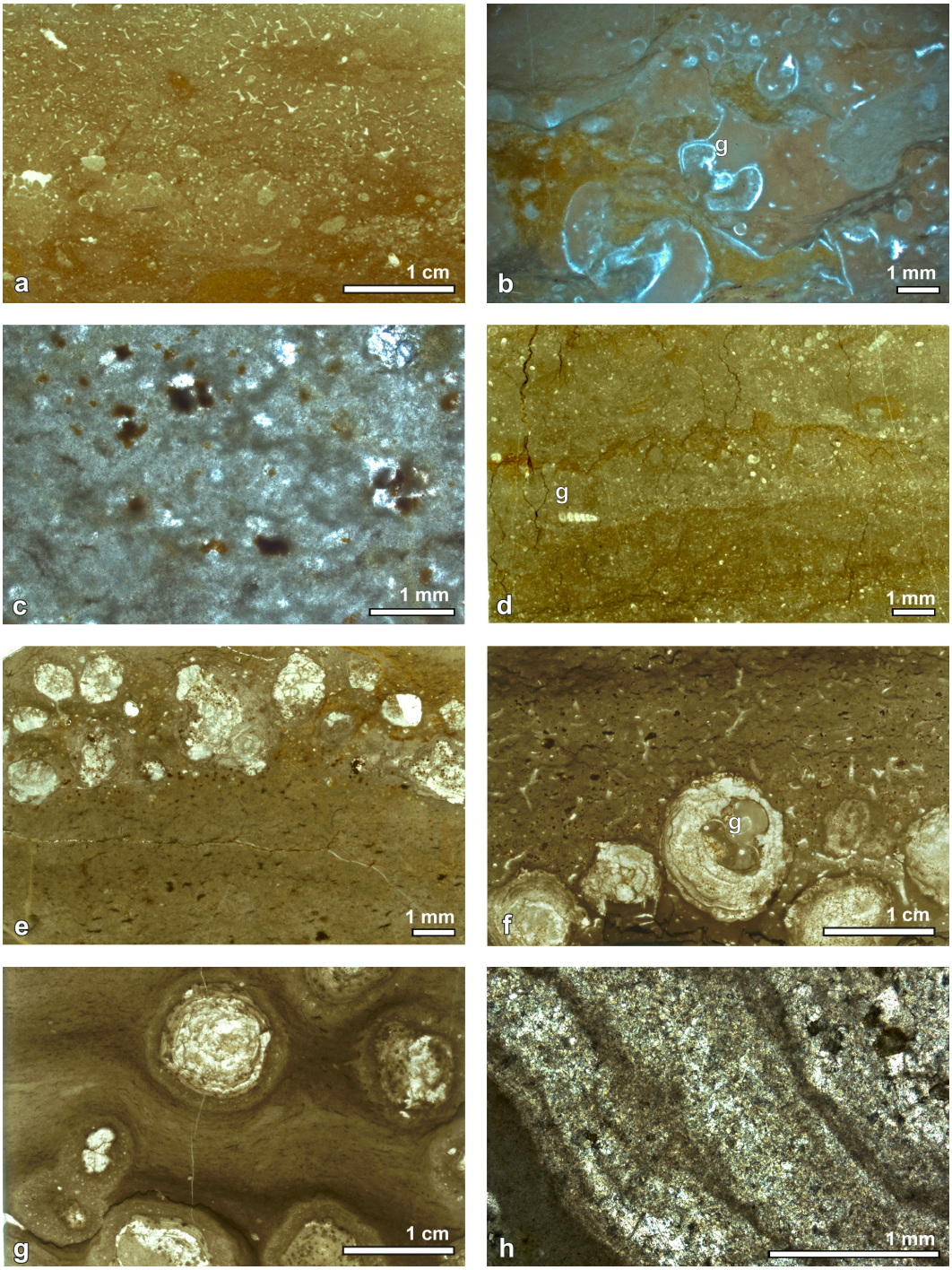

Figure 21 Carbonate microfacies of the *Claraia* Beds at Zal. a – Sponge gastropod wackestone, +0.42 m. b – Bellerophontid wackestone. The bellerophontids (g) are poorly preserved and deformed. The shell has been dissolved and the chambers are filled with sediment and calcite spar, +0.43 m. c – Laminated bindstone with algal/microbial mat, +2.45 m. d – Bioclastic wackestone with high-spired gastropods (g), +1.90 m. e – Horizon with sparry calcite spheres of the seafloor cement crusts, +4.05 m. f – Oncoid floatstone. The nucleus is a recrystallized bellerophontid (g), +7.15 m. g – Spherical, laminated (sl) oncoids as well as non-laminated, micritic oncoids with sparry spots, +10.05 m. h – Micrite and sparite lamina couplets of the oncoid cortex, +7.15 m.

Aggregate grain grapestone

This microfacies forms a one centimetre thick horizon and occurs within oncoid wackestone/floatstone only in the Zal section 2.48 m above the extinction horizon. Up to 5 mm large, strongly fractured, poorly preserved, recrystallized grains are embedded in microsparite with honey-colored euhedral and anhedral dolomite crystals within the matrix. The spherical aggregates have lobate outlines and are composite grains consisting of ooids and peloids. Some of the aggregates exhibit thin oolitic coatings (botryoidal lumps). The grains are bound together by carbonate cement.

Oncoid wackestone/floatstone

This microfacies shows oncolitic structures attached to microbial films and mats. Spherical, ellipsoidal, non-flattened, irregular oncoids with lobate, bored and encrusted surfaces are well preserved. The prevailing size of the oncoids is 2-20 mm. There are two types of the cortex. The first one adjoints directly to the nucleus and is usually laminated with distinct and vaguely concentric, non-discontinuous and crenulated micritic and sparry laminae (Fig. 22h). The second generation is a non-laminated micrite with tiny sparry spots (Fig. 21g). The nuclei are larger than the cortex and are either abiotically precipitated calcite spar or single, poorly preserved crinoid elements. The nuclei are occluded by brown dolomite crystals; in one case the nucleus is a bellerophontid gastropod (Fig. 21f). The oncoids are here classified as micrite R type oncoids (randomly arranged hemispheroidal layers) and C type oncoids (concentrically stacked spheroid layers); they are preserved as single oncoids. The oncoid-bearing limestone is a wackestone/floatstone with inhomogeneous matrix (irregular and tufted masses of clotted micrite), containing filaments of black organic matter, dolomite crystals and clay seams. An irregular, knobby surface of oncoids favors in situ development. The oncoids are interpreted here as microbial micrite oncoids. They may also be completely recrystallized spongiostromate oncoids.

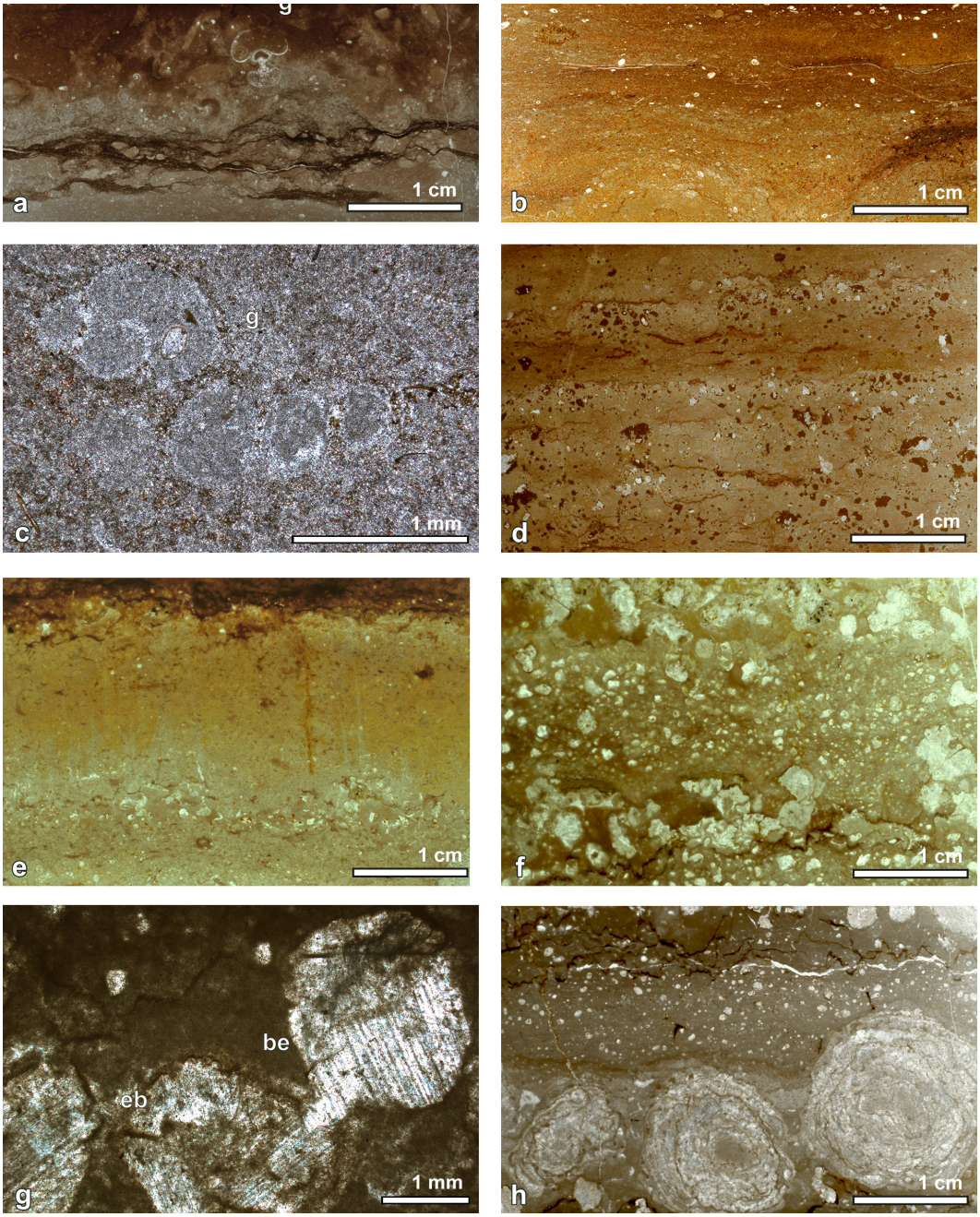

Figure 22 Carbonate microfacies of the *Claraia* Beds. a – Bellerophontid wackestone with marly and burrowed matrix. A well-preserved bellerophontid (g) conch is filled with crystal silt. Ali Bashi 1, +1.25 m. b – Yellow-brown, burrowed bioclastic wackestone with skeletal components of ostracods, gastropods, spirobids and foraminifera. Ali Bashi 1 +1.61 m. c – Poorly preserved gastropods (g), +1.61 m. d – Irregular, diffuse lamination and bindstone, and small, sparry calcite spheres of a bindstone. Ali Bashi 1, +2.20 m. e – Marly wackestone with dense micrite and with small sparry calcite spheres. Ali Bashi 1, +3.01 m. f – Wackestone with sparry calcite spheres of the seafloor cement crusts. Ali Bashi 1, +3.65 m. g – Sparry calcite spheres with traces of borings (eb), biogenic encrustation (be), and dense micrite envelope. Ali Bashi 1, +4.15 m. h – Oncoid wackestone/floatstone. Ali Bashi N, +7.10 m.

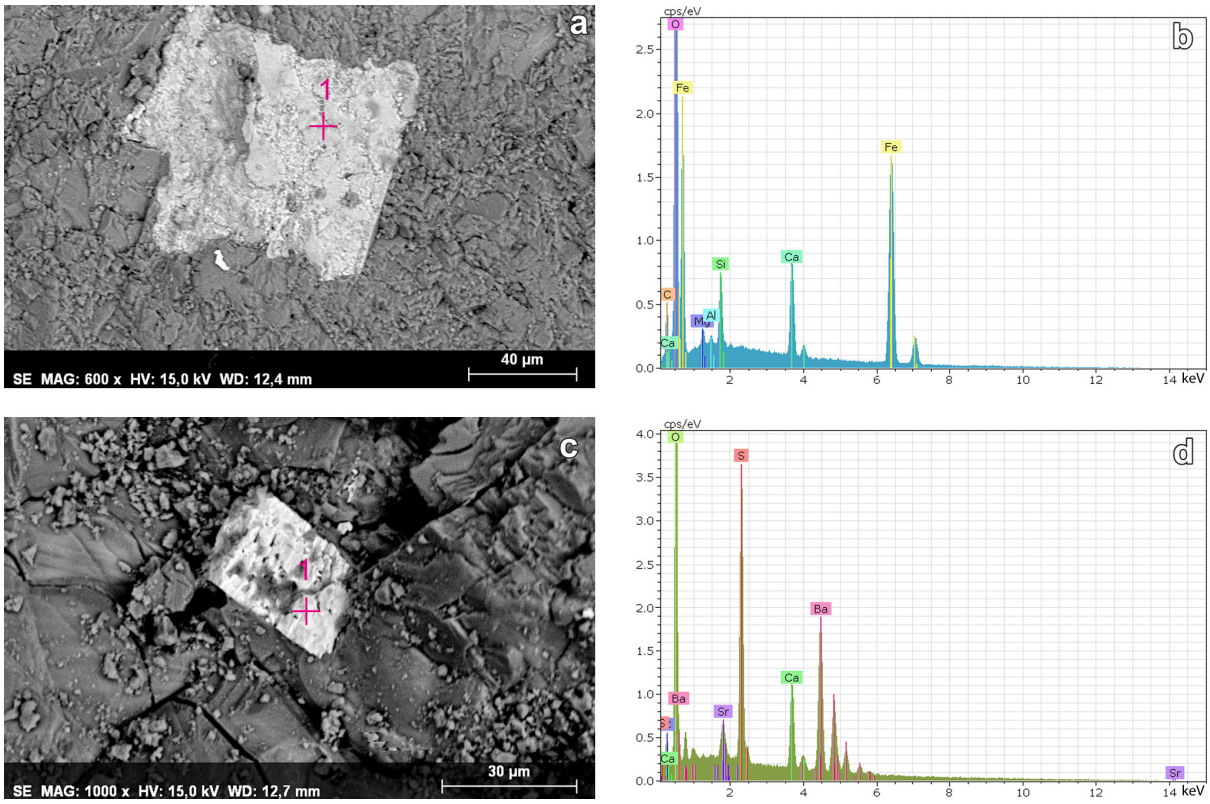

Figure 23 SEM-EDX characteristics of the floatstone with sparry calcite spheres at Zal (at +5.90 m). a – EDX image of an Fe-rich phyllosilicate crystal. A cross in pink in the centre of the crystal shows a place, where an EDS analysis was obtained. b – EDX spectrum of a crystal in a. c – EDX image of a celestine crystal. A cross in pink in the centre of the crystal shows a place, where the EDX measurement was taken. a – EDX spectrum of a celestine crystal in c.

4.1.3 Non-metric multidimensional scaling (NMDS)

The two-dimensional scatter plot shows a triangular arrangement of the data points, each of which represents one thin section (Fig. 24). For an illustration of microfacies changesthroughout the Ali Bashi 1 section, we calculated the position of the centroid for distinct intervals. In the scatter plot, all data points for the lower portion of the *Paratirolites* Limestone (from 5.00 m to 0.56 m below the reference horizon) form a cluster with clear limits, and the centroids of the four separated units within this interval are closely positioned. The upper portion of the *Paratirolites* Limestone differs and forms a separate small cluster (with the exception of sample -0.20). This is a first step of a migration across the facies morphospace, followed by the Aras Member and the lowermost portion of the Elikah Formation, which then continuously become more distant from the *Paratirolites* Limestone. Finally, the samples of the Elikah Formation from +2.30 to +4.60 form a very dense cluster opposite the *Paratirolites* Limestone. This migration demonstrates that the lowermost portion of the Elikah Formation has, with respect to its carbonate microfacies, much more in common with the *Paratirolites* Limestone than the Elikah Formation.

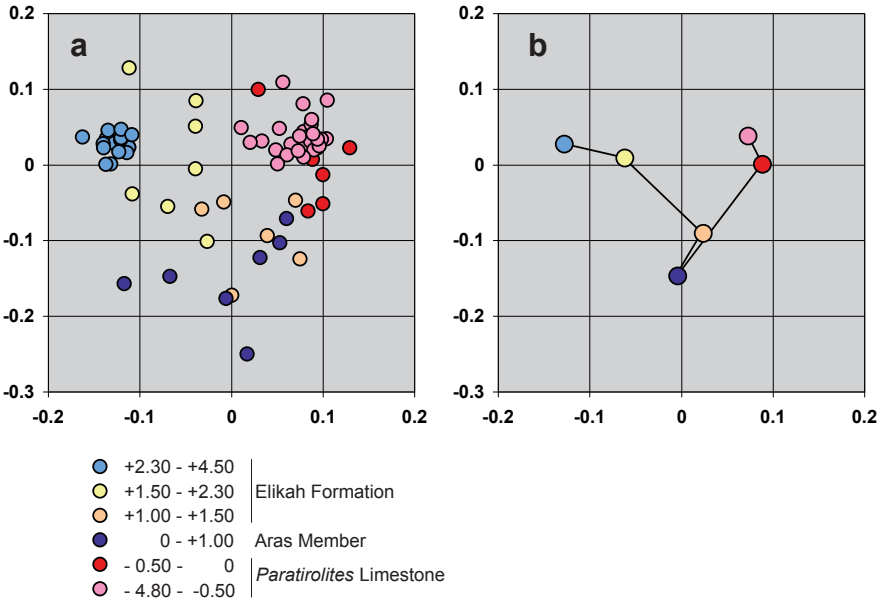

Figure 24 Non-metric multidimensional scaling (NMDS) of the microfacies data from the Ali Bashi 1 section. a – Scatter plot for each thin section of the *Paratirolites* Limestone, Aras Member and the base of the Elikah Formation. b – Position of the centroids for the subunits.

Table 3 Detailed facies description of the investigated Permian and Triassic beds in the Ali Bashi 1 section.

Interval (m)	Biogenic and abiogenic content	Microfacies type	Depositional setting (Flügel 2004)	Fig.
+3.15 to +4.56	biogenic: peloids, cortoids; abiogenic: sparite-filled voids, hematite coatings, pyrite	floatstone with sparry calcite spheres	open marine platform	22f, g
+2.01 to +3.12	biogenic: bivalves, foraminifera, crinoids, algal filaments, calcimicrobes, peloids; abiogenic: sparry calcite spheres	densely laminated bindstone (SMF 19)	restricted platform interior (FZ 8)	22d, e
+1.41 to +1.96	biogenic: gastropods, bellerophontids, ostracods, foraminifera, bivalves, microconchid molluscs, algae; abiogenic: sparry calcite spheres	bioclastic wackestone with diverse fossils (SMF 8; RMF 3)	open marine platform	22b, c
+1.27 to +1.39	biogenic: bellerophontids, sponges, ostracods, calcispheres	bellerophontid wackestone	open marine platform interior (FZ 7)	20f, 22a,
+1.20	biogenic: sponges, ostracods; abiogenic: micrite clasts	sponge-ostracod lime mudstone	deep shelf to basin	
+0.95	biogenic: sponges	strongly burrowed lime mudstone (RMF 2)	outer ramp, basin	
+0.75 to +0.88	biogenic: ostracods, sponges radiolaria, echinoderms; abiogenic: Fe-Mn crusts	burrowed and bioturbated ostracod-sponge lime mudstone	deep shelf to basin (FZ 1B, FZ 2)	20b,d, 20g, h
+0.42 to +0.58	biogenic: sponges	sponge lime mudstone	deep shelf to basin (FZ 1B, FZ 2)	20a, c
-0.02 to 0.00	biogenic: sponges	sponge packstone (SMF 1)	deep shelf to basin (FZ 1B, FZ 2)	17, 18b 19
-0.05 to -0.02	biogenic: sponges, radiolaria, ostracods, ammonoids, biogenic encrustation; abiogenic: micrite clasts, micro-cracks	micrite clast wackestone (RMF 11)	mid-ramp, outer ramp	17g, 18c,d, 19c
-0.68 to -0.07	biogenic: radiolaria, ostracods, echinoderms sponges, ammonoids, and single corals, encrustations	strongly burrowed, fossiliferous argillaceous lime mudstone (RMF 2)	outer ramp, basin	15h, 17c, h
-2.67 to -0.75	biogenic: ammonoids, echinoderm remains, foraminifera, ostracods, radiolaria, bivalves, gastropods, encrustations; abiogenic: Fe-Mn crusts, stylobreccia, hardground, intraclasts	nodular burrowed bioclastic lime mudstone and wackestone (SMF 9; RMF 2, RMF 3)	deep shelf (FZ 2)	15a-d, 15f, 17f
-2.95	biogenic: bivalves, echinoderms, ostracods, foraminifera; abiogenic: stylolite seams	thin-shelled filament bivalve wackestone (SMF 3-Fil)	toe of slope (FZ 3), deep shelf (FZ 2), and basin (FZ 1)	15g

-5.00 to -3.16	biogenic: echinoderms, ostracods, foraminifera, radiolaria; abiogenic: micrite clasts, matrix partly recrystallized to microspar	burrowed argillaceous bioclastic lime mudstone and wackestone (RMF 2)	outer ramp, basin	
-5.88 to -5.70	biogenic: ostracods, echinoderms, bivalves, foraminifera, brachiopods, nautiloids; abiogenic: Fe-Mn crusts, stylolite seams	burrowed bioclastc wackestone with diverse fossils (RMF 3)	mid-ramp, outer ramp	14a, b
-7.10 to -6.80	biogenic: ostracods, foraminifera, echinoderms, calcispheres; abiogenic: stylolite seams	argillaceous burrowed lime mudstone (RMF 2)	outer ramp	14c
-9.00 to -8.95	biogenic: ostracods, foraminifera, peloids	argillaceous peloidal lime mudstone	outer ramp	
-10.00 to -9.90	biogenic: ostracods, foraminifera, echinoderms, peloids	argillaceous burrowed lime mudstone (RMF 2)	outer ramp	
-10.87 to -10.80	biogenic: ostracods, foraminifera, echinoderms, calcispheres; abiogenic: sulphide patches	peloidal lime mudstone	outer ramp, basin, open shelf	14d
-12.50 to -12.40	biogenic: ostracods, foraminifera, echinoderms, calcispheres; abiogenic: stylolite seams	nodular burrowed fossiliferous lime mudstone (RMF 2)	outer-ramp	
-13.67 to -12.90	biogenic: echinoderms, ostracods, foraminifera	burrowed fossiliferous lime mudstone (RMF 2)	outer-ramp	
-14.95 to -14.90	biogenic: sponges, ostracods, echinoderms	burrowed fossiliferous lime mudstone (RMF 2)	outer-ramp	
-15.43 to 15.35	biogenic: sponges, ostracods, gastropods, shell debris	burrowed bioclastic wackestone (SMF 2)	outer-ramp	
-16.12 to -16.05	biogenic: sponges, ostracods, gastropods, echinoderms, shell debris; abiogenic: geopetal fabric	nodular burrowed sponge spicule wackestone (SMF 1 -burrowed)	basin (FZ 1), open sea shelf (FZ 2)	
-17.55 to -17.40	biogenic: ostracods, foraminifera, echinoderms; abiogenic: stylolite seams	nodular burrowed bioclastic wackestone (SMF 1-burrowed)	basin (FZ 1), open sea shelf (FZ 2)	
-18.26 to -17.98	biogenic: ostracods, sponges, foraminifera, gastropods; abiogenic: Fe-Mn crust	fossiliferous lime mudstone	open sea shelf (FZ 2)	
-18.37 to -18.25	biogenic: ostracods, sponges, foraminifera, gastropods; abiogenic: Fe-Mn crust	burrowed bioclastic wackestone with ostracods (SMF 1-burrowed; RMF 18)	open sea shelf (FZ 2)	
-19.10 to -19.05	biogenic: ostracods, echinoderms, foraminifera, shell debris	burrowed bioclastic wackestone (SMF 1; RMF 2)	basin , open sea shelf (FZ2), outer ramp	

-20.03 to -19.95	biogenic: peloids, foraminifera, ostracods, shell debris; abiogenic: lamination	laminated peloidal wackestone (RMF 4)	outer ramp	13a, b
-20.49 to -20.37	biogenic: ostracods, echinoderms, radolaria, sponges, shell debris; abiogenic: micrite clasts	burrowed bioclastic wackestone (SMF 1-burrowed)	basin (FZ 1), open sea shelf (FZ 2)	
-21.60 to -21.55	biogenic: ostracods, echinoderms, radiolarian, foraminifera, brachiopods, bivalves, fish remains	burrowed bioclastic packestone, SMF 1-burrowed	basin, open sea shelf (FZ 2), outer ramp	13c, d

Table 4 Detailed facies description of the investigated Permian beds in the Ali Bashi 4 section.

Interval (m)	Biogenic and abiogenic content	Microfacies type	Depositional setting (Flügel 2004)	Fig.
-0.01 to 0.00	biogenic: sponges	sponge packstone (SMF 1)	deep shelf to basin (FZ 1B, FZ 2)	17d, 18a
-0.03 to -0.01	biogenic: sponges, radiolaria, ostracods, ammonoids; abiogenic: micrite clasts, lithoclasts, mud peloids, micro-cracks, geopetal fabric	micrite clast wackestone (RMF 11)	mid-ramp, outer ramp	19a, b
-0.60 to -0.03	biogenic: radiolaria, ostracods, echinoderms, sponges, foraminifera, calcareous algae, ammonoids, mollusc remains; abiogenic: micrite clasts, micro-cracks, encrustations, Fe-Mn crusts, geopetal fabric	strongly burrowed, fossiliferous argillaceous lime mudstone (RMF 2)	outer ramp, basin	

Table 5 Detailed facies description of the investigated Triassic beds in the Ali Bashi N section.

Interval (m)	Biogenic and abiogenic content	Microfacies type	Depositional setting (Flügel 2004)	Fig.
+7.10 to +7.30	biogenic: oncoids, filaments, borings; abiogenic: sparite-filled voids, stylolite seams	oncoid wackestone/ floatstone (SMF 22)	open marine platform	22h
+5.25 to +5.45	biogenic: peloids, cortoids, gastropods; abiogenic: sparite-filled voids, hematite coatings, stylolite seams	floatstone with sparry calcite spheres	open marine platform	

Table 6 Detailed facies description of the investigated Permian and Triassic beds in the Aras Valley section.

Interval (m)	Biogenic and abiogenic content	Microfacies type	Depositional setting (Flügel 2004)	Fig.
+3.80 to +5.00	biogenic: peloids, borings; abiogenic: sparite-filled voids, calcite rhombs, celestine crystals	floatstone with sparry calcite spheres	open marine platform	16g
+2.30 to +2.45	biogenic: sponges, gastropods; abiogenic: micrite clasts	sponge gastropod packstone	restricted platform interior (FZ 8)	16f
+1.65 to +1.72	abiogenic: calcite crystal fibres, spherulites and mineral splays	strongly burrowed and fractured lime mudstone with 'calcite fan'- like structures	open marine platform	16e
-0.01 to 0.00	biogenic: sponges; abiogenic: geopetal fabric	sponge packstone (SMF 1)	deep shelf to basin (FZ 1B, FZ 2)	16d
-0.02 to -0.01	biogenic: ammonoids; abiogenic: crystal silt-filled and spar-filled interparticle cavities, mould peloids	fenestral wackestone with ammonoids	mid-ramp, outer ramp	
-0.04 to 0.02	biogenic: radiolaria, ostracods, ammonoids, biogenic encrustation; abiogenic: micrite clasts, lithoclasts, micro-cracks	micrite clast wackestone (RMF 11)	mid-ramp, outer ramp	
-0.13 to -0.04	biogenic: ostracods, mold peloids, gastropod molds; abiogenic: sulphide patches	fractured lime mudstone	outer ramp, basin	
-0.45 to -0.30	biogenic: foraminifera, echinoderm, shell debris, biogenic encrustation; abiogenic: lithoclast, micrite clasts	burrowed bioclastic wackestone	outer ramp, basin	16b, c
-2.05 to -0.75	biogenic: foraminifera, radiolaria, ostracods, echinoderms, ammonoids, microbial crust, biogenic encrustation; abiogenic: Fe-Mn crust	nodular burrowed bioclastic lime mudstone and wackestone (SMF 9; RMF 2, RMF 3)	deep shelf (FZ 2)	16a, 17e
-2.25 to -2.05	biogenic: foraminifera, algae, peloids, cortoids	foraminifer-algae packstone	lagoon	
-3.40 to -2.60	biogenic: radiolaria, echinoderms, foraminifera, ostracods, ammonoids; abiogenic: Fe-Mn crusts, stylobreccia, dendrites	nodular burrowed bioclastic lime mudstone (SMF 9; RMF 2, RMF 3)	deep shelf (FZ 2)	
-5.00 to -3.40	biogenic: foraminifera, ostracods, echinoderms, ammonoids, calcimicrobes; abiogenic: micrite clasts, Fe-Mn crusts	burrowed argillaceous bioclastic lime mudstone and wackestone (RMF 2)	outer ramp, basin	
-5.70 to -5.35	biogenic: echinoderms; abiogenic: micrite flakes	burrowed lime mudstone	outer ramp	
-7.45 to -7.05	biogenic: ostracods; abiogenic: fractures	fractured lime mudstone	outer ramp	

-9.30 to -8.15	biogenic: ostracods; abiogenic: Fe-Mn crusts	lime mudstone	outer ramp	
-10.40 to -10.30	biogenic: ostracods, foraminifera, echinoderms; abiogenic: dendrites	argillaceous burrowed lime mudstone (RMF 2)	outer ramp	
-15.85 to -12.85	biogenic: ostracods, brachiopods, calcimicrobes; Fe-Mn crusts	lime mudstone	outer ramp	
-18.10 to -17.90	biogenic: calcerous algae, ostracods, peloids	peloidal packestone with algae	lagoon	
-21.70 to -19.85	biogenic: ostracods, echinoderms, foraminifera, shell debris	burrowed bioclastic wackestone (SMF 1; RMF 2)	basin, open sea shelf (FZ2), outer ramp	
-27.95 to -22.95	biogenic: echinoderms (crinoids), brachiopods, corals, gastropods, shell debris, peloids; abiogenic: calcisiltite matrix	crinoid wackestone to packstone	mid-ramp	
-29.15 to 28.95	biogenic: ostracods	lime mudstone	outer ramp	

Table 7 Detailed facies description of the investigated Permian and Triassic beds in the Zal section.

Interval (m)	**Biogenic and abiogenic content**	**Microfacies type**	**Depositional setting (Flügel 2004)**	**Fig.**
+7.15 to +12.00	biogenic: oncoids, single bellerophontid	oncoid wackestone/ floatstone (SMF 22)	open marine platform	21f-h
+4.80 to +6.85	biogenic: peloids, cortoids; abiogenic: sparry calcite spheres, hematite coatings, pyrite	floatstone with sparry calcite spheres	open marine platform	21e 22f, g 23
+4.17	biogenic: oncoids	oncoid wackestone/ floatstone (SMF 22)	open marine platform	
+2.40 to +3.65	biogenic: bivalves, foraminifera, crinoids, algae filaments, calcimicrobes, peloids; abiogenic: sparry calcite spheres	densely laminated bindstone (SMF 19)	restricted platform interior (FZ 8)	21c
+2.42	biogenic: ooids, peloids	aggregate grain grapestone (SMF 17)	restricted platform interior (FZ 8), open marine platform interior (FZ 7)	
+0.50 to +2.02	biogenic: gastropods, bellerophontids, ostracods, sponges, foraminifera, bivalves microconchid molluscs, algae; abiogenic: sparry calcite spheres	bioclastic wackestone with diverse fossils (SMF 8; RMF 3)	open marine platform interior (FZ 7)	21a, d
+0.40	biogenic: bellerophontids, sponges, ostracods, calcispheres	bellerophontid wackestone	open marine platform interior (FZ 7)	21b

+0.05 to +0.20	abiogenic: micro-cracks filled with calcite cement, stylolite seams form stylobedding	non-fossiliferous, fractured argillaceous lime mudstone (SMF 23)	deep shelf to basin (FZ 1B, FZ 2)	
-1.33 to +0.00	biogenic: ammonoids, echinoderm remains, foraminifera, ostracods, radiolaria, bivalves, gastropods, biogenic encrustations; abiogenic: Fe-Mn crusts, stylobreccia, hardground, intraclasts, micrite clasts	nodular burrowed bioclastic lime mudstone and wackestone (SMF 9; RMF 2, RMF 3)	deep shelf (FZ 2)	
-2.00	biogenic: echinoderms, ostracods, bivalves, gastropods; abiogenic: calcite veins, microcracks, fractures	fractured fossiliferous lime mudstone	deep shelf (FZ 2)	
-3.70 to -2.85	biogenic: echinoderms, ostracods, radiolaria, foraminifera, shell debris; biogenic encrustation, abiogenic: micrite clasts, lithoclasts, stylolite seams	nodular burrowed bioclastic wackestone (SMF 9); RMF 3	deep shelf (FZ 2)	
-5.00	biogenic: echinoderms, ostracods, shell debris	argillaceous burrowed mudstone (RMF 2)	mid-ramp, outer ramp, basin	
-6.30	biogenic: peloids, echinoderms, calcimicrobes, gastropods, ostracods, single corals and ammonoids; abiogenic: lithoclasts, micrite clasts	burrowed fine-bioclastic peloidal wackestone	mid-ramp, outer ramp, basin	
-8.25	biogenic: gastropods, ostracods, echinoderms	burrowed mudstone (RMF 2)	mid-ramp, outer ramp, basin	
-11.70	biogenic: foraminifera, radiolarian, sponges, calcimicrobes, ostracods, echinoderms	burrowed bioclasic wackestone with pelagic and benthic biodetritus (SMF 1-burrowed)	basin (FZ1), open sea shelf (FZ2), outer ramp	
-13.70	biogenic: ostracods, echinoderms, cortoids	non-burrowed lime mudstone (RMF 19)	outer ramp, basin	
-16.80	biogenic: sponges, ostracods, echinoderms, cortoids	sponge spicule mudstone (RMF 1)	outer ramp, basin	
-17.75	biogenic: ostracods, foraminifera, echinoderms, shell debris; abiogenic: dolomite	dolomitic lime mudstone	outer ramp	
-18.25	biogenic: foraminifera, ostracods, echinoderms, radiolarian, gastropods; abiogenic: dolomite	burrowed pelagic lime mudstone with benthic foraminifera (SMF 3-FOR)	basin (FZ 1B), open deep shelf (FZ 3)	
-20.00	biogenic: ostracods, calcimicrobes, echinoderms, sponges	burrowed, fossiliferous mudstone (RMF 2)	mid-ramp, outer ramp, basin	
-21.00	biogenic: calcimicrobes, sponges, bivalves, gastropods peloids	calcimicrobial wackestone	tidal, subtidal	

4.1.4 Biostratigraphic subdivision

Biostratigraphic subdivision of the Iranian P-Tr boundary sections was achieved with the use of ammonoids and conodonts. A biostratigraphic subdivision using conodonts was established in a pioneering study by Sweet (in Teichert et al. 1973). A revision of this subdivision was suggested by Shen and Mei (2010), who proposed a zonal scheme with eight zones spanning the interval from the Wuchiapingian *C. orientalis* Zone to the topmost Permian *C. hauschkei* Zone (Fig. 25). Kozur (2005, 2007) sampled the sections at greater resolution and subdivided the Changhsingian successions of northwest and central Iran into 10 conodont biozones, in ascending order: the *Clarkina hambastensis*, *C. subcarinata*, *C. bachmanni*, *C. nodosa*, *C. changxingensis–C. deflecta*, *C. zhangi*, *C. iranica*, *C. hauschkei*, *C. meishanensis–Hindeodus praeparvus* and *Merrillina ultima–Stepanovites* ?*mostleri* zones. The correlation of the two schemes reveals several problems in the number of discriminated zones, their thicknessess, their names and also in their positions. While Kozur (2007) distinguished between six zones within the *Paratirolites* Limestone and two in the Aras Member, Shen and Mei (2010) used only five zones with imprecise duration for this interval. The conodont zones proposed by Kozur (2007) differ significantly in their thicknesses. While the *C. bachmanni* Zone at the base of the *Paratirolites* Limestone has a thickness of about two meters, the topmost two zones (*C. iranica* Zone, *C. hauschkei* Zone) of this rock interval are only represented by thin limestone beds of 5 cm thickness each. The new investigations of Ghaderi et al. (2014), including a revision of the biostatigraphy, led to the separation of ten conodont biozones for the Changhsingian sections of the Julfa area (from bottom to top: *Clarkina orientalis–C. subcarinata* interval zone, *C. subcarinata*, *C. changxingensis*, *C. bachmanni*, *C. nodosa*, *C. yini*, *C. abadehensis*, *C. hauschkei*, *Hindeodus praeparvus–H. changxingensis* and *Merrilina ultima–Stepanovites* ?*mostleri* zones) and of four conodont zones for the Induan stage (*Hindeodus parvus*, *H. lobota*, *Isarcica staeschei*, *I. isarcica* zones) (Fig. 25). The base of the Changhsingian stage in the NW Iranian sections was defined by Ghaderi et al. (2014) with the *C. orientalis–C. subcarinata* interval zone, which was taken as equivalent to the absent Changhsingian conodont marker species *C. wangi* (Jin et al. 2006, fig. 10). The stage boundary is located close to the base of the Zal Member. The extinction horizon (EH) marks the boundary between the *C. hauschkei* and *Hindeodus praeparvus–H. changxingensis* zones. The upper limits of these intervals are characterized by the first appearance of *Hindeodus parvus*, which indicates the Permian–Triassic boundary. As Ghaderi et al. (2014) based the subdivision on much finer resolution of bed-by-bed sampling, I will refer to their stratigraphic scheme in the following chapters. Ghaderi et al. (2014) applied the sample-population taxonomic approach and collected material from all limestone, marly and shaly horizons from five NW Iranian sections: Aras ValleyAli Bashi 1, Ali Bashi 4, Ali Bashi M, Ali Bashi N, and Zal.

Ghaderi (in Ghaderi et al. 2014) largely confirmed the subdivision within the Changhsingian by Kozur (2007) and Shen and Mei (2010) with some exceptions. Kozur (2004) regarded *C. hambastensis* as the best index species for a definition of the Wuchiapingian-Changhsingian boundary. He reported the species *C. hambastensis* only from the Shahreza section and from sections V and VI of the Hambast Mountains, but not from the Julfa area. Ghaderi et al (2014) assumed that there is no *C. hambastensis* in the sections of the Julfa area. At the same time, there are no

traces of a sedimentary gap between the *C. orientalis* and *C. subcarinata* biozones. Additionally, Ghaderi et al. (2014) proposed the *Hindeodus praeparvus-H. changxingensis* zone instead of Kozur's *C. meishanensis–Hindeodus praeparvus* zone as the first conodont zone within the Aras Member. The lack of *Clarkina meishanensis* in the sections in the vicinity of the Julfa area and rarity of this species led Ghaderi et al. (2014) not to use very sparse species as a zonal marker or in the name of a biozone. The extinction horizon (EH) marks the boundary between the *C. hauschkei* and *Hindeodus praeparvus-H. changxingensis* zones. The upper limits of these intervals are characterized by the first appearance of *Hindeodus parvus*, which indicates the Permian–Triassic boundary. Characteristic conodont specimens are illustrated in Fig. 26).

A total of eleven ammonoid biozones (from bottom to top) within the Changhsingian interval can be used for regional correlation (Korn et al. 2016; Fig. 27). The lower three biozones (from bottom to top: the *Iranites transcaucasius–Phisonites triangulus*, *Dzhulfites nodosus*, *Shevyrevites shevyrevi* zones) represent the lower shaly portion (Zal Member) of the Ali Bashi Formation and the upper eight (*Dzhulfites zalensis*, *Paratirolites trapezoidalis*, *Paratirolites kittli*, *Stoyanowites dieneri*, *Alibashites mojsisovicsi*, *Abichites abichi*, *Abichites stoyanowi* and *Arasella minuta* zones) the *Paratirolites* Limestone (characteristic ammonoid specimens are illustrated in Fig. 28).

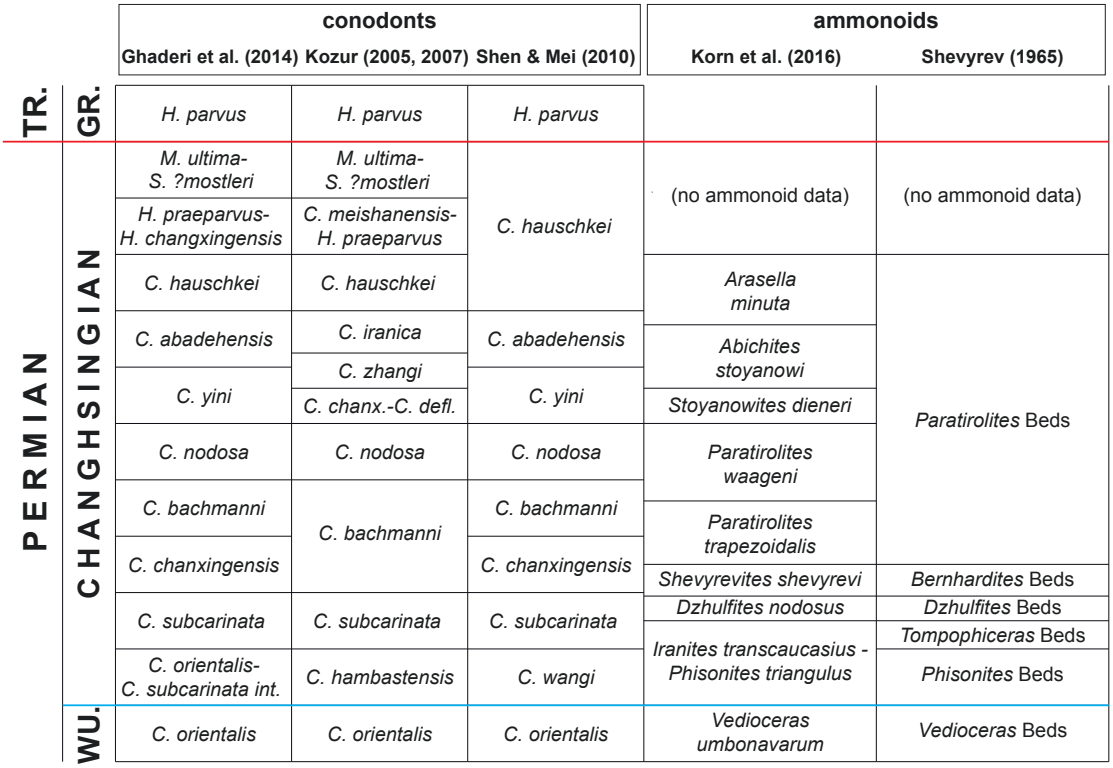

Figure 25 The correlation of the conodont schemes by Kozur (2005, 2007), Shen and Mei (2010) and Ghaderi et al. (2014) with the ammonoid stratigraphy by Shevyrev (1965) and Korn et al. (2016). Triassic (Tr.), Griesbachian (Gr.),Wuchiapingian (Wu.).

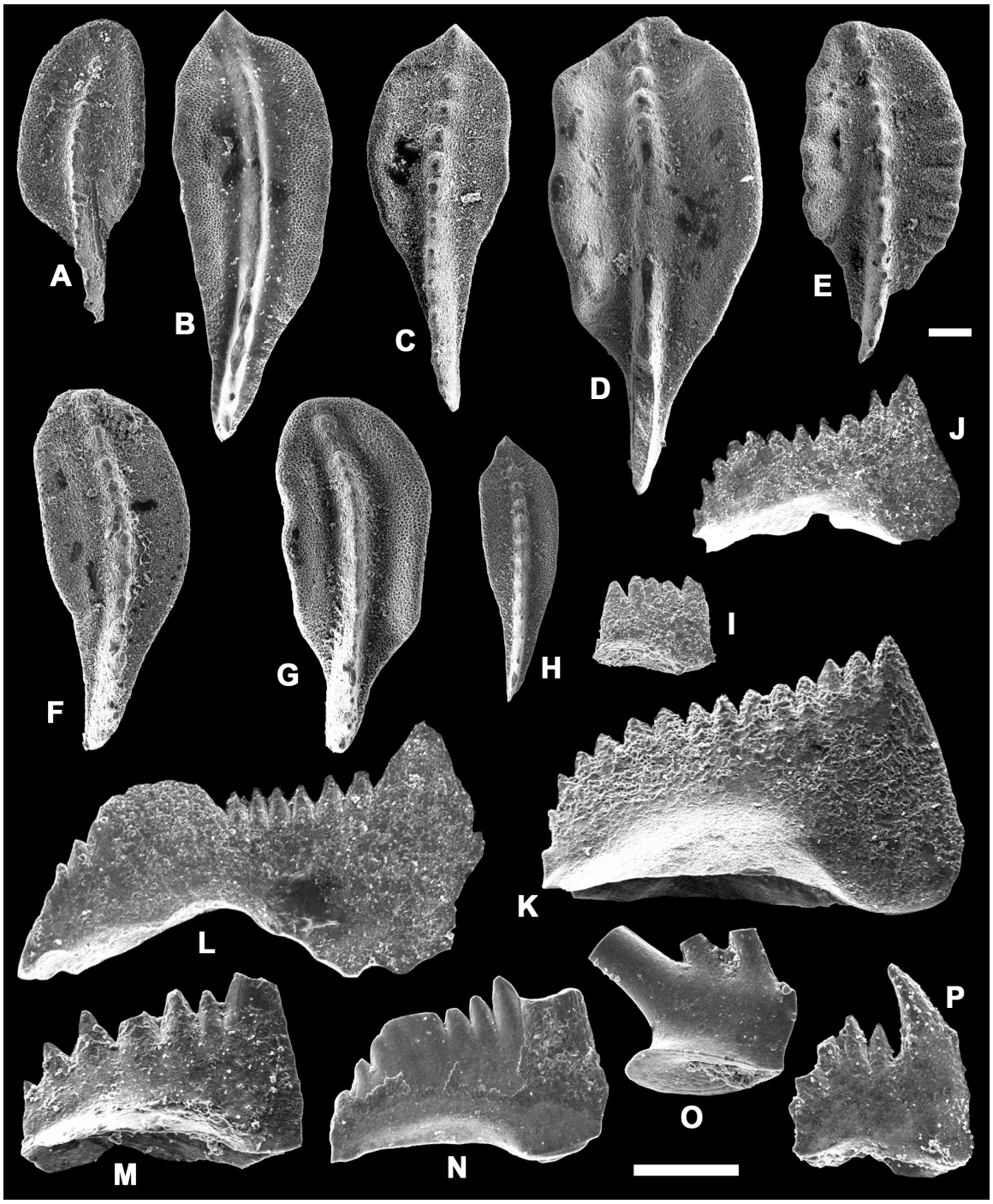

Figure 26 Characteristic Late Permian–Early Triassic conodonts from the Julfa region (from Ghaderi et al. 2014); all scale bars are 100 μm. All specimens stored in the collection of the Ferdowsi University of Mashhad. a – *Clarkina orientalis* (Barskov and Koroleva, 1970); FUM#1J192.1; Upper Julfa Beds (*Vedioceras* Beds), Ali Bashi 1 section. b – *Clarkina subcarinata* Sweet, 1973; FUM#4J142.8; Zal Member (Ali Bashi Formation), Ali Bashi 4 section. c – *Clarkina changxingensis* Wang and Wang, 1981; FUM#4J153.1; Zal Member (Ali Bashi Formation), Ali Bashi 4 section. d – *Clarkina bachmanni* Kozur, 2004; FUM#AJ185.23; *Paratirolites* Limestone (Ali Bashi Formation), Aras Valley section. e – *Clarkina nodosa* Kozur, 2004; FUM#G249.16; *Paratirolites* Limestone (Ali Bashi Formation), Ali Bashi M section. f – *Clarkina yini* Mei, 1998; FUM#AJ192.4; *Paratirolites* Limestone (Ali Bashi Formation), Aras Valley section. g – *Clarkina abadehensis* Kozur, 2004; FUM#1J248.9; *Paratirolites* Limestone (Ali Bashi Formation), Ali Bashi 1 section. h – *Clarkina hauschkei* Kozur, 2004, FUM#1J249D.9; *Parati-*

rolites Limestone (Ali Bashi Formation), Ali Bashi 1 section. i – *Hindeodus eurypyge* Nicoll, Metcalfe and Wang, 2002, FUM#1J255.7; Zal Member (Ali Bashi Formation), Ali Bashi 1 section. j – *Hindeodus typicalis* Sweet, 1970, FUM#G233.5; *Paratirolites* Limestone (Ali Bashi Formation), Ali Bashi M section. k – *Hindeodus typicalis* Sweet, 1970, FUM#4J200.56; *Paratirolites* Limestone (Ali Bashi Formation), Ali Bashi 4 section. l – *Hindeodus julfensis* Sweet, 1973, FUM#1J198.4; Zal Member (Ali Bashi Formation), Ali Bashi 4 section. m – *Hindeodus praeparvus* Kozur, 1996, FUM#G274.6; Aras Member (Elikah Formation), Ali Bashi M section. n – *Hindeodus changxingensis* Wang, 1995, FUM#4J201.6 (cusp broken); Aras Member (Elikah Formation), Ali Bashi 4 section. o – *Merrillina ultima* Kozur, 2004, FUM#AJ204.13; Aras Member (Elikah Formation), Aras Valley Section. p – *Hindeodus parvus* Kozur and Pjatakova, 1976, FUM#4J213.1; Elikah Formation; Ali Bashi 4 section.

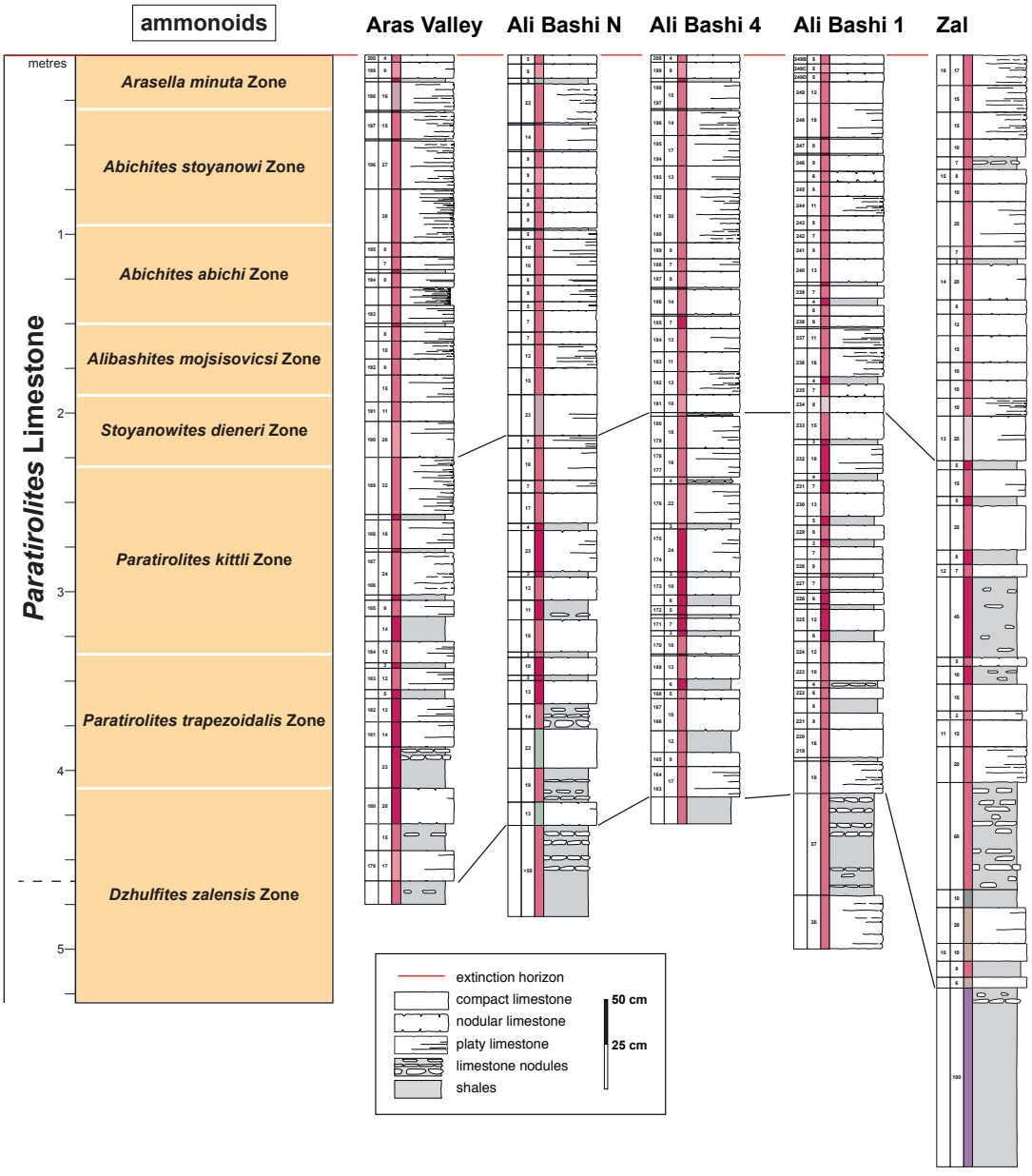

Figure 27 Columnar sections of the *Paratirolites* Limestone in the Aras Valley, Ali Bashi 4, Ali Bashi 1 and Zal sections, with their ammonoid zonation. From Korn et al. (2016, fig. 5).

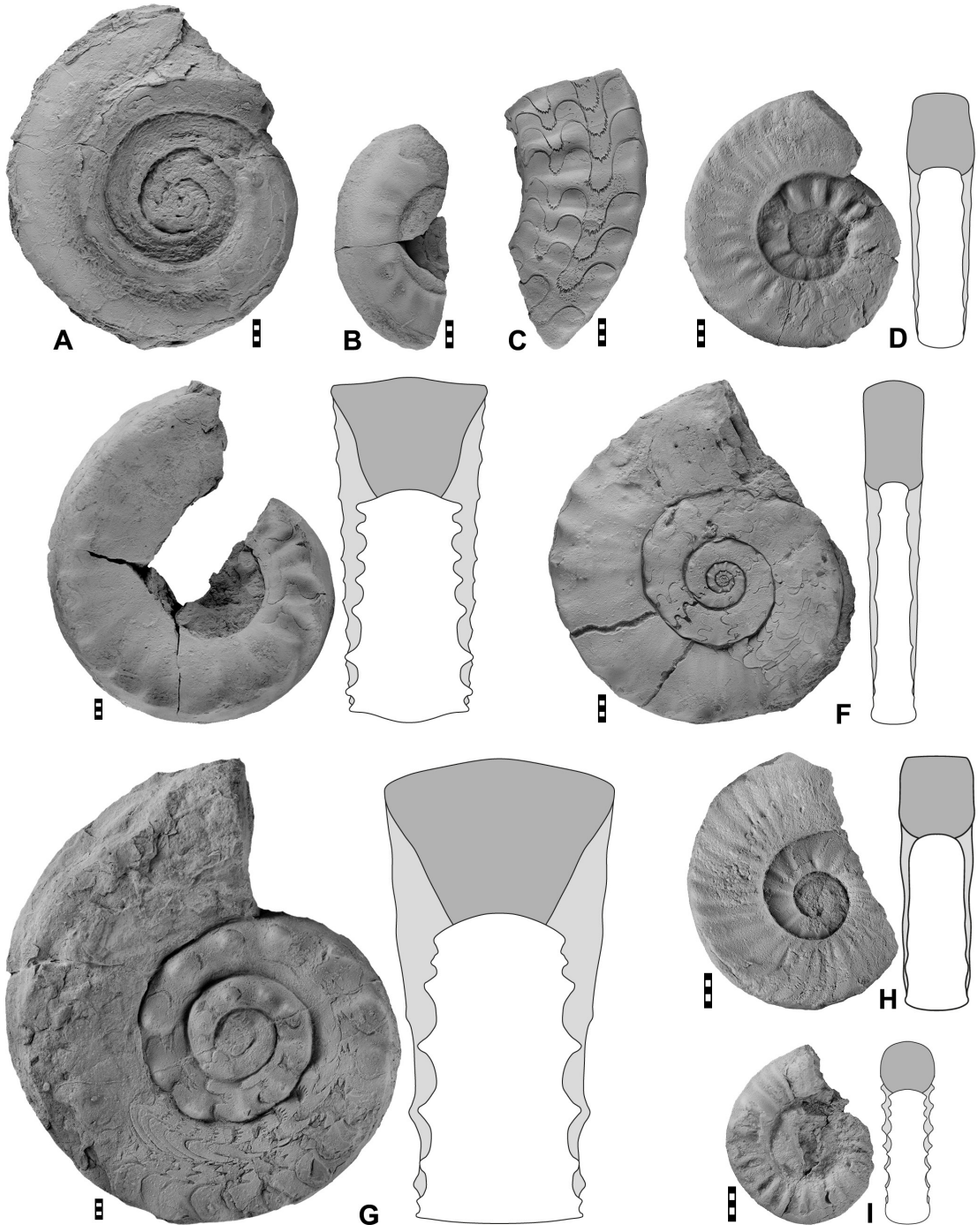

Figure 28 Characteristic Changhsingian ammonoids from the Julfa region (Ghaderi et al. 2014, Fig. 7); scale bars equal to 5 mm. All specimens stored in the collection of the Museum für Naturkunde, Berlin. a – *Phisonites triangulus* (Shevyrev 1965) from the Aras Valley section, specimen MB.C.22703. b – *Iranites transcaucasius* (Shevyrev 1965) from the Aras Valley section, specimen MB.C.22704. c – *Dzhulfites nodosus* (Shevyrev 1965) from the Aras Valley section, specimen MB.C.22705. d – *Shevyrevites nodosus* (Shevyrev 1965) from the Aras Valley section, specimen MB.C.22706. e – *Paratirolites trapezoidalis* (Shevyrev 1965) from the Ali Bashi 4 section, specimen MB.C.22707. f – *Stoyanowites dieneri* (Stoyanow 1910) from the Aras Valley section, specimen MB.C.22708. g – *Paratirolites vediensis* (Shevyrev 1965) from the Ali Bashi N section, specimen MB.C.22709. h – *Abichites stoyanowi* (Kiparisova 1947) from the Ali Bashi N section, specimen MB.C.22715. i – *Arasella minuta* (Zakharov 1983) from the Ali Bashi N section, specimen MB.C.22711.

4.2 Baghuk Mountain

4.2.1 Macroscopic petrography

The Palaeozoic-Mesozoic transition in the Baghuk Mountain area is represented by complete sedimentary successions (Leda et al. 2014). These sections show a similar lithological succession to the sections at Kuh-e-Hambast (SE of Abadeh) and Shahreza (14.5 km NNE of Shahreza village) (Baud et al. 1997; Besse et al. 1998; Gallet et al. 2000; Partoazar 2002; Yazdi and Shirani 2002; Kozur 2004, 2005, 2007; Horacek et al. 2007; Richoz et al. 2010). The lithological units of the Permian-Triassic rock formations in the Abadeh region were refined by Taraz et al. (1981), who identified seven lithological units for the Permian Surmaq and Hambast formations (1–7) and five for the Triassic Elikah Formation (A–E). In my study, particular attention has been paid to the Early Triassic Shahreza Formation (Unit A of Taraz et al. 1981; *Claraia* Beds of Ghaderi et et al. 2014). I investigated the basal 20 m of the Shahreza Formation with a special focus on microbial deposits.

The succession in the Baghuk Mountain section 1 is composed, in ascending stratigraphic order, of the following rock units:

(1) Hambast Formation (24 m thick); Wuchiapingian to Changhsingian in age. It can be subdivided into three subunits:

(a) The lower grey portion (16 m thick) is composed of thin-bedded, light-grey, argillaceous lime mudstone.

(b) The middle part (12.8 m thick) consists of thin-bedded, red nodular limestone with few ammonoids. At the microscopic scale, it is an argillaceous lime mudstone and bioclastic wackestone with bivalves, ostracods, radiolaria and foraminifera.

(c) The upper part (5.2 m thick) can, at least partly, be correlated with the *Paratirolites* Limestone of the Julfa region; it is late Changhsingian in age (Ghaderi et al. 2014). It is composed of thin (up to 3 cm) nodular limestone horizons, which alternate and form packages of 30 cm thickness. Only a few more compact limestone beds exist, with the most conspicuous one being a 10 cm thick, dark red marly limestone bed, 3.25 m below the base of the 'Boundary Clay' (Fig. 29). The base of the unit bearing *Paratirolites* and closely related genera does not show the sharp lithological contrast seen in the sections at Julfa and has a position within a succession of reddish nodular limestone. It is therefore not possible to correlate the base of the *Paratirolites* Limestone of Baghuk Mountain on the basis of lithology. The mass occurrence of the ammonoid genus *Shevyrevites*, which in the Julfa area occurs below the *Paratirolites* Limestone (Ruzhencev et al. 1965), 5 m below the extinction horizon, can be seen as evidence for similar thicknesses of the *Paratirolites*-yielding interval in the two regions.

Microfacies studies show that the upper 2.65 m of the Hambast Formation comprises red, nodular, burrowed lime mudstone and wackestone with foraminifera, ostracods, radiolaria, bellerophontids and ammonoids. The characteristic features of this microfacies type are breccia-like appearance, abundant fractures, and stylolite seams. The matrix features are, besides micrite, some minor sparry cement and in situ recrystallization (neomorphic spar). The top surface of the Hambast Formation with its sharp contact to the overlying 'Boundary Clay' marks the end-Permian mass extinction horizon and is referred to as the 'extinction horizon' (designated EH) (e.g., Kozur 2004; Korte and Kozur 2005; Leda et al. 2014). This interval is marked by a substantial decrease in fossil abundance (Leda et al. 2014, fig. 16). The top of the Hambast Formation in the Baghuk Mountain sections does not show the sharp lithological contact with the 'Boundary Clay' as observed in the Julfa region. At some places (e.g., Baghuk section C), very thin (0.5-1 cm) marly limestone nodules with many small ammonoids can be found within the lower part of the 'Boundary Clay' (Fig. 30).

(2) Shahreza Formation (sensu Heydari et al. 2008) (190 m thick). Two units are distinguished:

(a) 'Boundary Clay' (about 2 m thick); latest Changhsingian in age. The 'Boundary Clay' is made up of dark grey to greenish shale with thin horizons of light-grey and light-pink marl and platy limestone (Fig. 31). Microscopically, the platy limestone horizons comprise lime mudstone with sponges, single ostracods, gastropods and calcimicrobe filaments. The matrix consists of microcrystalline spar and micrite intersected by abundant anastomosing stylolites. In the transition from the 'Boundary Clay' to the overlying grey, platy limestone beds of the Elikah Formation one or more enigmatic 'calcite fan' layers occur, which form dome-shaped structures that resemble botryoids (Fig. 44b-d; see Chapter Microbial deposits and (sub)seafloor precipitates).

(b) Carbonate unit of the Shahreza Formation; Early Triassic (Griesbachian) in age. Its lowermost unit (about 1 m thick) is made up of grey, thin-bedded, platy and marly limestone. At the microscopic scale, it is a densely laminated bindstone with peloids, cortoids and sparite-filled voids. Higher in the section, alternations of dark grey and black, organic-rich shale and thin beds of pale grey marl characterize the 17 m of the Shahreza Formation. Small pyrite nodules occur occasionally in black shales at +4.40 m and +5.25 m. Brown and reddish marls and shales containing abundant specimens of *Claraia* occur in several horizons. Few specimens of *Claraia* occur in the platy limestone between +13.40 and +14.00 m. The fossil inventory of this interval consists of thin-shelled bivalves, gastropods, ostracods, foraminifers and ammonoids. The platy and marly limestone beds possess a recrystallized texture, suggesting microspar cementation and in situ recrystallization. The petrographic investigation of the carbonate allows distinction of several microfacies types according to fabrics and bioclast occurrences. I present below descriptions of only three microfacies types, which I studied most intensively because of their interesting features. A complete facies list and description of microfacies from all sections is given in Table 8 and their distribution pattern is given in Fig. 32.

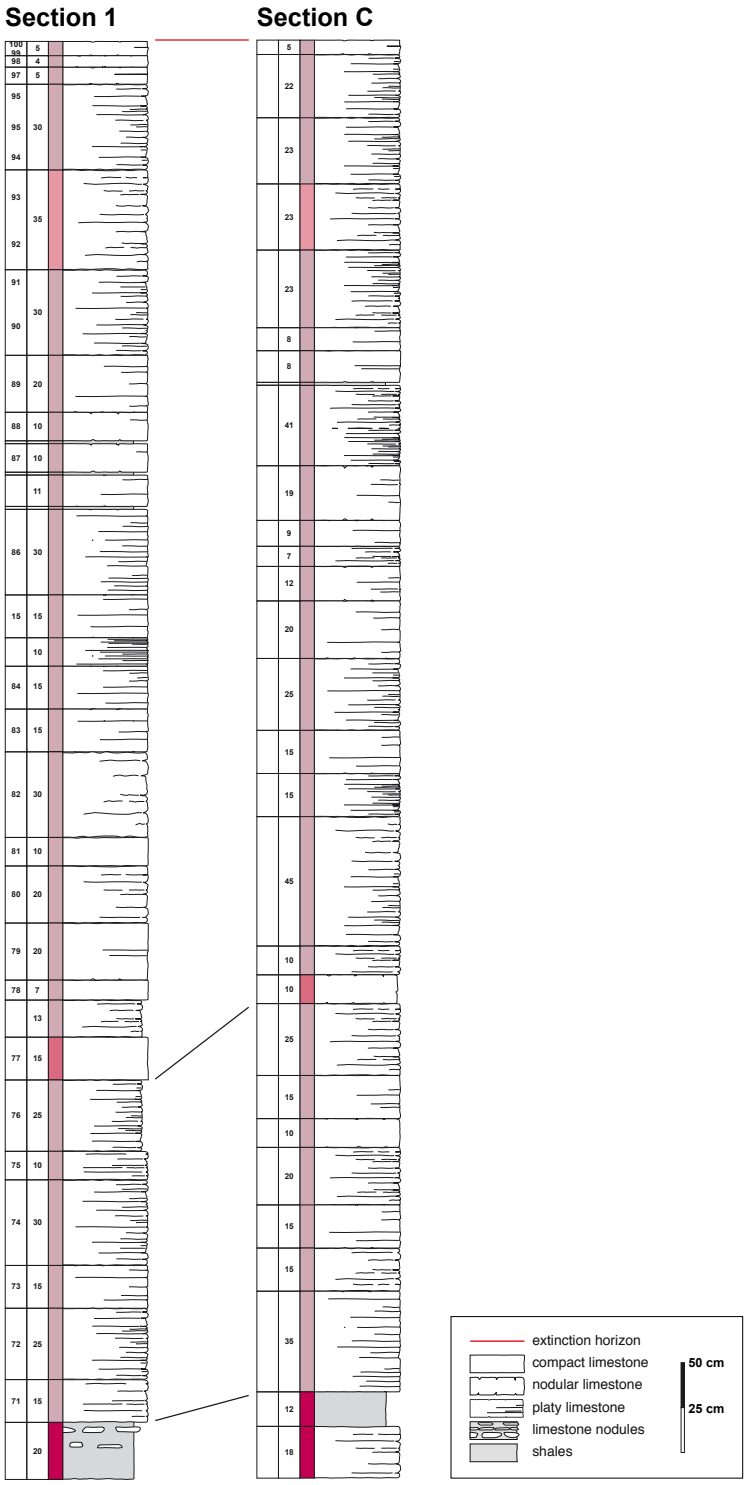

Figure 29 Two parallel sections of the uppermost 5 m of the Hambast Formation at Baghuk Mountain (section C is 100 m west of section 1). The sections have been aligned at the extinction horizon (top of the sections). The middle correlation line refers to a dark red index horizon in the lower half of the Hambast Formation, the lower correlation line refers to the index horizon rich in the ammonoid genus *Shevyrevites*.

Figure 30 Slab of a marly limestone within the lower part of the 'Boundary Clay' with many small ammonoids. Baghuk Mountain, C section.

4.2.2 Carbonate microfacies

Burrowed lime mudstone and wackestone

The characteristic feature of this microfacies type is the breccia-like appearance and recrystallization of the matrix to microspar. Fractures, microcracks and stylolite seams are very common. Geopetal structures occur within mollusc conchs as well as within synsedimentary, interskeletal cavities. Micrite clasts occur only occasionally. The biota inventory includes foraminifera, ostracods, radiolaria, bellerophontids, bivalves and ammonoids.

Lime mudstone

This microfacies shows iron and manganese oxides and sulphides that occur within a partly dolomitized matrix of lime mudstone to siltstone with sponges, single ostracods, gastropods and calcimicrobe filaments at +0.02 m, +0.40 m, +0.60 m and at + 0.96 m (Fig. 33a, c). They occur as small shrubs or branching columns with slightly bushy morphology and are brown or black in colour (Fig. 33b). These micro-arborescent structures possess grumeaux and clotted microtexture. They are probably hematite coated *Frutexites*. Additionally, there are loose, variously oriented straight micritic tubes at +0.96 m. These tiny calcified tubes are probably calcimicrobes (Fig. 33d).

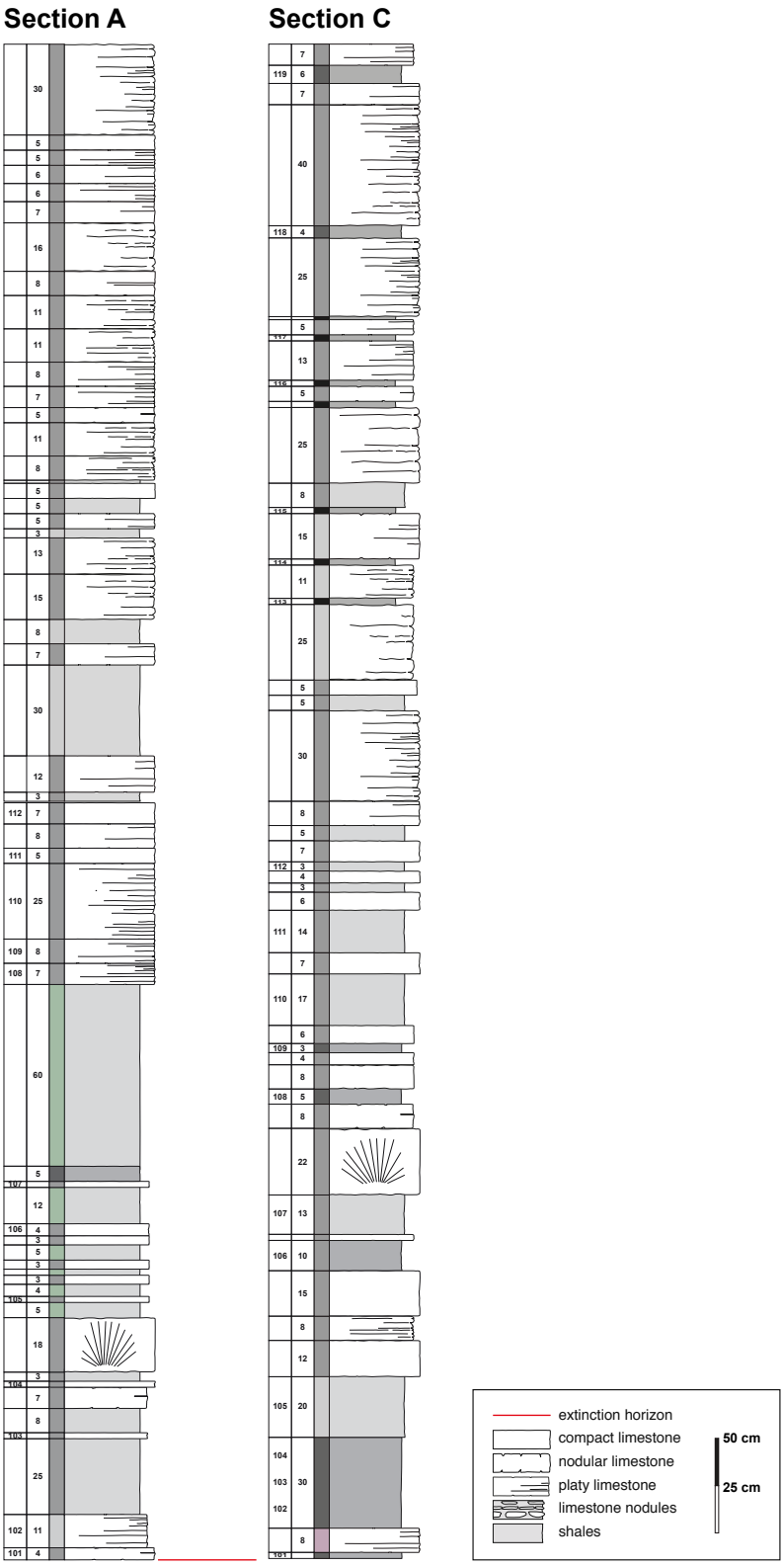

Figure 31 Two parallel sections across the 'Boundary Clay' and the base of the Shahreza Formation at Baghuk Mountain (section A is 600 m south-west of section C). All sections have been aligned at the extinction horizon (base of the sections). The upper correlation line refers to the top of the 'Boundary Clay'.

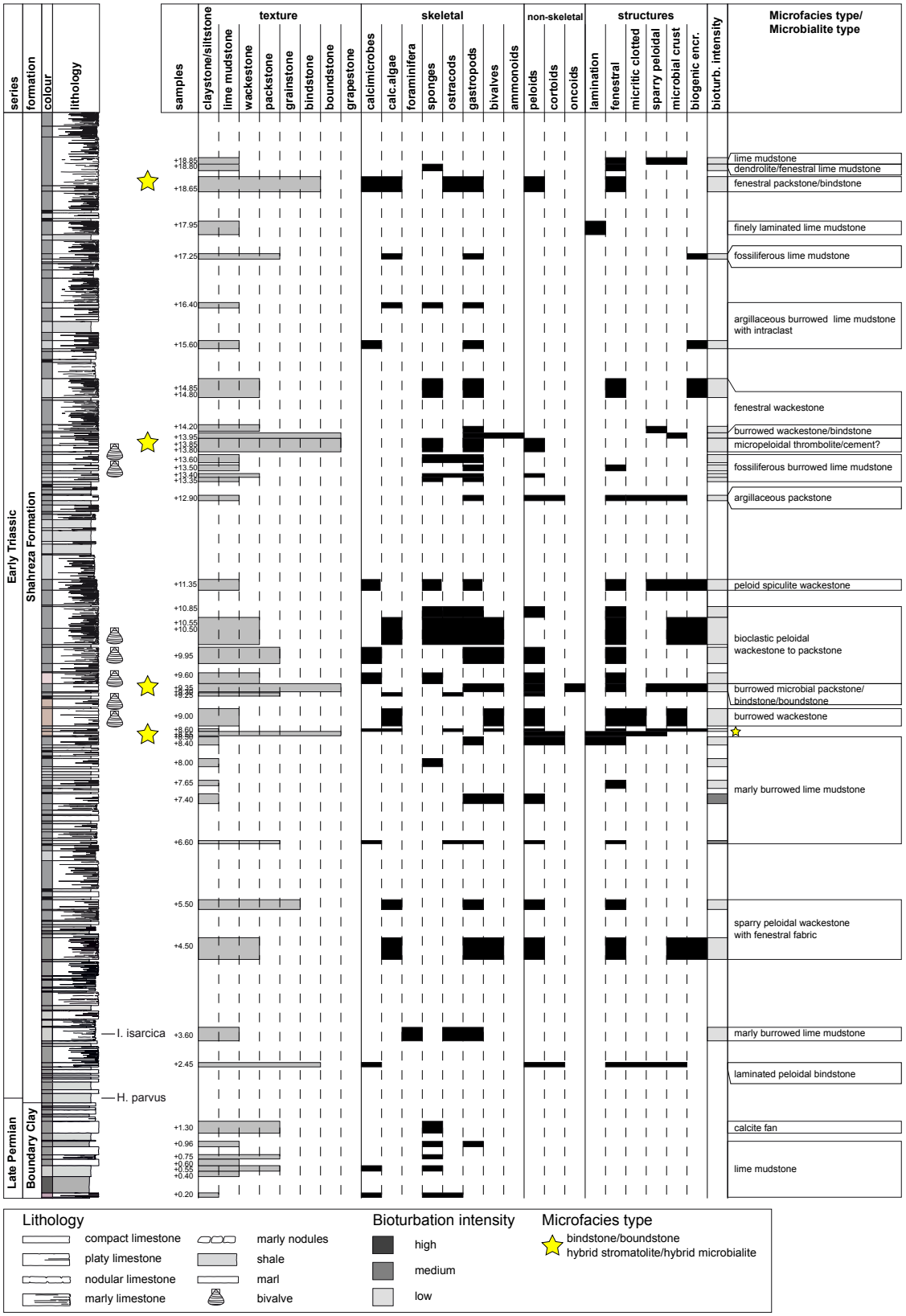

Figure 32 Composite log with carbonate microfacies characteristics of the Permian–Triassic boundary in the Baghuk Mountain sections.

Table 8 Detailed facies description of the investigated Permian and Triassic beds in the Baghuk Mountain sections.

Interval (m)	Biogenic and abiogenic content	Microfacies type(s)	Depositional setting (Flügel 2004)	See Fig.
+18.85	abiogenic: pseudobirdseyes, plant roots or burrows	lime mudstone	peritidal	
+18.80	abiogenic: digitate, dendrolitic crystals	dendrolite, fenestral lime mudstone	restricted platform interior (FZ 8)	39f-h,
+18.65	biogenic: cyanobactial tufts, dascyclads, gastropods, ostracods; abiogenic: peloids, spar-filled voids	fenestral packstone/ bindstone with porostromate bacteria (SMF 21-PORO)	restricted platform interior (FZ 8)	39e
+17.95	abiogenic: lamination	finely laminated lime mudstone (RMF 22, SMF 19)	restricted platform interior (FZ 8)	
+17.25	biogenic: gastropods, calcareous algae, sponge spicule remains	fossiliferous lime mudstone	restricted platform interior (FZ 8)	
+15.60 to 16.40	biogenic: gastropods, intraclasts	argillaceous burrowed lime mudstone with intraclast (RMF 24)	peritidal	
+14.20 to +14.85	biogenic: gastropods, bellerophontids; abiogenic: fenestral fabric	fenestral wackestone	restricted platform interior (FZ 8)	
+13.95	biogenic: ammonoids, bivalve, mollusc remains, microbial crust	burrowed bioclastic wackestone/bindstone	open marine platform (FZ 7)	50d
+13.80 to +13.85	biogenic: peloids; abiogenic: crystal splays, botryoids, calcite spherulites	thrombolite	restricted platform interior (FZ 8)	38d, 39b-d, 40a
+13.35 to +13.60	biogenic: sponges, ostracods, gastropod; abiogenic: fenestral fabric	fossiliferous burrowed lime mudstone	open marine platform (FZ 7)	39a, 40b
+12.90	biogenic: gastropods, microbial crust, sparry peloids, ferriginous microstromatolites; abiogenic: clay seams	argillaceous packstone	restricted platform interior (FZ 8)	
+11.35	biogenic: calcimicrobes, sponges, gastropods; microbial crust; abiogenic: fenestral fabric	peloid spiculite wackestone	restricted platform interior (FZ 8)	
+9.60 to +10.85	biogenic: calcimicrobes, sponges, gastropods, bivalves, peloids; abiogenic: fenestral fabric	bioclastic peloidal wackestone to packstone	open marine platform (FZ 7)	
+9.35	biogenic: peloids; abiogenic: lamination, geopetal fabric	boundstone/bindstone	restricted platform interior (FZ 8)	50e
+9.30	biogenic: bivalves, gastropods, biogenic encrustation, microbial crust; abiogenic: stylolite seams, fenestrae, sparite-filled voids	burrowed microbial packestone (SMF 21-FEN)	restricted platform interior (FZ 8)	50f-h

+9.25	abiogenic: peloids, lamination, geopetal fabric	boundstone/bindstone	restricted platform interior (FZ 8)	
+9.00	biogenic: bivalves, biogenic encrustation, Fe-Mn crust	burrowed wackestone	open marine platform (FZ 7)	
+8.60 to +8.80	biogenic: bivalves, sponge spicule remains, gastropods, ostracods, calcispheres, peloids; abiogenic: geopetal fabric	boundstone/bindstone	restricted platform interior (FZ 8)	50c
+8.55	biogenic: sponge spicule remains. abiogenic: lamination, fan-shaped crystals	club-shaped hybrid stromatolite, mushroom-shaped hybrid microbialite	restricted platform interior (FZ 8)	50a, b
+6.60 to +8.40	biogenic: ostracods, mollusc remains; abiogenic: stylolite seams, fenestrae, fractures	marly burrowed lime mudstone	open marine platform (FZ 7)	
+4.50 to +5.50	biogenic: single gastropods, algae, peloids; abiogenic: sparite-filled voids, sparry calcite spheres	sparry peloidal wackstone with fenestral fabric	open marine platform (FZ 7)	
+3.60	biogenic: ostracods, mollusc remains; abiogenic: calcisiltite	marly burrowed lime mudstone	open marine platform (FZ 7)	
+1.90 to +2.50	abiogenic: peloids, cortoids, sparite-filled voids	laminated peloidal bindstone (SMF 19)	restricted platform interior (FZ 8)	49
+0.02 to +0.98	biogenic: sponges, single ostracods, gastropods, calcimicrobes; hematite coated *Frutexites*; abiogenic: hematite veils	lime mudstone	deep shelf to basin (FZ 1B, FZ 2)	30, 33, 45c, d
-2.65 to 0.00	biogenic: foraminifera, ostracods, radiolarian, bellerophontids, ammonoids; abiogenic: fractures, micro-cracks, stylolite seams	burrowed lime mudstone and wackestone (SMF 3)	toe of slope (FZ 3), deep shelf (FZ 2), and basin (FZ 1)	17b
-3.55	biogenic: ostracods, microbial crusts; abiogenic: sulphidic mineralization	poorly fossiliferous lime mudstone	basin	
-4.80 to -4.40	biogenic: ostracods, echinoderms, foraminifera; abiogenic: micro-cracks, fractures, breccia-like appearance	burrowed red nodular lime mudstone (RMF 2)	outer ramp, basin	

Laminated peloidal bindstone

This microfacies is characterized by an accumulation of very small, grain-supported, sparitic peloids and micritic cortoids. The peloids form irregularly distributed pelmicrite and pelsparite fabrics. Wavy, irregular micritic lamination is also common. The peloids are classified as microbial peloids.

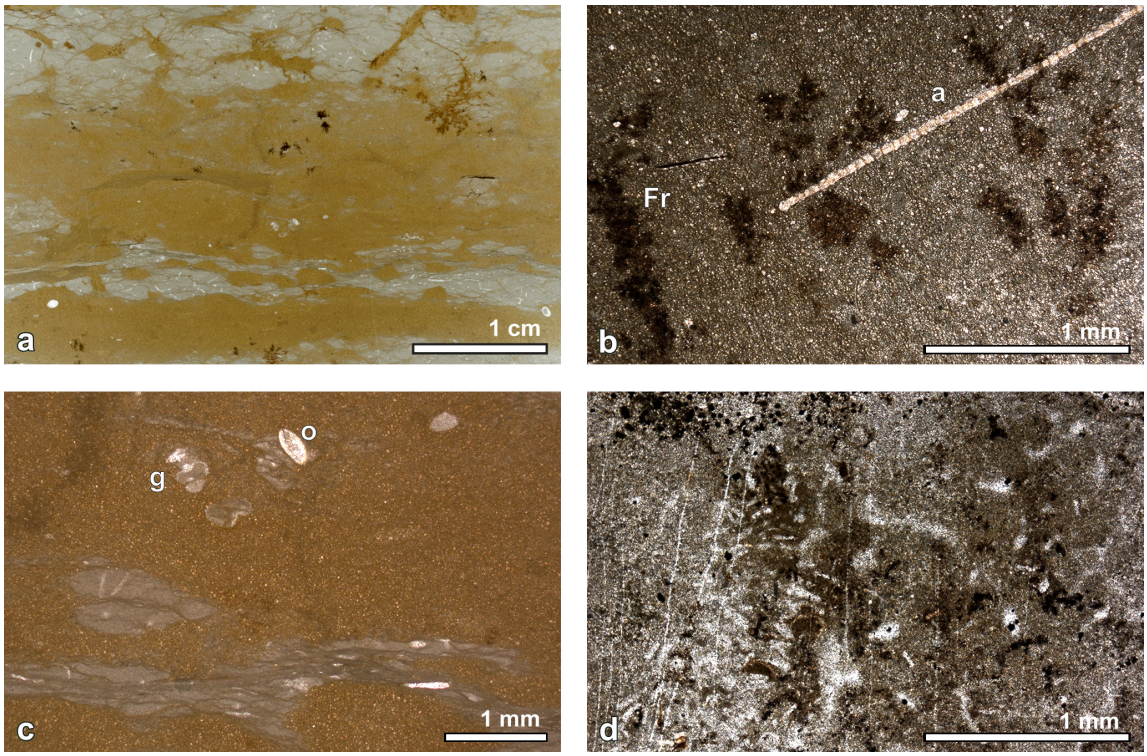

Figure 33 Carbonate microfacies of the 'Boundary Clay' at Baghuk Mountain. a – Marly nodules with sponge remains and single ostracods embedded in marly siltstone. Baghuk Mountain, A section, +0.02 m. b – Hematite coated Frutexites (Fr) and algae segments (a) within microsparitic matrix. Baghuk Mountain, A section, +0.40 m. c – Single ostracod shells (o) and bellerophontid gastropod remains (g) embedded in marly siltstone, Baghuk Mountain, A section, +0.40 m. d – Irregular masses of calcified tubes of microfossils. Baghuk Mountain, A section, +0.69 m.

4.2.3 Biostratigraphic subdivision

The biostratigraphic subdivision of the P-Tr boundary sections at Baghuk Mountain has been achieved with the use of conodonts. Only conodonts, however, appear to be suitable for a correlation of distant regions (Kozur 2004, 2005, 2007; Henderson et al. 2008; Shen and Mei 2010). Kozur (2005, 2007) sampled the Hambast section and subdivided the late Permian successions into ten conodont biozones and the early Triassic successions into 2 conodont biozones; in ascending order: the *Hindeodus parvus* and the *Isarcicella isarcica* zones. Recently, Ghaderi et al. (2014) investigated the sections in the Julfa area (NW Iran) reaching a fine resolution using bed-by-bed sampling. Their revision of biostatigraphy led to the separation of four conodont zones for the Griesbachian substage (from bottom to top *Hindeodus parvus*, *H. lobota*, *Isarcicella staeschei* and *I. isarcica* zones) (Fig. 34). A biostratigraphic subdivision of the Baghuk Mountain sections using conodonts was established by Farshid et al. (2016). They established seven conodont zones for the Changhsingian sections (from bottom to top the *Clarkina subcarinata*, *C. changxingensis*, *C. bachmanni*, *C. nodosa*, *C. yini*, *C. abadehensis*, *C. hauschkei* zones) and two conodont biozones for the Griesbachian successions, in ascending order the *H.*

parvus and the *Isarcicella isarcica* zones. Index conodonts of the *Clarkina orientalis–C. subcarinata* Zone were not traced within the collected material from Baghuk Mountain. Instead, *Hindeodus julfenis* occurs and the last occurrence datum (LOD) of *C. orientalis* is in sample B63 (8.90 m below the extinction horizon). Most probably the Wuchapingian-Changhsingian boundary lies within an interval straddling the B63 to B64 samples (between 8.90 m and 8.00 m below the EH). The highest recorded taxon in the Permian is *C.* cf. *hauschkei*, which has a first occurrence datum (FOD) in sample B100 (0.02 m below the EH), marking the base of the *C. hauschkei* Zone. The extinction horizon (EH) marks the boundary between the *C. hauschkei* and *Hindeodus praeparvus–H. changxingensis* zones (Ghaderi et al. 2014). Unfortunately, neither the *H. praeparvus–H. changxingensis* nor the *Merrillina ultima–Stepanovites*? *mostleri* zones were traced in the Baghuk Mountain sections. The first appearance of *Hindeodus parvus* indicates the administrative Permian-Triassic boundary. However, there is a problem with the precise position of the P-Tr boundary, because the first occurrence of *H. parvus* is in sample +1.85 m and marks the base of the *H. parvus* Zone, although this is based solely on a broken element. Well-preserved *H. parvus* (actually *H. parvus erectus*) platform elements come from sample +2.00 m. *Isarcicella isarcica* occurs first in sample +3.71 m, defining the base of the *I. isarcica* Zone. *Hindeodus lobota* was not found in the Baghuk Mountain sections. *Isarcicella staeschei* was found but co-occurs with *Isarcicella isarcica* (V. Hairapetian, pers. commun.).

<table>
<tr><th colspan="2">NW Iran (Ghaderi et al. 2014)</th><th colspan="2">Abadeh, central Iran (Kozur 2007)</th><th colspan="2">Meishan, south China (Yuan et al. 2014)</th></tr>
<tr><td>I. isarcica</td><td>(15)</td><td>I. isarcica</td><td>(h)</td><td colspan="2" rowspan="2"></td></tr>
<tr><td>I. staeschei</td><td>(14)</td><td></td><td></td></tr>
<tr><td>H. lobota</td><td>(13)</td><td colspan="2" rowspan="2"></td><td colspan="2" rowspan="2"></td></tr>
<tr><td>H. parvus</td><td>(12)</td><td>H. parvus</td><td>(g)</td></tr>
<tr><td>M. ultima - S. ?mostleri</td><td>(11)</td><td>M. ultima - S. ?mostleri</td><td>(f)</td><td>C. zhejiangensis - H. changxingensis</td><td>(IV)</td></tr>
<tr><td>H. preaparvus - H. changxingensis</td><td>(10)</td><td>H. changxingensis - C. meishanensis</td><td>(f)</td><td colspan="2" rowspan="2"></td></tr>
<tr><td>C. hauschkei</td><td>(9)</td><td>C. hauschkei</td><td>(e)</td></tr>
<tr><td rowspan="2">C. abadehensis</td><td rowspan="2">(8)</td><td>C. iranica</td><td>(d)</td><td rowspan="2">C. meishanensis</td><td rowspan="2">(III)</td></tr>
<tr><td>C. zhangi</td><td>(c)</td></tr>
<tr><td>C. yini</td><td>(7)</td><td>C. changxingensis - C. deflecta</td><td>(b)</td><td rowspan="3">C. yini</td><td rowspan="3">(II)</td></tr>
<tr><td>C. nodosa</td><td>(6)</td><td>C. nodosa</td><td>(b)</td></tr>
<tr><td>C. bachmanni</td><td>(5)</td><td rowspan="2">C. bachmanni</td><td rowspan="2">(b)</td></tr>
<tr><td>C. chanxingensis</td><td>(4)</td><td>C. chanxingensis</td><td>(I)</td></tr>
<tr><td>C. subcarinata</td><td>(3)</td><td>C. subcarinata</td><td>(a)</td><td>C. subcarinata</td><td></td></tr>
<tr><td>C. orientalis - C. subcarinata int.</td><td>(2)</td><td>C. hambastensis</td><td>(a)</td><td>C. wangi</td><td></td></tr>
<tr><td>C. orientalis</td><td>(1)</td><td colspan="2"></td><td colspan="2"></td></tr>
</table>

Figure 34 A scheme for the conodont zones of NW Iran, central Iran (Abadeh section) and South China (Meishan section). A correlation based on conodont zones between NW Iran and central Iran follows Ghaderi et al. (2014). A correlation between South China and the P-Tr interval in Iran can only be achieved, with great confidence, for the thick lined conodont zones and the extinction horizon (red line). Modified after Schobben (2014; PhD thesis).

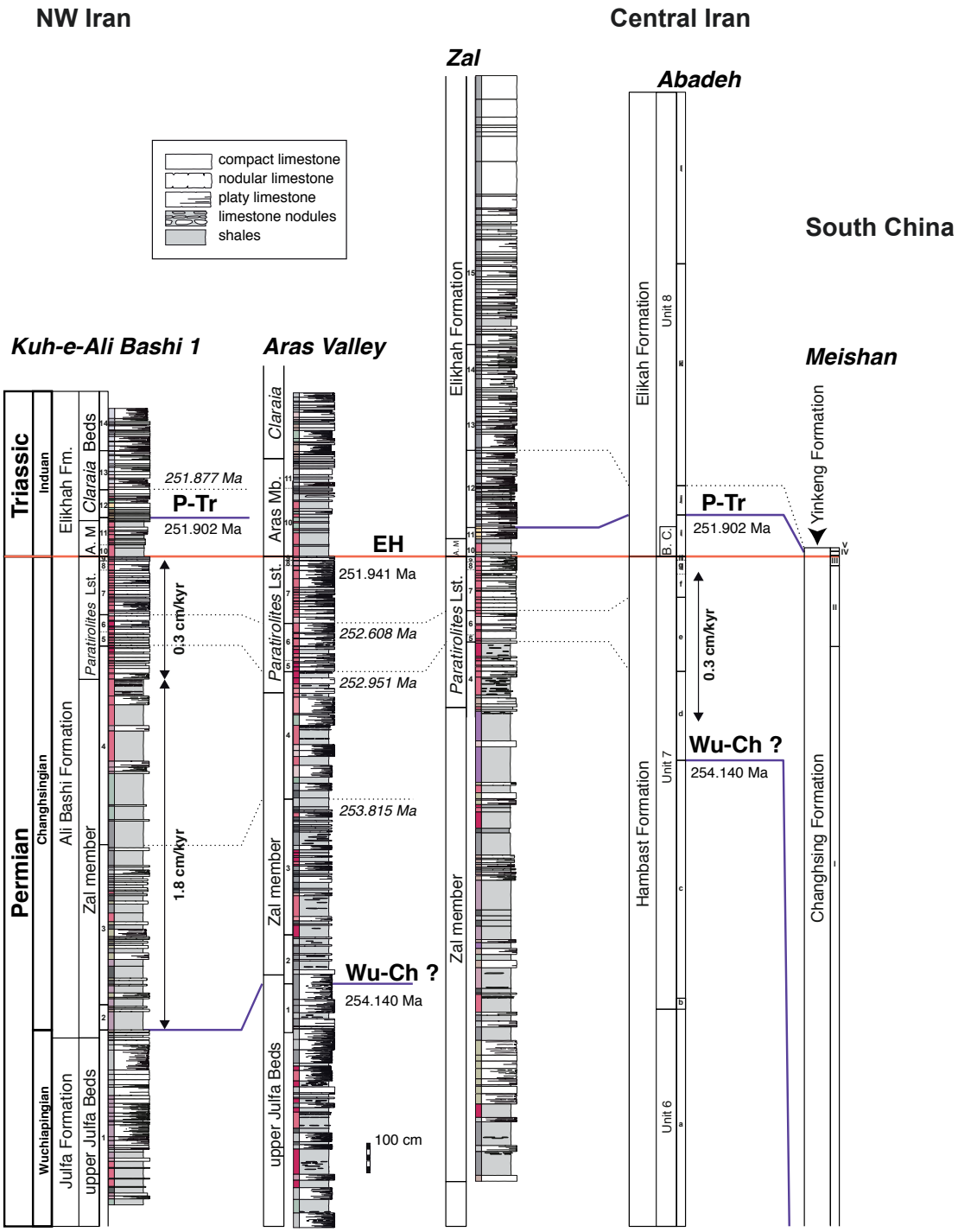

Figure 35 Combined litho- and biostratigraphy scheme for the P-Tr sections of the Julfa region (from Schobben 2014, PhD thesis). Conodont zonation as in Ghaderi et al. (2014) and Schobben et al. (2016). Radiometric and calculated datums for the Meishan P-Tr GSSP section for the Wu-Ch of Shen et al. (2011) as well as the P-Tr boundary and the extinction horizon (South China) of Burgess et al. (2014). *H. praeparvus-H. changxingensis* as well as the *M. ultima-S.? mostleri* conodont zones. Lithology and conodont zones are according to reports by Korte et al. (2004b) for the Abadeh section and Yuan et al. (2014) for the Meishan section. Conodont zones NW Iran, Abadeh and Meishan are numbered according to Fig. 34.

4.3 Timescale

Schobben (2014) showed that it is possible to correlate the P-Tr sections of the Julfa region with other P-Tr sections in Iran and south China - in particular, the P-Tr GSSP defined at Meishan. The time constraint for the Wuchiapingian-Changhsingian boundary, the extinction horizon, through the first appearance datums (FADs) of *H. parvus* and *I. isarcica* (*I. staeschei* for NW Iran) at the Meishan section (Burgess et al. 2014; Shen et al. 2012) and their correlation of this marker with sections in Iran allowed the construction of a timeframe (Fig. 35). Schobben (2014) used the radiometric data of Burgess et al. (2014) to make linear interpolations for conodont zones of the Meishan section, taken from Yuan et al. (2014). Notably the top of *H. hindeodus* is at 251.873 ± 0.004 Ma and the FAD of *C. yini* is at 252.046 Ma. In addition, the FAD of *H. parvus* is at 251.902 ± 0.024 Ma, the extinction horizon (base bed 25 Meishan) is at 251.941± 0.037 Ma (from Burgess et al. 2014), the FAD of *C. wangi* is at 254.150 Ma (from Shen et al. 2011). All these values were used in the age model by Schobben (2014). The Zal Member and the *Paratirolites* Limestone have been related to a deepening of the marine basin, accompanied by lower sediment accumulation rates for the latter unit (Aghai et al. 2009; Richoz et al. 2010). To adjust for this change in accumulation rate for the Julfa sections, a separate sedimentation rate for the nodular limestone unit of the Abadeh section was calculated. This calculation can be achieved, as this locality has a nearly homogeneous nodular limestone lithology for the complete Changhsingian stage. Based on the data for the extinction horizon and the Wu-Ch boundary, this calculation equates to a 0.3 cm/kyr accumulation rate for the topmost *Paratirolites* Limestone. The nearly identical latest Changhsingian lithology in NW Iran (e.g., Leda et al. 2014) allows an extrapolation of this sedimentation rate to these sites (Fig. 36), which also agrees with sedimentation rate estimates of Richoz et al. (2010).

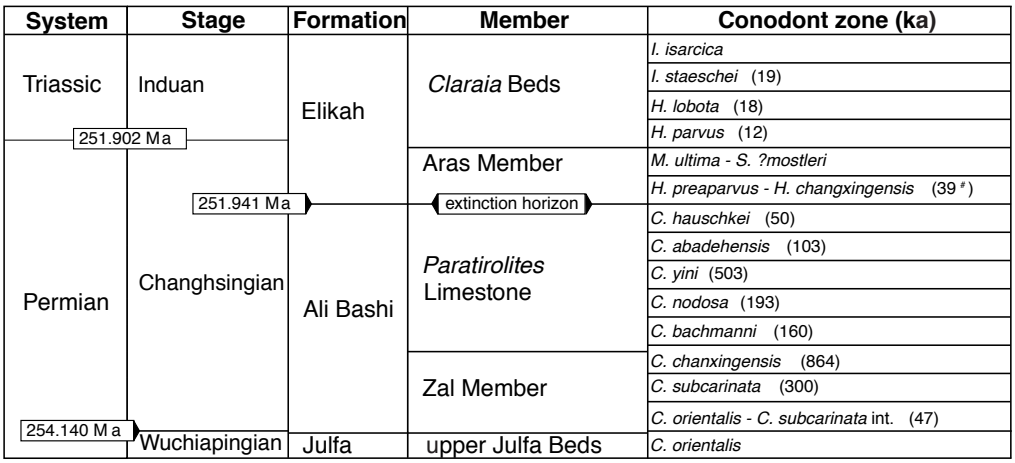

Figure 36 A scheme for the conodont zones of NW Iran, central Iran (Abadeh section) and South China (Meishan section) (from Schobben 2014, PhD thesis). The correlation based on conodont zones between NW Iran and central Iran follows Ghaderi et al. (2014). The correlation between South China and the P-Tr interval in Iran can only be achieved, with great confidence, for the thick lined conodont zones and the extinction horizon (red line).

5 MICROBIAL DEPOSITS AND (SUB)SEAFLOOR PRECIPITATES

In the aftermath of the end-Permian mass extinction (EPME), microbial deposits were formed in several regions of Iran, including the Alborz Range (Ruteh and Elikah Valley sections), NW Iran (Aras Valley, Ali Bashi and Zal sections), Zagros (Aliguordaz, Dena and Surmeh sections), and the Shahreza-Abadeh area (Shahreza, Asadabad, Baghuk Mountain and Hambast sections) (for references see Table 9). The Early Triassic sections at Baghuk Mountain (Shahreza-Abadeh area) display a succession of biogenic as well as abiogenic carbonates, which were deposited on a carbonate shelf in near-equatorial latitudes of the central Tethys (Leda et al. 2014). The Early Triassic successions at Baghuk Mountain appear to contain the most prominent microbial carbonates in the form of sheets, mounds, and crusts of ambiguous origin.

5.1 Morphology of (sub)seafloor precipitates

The external morphology of the microbialites shows a vast variety in shape and size, which range from giant domes to small digitate and flower-like shapes (Fig. 37). Based on a variety of morphological features of the microbialites, three morphotypes that summarize the macro- and mesostructures were distinguished:

- Morphotype 1: Dome-shaped, conical and/or bulbous in shape with protuberance on top and round to ellipsoid form; they have a regular margin and a rough surface. The buildups are steep-sided, narrower than high, and may reach the size of one metre.

- Morphotype 2: Planar and lens- to dome-shaped forms with protuberance on top. They are flat-sided and wider than high. Planar layers of these features extend laterally up to a few tens of metres, forming biostromes. Lenticular forms form gentle domes.

- Morphotype 3: Club-shaped and inverted cones in cross-section, with concave upper surface and irregular or regular margins. This morphotype comprises flower-shaped and other forms that occur variably isolated or amalgamated. The upper part is either flat with a rough surface or concave with a collapsed surface filled with later deposits.

Regarding mesostructure, each morphotype may occur in four forms: as dendrolite (dendritic), stromatolite (laminated), thrombolite (clotted), or leiolite (structureless, aphanitic). Microbialites of morphotype 3 grow frequently on bivalve and ammonoid shells and occur either as individual structures or small communities with several individuals growing close to one another. They appear structureless at the macroscale level in longitudinal section.

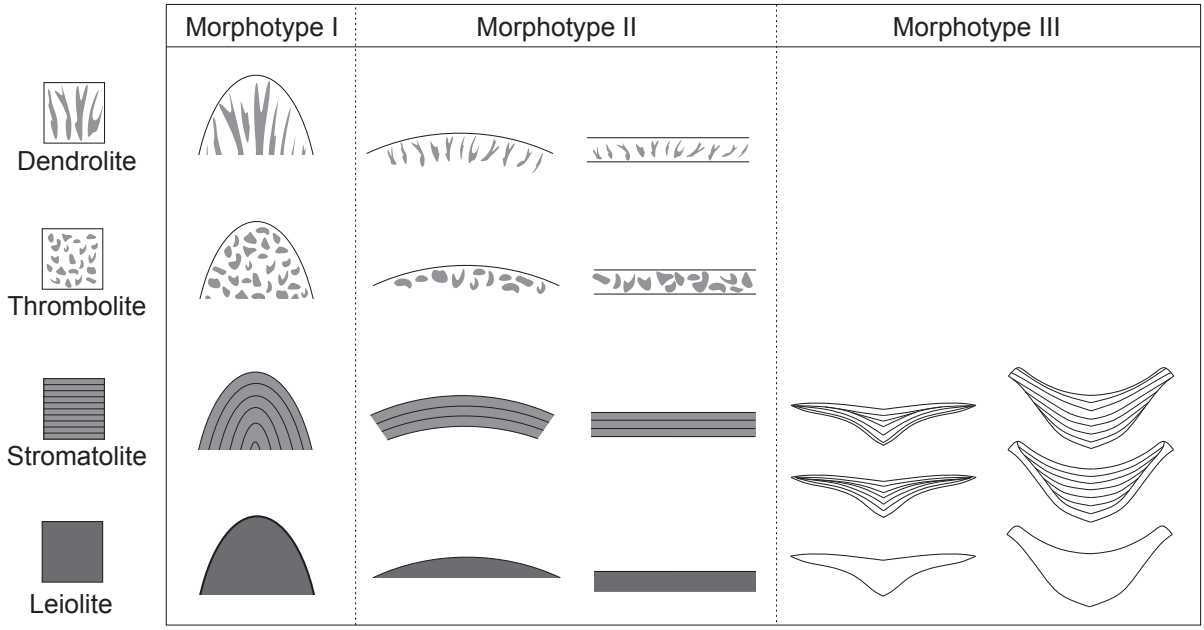

Figure 37 Morphological classification of microbial build-ups at Baghuk Mountain based on macro- and meso-structural features. Not to scale.

Table 9 References for the P-Tr boundary sections and regions in Iran with investigated microbialite structures and direct precipitates from seawater.

Section(s)	Region	Microbialite type(s)	Depositional setting	References
Abadeh	Shahreza-Abadeh area	algal biolithite	calm, intertidal or subtidal	Taraz et al. 1981
Abadeh	Shahreza-Abadeh area	ooid grainstone, synsedimentary carbonate cement	shallow to subtidal oxygenated waters	Heydari et al. 2003
Abadeh	Shahreza-Abadeh area	thrombolite	not given	Richoz 2006
Ali Bashi 1	NW Iran	densely laminated bindstone, floatstone with sparry calcite spheres	restricted platform interior, open marine platform	Leda et al. 2014
Aras Valley	NW Iran	'calcite fan'-like textures	open marine, below wave base	Leda et al. 2014
Aliguordaz	Zagros Range	planar stromatolite	not given	Baghbani 1993; Wei et al. 2005; Wang et al. 2007

C section; A section Baghuk Mountains	Shahreza-Abadeh area	this study	low-energy restricted platform interior	Leda et al. 2014; this study
Hambast	Shahreza-Abadeh area	thrombolite, peloidal grainstone	low energy subtidal	Heydari et al. 2000
Hambast	Shahreza-Abadeh area	branching laminated microbialite, microbial oncoids	not given	Baud et al. 2007
Hambast	Shahreza-Abadeh area	crystal fan, branching stromatolite	not given	Richoz et al. 2010
Ruteh, Elikah Valley	Alborz Range	branched microbialite, stromatolite thrombolite	not given	Altiner et al. 1980, Taraz et al. 1981; Gaetani et al. 2009
Shahreza	Shahreza-Abadeh area	branching laminated microbialite, crystal fan	not given	Baud et al. 2007
Shahreza	Shahreza-Abadeh area	digitate branched stromatolite, seafloor crust	low energy below the wave base	Richoz 2006; Baud et al. 2007; Richoz et al. 2010
Shahreza	Shahreza-Abadeh area	domal stromatolite, calcite crystal fan	not given	Heydari et al. 2008
Kuh e Surmeh, Kuh e Dena	Zagros Range	thrombolitic-stromatolitic boundstone, oolitic peloidal grainstone	shallow subtidal to intertidal	Insalaco et al. 2006
Zal	NW Iran	microbial oncoids, seafloor cement	not given	Richoz et al. 2010
Zal	NW Iran	grapestone densely laminated bindstone, floatstone with sparry calcite spheres, oncoid floatstone	restricted platform interior, open marine platform	Leda et al. 2014

5.2 Microbialite distribution and description

Microbialites occur in several forms in the Baghuk Mountain sections: large-scale structures are easily recognizable in the field, whereas small-scale structures on bedding surfaces of limestone beds are visible only under the microscope. Large-scale structures reach lengths up to one metre. Three large-scale structures were found in the field: (1) 'calcite fans' occuring as planar layers (Fig. 38a), (2) a single domal dendrolite (Fig. 38b), and (3) a conical columnar thrombolite (Fig. 37c). All of them occur in the latest Permian 'Boundary Clay'. Small-scale structures are a few centimetres in size and were found either in situ on bedding surfaces of limestone beds (Figs. 38d, 39a, 40) or as float specimes, where parts of limestone bedding surfaces were detached (Figs. 41, 42).

Figure 38 Field photographs of in situ microbialite occurences in the Baghuk Mountain area (photographs of V. Hairapetian). a – 'Calcite fan' layer in the 'Boundary Clay' showing digitate, upward-growing branches growing together during botryoidal growth. b – A giant domal dendrolite. It shows massive, plano-convex, low relief and lenticular general morphology. Seen in cross-section these mesoclots are composed of digitate columns of laminated nature, growing in vertical and horizontal direction. c – A conical, columnar thrombolite mound with a hemispheroidal macrostructure and clotted mesofabric. d – Small-scale microbial structures on the bedding plane of platy limestones of the Shahreza Formation. C section, +13.80 m.

The carbonates of the Shahreza Formation in the Baghuk Mountain sections underwent intense diagenetic alteration. The microbialites are very distinctive in lithology, and a study of the internal structure is difficult because of recrystallization and/or neomorphism. In the interval between +8.55 m and +18.85 m, arborescent microbialites are most abundant and diverse, and occur in situ on most bedding planes. Their occurrence coincides with the appearance of brownish-weathered marl containing the bivalve *Claraia* (Fig. 32). Microbialites occur here as small-scale, club-shaped features. The microbialites encrust muddy sediments (wackestone, mudstone and ocassionally also packstone) containing ostracods, gastropods, thin-shelled bivalves, foraminifers and ammonoids. The sampling approach allowed to recognize several horizons with arborescent microbialites (Fig. 32). Three microbialite types are preserved as small-scale individual forms: a hybrid microbialite (at +8.55 m), a knobby micropeloidal thrombolite (at +13.80 and at +13.85 m), and a dendrolite (at +18.80 m). Other microbialites do not occur as small-scale buildups, but as layers with microbial fabric. These are: laminated peloidal bindstone (at +2.50 m), burrowed microbial packstone (at +9.30 m), and fenestral packstone/bindstone with porostromate microfossils (at +18.65 m). An additional group forms sparry calcite and micritic crusts that were found on the skeletal elements of bivalves and ammonoids. They are classified as boundstone/bindstone (at +8.70 m, +8.80 m and at +13.95 m). Below detailed descriptions of only a few in situ microbialite types from sections A and C are presented, which were studied most intensively. In parts of the sections with good stratigraphic control, i.e., where separation of conodont zones was possible, conodont zones were used to provide a time framework for microbialite successions. A complete facies list is included in Table 8 and the microbialite distribution pattern is given in Fig. 32.

‘*Calcite Fan’*

In the transition from the ‘Boundary Clay’ to the overlying grey, platy limestone beds of the Shahreza Formation one enigmatic ‘calcite fan’ layer of 0.18 m thickness occurs at +0.62 m in section A. Three ‘calcite fan’ layers of 0.20 m thickness at +0.55 m, of 0.08 m thickness at +0.75 m, and of 0.22 m thickness at +1.30 m occur in section C. The base of the ‘calcite fan’ horizon is planar, the top has an undulose topography. The ‘calcite fan’ layers form dome-shaped, upward-branching, digitate structures (Fig. 44b-d). These structures consist of 10 to 20 cm long, elongated to cup shaped, thinly laminated branches with angular terminations (Fig. 45a, d). The branches amalgamate occasionally and form fans that developed during botryoidal growth. Occasionally pseudomorphs of elongated calcite crystals along the branches occur (Fig. 45a, c-d). The matrix between the branches is a fine-grained, equigranular micrite with a mesh of filaments. The ‘calcite fan’ is riddled with millimetre-sized cavities filled with cubic, euhedral magnetite crystals (Fig. 46). SEM-EDX studies show that the main components of the branches are Ca and C, whereas the main components of the matrix are Ca, Mg, Si, and Sr (Fig. 47). In addition, the matrix contains µm-sized magnetite crystals. EDX spectra show that there is no evidence of dolomitization in the ‘calcite fan’ structures.

A cathodoluminescence study illustrates a difference in luminescence between the matrix and the calcitic branches (Fig. 48). The matrix has uniform, dull, orange and red luminescence,

whereas the calcite crystals show non-uniform, dull as well as bright, orange and red luminescence. The grains are a mosaic of strongly and weakly luminescent crystals (Fig. 48Cd, d, f, h). Non-luminescent stylolite seams occur in the matrix and within the crystal aggregates. Intense luminescence of the branches can already be seen at a low beam current (0.04 mA). Even while the cathode was off, sub-crystals continued to fluoresce. While the angular ends of the branching crystals are easy to recognize under transmitted light in the polarizing microscope, they are not clearly discernible by cathodoluminescence microscopy.

Richoz et al. (2010) interpreted the matrix of microbialites as bioturbated, red bafflestone with a mesh of algal filaments (cf. *Reduviasporonites*). In contrast, Horacek et al. (2007) described the matrix as mudstone containing filaments of probable fungal origin. In my opinion, the mesh of filaments results from remains of calcified sponge spicules with predominant triaxon-like morphologies. The 'calcite fan' structures at Baghuk Mountain are embedded in a fine-grained, equigranular micrite and microsparite with single ostracods, gastropods, calcimicrobes and hematite veils, and with a mesh of filaments that I relate to be remains of calcified sponge spicules (Leda et al. 2014). 'Calcite fan'-like textures occur within the 'Boundary Clay' in the Aras Valley section at +1.65 m, within the *H. praeparvus – H. chanxingensis* Zone (Leda et al. 2014, fig. 12g). These enigmatic features occur in a strongly burrowed and fractured lime mudstone with abundant micrite-filled and calcite-filled burrows and with single sponge remains (Fig. 16e). The 'calcite fan' of the Aras Valley section does not occur as branching digitate structures as in the Baghuk Mountain sections, but as reworked and broken crystals that are probably aragonite pseudomorphs. They have forms of radiating crystal fibres, spherulites, and mineral splays. Several types of cement occur here: (1) microcrystalline with rhombic crystals, (2) bladed crystals with broad, flattened terminations, and (3) heterogranular blocky calcite, characterized by inequigranular, xenotopic, and hypidiotopic fabrics. Additionally, crystal silt occurs in voids. Abundant subtle fractures and stylolite seams cut the crystals and matrix.

Laminated peloidal bindstone

Microbialites deposited in the immediate aftermath of the end-Permian mass extinction within the basal Triassic *Hindeodus parvus* Zone have been termed 'earliest Triassic microbialites' (ETMs) by Kershaw et al. (2007). The *H. parvus* Zone has, in the Baghuk Mountain sections, a thickness of about 1.85 m. The microbial deposit occurring within this conodont zone is a laminated peloidal bindstone. This microfacies type is characterized by an accumulation of very small, grain-supported sparitic peloids and micritic cortoids (Fig. 49c, d). The peloids form irregularly distributed pelmicrite and pelsparite fabrics. Wavy, crude and diffuse lamination with gradual boundaries, in which micrite laminae, sparite laminae, and peloidal laminae alternate and overlap, occurs at +2.30 m and at +2.43 m in section A. Microbial peloids co-occur here as amalgamated masses. This laminated peloidal bindstone is a microbial deposit and possesses a poorly structured thrombolitic texture (Fig. 49a). It has a laminated, fine-grained, agglutinated stromatolitic fabric with wavy and smooth laminae that overlap in some cases (Fig. 49b). This microbialite type is considered equivalent to the fine-grained crust of Riding (2008).

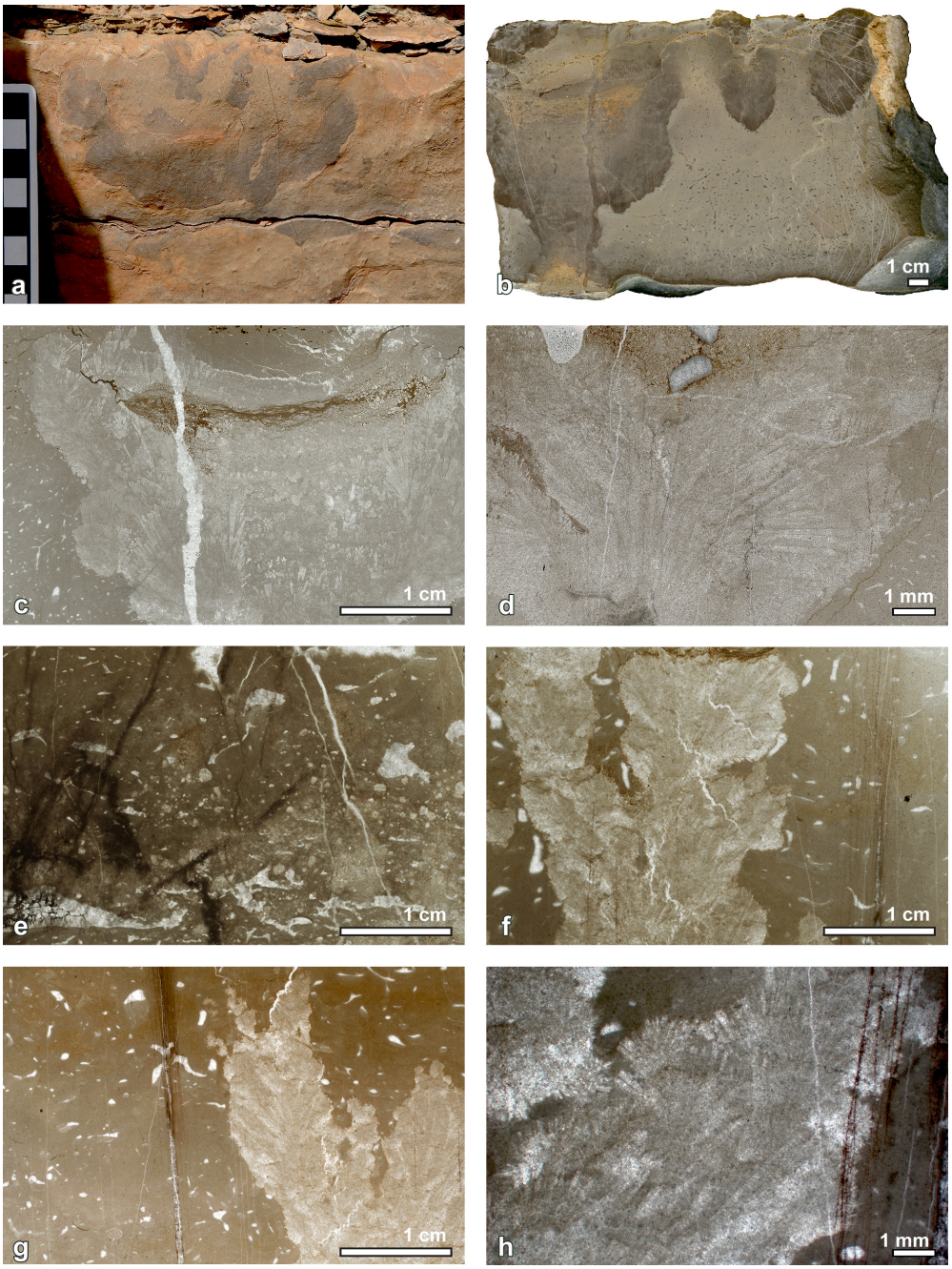

Figure 39 Details of in situ microbialites from the Shahreza Formation. a – Field photographs of in situ microbialites. C section, +13.60 m (photograph of V. Hairapetian). b – Scanned polished slab of knobby micropeloidal thrombolite/ precipitated cement. C section +13.85 m. c – Scanned thin section of an arborerescent thrombolite with fan-shaped crystals. C section, +13.85 m. d – Rod-like crystals of a knobby micropeloidal thrombolite. C section +13.80 m. e – A framework of fenestral packstone/bindstone with porostromate microfossils, consisting of cyanobacteria and algae with spar-filled fenestral voids. C section, +18.65 m. f – Scanned thin section of a digitate dendrolite showing lobate margins. C section, +18.80 m. g – Bush-like, vertically erect, radial fabric of a dendrolite. C section, +18.80 m. h –Microphotograph of a dendrolite showing internal structure composed of acicular crystals. C section, +18.80 m.

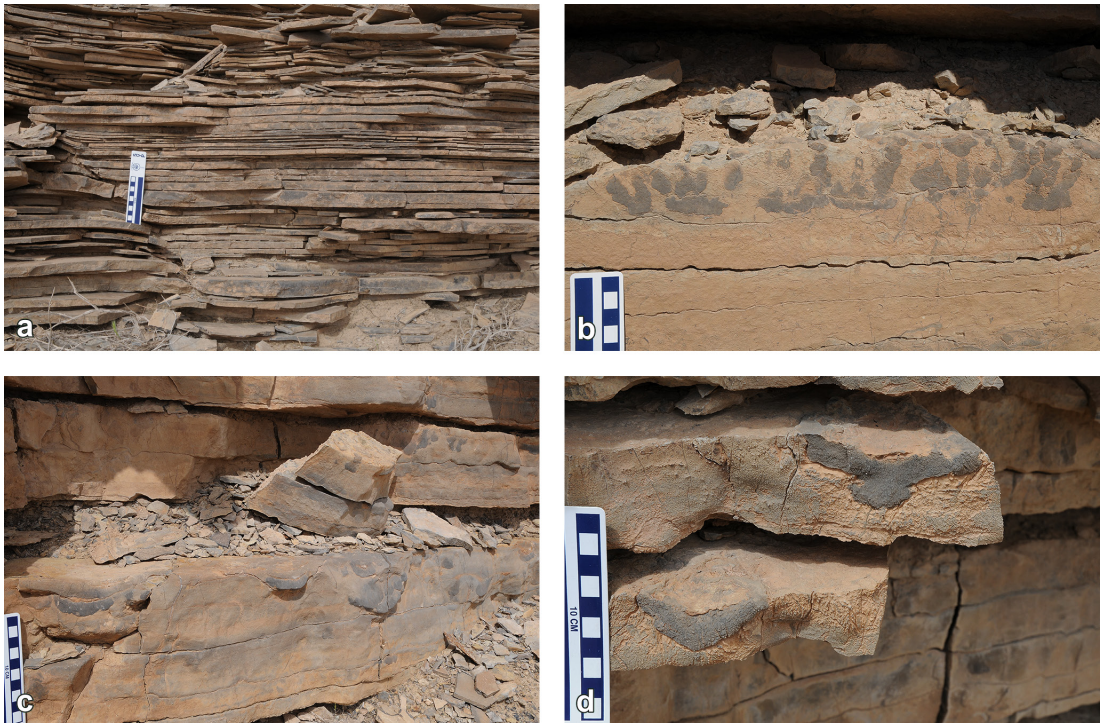

Figure 40 Field images of limestone outcrop of the Shahreza Formation at C section (photographs by V. Hairapetian). a – Thin, platy limestone beds of the Shahreza Formation. b – Branching, dendroid-like, knobby microbialites at +13.80 m. c – A horizon with abundant microbialites at +13.60 m. d – Club-shaped microbialite with 'holdfast' on the upper bedding plane and inverted conical microbialite on the lower bedding plane.

Club-shaped hybrid stromatolite, mushroom-shaped hybrid microbialite

An interval with arborescent microbialites begins at +8.55 m with an occurence of two microbialite types occuring in the same horizon: a club-shaped hybrid stromatolite (Fig. 50a, b) and mushroom-shaped hybrid microbialite (Fig. 50). Seen on a polished slab, the hybrid stromatolite has a columnar to club-shaped form. Crude and diffuse lamination of the columns is visible under the microscope (Fig. 50a). The columns are of various widths, and are laterally linked and separated by micritic sediment. On the microscale, this microbialite possesses laminated, micropeloidal to agglutinated, micritic to microsparitic fabric. A common additional fabric is composed of layers of sparite that are made of fan-shaped tufts of elongated, acicular crystals, forming laminated crust (Fig. 50b). This microbialite can be classified as hybrid crust after Riding (2008), containing both cement fans and apparent microbial fabric. The mushroom-shaped hybrid microbialite is characterized by a thick, sparitic 'holdfast', and it is covered by a sparitic 'lid' (Fig. 51). It has sparry calcite walls and uneven, irregularly laminated, internal structure. Its infill comprises mud- to silt-sized siliciclastic material that alternates with the sparry calcite. The internal structure of this microbialite can be classified as hybrid microbialite, where stromatolite is surrounded by leiolite. Additionally, small microbial, stromatolitic columns are visible in this specimen. The micritic matrix contains small sparitic voids and filaments. This microbialite can be classified as coarse-grained crust after Riding (2008).

Boundstone/bindstone on bivalve and ammonoid shells

Microbialites at +8.70 m and +8.80 m consist of small, possible sponges encrusting thin bivalve shells that served as attachment for their growth and probably facilitated their settlement (Fig. 50c). These small encrusting forms do not display any wall structure. The spiculitic framework is strongly recrystallized and is partially to completely dissolved and replaced by calcite-cemented cavities. However, the nature of the spicules remains to be determined. Peloids are abundant in the recrystallized micritic matrix. The upper surfaces of the bivalve shells at +8.80 m are filled with spar and form a geopetal fabric. Small, recrystallized gastropods and ostracods occur within the matrix. At +9.35 m the activity of benthic microbial communities resulted in biolaminated sedimentary structures (stromatolites) (Fig. 50e). A burrowed bioclastic wackestone with mollusc remains, which occurs at +13.95 m, is characterized by an occurence of domal, dish-shaped, micritic and microsparitic microbial crust (bindstone) growing upward on an ammonoid shell and also forms a lenticular microbial crust on the thin-shelled bivalve. Ammonoid and bivalve shells served as hard substrate for the growth of the crust (Fig. 50d).

Burrowed microbial packstone

This microfacies type (at +9.30 m) is a burrowed microbial packstone with fenestrae (Fig. 50f). Irregular, columnar and spherical bodies are made of microcrystalline, peloidal spar and contain tiny filaments. Irregular, anastomosing stylolite seams form stylobedded structures. Many birdseye-type fenestrae occur within the matrix; they occur as isolated, spar-filled voids that have irregular roofs (Fig. 50Mh). Two rounded structures on the middle left of the thin section resemble oncoids, although no lamination and no nucleus is visible (Fig. 50Mg). Biogenic encrustations are common.

Knobby micropeloidal thrombolite/ cement?

This microbialite at +13.80 m possesses a knobby, arborescent macrostructure with micropeloidal mesoclots. The clots have a blotchy, microsparitic fabric and peloidal microcrystalline texture. Subrounded, grape-like and microspherulitic mesoclots are interconnected and amalgamated. The microscale clots consist of fan-like splays and botryoids (Fig. 38c). Straight and branched rods and acicular crystals are also abundant (Fig. 38d). At +13.85 m, a microbialite studied on a polished slab has an arborescent, club-shaped form (Fig. M5b). On the microscale, dendritic calcite spherulites as well as fibrous and botryoidal cements are visible (Fig. 38c). Both microbialites can be classified as sparry crust after Riding (2008) and as arborescent thrombolite with dendritic fabric (Armella 1994).

Fenestral packstone/bindstone with porostromate microfossils (*SMF 21-PORO*)

This microfacies type occurs at +18.65 m and is characterized by small spar-filled cavities (birdeyes) and larger irregular voids (stromatactoid shapes). The sedimentary framework consists of peloids (pelmicritic framework) and cyanobacteria tufts with single dasyclads. Densely growing tufts of porostromate cyanobacteria are visible (Fig. 39e).

Dendrolite

This microbialite occurs at +18.80 m and possesses a distinct, vertically erect, dendrolitic mesofabric (Fig. M5g). It comprises convex-shaped, hemispherical bodies, which are juxtaposed, and have roughly superimposed lobate margins (Fig. 39f). On the microscale, this microbialite has a digitate, dendrolitic, fan-like character with radiating, elongated crystal and mineral splays. The crystals are mostly rectangular and show displacive growth; straight and branched rods, and fibrous and acicular crystals are also abundant (Fig. 39h). In some cases, thin micritic films overlie the crystals. Dendrolite is enclosed in fenestral lime mudstone with sparry filaments. This microbialite can be classified as sparry crust after Riding (2008).

5.3 Petrography of small-scale structures from float specimens

Morphological variation - at macro- and mesoscales - of the upper surfaces of microbialites is best reflected by float samples, of which a large number has been investigated. They show details of the retained synoptic relief and occasionally also cross-sections of microbialites (Fig. 42). They possess various morphologies, e.g., heart-shaped, loaf-shaped, flower-shaped, kidney-shaped forms, and have either flat or concave tops that are filled with a micritic matrix (Figs. 41, 42, 43). They occur as isolated forms or in clusters. Occasionally they are laterally amalgamated. Isolated forms reach 11 cm length and 5 cm width. Morphology and internal structure of the microbialites of these float specimens clearly correspond to those of the microbialite samples of known stratigraphic position, i.e., from the interval between +8.55 m and +18.85 m.

Skeletal stromatolite and cement crust

This microbialite grows upward on a skeletal fragment of a bivalve shell (Fig. 52c). It is enclosed in a burrowed, skeletal lime mudstone rich in ostracods, filaments probably derived from sponges, and sparry peloids. This microbial structure could be classified as skeletal stromatolite; a skeletal framework of this stromatolite consists of tiny filaments of unknown origin (porostromate microfossils and/or sponge spicule remains). On the lower half of the thin section, isopachous cement crusts grow on a skeletal fragment of a bivalve shell.

Digitate isopachous crust

This microbialite began to grow on an ammonoid shell (Fig. 52a, b). It has a columnar, digitate form. It forms on the microscale an isopachous, fibrous crust (Fig. 52b). This microbialite is enclosed in a burrowed, skeletal lime mudstone rich in ostracods, filaments of probable sponges, and sparry peloids. Regular alternation of cement layers and micrite layers is visible. Stylolite seams are common and are overgrown by filamentous microfossils, forming microstromatolites. Synsedimentary microfractures (sheet cracks) cut the microbialite and are filled by cement. This microbialite type can be considered a seafloor crust (Fischer and Garrison 1967). Isopachous sparry calcite crust on a bivalve shell is visible in Fig. 52d.

Club-shaped, hybrid microbialite

On a polished slab, microbialites are seen to have an arborescent, club-shaped form (Fig. 53b, c, d). On the microbialite margins, the crystals have spherulitic, acicular form and exhibit a botryoidal growth pattern (Fig. 53b). Elongated crystals are arranged in fan arrays, forming dendritic calcite spherulites (Fig. 53c). They have incorporated on top a significant amount of siliciclastic material (Fig. 53d). The microbialite is developed in a fenestral wackestone with geopetal fabric and small birdseye-type cavities that are filled by sparitic cements.

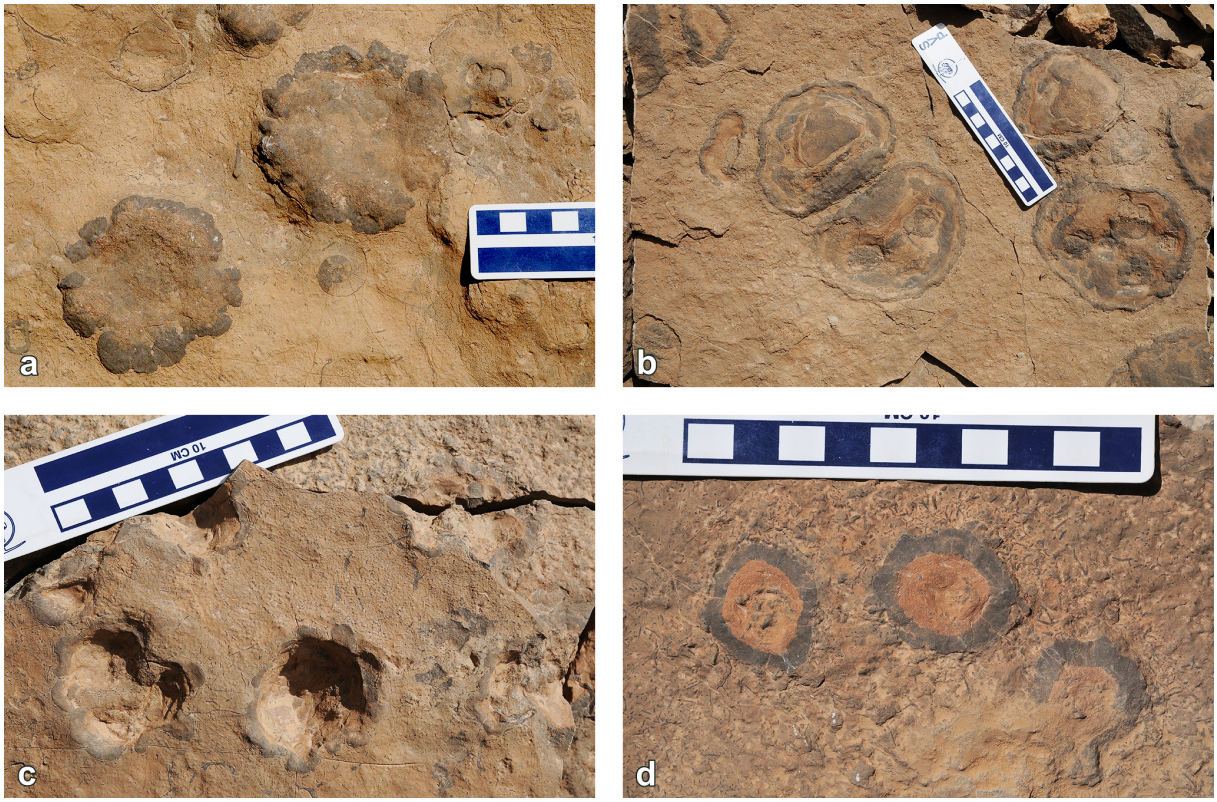

Figure 41 Field photographs of the Early Triassic coalescent microbialites (float specimens) (photographs by V. Hairapetian). a – Dark-grey, flower-shaped, sparry calcite microbialite developed in the pale brown micritic matrix, containing filaments, bivalve shell fragments, ammonoids, and high-spired gastropods. b – Kidney-shaped microbialite characterized by irregular, partly concentric structure, where micrite and sparite alternate. c – Concave, flower-shaped microbialite embedded in the fenestral, filament-rich micritic matrix. d – Dark-grey, ovoidal, lenticular sparry calcite microbialite developed in the pale brown micritic matrix, containing abundant filaments (probably sponge spicule remains). The microbialite is filled by an argillaceous micrite.

Figure 42 Field photographs of the Early Triassic microbialites (float specimens) (photographs by V. Hairapetian). a – Bedding plane of platy limestone with closely packed small microbial structures. b – Kidney-shaped microbialite formed by amalgamation of two single ovoidal specimes and/or coalescent sponge with a dermal surface. c – Dark-grey, ovoidal, sparry calcite microbialite. Note the mineralization in the centre of the structure within the micritic matrix. d – Leaf-like, lobated microbialite with sparry calcite on the rims. Partly stromatolitic seen in a cross-section.

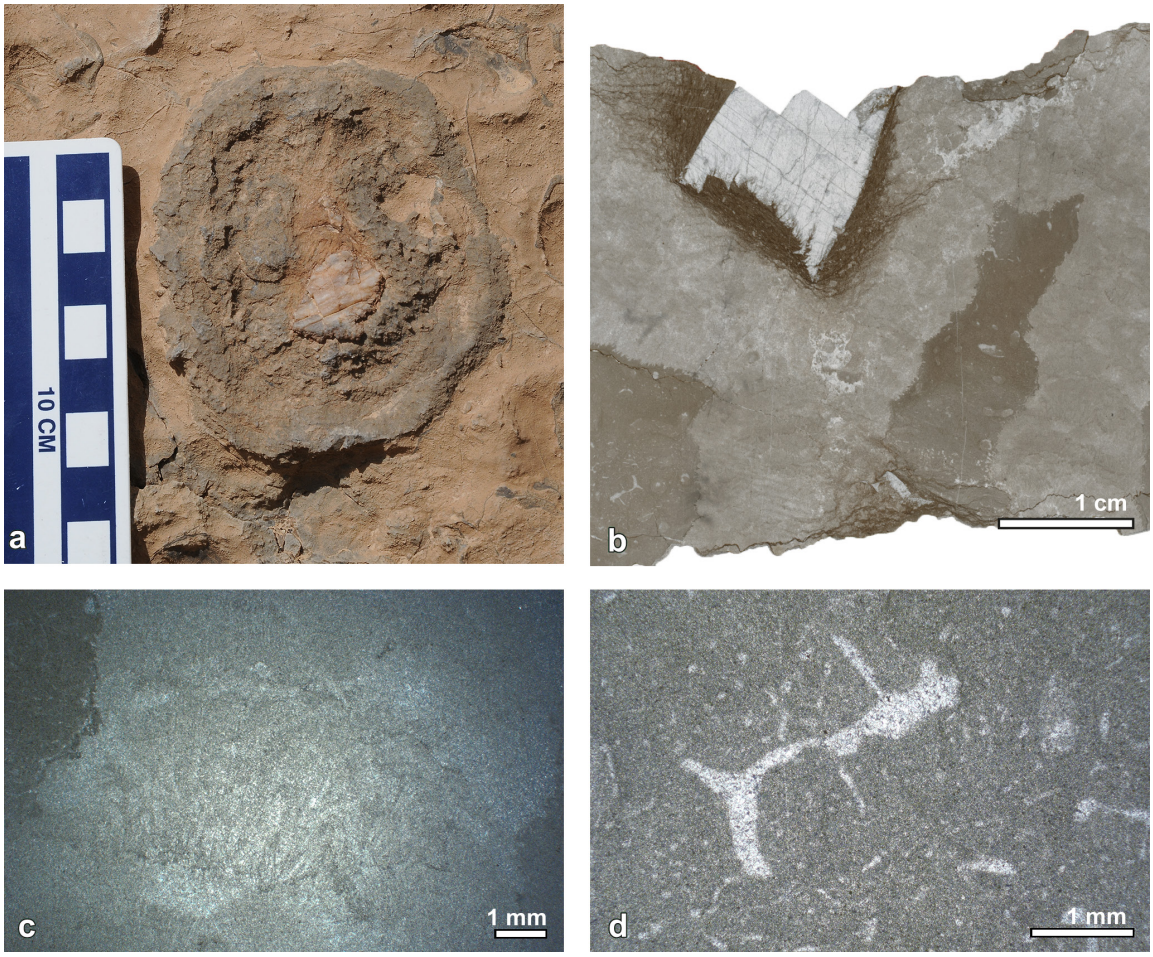

Figure 43 Details of the Early Triassic microbialites from float material. a – Field photograph of an ovoidal microbialite with a large calcite crystals in their interior (photograph by V. Hairapetian). b – Scanned thin-section of an ovoidal microbialite in picture a showing an inverted conical (club-shaped) microbialite with dendrolitic and aphanitic microstructure embedded in a micritic matrix containing filaments. c – Details of microbialite in b showing bundles of rod-like calcite crystals. d – Small cuspate to vermiform microfenestrae within the matrix.

Figure 44 Field photographs of the 'Boundary Clay' and the Shahreza Formation at Baghuk Mountain (photographs by V. Hairapetian). a – Outcrop of shales and clays of the 'Boundary Clay'. b – 'Calcite fan' layer at C section. c – Dome-shaped buildups containing the 'Calcite fan' at K section. d – Enlarged view of white rectangle in c showing a botryoidal fan.

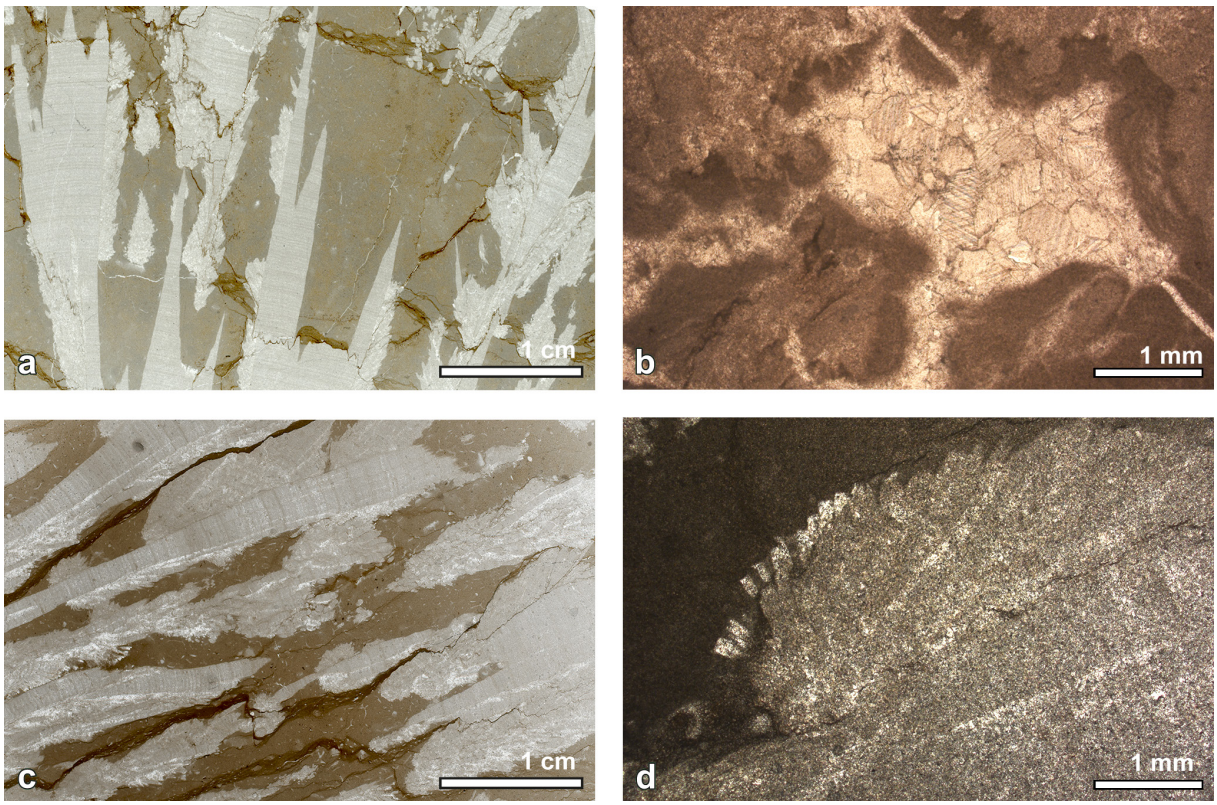

Figure 45 Microphotographs of the 'Calcite fan'. a – Scanned thin-section showing fanning aragonite pseudomorphs with irregular margins, enclosed in grey-colored micrite matrix with mesh of filaments. Internal lamination disturbed by stylolites. Baghuk Mountain, C section, +1.30 m. b – Sparry calcite-filled void with a dense bushy micrite crust. Baghuk Mountain, C section, +1.30 m. c – Scanned thin-section showing calcite fans with botryoidal, upward-branching crystals. Baghuk Mountain, C section, +0.80 m. d – Crystals with blades with broad, flattened terminations. Aggrading neomorphism produced calcite crystal mosaic of inequigranular fabric. Baghuk Mountain C section, +0.80 m.

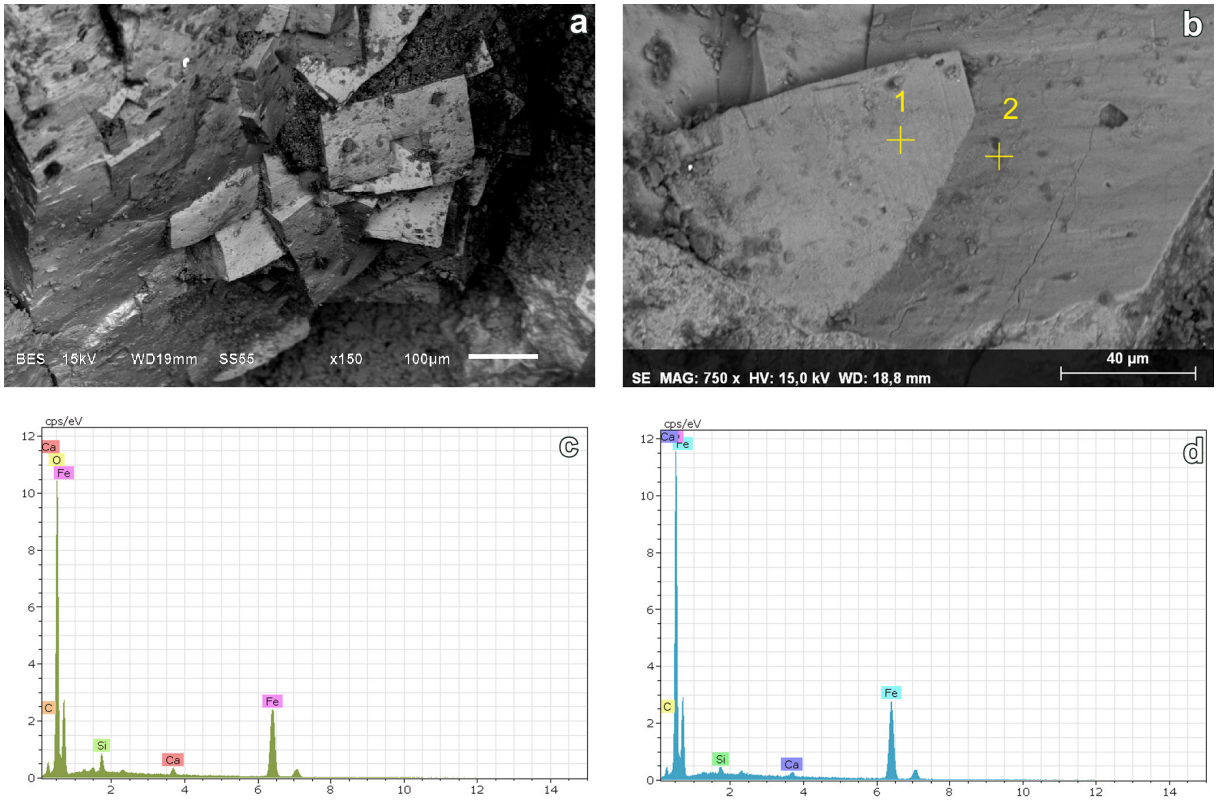

Figure 46 SEM-EDX characteristics of the 'Calcite fan'. a – Backscattered electron image (SEM-BSE) of cubic magnetite crystals within the 'calcite fan' botryoids. b – Secondary electron image (SEM-SE) image of magnetite crystals; crosses show a place where measurements were taken and numbers 1 and 2 are spectrum numbers. c – EDX spectrum of a point 1 in b showing that analyzed crystal is a magntetite, not pyrite. d – EDX spectrum of a point 2 in b (magntetite). Baghuk Mountain, C section, +1.30 m.

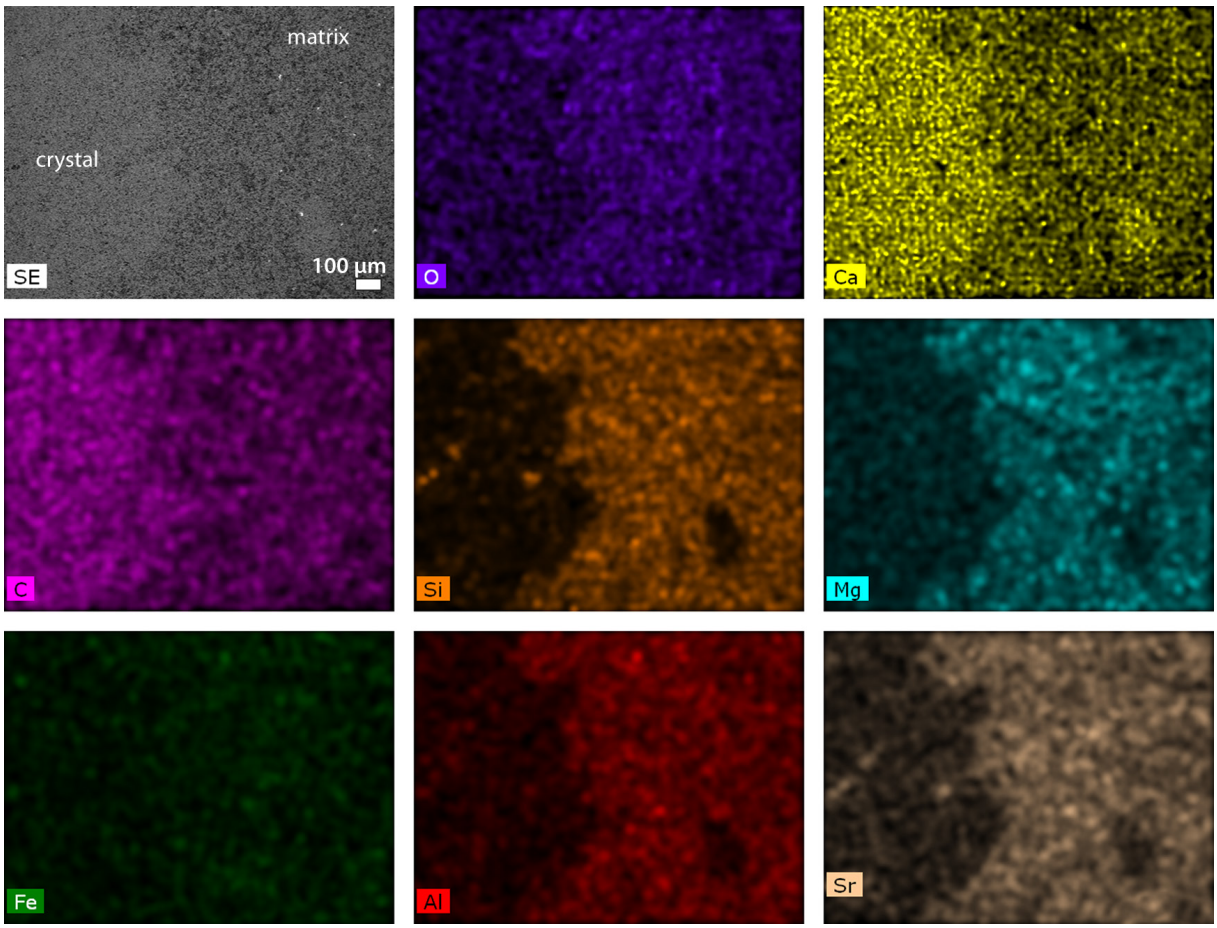

Figure 47 Elemental distribution maps illustrating differences in composition betwen ‘calcite fan’ crystals and surrounding matrix. Baghuk Mountain, C section, +1.30 m.

.

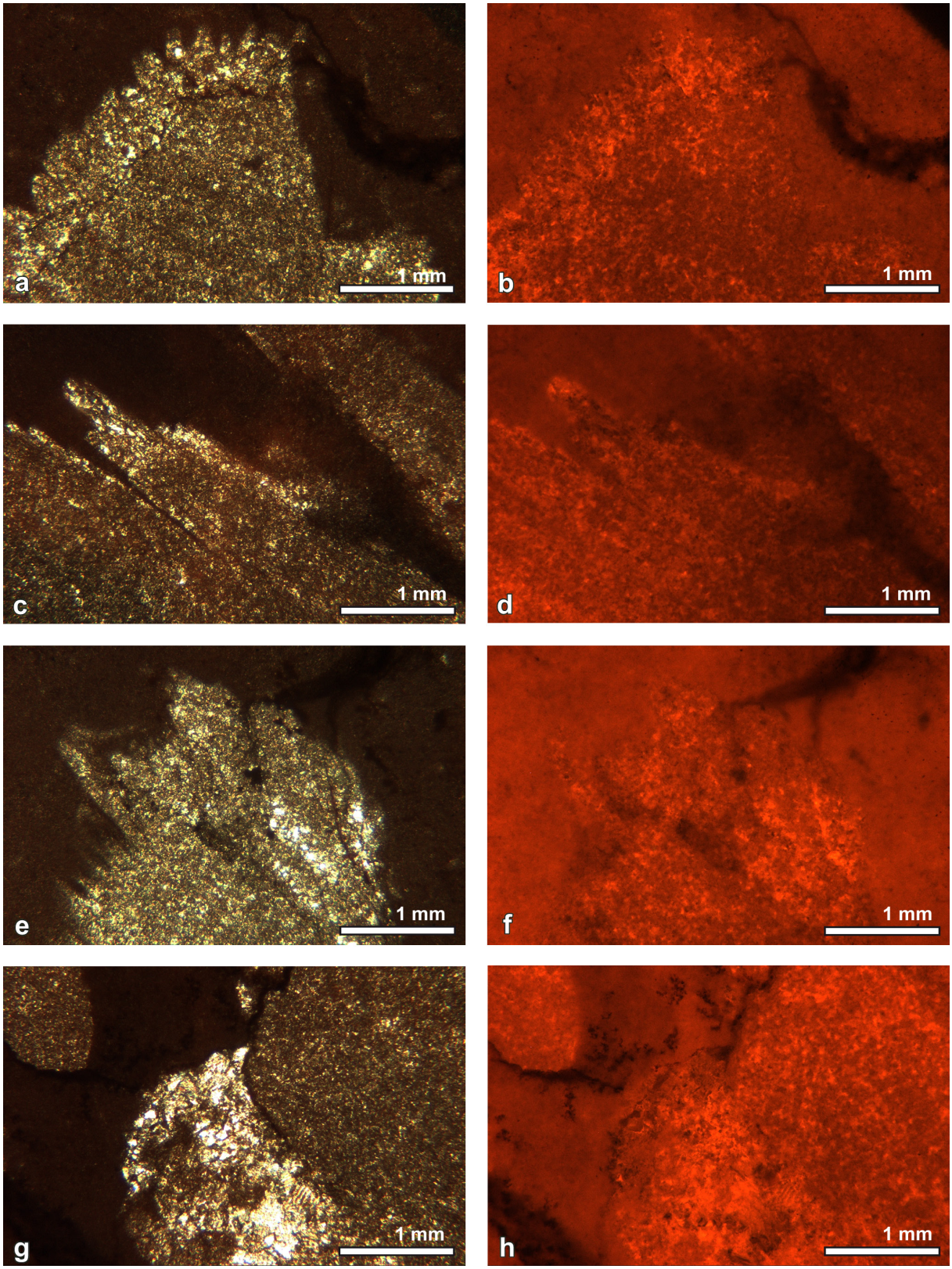

Figure 48 Plane polarized light images of the 'calcite fan' crystals and surrounding matrix in a, c, e, g and with corresponding optical cold-cathode cathodoluminescence images in b, d, f, h. Baghuk Mountain, C section, +1.30 m.

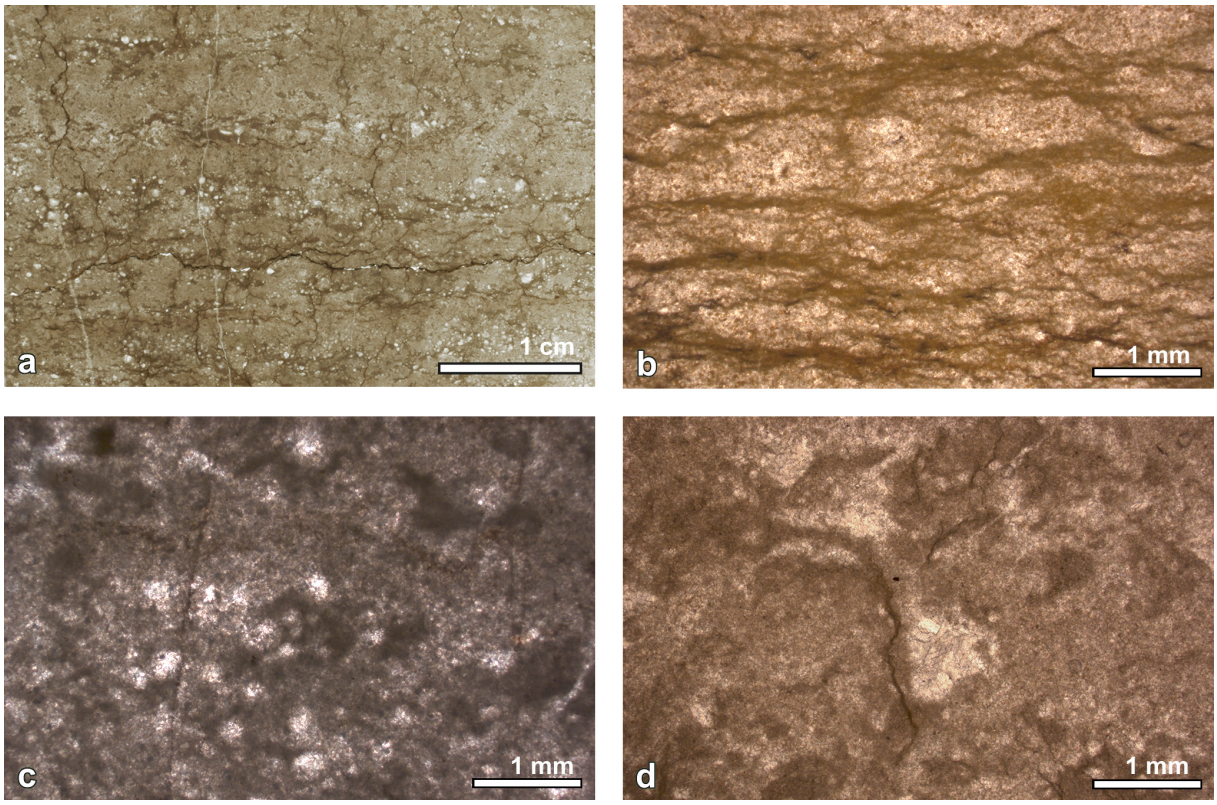

Figure 49 Microphotographs of a peloidal bindstone. a – Scanned thin-section showing alternating couplets of micritic and peloidal layers. Peloidal clotted and grumous micrite of a thrombolite with small sparite-filled cavities. Baghuk Mountain, A section, +2.20 m. b –Bundles of close-packed micrite threads in a partly dolomitized microsparitic matrix – Baghuk Mountain, C section, +2.43 m. c – Sparry calcite spheres and dense micrite of Baghuk Mountain, C section, +2.45 m. d – Bushy micrite with poorly defined margin and locally showing transition to a microsparite. Baghuk Mountain, C section, +2.20m.

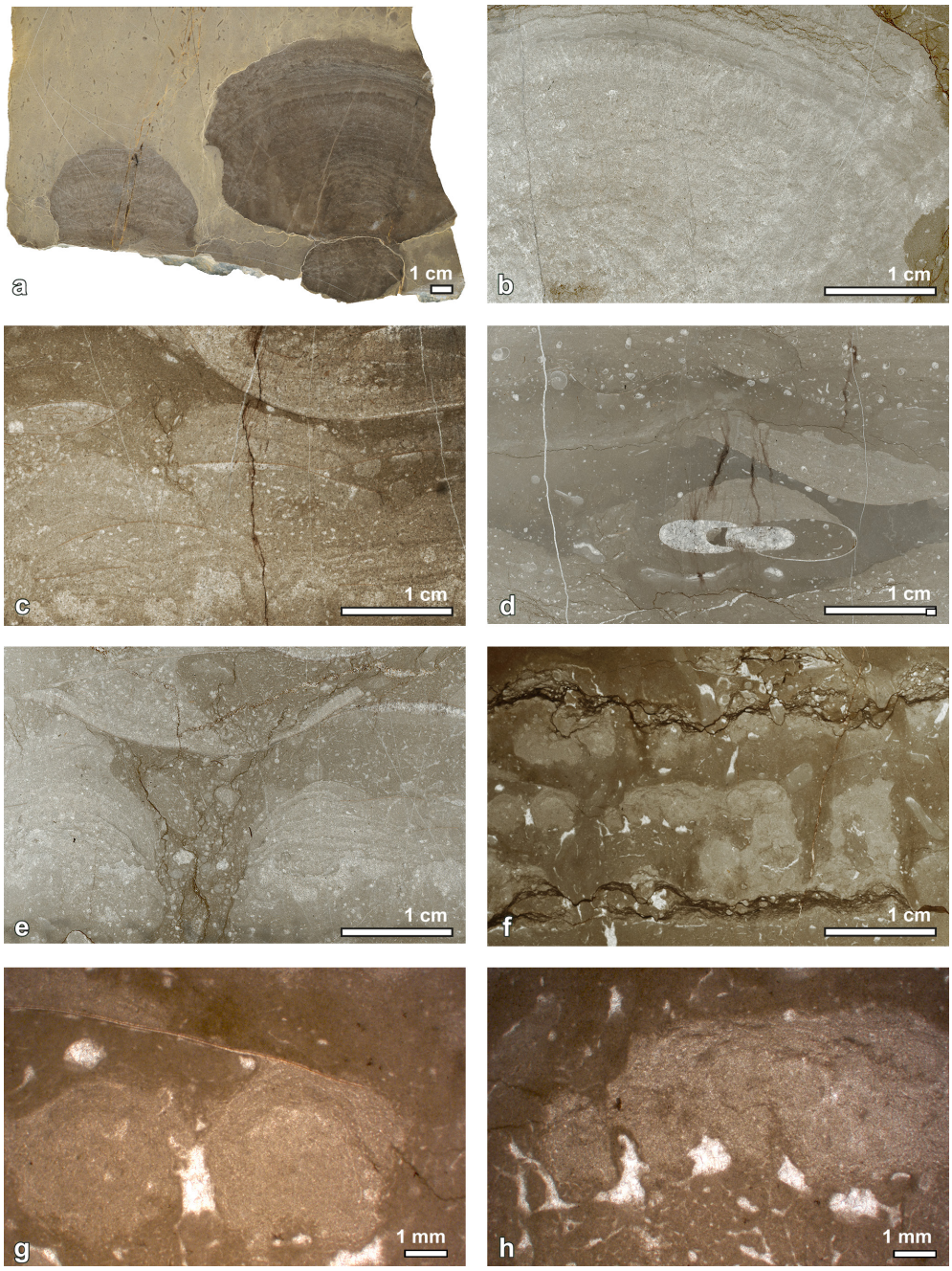

Figure 50 Details of in situ microbialites from the Shahreza Formation. a – Scanned polished slab of a club-shaped hybrid stromatolite. C section, + 8.55 m. b – Details of a stromatolitic lamination – alternation of a dense micrite layers with sparry calcite layers with fan-shaped crystals. C section, + 8.55 m. c – Bindstone/boundstone on a bivalve shells that acted as substrate for growth of microbial, micritic and microsparitic crusts. C section, + 8.70 m. d – Micritic microbial crust on skeletal elements of an ammonoid and of a bivalve. Note abundant gastropod (g) shells in the matrix. C section, + 13.95 m. e – Benthic microbial communities (BMC). C section, + 9.35 m. f – Scanned thin section of a microbial packstone showing irregular, columnar and spherical, peloidal, microsparitic bodies. C section, + 9.30 m. g – Micritic, microbial ooids. C section, + 9.30 m. h – Fenestral voids with irregular roofs filled with a sparry calcite. C section, + 9.30 m.

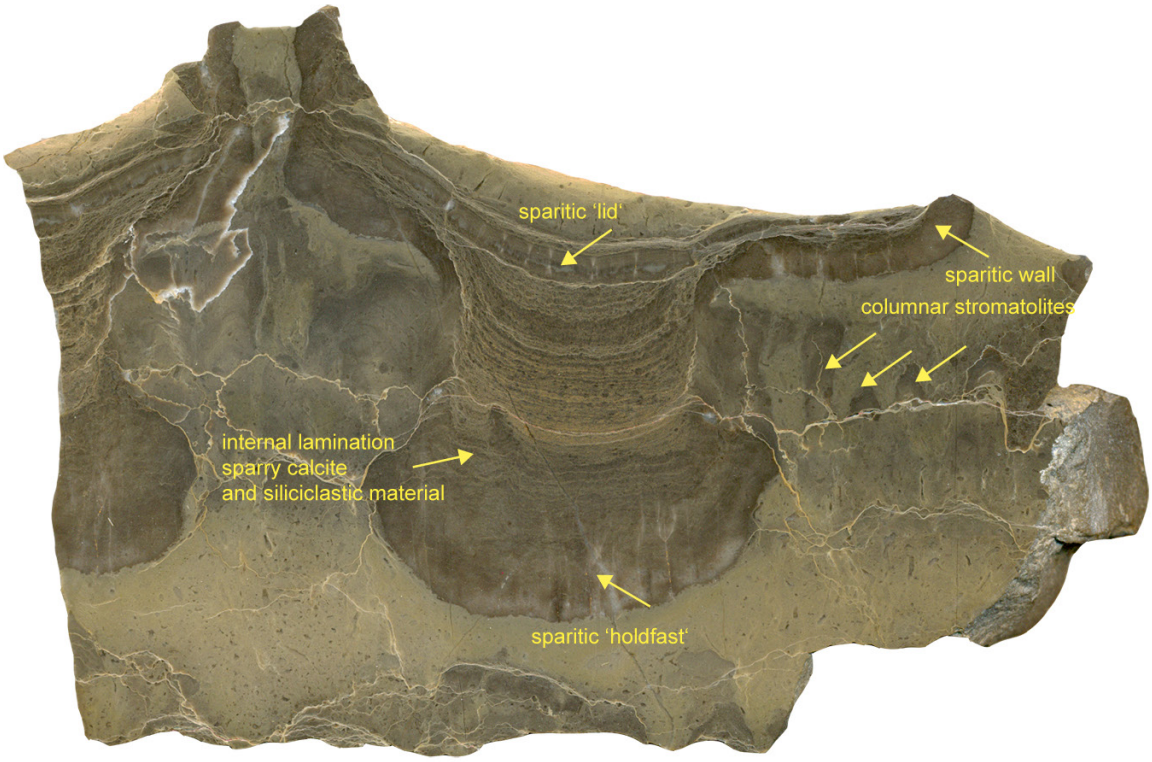

Figure 51 Scanned polished slab of a mushroom-shaped hybrid microbialite. This microbialite is characterized by a thick sparitic, partly laminated 'holdfast' and is covered by a sparitic 'lid'. Internal structure is composed of alternating layers of sparry calcite and mud-to silt-sized material. The sparitic 'lid' is cracked. This microbialite can be classified as hybrid microbialite, where stromatolitic lamination is preserved in the centre of the specimen, whereas its walls and edges are made of leiolite (structureless sparry calcite of the walls). The hybrid microbialite is enclosed in a burrowed, partly recrystallized lime mudstone with remains of sponge spicules. The slab has a size of 20 x 15cm.

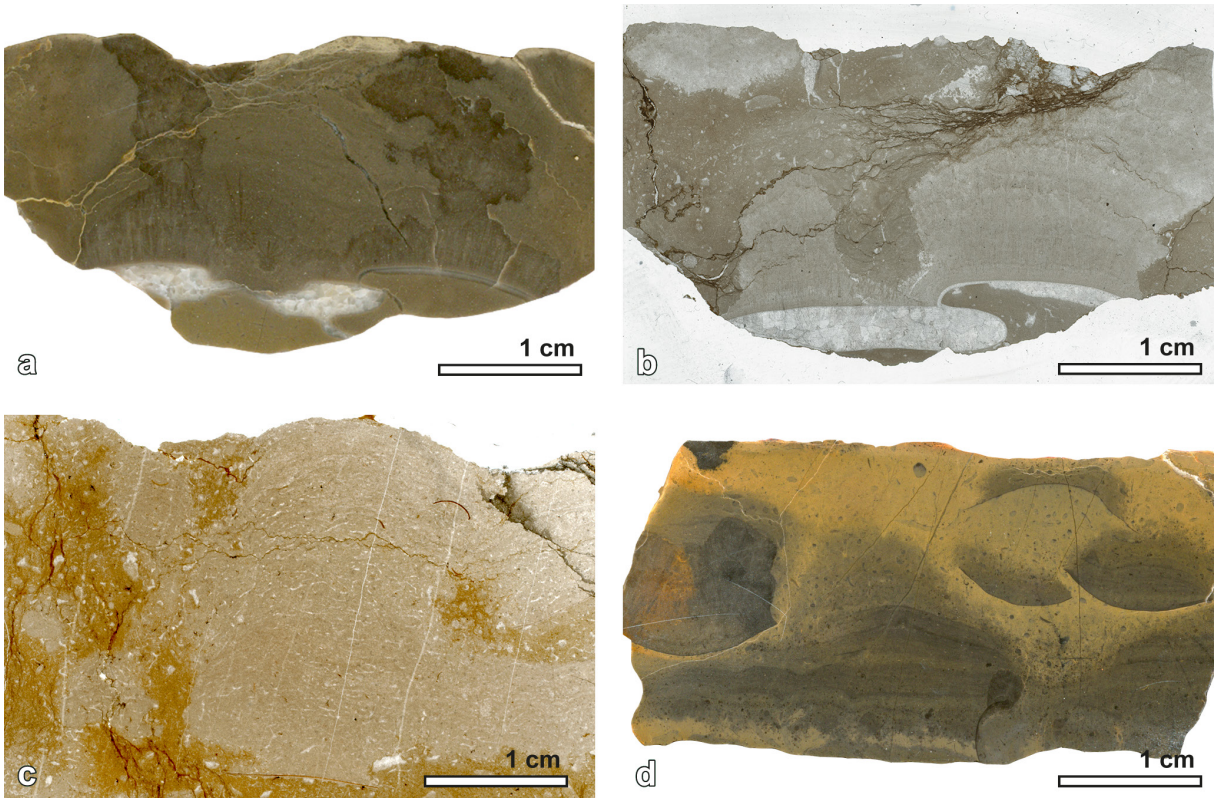

Figure 52 Bindstones/cement crust from float specimens at Baghuk Mountain. a – Scanned polished slab of a digitate, isopachous crust on an ammonoid shell. b – scanned thin section showing isopachous, fibrous crust. c – Skeletal stromatolite composed of tiny filaments that are probably sponge spicule remains or algal threads. d – Scanned polished slab showing biolaminated structures as well as micritic and sparitic crust on a bivalve shell.

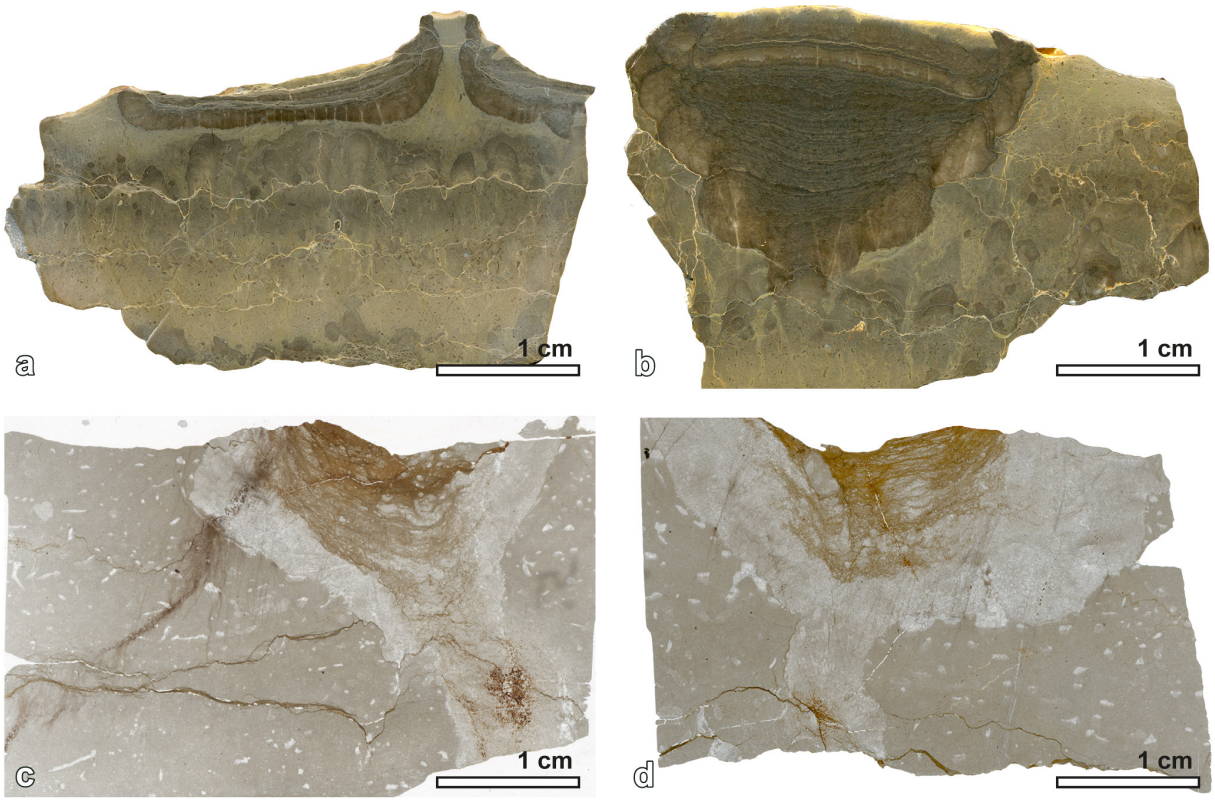

Figure 53 Hybrid microbialites from the Baghuk Mountain float specimens. a – Scanned polished slab of an hybrid microbialite showing sparitic 'lid' and small stromatolitic columns. b – Scanned polished slab of an hybrid microbialite. It is characterized by a stromatolitic lamination in the centre, lobate margins of dendritic spar and spartic 'lid' in the uppermost part of the specimen. c – Scanned thin-section of a club-shaped microbialite with dendritic calcite crystals on the edges, embedded in a fenestral wackestone. d – Scanned thin-section of a club-shaped microbialite with microfabric made of granular calcite crystals.

6 DEPOSITIONAL SETTINGS

6.1 Julfa area

The red nodular *Paratirolites* Limestone is probably analogous to some Alpine-Mediterranean Jurassic limestone formations (e.g., Ammonitico Rosso; Jenkyns 1974) and to Devonian to Viséan examples of griotte nodular limestone formations of the Montagne Noire and the Cantabrian Mountains (e.g., Jenkyns 1971, 1974; Cecca et al. 1992). The limestone-marl alternation (limestone-marl, limestone-shale and nodular limestone) of the *Paratirolites* Limestone has been formed in a tropical, passive margin environment of the central Tethys during a transgressive period. The distribution of such types of rhythmite coincides with the distribution of intensive aragonite production in the tropics and subtropics where surface waters were supersaturated with respect to calcium carbonate (Rao 1996; Westphal and Munnecke 2003; Westphal et al. 2008). The nodularity appears to be the result of different factors like bioturbation, bottom current action, and diagenetic history (Schlager 1974; Jenkyns 1974). The nodular fabric was generated by aragonite dissolution at the sedimentary surface, followed by descending calcite-supersaturated pore waters. Calcite precipitation occurred a few centimetres below the sediment surface; the nodules were cemented at the sea floor during early diagenesis (Jenkyns 1974). The sedimentary structures (hardgrounds, biogenic encrustation, microcracks, Fe-Mn crusts, hardground intraclast) are a consequence of extremely slow rates of carbonate accumulation, early lithification and sea-floor dissolution. Micrite clasts and pebbles in the upper 0.45 m of the *Paratirolites* Limestone represent partly lithified carbonate mud, which has been eroded and locally reworked soon after deposition. The mass occurrence of sponges in the topmost *Paratirolites* Limestone in the sections near Julfa may point to low sedimentation rates, which enabled colonization of the seafloor. The presence of hard substrates (hardgrounds, molluscan shells, etc.) allowed encrustation by sessile organisms and may point at a decrease of carbonate production. Irregularly distributed spicules without any arrangement suggest that they have been reworked prior to final deposition.

The red color of the limestone may be related to bacterial activity at dysoxic/anoxic interfaces near the water-sediment interface, where microorganisms (bacteria and fungi) precipitated iron-manganese oxy-hydroxides. The red pigmentation possibly resulted from accumulation and dispersion of sub-micrometric hematite in poorly oxygenated marine environments during early diagenesis (e.g., Préat et al. 1999, 2000, 2006, 2008; Mamet and Préat 2003, 2005, 2006a, b). In contrast, Heydari et al. (2003) assumed well-oxygenated bottom waters during deposition; they related the red color of the latest Permian carbonates to Fe-rich detrital clay particles. Benthic ostracod assemblages from the Abadeh section studied by Kozur (2007) also indicated a high oxygen content in the bottom water during sedimentation of the red limestone of the Hambast Formation.

In my opinion, the *Paratirolites* Limestone originated in a well-aerated deep shelf environment under oxic conditions. The occurrence of the pelagic fauna (ammonoids,conodonts, radiolari-

ans, sponges), the frequent occurrence of ostracods, and the intensive bioturbation support this opinion. The nodular limestone-marl succession of the *Paratirolites* Limestone was deposited in the open sea; the setting was in the dysphotic zone at a depth of about 100-200 m, below the wave base and within the range of the aragonite lysocline. Mohtat Aghai et al. (2009) postulated that the Aras Member (= 'Boundary Clay') was probably deposited in a low-energy environment with quiet and stagnant water at relatively shallow water depths of a few tens of meters. I agree that the lime mudstone and wackestone of the Aras Member were deposited in a low-energy environment, below the storm wave base, on a deep shelf with dysoxic/weak suboxic conditions. The lamina with densely packed, complete and disarticulated ostracod valves of the sponge ostracod wackestone in the Ali Bashi 1 section may point to storm-flow processes. The accumulation of reworked ostracod shells may be interpreted as the result of accumulation of a distal tempestite.Thin-bedded, bioturbated to nodular limestone beds of the lower Elikah Formation (= *Claraia* Beds) suggest sedimentation below the wave base under deep-water conditions. The unfossiliferous, non-laminated, fractured lime mudstone within the Aras Member at Zal, 0.20 m above the extinction horizon, is classified as Standard Microfacies Type 23 (SMF 23) (Wilson 1975). This microfacies type has been distinguished for sediments with authigenic evaporite minerals, which characterize arid platform interiors. In that case the lack of fossils is caused by the mass extinction, not by a sampling effect, and an absence of evaporite minerals implies deposition in a deep basin Facies Zone 1 (FZ 1). I postulate that the sponge spicule wackestone and sponge-ostracod wackestone of the *Claraia* Beds were deposited on a deep carbonate shelf and represent the same pelagic setting as the upper part of the *Paratirolites* Limestone. The bellerophontid wackestone and bioclastic wackestone with diverse fossils were deposited under low-energy, normal, open marine conditions of the platform interior. The laminated peloidal bindstone was formed in the restricted platform interior. The floatstone with sparry spheres was deposited in a low-energy environment with low sedimentation rates of the open-marine carbonate platform. The aggregate grain grapestone and oncoid wackestone/floatstone formed in a partially agitated, high-energy environment of the carbonate platform. Occurrences of aggregate grains, cortoids, sparry spheres, and ooids of the aggregate grain grapestone characterize higher-energy settings (platform-margin sand shoals), and these grains originated in the well-lit euphotic zone. Micritic matrix of carbonates of the *Claraia* Beds has been interpreted as microbial in origin and was classified as a cryptic calcimicrobial lime mud, produced at water depths below the wave base (Richoz 2006).

6.2 Baghuk Mountain

Although differences in microfacies characteristics of the *Paratirolites* Limestone exist between sections in the Julfa and Abadeh regions, I postulate that the uppermost 5 m of the Hambast Formation at Baghuk Mountain originated similarly to the section near Julfa on a shallow-marine continental margin, on a drowned pelagic carbonate platform, below storm wave-base, in the dysphotic zone. The lime mudstone of the 'Boundary Clay' was formed in a low-energy basinal environment below the storm wave-base. In my opinion the 'calcite fan' was formed in a low-energy basinal environment in water depths below the wave base, in open

marine conditions, and I surmise that its formation was not affected by sea-level fluctuations. The peloidal bindstone of the lowermost Shahreza Formation was formed under quiet water conditions of the restricted platform interior, and lamination formed in a low-energy environment. The microbialites from the interval between +8.55 and +18.85 are embedded in grey, bioclastic to fenestral lime mudstone to packstone with a restricted fauna, i.e., low diversity skeletal components, including sponge spicule remains, ostracods, gastropods, algae, bivalves, ammonoids, and benthic foraminifera. Their widespread association with micritic sediment may indicate that they grew under low-energy conditions, possibly below the fair-weather wave base and above but near the storm-weather base, in the photic zone. No examples of brecciated microbialites were seen and fragments are rare, suggesting growth in quieter water, in a calm depositional environment. Uncommon bioclast levels (with *Claraia* and other bivalves) in the microbialites are recorded at +8.70 m, +8.80 m, +9.35 m, and +13.95 m. The shells are chaotically distributed and are preserved either concave-up or convex-up. These bioclastic levels are related to occasional currents in a normally calm depositional environment. These bioclast accumulations acted as hard substrates for the growth of microbial forms. Fenestral packstone/bindstone with porostromate microfossils that occurs at +18.65 m is interpreted here as having been deposited in a shallow subtidal environment of the platform interior. I postulate that a dendrolite at +18.80 m grew a short distance above the sediment-water interface and kept pace with sedimentation. The matrix of burrowed lime mudstone to packstone contains abundant benthic shell organisms like ostracods, microgastropods, algae and benthic foraminifera, suggesting an oxygenated habitat during the time of accumulation. Early lithification and rapid cementation allowed accretion and preservation of the microbialites. Input of siliciclastic material probably inhibited the growth of the microbialites.

7 STABLE ISOTOPE STRATIGRAPHY

7.1 Marine geochemistry of carbon (background)

The element carbon has the two stable isotopes ^{12}C and ^{13}C (atomic masses of 12 and 13, respectively). ^{12}C is far more abundant (98.89 at%) in nature than ^{13}C (1.11 at%). After the abundance determination of the two isotopes in a sample, their ratio ($^{13}C/^{12}C$) relative to the Vienna PeeDee Belemnite standard (VPDB) is expressed in delta (δ) notation and given by:

$$\delta^{13}C \text{ sample} = 1000 * (R_{sample}/R_{standard} -1)$$

where R represents the ratio of ^{13}C to ^{12}C in the sample and standard.

The $^{13}C/^{12}C$ ratio of VPDB is 0.01124 and by definition the $\delta^{13}C$ of VPDB is 0 ‰ (Craig 1957). As the original PDB material (powdered specimen of *Belemnitella americana*) is exhausted, the Vienna PBD was introduced as NBS 19 as the international isotope reference standard. It has a $\delta^{13}C$ value of +1.95 ‰ and is now the accepted means for calibrating the PDB scale.

A change of the isotopic composition from the respective carbon source or reactant ($\delta^{13}C_{source}$) to its product ($\delta^{13}C_{product}$) is called an isotope fractionation. The degree of isotopic fractionation associated with a reaction is commonly expressed as a dimensionless fractionation factor (α):

$$\alpha = {}^{14}k/{}^{15}k$$

where k represents the rate constants of the light and heavy isotope (i.e. ^{13}C and ^{12}C) for molecules containing both isotopes. Most biogeochemical reactions discriminate against the heavier isotope, yielding α>1 (Montoya 2008). It is, however, more convenient in stable isotope geochemistry to define an isotopic discrimination factor (ε = kinetic isotope effect) that more clearly highlights this range of variation and is given in per mil (‰) as:

$$\varepsilon = (\alpha -1) * 1000$$

The discrimination factor is essentially equal to the difference between the $\delta^{13}C$ of the source (substrate) and the $\delta^{13}C$ of the product of a fractionation reaction:

$$\varepsilon \approx \delta^{13}C_{source} - \delta^{13}C_{product}$$

Positive ε values denote a ^{13}C depletion in the product compared to the source, hence the product is isotopically lighter than the source. If the reaction has reached chemical equilibrium, the fractionation is called equilibrium fractionation. In contrast, kinetic fractionation describes the fractionation associated with the unidirectional conversion of a source into the product. While equilibrium fractionation often occurs during phase transitions or diffusion, kinetic fractionation typically occurs during biological processes (Raven 1997). The isotopic composition of a

compound can undergo changes during physical, chemical or biological processes that favor one isotope over the other. The light ^{12}C diffuses faster than the heavy ^{13}C and reacts faster with other substances. ^{12}C is preferentially incorporated into organic compounds (CH_2O), whereas ^{13}C is preferentially incorporated into inorganic compounds (CO_2, HCO_3^-, CO_3^{2-}). The most important process producing isotopic fractionation of carbon is photosynthesis; photosynthetic fractionation is primarily kinetic. Isotope fractionation of carbon fixation is dependent on the partial pressure of CO_2 of the system. ε can vary from -17 to -40 ‰ (O'Leary 1981).

$\delta^{13}C$ values of carbonates

The carbon isotopic composition of carbonate sediments is controlled by the isotopic composition of the carbonate dissolved in the ocean. The magnitude of fractionation is determined by mineralogy of precipitating carbonate and by the carbon ion concentration (Grossman and Ku 1986). Most marine carbonates in the form of calcite form under near-equilibrium with dissolved inorganic carbon (DIC), primarily HCO_3^-, with an isotope fractionation effect (ε) of 1-2 ‰. Higher ε (average 2.7 ‰) has been reported for aragonite. Consequently, $\delta^{13}C$ values of calcite will be about 1.6 ‰ lower than $\delta^{13}C$ of aragonite precipitating from the same water. Average TDC (total dissolved carbon) for the bulk ocean has a $\delta^{13}C$ value of near 0 ‰. The fractionation during carbonate precipitation is small and relatively insensitive to temperature, so that $\delta^{13}C$ values of ancient marine carbonates reflect the $\delta^{13}C$ value of dissolved inorganic carbon in the past and are also close to 0 ‰ (Saltzman and Thomas 2012). The $\delta^{13}C$ values of TDC in the shallow near-surface photic zone of the oceans are higher than those in the overall ocean by about 1 to 2 ‰, due to the action of the biological pump (Anderson and Arthur 1983). Photosynthesizing organisms incorporate carbon and nutrients during their growth in the shallow ocean, and preferentially incorporate the lighter isotope ^{12}C in their tissues. Upon their death, they sink into the deep ocean, where they are oxidized, releasing the lighter isotope back to the surface ocean. This continuous removal of light isotope from the shallow ocean acts as CO_2 pump, transferring light carbon from shallow ocean into deeper levels of the ocean, causing a fractionation of 1 to 2 ‰ between the two ocean reservoirs. Marine plankton lives in disequilibrium with dissolved inorganic carbon (DIC), primarily CO_2. Biogenic carbonates are also rarely deposited in carbon isotope equilibrium with DIC; it is connected with a process known as the *vital effect* that is explained by a combination of metabolic and kinetic effects (McConnaughey 1989a, 1989b). Marine plankton is formed in disequilibrium with dissolved inorganic carbon (DIC), primarily CO_2. Locally and on relatively short timescales, the $\delta^{13}C$ value of DIC is related to productivity, ocean circulation, weathering, and/or rapid input of exotic carbon. On longer timescales (over 1 Ma) the $\delta^{13}C$ value of DIC in the ocean is a function of the relative proportion of inorganic to organic carbon (Scholle and Arthur 1980). Short-term 'spikes' in $\delta^{13}C$ values of carbonates are related to catastrophic changes in ocean productivity or inputs of light carbon. Locally, geographic effects like changing circulation, overturn, or changes in access to the open ocean may influence those short-time 'spikes'. Global significance of these 'spikes' must be identified in geographically distinct carbonate sections from all over the world.

$\delta^{13}C$ values of organic matter

The $\delta^{13}C$ composition of organic matter is initially controlled by variations in carbon fixation and inorganic carbon sources (Deines 1980). The photosynthtic organisms incorporate carbon and other nutrients into their tissues during growth. Photosynthesis by marine organisms uses the Calvin cycle of the C_3 plants (Attendorn and Bowen 1997). These organisms preferentially incorporate ^{12}C into their tissues, causing a ^{13}C enrichment in the remaining TDC of the shallow photic and deeper surface zone of the ocean. Organic matter falls through the water column and is decomposed by bacterial activity and converted to inorganic carbon, enriching deep water in ^{12}C. Thus biological activity causes pumping of carbon and particularly ^{12}C from the surface to deep waters. This continuous removal of light carbon from the shallow ocean acts as CO_2 pump and a source of O_2 for the ocean-atmosphere system. At steady-state conditions, the burial of organic carbon is balanced by the input of depleted ^{13}C from other reservoirs (mainly through recycling of reduced organic carbon). Photosynthesis usually produces organic matter that is characterized by $\delta^{13}C$ values from -28 to -12 ‰, depending on the environment (e.g., high-, mid-, or low-latitude), but mostly in the range between -25 and -20 ‰ for modern oxygenated oceans (Deines 1980; Westerhausen et al. 1993; Turekian 2001; Liu et al. 2007). Phytoplankton, which dominates the primary productivity at the ocean surface, has a $\delta^{13}C$ value of about -20 ‰. Where organic productivity is intense, there is corresponding depletion of surface water in ^{12}C. Recent marine sediments show a mean $\delta^{13}C$ of -25 ‰ (Deines 1980). $\delta^{13}C$ values of about -28 ‰ are recorded in redox-stratified marine environments (Abrajano et al. 2002). In environments with elevated methane fluxes like in the Black Sea (respective $\delta^{13}C_{carb}$ value of marine dissolved methane is about -48 ‰; Riedinger et al. 2010). Methanotrophic bacteria and archaea utilize CH_4 as the main carbon source, which results in extreme ^{13}C-depleted organic matter with $\delta^{13}C_{org}$ values down to -120 ‰ (Chevalier et al. 2013). Terrestrial C_3 plants have $\delta^{13}C$ values between -23 and -34 ‰, with an average of about -27 ‰. The very negative values for C_3 plants are essentially caused by intracellular kinetic fractionation during C fixation mediated by the enzyme known as 'rubisco'. The C_4 pathway involves a much smaller fractionation, so that C_4 plants have $\delta^{13}C$ between -9 and -17 ‰, with an average of about -13 ‰. Marine plants, which are all C_3, can utilize dissolved bicarbonate as well as dissolved CO_2. Seawater bicarbonate is about 8.5 ‰ heavier than atmospheric CO_2; as a result, marine plants average at about 7.5 ‰ heavier than terrestrial C_3 plants. Finally, marine cyanobacteria (blue-green algae) tend to fractionate carbon isotopes less during photosynthesis than true algae, so that they tend to average at 2 to 3 ‰ higher in $\delta^{13}C$ than those.

Preservation and alteration of the $\delta^{13}C$ signatures in sediments

Bulk sediment $\delta^{13}C$ values represent the average of the individual components (fossils, cements, micrite) that are additionally influenced by the DIC composition of ambient seawater, type of carbonate grains, vital effects, and diagenetic alteration. A variety of tools has been employed to assess the degree of diagenetic alteration, including trace element ratios and cathodoluminescence, as well as the relationship between trace element data and isotopic ratios, e.g., $\delta^{13}C_{carb}$ and $\delta^{18}O_{carb}$ records, and the covariance between $\delta^{13}C_{carb}$ and $\delta^{13}C_{org}$ records (Gross 1964;

Brand and Veizer 1980, 1981; Allan and Matthews 1982; Marshall 1992). Immediately after burial, biological organic matter is prone to complex diagenetic changes, whereby the activity of microorganisms plays a crucial role. Bacterial degradation of the biopolymers (e.g., proteins) preferentially eliminates ^{13}C-enriched carbohydrates and proteins, and preserves ^{12}C-enriched lipids. Some ^{13}C loss occurs with transformation to kerogen, leading to an average $\delta^{13}C$ value of -27.5 ‰ (Hayes et al. 1983). During early diagenesis, bacterial degradation can cause a depletion of sedimentary $\delta^{13}C_{org}$ by 1 to 2 ‰ (Ader et al. 2009). Diagenetic modification of carbonates can be divided into two pathways: meteoric and burial diagenesis (Veizer 1992). During meteoric diagenesis, both $\delta^{13}C$ and $\delta^{18}O$ can be shifted to lower values (Allan and Mathews 1987). However, lithological evidence for exposure surfaces should be recognized in such cases. The cross-plot of $\delta^{13}C$ and $\delta^{18}O$ values of carbonate cements exhibits a typical inverted 'J' trend (Lohman 1987). Shallow marine deposits may have been periodically subaerially exposed during sea-level oscillations; it has been shown that freshwater alteration may generate negative $\delta^{13}C_{carb}$ excursions (Swart and Kennedy 2011). Carbon and oxygen isotopes of sediments are widely used as sensitive indicators of diagenetic overprint, because their isotopic values change characteristically during burial diagenesis (Knauth and Kennedy 2009). Thereby $\delta^{18}O$ values < -10 ‰ and a positive correlation between $\delta^{13}C$ and $\delta^{18}O$ are usually interpreted as evidence for alteration (Derry 2010; Li et al. 2013). Among different diagenetic processes that can affect the isotopic composition of carbonates, degradation of organic matter is the most significant (Irwin et al. 1977). During anoxic early diagenesis, bacterial sulfate reduction of organic matter and CO_2 production take place, producing carbonates with low $\delta^{13}C$ values. In contrast, methanogenesis may produce ^{13}C-enriched cements. Carbonate cements with low $\delta^{13}C$ values can be formed during burial diagenesis due to organic matter decomposition under increased temperatures (Heydari 1997).

The marine carbon cycle during the P-Tr transition

Carbon isotope studies across the Permian-Triassic boundary have been performed on numerous marine and continental sections (for a summary see Korte and Kozur 2010). Results from P-Tr 'Boundary Clay' sections (e.g., Abadeh and Meishan) and shallow-water sections that lack a 'Boundary Clay' (e.g., Nhi Tao and Gartnerkofel) are marked by a ~2 ‰ decrease in $\delta^{13}C$ in pre-extinction strata (Holser et al. 1989; Algeo et al. 2007, 2008). A shift to more negative carbon isotope values directly at the extinction horizon has been recorded for the Kuh-e-Ali Bashi, Abadeh and Meishan sections (Schobben et al. 2017). This negative trend is strongly enhanced in the uppermost part of the *Paratirolites* Limestone in the Ali Bashi 1 section (from -0.48 m upwards), where the values decrease from about +2.4 ‰ to +0.6 ‰. The rapid secondary negative $\delta^{13}C$ fluctuation of ~7 ‰ at the extinction horizon at the Meishan D section is possibly contained in an interval of ~2-20 kyr based on radiometric dates (Burgess et al. 2014). This $\delta^{13}C$ excursion has been explained by carbon isotope injection of isotopically depleted methane produced by a new clade of methanogenetic bacteria (Rothman et al. 2014). In contrast, the $\delta^{13}C$ record of shallow-water sections (Zal, Nhi Tao and Gartnerkofel) shows either a gradual depletion or even a stagnation (or plateau) across the extinction horizon. A minimum in the "first-order" trend at Iranian sections (Kuh-e-Ali Bashi, Zal, Abadeh) closely corresponds

to the stratigraphic position of the FAD of *H. parvus* and represents an important stratigraphic marker according to Korte and Kozur (2010). An Early Triassic "second-order" negative $\delta^{13}C$ excursion is often recognized in the *I. isarcica* zone such as in the Gartnerkofel core (~ -2 ‰) and in the Ali Bashi 1 section (~ -1 ‰) (Hermann et al. 2010; Korte and Kozur 2010). Such double-peaked $\delta^{13}C_{carb}$ minima have been related to two episodes of increased environmental disturbance and a second biodiversity crash (Jin et al. 2000; Xie et al. 2007a, 2007b; Yin et al. 2012).

7.2 Marine geochemistry of nitrogen (background)

The element nitrogen has the two stable isotopes ^{14}N and ^{15}N (atomic masses of 14 and 15, respectively). ^{14}N is by far more abundant, comprising 99.63 at% of the global pool of nitrogen, whereas the heavier ^{15}N only accounts for 0.37 at% of the global pool of nitrogen (Nier 1950). During physical and biochemical processes, organisms discriminate between these two isotopes, which leads to subtle, but still measurable differences in the ratio of ^{15}N to ^{14}N among the various forms of nitrogen molecules in the biosphere (Sigman et al. 2009). After the abundance determination of the two isotopes in samples, their ratio ($^{15}N/^{14}N$) relative to a nitrogen standard is expressed in delta (δ) notation and given by:

$$\delta^{15}N_{sample} = 1000 * (R_{sample}/R_{standard} - 1)$$

where R represents the ratio of ^{15}N to ^{14}N in the sample and standard. The $^{15}N/^{14}N$ ratio of air is 0.00367647. Because this ratio is constant, atmospheric dinitrogen (N_2) is taken as a reference standard for nitrogen isotopic analyses (Mariotti 1983). Its $\delta^{15}N$ value is defined as 0 ‰.

Biological fixation of atmospheric dinitrogen (N_2) in the subsurface ocean is achieved by oxic phototrophic cyanobacteria, often called 'diazotrophs'. These bacteria do not discriminate strongly between ^{15}N and ^{14}N; they incorporate both molecules with no significant preference, so the isotope fractionation associated with fixation is small or absent (ε of 0-2 ‰; Macko et al. 1987; Montoya et al. 2002; Altabet 2007). The new nitrogen that enters the ocean is only slightly depleted relative to atmospheric N_2 and is characterized by a $\delta^{15}N$ close to 0 ‰ (Struck 2012). At the ocean surface, phytoplankton assimilates fixed N (nitrate, ammonium, nitrite, urea and other organic N compounds). Assimilation of these molecules causes significant but variable isotopic discrimination. As phytoplankton preferentially consumes the lighter ^{14}N relative to ^{15}N, removal of ^{14}N will naturally lead to a progressive increase in the $\delta^{15}N$ of the remaining substrate pool. Phytoplankton biomass originates from deep-water nitrate, which is the largest pool of fixed nitrogen in the ocean. The isotope effect of nitrate assimilation therefore has a major impact on the isotopic distribution of all N forms in the ocean (Sigman et al. 2009). Field estimates of isotope fractionation effects (ε) for nitrate incorporation are usually small (prokaryotic strains ≤5 ‰, for eukaryotes ~5 to 8 ‰; Granger et al. 2010), which is reflected by sedimentary $\delta^{15}N$ values ranging from ~3 to 8 ‰ (Sigman et al. 2009). The assimilation of ammonium by phytoplankton causes higher isotope effects (up to ~20 ‰), which, in turn, affects the $\delta^{15}N$ of their biomass that is in the range from -1 to -8 ‰ (Ohkouchi et al. 2005; Montoya

2008). After the death of marine organisms, their tissues are subject to mineralization (ammonification) that leads to release of nitrogen stored in amino acids and lipids. The return of organic N to nitrate occurs in two steps: in the first, one organic N is degraded to ammonium, and in the second step, ammonium is transformed to nitrate (nitrification) due to bacterial oxidation. Under oxygenated conditions organic molecules are transformed to NO_2^-/NO_3^- and under oxygen deficiency they are transformed to NH_4^+.

The isotope fractionation (ε) associated with the breakdown of organic matter to NH_4^+ is usually small (up to 3 ‰) (Sigman et al. 2009). The fractionation of ammonium through nitrite to nitrate may yield values from 15 to 25 ‰ (see Struck 2012 and references therein), depending on ambient conditions and proportions of ammonium and nitrate after reaction. If all ammonium is converted to nitrate in a 'closed system', then the $\delta^{15}N$ of the nitrate will be the same as that of the source (ammonium). Only the last step (transformation of NO_2^- to NO_3^-) is quantitative, meaning that all nitrite is converted to nitrate. There is no isotope fractionation associated with this step (Sharp 2007). Denitrification occurs in both the water column and the sediment where oxygen concentration is low (<5 μM) (Sigman et al. 2009). Denitrification strongly discriminates against the heavier isotope ^{15}N. ^{14}N contained in oceanic nitrate returns preferentially to the atmosphere, leaving the seawater nitrate pool enriched in ^{15}N as nitrate consumption proceeds, leading to elevated $\delta^{15}N$ values in the deep-water nitrate reservoir (Wada et al. 1975; Mariotti et al. 1980; Liu and Kaplan 1988; Voss et al. 2001). Denitrification in the water column and in oxygen-poor areas causes higher $\delta^{15}N$ values of nitrate (ε ~20 to 30 ‰) (Kessler et al. 2014). For this reason, $\delta^{15}N$ values for global ocean nitrate are higher than that of the N source from N_2 fixation, which constitutes the dominant input (Sigman et al. 2009). Upwelled dissolved nitrate that is used by marine phytoplankton in biomass production in surface waters is characterized by a $\delta^{15}N$ value of 4.8 ‰, whereas organisms using N_2 as their main nitrogen source are characterized by $\delta^{15}N$ values between 0 and 3 ‰ (Sigman et al. 2009). In contrast to denitrification in the water column, denitrification in sediments leads to small isotope fractionation (ε ~3 ‰) that is expressed by $\delta^{15}N$ values between 8 and 12 ‰ (Table 10).

$\delta^{15}N$ as a geochemical proxy

Bulk sedimentary $\delta^{15}N$ represents the isotopic composition of all combustible nitrogen in the sediment. Stable nitrogen isotopic composition in recent and ancient sediments has been utilized as an indicator of changes of the nitrogen cycle and processes occurring therein (e.g., Wada and Hattori 1991; Altabet and François 1994; Ganeshram et al. 1995; Haug et al. 1998; Holmes et al. 1999; Struck et al. 2000, 2001, 2004). On the global scale, changes in the rates of denitrification and nitrogen fixation (output-input budget) cause global shifts in the average $\delta^{15}N$ of marine ecosystems. At a smaller scale, sedimentary $\delta^{15}N$ may help to characterize internal nitrogen cycling (nutrient utilization in the water column) (François et al. 1992; Altabet and François 1994). Changes in the global N isotopic record also may be viewed as a palaeoredox proxy, because denitrification (i.e., the respiration of organic matter using NO_3^-) occurs under suboxic conditions (Jenkyns et al. 2001; Galbraith et al. 2004; Jaccard and Galbraith 2012).

Nitrogen isotopes offer very valuable proxy parameters for past environmental changes related to climate (Saitoh et al. 2014; Luo et al. 2016). In a system where the availability of NO_3^- in the euphotic zone is limited, i.e., where loss by denitrification or assimilation exceeds nitrogen supply in the pool, nitrogen fixation is promoted. Replenishment of N-fixing organisms occurs today in the Baltic Sea and Black Sea, where oxic surface waters overlie vertically redox-stratified water masses and deep-water anoxia (Struck et al. 1998; Emeis et al. 2000). Anoxic conditions in such aquifers favor the recycling of phosphate from sediments that is upwelled into oxygenated photic zones. In these settings, the available amount of phosphorous exceeds the amount of nitrogen required for plankton growth and results in changes of the N/P Redfield ratio (e.g., ≠16:1) (Fry et al. 1991). (In 1934, Alfred Redfield discovered that the ratio of carbon to nitrogen to phosphorus is a nearly constant 106:16:1 throughout the world's oceans, in both phytoplankton biomass and in dissolved nutrient pools). Phosphorous excess gives rise to diazotrophic bacteria blooms that introduce atmospheric nitrogen of low N-isotope composition ($\delta^{15}N$ of 0 ‰) to the marine cycle (Struck et al. 2004). Bulk sediment $\delta^{15}N$ values can become even negative in those settings, where phototrophic primary production occurs under oxygen depletion (Milder et al. 1999; Struck et al. 2001; Arnaboldi and Meyers 2006; Fuchsman et al. 2008). Examples of such settings are meromictic lakes (e.g., Lake Alat of the Bavarian Alps; Falk 2011) and some closed basins like the Black Sea and the Cariaco Trench that are highly redox-stratified aquatic areas, where photic zone anoxia is permanent, as the anoxic water body rises into the photic zone during long periods of stagnation (Repeta et al. 1989; Ohkouchi et al. 2005; Fuchsman et al. 2008; Halm et al. 2009; Struck et al. 2009). These settings are characterized by photic zone anoxia, euxinic bottom water conditions and excess availability of NH_4^+. A dense population of purple and green sulfur bacteria occurs in the uppermost part of the anoxic water body and consumes ammonium. Ammonium uptake is involved with large isotopic fractionation ($\varepsilon = \sim 10$ to 20 ‰), so that their biomass is strongly depleted in ^{15}N leading to $\delta^{15}N$ values of -1 to -8 ‰ (Ohkouchi et al. 2005; Montoya 2008; Sigman et al. 2009). Such negative values were recorded from, e.g., organic matter-rich sediments like black shales of the Cretaceous Oceanic Anoxic Event II, where occurrence of specific biomarkers characteristic for anoxygenic phototrophs were established (Pancost et al. 2004; Junium and Arthur 2007; Higgins et al. 2012).

Modern open marine productivity is characterized by an equilibrium state between nitrate assimilation, N_2 fixation, and denitrification (the so-called 'normal marine production'). Modern oceanic $\delta^{15}N$ values are within the range from +2 ‰ to +6 ‰. Modern marine sediments are characterized by an average $\delta^{15}N$ value of +5 ‰ (Altabet and François 1994), which confirms essentially complete nitrate utilization in the recent ocean, in so far as the $\delta^{15}N$ value of dissolved nitrate averages 4.8 ‰ (Sigman et al. 2000) (Table 11). In high productivity regions such as in the Peruvian, the Namibian, and the Californian ocean enormous bioproductivity occurs in surface waters as a result of upwelling of nutrient-rich deep-water that is rich in nitrate, phosphate, and silicate. Sediments from such eutrophic conditions (e.g., phosphorites) reveal elevated $\delta^{15}N$ values in comparison to open marine conditions with values in the range from +6 to +12 ‰ (Ganeshram et al. 1995; Pride et al. 1999; Altabet et al. 2002; Struck et al. 2002; De Pol-Holz et al. 2006; Emeis et al. 2009). Such elevated $\delta^{15}N$ accompanied by high organic mat-

ter concentration in upwelling areas is generally explained to result from high $\delta^{15}N$ in oceanic nitrate, which formed during periods of extensive denitrification or from the anammox process (the anaerobic oxidation of ammonium by nitrite to yield N_2) within oxygen minimum zone (OMZ) waters (Ganeshram et al. 1995; Pride et al. 1999; Voss et al. 2001; Kuypers et al. 2005).

Table 10 Approximate estimates of typical ranges of sedimentary bulk $\delta^{15}N$ values in relation to the respective governing processes affecting marine nitrogen cycle and their typical marine environments (modified after Struck 2012 and Cremonese et al. 2013).

Dominant process in seawater	Range of sedimentary $d^{15}N$	Environment
Ammonium assimilation	< 0‰	Photic zone anoxia and euxinia with elevated productivity
Dinitrogen fixation	< 0‰	Photic zone anoxia and euxinia
Dinitrogen fixation	0 to +3 ‰	Oxic part of the photic zone
Nitrate assimilation	+3 to +8	Open marine, oxic surface water (‘normal marine production’)
Denitrification	+8 to +12	Within the sediment and in the oxygen-deficient zones (e.g coastal upwelling with OMZ)

Table 11 Average $\delta^{15}N$ values of different substrates.

Material/molecule	Average $d^{15}N$	References
Dissolved N_2	+0.6 ‰	Sigman et al. 1999
Dissolved nitrate	+4.8 ‰	Liu and Kaplan 1989; Sigman et al. 2000
Modern marine sediments	+5.0 ‰	Altabet and Francois 1994
Detrital organic matter in a river	+2.8 ‰	Wada et al. 1987
Soil organic matter	+4.1	Wada et al. 1987
Land plants	-1.8 ‰	Wada et al. 1987

Preservation and alteration of the $\delta^{15}N$ signatures in sediments

Nitrogen concentration and $\delta^{15}N$ values of sedimentary rock may reflect the origin of accumulated organic matter. However, the $\delta^{15}N$ of bulk marine sediment may represent the isotopic composition not ultimately linked to marine organics that escape mineralization and reach the seafloor to become trapped in sediments as kerogen, but it may also be related to isotopic signatures of other components like terrestrial organic matter and inorganic nitrogen (mainly NH_4^+). The analyses of $\delta^{15}N$ in extracted specific biomarkers (chlorophyll and chlorophyll degradation products) or from nitrogen-bearing fossil remains are valuable proxies to estimate the sample quality and to assess imprint derived from diagenesis (Struck et al. 1998). Bulk sedimentary nitrogen isotope ratios may be altered during burial and early sedimentary diagenesis, particularly outside of continental margin settings (Robinson et al. 2012). The majority of existing studies to date suggest that the $\delta^{15}N$ of sedimentary organic matter increases during alteration. Additionally, the degree of isotopic alteration appears to be a function of water depth, sedimentation rate, and oxygen exposure time of the sediment (Robinson et al. 2012). Bulk $\delta^{15}N$ values from sediments deposited under anoxic conditions that additionally promote organic matter preservation tend to obscure their original isotopic signal (Emeis et al. 1987). Stable nitrogen isotope analyses of bulk nitrogen and chlorine (degradation products of chlorophyll) in Pleistocene and Holocene sapropels from the Eastern Mediterranean Sea (that was during those times an oligotrophic, stratified basin with deep-water anoxia) showed that the sedimentary $\delta^{15}N$ value reflects the isotopic composition of the nitrogen used by biomass without significant alteration (Sachs and Repeta 1999; Higgins et al. 2010). Positive offsets were reported from sediments deposited under oxygenated conditions and in low-sedimentation regimes (Altabet and Deuser 1985; Freudenthal et al. 2001; Struck et al. 2001; Gaye-Haake et al. 2005).

The heterotrophic degradation of organic matter leads, however, to only small nitrogen isotope fractionation effects (less than 1 ‰) on total nitrogen (Robinson et al. 2012). These slightly increased $\delta^{15}N$ values in oxic environments in low sedimentation regimes compared to environments of sinking organic matter (lower $\delta^{15}N$) might be also attributed to the preferential loss of low $\delta^{15}N$ NH_4^+ into pore waters during deamination within the sediment. Other early diagenetic reactions in oxic or anoxic settings lead to larger, though still small, nitrogen isotopic variations (on the order of 2-3 ‰) (Robinson et al. 2012). During burial diagenesis and thermal maturation of organic matter the $\delta^{15}N$ of organic nitrogen remains largely unaffected (Ader et al. 2006). During diagenesis, labile organic matter is produced and may be transformed to inorganic nitrogen in the form of ammonium. Ammonium could be mobilized in anoxic pore fluids and can be adsorbed onto the interlayers of clay minerals, as it substitutes for K^+ in the interlayer exchange sites of illite (Müller 1977; Schubert and Calvert 2001). Ammonium may dominate sedimentary nitrogen contents and can be significant in areas of high clay input relative to organic matter sedimentation (Scheffer and Schachtschabel 1970; Müller 1977; Scholten 1991; Schubert and Calvert 2001; Kienast et al. 2005). In organic-poor sediments, inorganic N can make up 94 % of the total N (Schubert and Calvert 2001). Clay-bound $\delta^{15}N$ values from modern ocean sediments are around +3 ± 1.2 ‰ (Schubert and Calvert 2001). In contrast to organic matter, high-temperature metamorphism of ammoniated phyllosilicates may cause an increase of $\delta^{15}N$

values by about 1-2 ‰ for greenschist facies, 3-4 ‰ for amphibolite facies, and up to 6-12 ‰ for upper-amphibolite facies temperatures (Bebout and Fogel 1992; Boyd and Philippot 1998).

The marine nitrogen cycle during the P-Tr transition

Nitrogen isotope studies across the Permian-Triassic boundary have been performed several times. These previous studies reported a negative shift across the extinction horizon (Saitoh et al. 2014, figs. 1B, C and 8). This $\delta^{15}N$ shift is well correlated on a global scale and is interpreted to record enhanced nitrogen fixation in the oceans in the aftermath of the extinction (Luo et al. 2011; Knies et al. 2013). Cao et al. (2009) reported a progressive shift of $\delta^{15}N$ values of organic nitrogen from positive values around +2 or +3 ‰ during the Changhsingian to −1 ‰ at the top of Bed 24 (= extinction horizon) in the Meishan section. Those negative $\delta^{15}N_{org}$ values were thought to reflect ecological disturbance and a nitrogen cycle with reduced involvement of oxidized species (nitrate and nitrite) and increased nitrogen fixation (Altabet and François 1994). These 'light' nitrogen isotopic data have been hypothesised to signal significantly enhanced cyanobacterial N-fixation (Dumitrescu and Brassell 2006; Ohkouchi et al. 2006). Luo et al. (2011) reported an abrupt negative shift in $\delta^{15}N$ from ~ +3 ‰ to ~ 0 ‰ that occurred immediately after the latest Permian mass extinction (LPE) in the Taiping and Zuodeng sections (Nanpanjiang Basin, south China). An abrupt negative shift in $\delta^{15}N$, from +3 ‰ to < +1 ‰, occured at the transition from skeletal limestone to microbialite. The N isotopic composition of the microbialite (−1 ‰ to +1 ‰) reported by Luo et al. (2011) was similar to that of atmospheric N_2 (0 ‰), consistent with the limited fractionation associated with diazotrophic (N fixing) marine cyanobacteria (Carpenter et al. 1997). The persistently low values of $\delta^{15}N$ measured in the microbialite interval led Luo et al. (2011) to suggest that, following the LPE, microbial nitrogen fixation became the main source of biologically available nitrogen in the Nanpanjiang Basin. Strong nitrogen fixation in the Late Permian Nanpanjiang Basin implied a deficit of bioavailable N in contemporaneous seawater, being the result of enhanced loss of nitrate under oxygen-poor conditions (Luo et al. 2011).

A negative N isotope excursion (to −2 ‰) was reported immediately above the latest Permian extinction horizon at Guryul Ravine (northern India) by Algeo et al. (2007), suggesting that N fixation may have been prevalent throughout the Tethyan Ocean region. Finally, $\delta^{15}N$ values from West Blind Fiord on Ellesmere Island (Canadian Arctic) shift between the Arctic Extinction Event (AEE) and the latest Permian mass extinction (LPME) toward more ^{15}N-enriched compositions consistent with enhanced denitrification under suboxic conditions (Algeo et al. 2012). At Chaotian in northern Sichuan (South China), Saitoh et al. (2014) performed bulk-rock $\delta^{15}N$ analysis on limestones, mudstones and dolostones; the $\delta^{15}N_{TN}$ values are positive and around +1 to +2 ‰ in the upper Wujiaping Formation, implying denitrification and/or anammox in the ocean. $\delta^{15}N_{TN}$ values gradually decrease from -2 ‰ to -1 ‰ in the lower Dalong Formation and are consistently low (around 0 ‰) in the middle Dalong to lowermost Feixianguan Formation, suggesting enhanced nitrogen fixation in the ocean during the Changhsingian at Chaotian. Saitoh et al. (2014) concluded that $\delta^{15}N_{TN}$ values are rather constant and no clear stratigraphic change is recognized around the extinction horizon at Chaotian, although $\delta^{15}N_{TN}$

values of some gray marl and muddy carbonates are probably influenced by addition of nitrogen from clay minerals. They suggested that the oceanic nitrogen cycle was not disturbed significantly during the extinction event.

8 ISOTOPE RESULTS

8.1 Carbonate carbon isotope results

Carbon and oxygen isotope values for carbonate-bearing rocks from the various study sections of Iran yielded the following ranges (Appendix; Tables A.1-A.5):

Ali Bashi 1 and Ali Bashi 4: -2.8 to +4.1 ‰ and -4.4 to +1.8 ‰ for $\delta^{13}C$ (VPDB) and -8.1 to -4.0 ‰ and -7.0 to -5.5 ‰ for $\delta^{18}O$ (VPDB).

Aras Valley and Zal sections: -1.1 to +4.3 ‰ and -0.9 to +3.7 ‰ for $\delta^{13}C$ (VPDB), and -6.5 to -3.0 ‰ and -9.3 to -3.0 ‰ for $\delta^{18}O$ (VPDB).

Baghuk Mountain sections: -2.6 to +4.8 ‰ for $\delta^{13}C$ (VPDB), and -9.6 to -0.4 ‰ for $\delta^{18}O$ (VPDB).

The $\delta^{13}C_{carb}$ data are presented according to the conodont zonation scheme of Ghaderi et al. (2014), Kozur (2007), and Farshid et al. (2016). The Aras Valley section, which was studied with the highest sample density, serves as the key section for defining the high-resolution chemostratigraphic scheme presented here (Fig. 54). The $\delta^{13}C_{carb}$ values oscillate between +3.0 ‰ and +4.0 ‰ in the *Clarkina orientalis–C. subcarinata*, *C. subcarinata*, and *C. changxingensis* Zones. Within the *C. bachmanni* Zone the values are about +3 ‰. A gradual and continuous decrease of the $\delta^{13}C_{carb}$ values starts in the *C. yini* Zone. The $\delta^{13}C_{carb}$ values reach a value of +1.2 ‰ at the top of the *C. hauschkei* Zone (at the extinction horizon). Post-extinction $\delta^{13}C_{carb}$ values remain lower relative to the pre-extinction values and are between -1 ‰ and 0 ‰ in the *H. praeparvus - H. changxingensis and M. ultima–S? mostleri* Zones. A minimum (-1.1 ‰) of the "first-order" $\delta^{13}C_{carb}$ trend occurs before the stratigraphic height of the FAD of *H. parvus* in the *M. ultima–S? mostleri* Zone. Post-PTB $\delta^{13}C_{carb}$ values are around 0 ‰. The "first-order" $\delta^{13}C_{carb}$ isotope record of the Aras Valley section does not show any significant sudden variation; the trend is continuous and shows a progressive decrease across the P-Tr boundary. For the entire section fluctuations of 5.3 ‰ for the $\delta^{13}C_{carb}$ are recorded. The "first-order" $\delta^{13}C_{carb}$ isotope excursion at the Permian-Triassic boundary interval has been separated into three distinct parts. The first part of the negative excursion between the base of the *C. bachmanni* Zone (or in case for the Aras Valley section the base of the *C. yini* Zone) and the top of the extinction horizon is here called the pre-extinction event decrease. The interval between the extinction horizon and the P-Tr boundary is here called the post-extinction interval. The post-PTB interval is the interval between the *H. parvus* and *I. isarcica* Zone.

Correlation with other Iranian sections

Ali Bashi 1 section – The carbon isotope curve for the Ali Bashi 1 section starts at +3.5 ‰ in the late *C. orientalis* Zone, and increases to +4.1 ‰ in the *C. subcarinata* Zone. It varies between +2.6 ‰ and +3.5 ‰ in the *C. changxingensis* Zone (Fig. 55). In comparison to the Aras

Valley section, a gradual and continuous decrease of the $\delta^{13}C_{carb}$ values starts already in the *C. bachmanni* Zone. In contrast to the Aras Valley section, this general negative trend is strongly enhanced in the *C. yini*, *C. abadensis* and *C. hauschkei* zones, where the $\delta^{13}C_{carb}$ value decreases to +0.6 ‰ at the top of the *C. hauschkei* Zone. An inflection to even lower bulk rock values marks the transition towards the Aras Member (with a $\delta^{13}C_{carb}$ value of -0.9 ‰ at the base of the *Hindeodus praeparvus–H. changxingensis* Zone) and culminates with the lowest value (-2.8 ‰) at the Permian-Triassic boundary (base of the *H. parvus* Zone). Post-PTB $\delta^{13}C_{carb}$ values remain, similarly to the Aras Valley section, lower relative to pre-extinction values, and are between 0 ‰ and -1 ‰ in the *H. lobota* and *I. staeschei* zones. One additional "second-order" negative $\delta^{13}C_{carb}$ excursion (-1.4 ‰) occurs in the *I. staeschei* Zone. Additionally, the Ali Bashi 1 section is marked by two other "second-order" minima of -1.4 ‰ and -0.7 ‰ at -1.70 m and -0.71 m below the extinction horizon, respectively. There is a weak "second-order" positive $\delta^{13}C_{carb}$ excursion of +0.4 ‰ in the *M. ultima–S.? mostleri* Zone, whereas in the Aras Valley section the lowest $\delta^{13}C_{carb}$ value of the "first-order" trend has been recorded. For the entire Ali Bashi 1 section fluctuations of 6.9 ‰ for the $\delta^{13}C_{carb}$ are recorded.

Ali Bashi 4 section – The pre-extinction values oscillate between 0 and +2 ‰. In the *M. ultima–S? mostleri* Zone $\delta^{13}C_{carb}$ values oscillate between -2.0 ‰ and 0 ‰ (Fig. 56). The lowest $\delta^{13}C_{carb}$ value of -4.4 ‰ occurs in the *H. parvus* Zone. For the entire section fluctuations of 6.2 ‰ are recorded for the $\delta^{13}C_{carb}$.

Zal section – Similar to the Aras Valley section, the $\delta^{13}C_{carb}$ values oscillate between +3.0 ‰ and +4.0 ‰ in the *Clarkina orientalis–C. subcarinata*, *C. subcarinata*, and *C. changxingensis* zones (Fig. 57). A gradual and continuous decrease of the $\delta^{13}C_{carb}$ values starts, in contrast to the Aras Valley section, already in the *C. bachmanni* Zone. The lowest $\delta^{13}C_{carb}$ value (-0.9 ‰) occurs within the *H. parvus* Zone. Similarly to the Aras Valley section, there is no inflection to lower $\delta^{13}C_{carb}$ values at the transition to the Aras Member; the $\delta^{13}C_{carb}$ value fluctuates here around +1.5 ‰. Post-PTB $\delta^{13}C_{carb}$ values are positive, around +1 ‰. For the entire section fluctuations of 4.8 ‰ are recorded for the $\delta^{13}C_{carb}$.

Baghuk Mountain sections 1, A, and C – The $\delta^{13}C_{carb}$ values oscillate between +3 and +5 ‰ up to the *C. changxingensis* Zones (Fig. 58). In comparison to the Aras Valley section, a gradual and continuous decrease of the $\delta^{13}C_{carb}$ values starts in the *C. bachmanni* Zone. In comparison to the Aras Valley section the bulk-rock $\delta^{13}C$ minimum (-1.4 ‰) is observed higher in the profile (in the *H. lobota*? Zone). There is a post-PTB shift of $\delta^{13}C_{carb}$ to more positive values, but the values remain lower relative to the pre-extinction values and oscillate between -2.5 ‰ and +1 ‰. For the entire section fluctuations of 6.5 ‰ are recorded for the $\delta^{13}C_{carb}$.

The total organic carbon (TOC) obtained from the *Paratirolites* Limestone unit ranges from 0.01 to 0.02 %, with organic carbon $\delta^{13}C$ values of –25.4 to –23.2 ‰ (VPDB).

Comparison of variations in $\delta^{13}C_{carb}$ between sections

The $\delta^{13}C_{carb}$ isotope record of most of the sections does not show any sudden, strong variation;

the trend is continuous and shows a progressive decrease across the P-Tr boundary (Fig. 59). The $\delta^{13}C_{carb}$ values in the interval between the Wuchiapingian-Changhsingian boundary and the base of the *C. bachmanni* Zone fluctuate in most of the sections between 3 and 4 ‰. This is a value that is typical of the Late Permian strata in Iran (Korte et al. 2005). We observe a general decline in $\delta^{13}C_{carb}$ upsection in most of the sections (Ali Bashi 1, Zal, Abadeh and Baghuk Mountain) starting within the *C. bachmanni* Zone, about 1 Ma prior to the extinction horizon. In comparison, Korte and Kozur (2010) concluded that the negative shift started 0.45–0.50 Ma before the end-Permian crisis. Only in the Aras Valley section, the $\delta^{13}C$ decline begins earlier, in the *C. yini* Zone, about 0.7 Ma prior to the extinction horizon. The decrease recorded for the pre-extinction event period is characterized by very few second-order variations (Fig. 59). The decrease of the $\delta^{13}C_{carb}$ values is more pronounced in the uppermost part of the *Paratirolites* Limestone at Ali Bashi 1, where the $\delta^{13}C_{carb}$ value decreases from +3 ‰ within the *C. yini* Zone to +0.6 ‰ at the top of the *C. hauschkei* Zone (over a 2 m thick interval). The post-extinction interval is marked by enhanced heterogeneity in stratigraphic whole-rock $\delta^{13}C$ patterns between the different sites due to small-scale secondary $\delta^{13}C_{carb}$ fluctuations. There is a positive ”second-order” $\delta^{13}C_{carb}$ excursion in the Ali Bashi 1 section, whereas in the Zal section a gradual depletion or even a stagnation (or plateau) is recorded. The post-PTB horizon (between the *H. parvus* and *I. isarcica*) is marked by a shift back toward heavier $\delta^{13}C_{carb}$ values that are, however, lower relative to the pre-extinction values. There is one additional “second-order” negative $\delta^{13}C_{carb}$ excursion in the *I. staeschei* Zone at Ali Bashi 1.

Stratigraphic median $\delta^{13}C_{carb}$

For this method the studied sections (also using unpublished data of M. Schobben from the Abadeh section in Central Iran) are subdivided into conodont-based stratigraphic intervals (*C. orientalis*, *C. subcarinata*, *C. changxingensis*, *C. yini* (including also *C. bachmanni* and *C. nodosa* Zones), *C. abadehensis*, *C. hauschkei*, *H. praeparvus* (including *Hindeodus praeparvus–H. changxingensis* and *Merrilina ultima–Stepanovites* ?*mostleri* Zones), *H. parvus*, *I. isarcica* (including *H. lobota*, *I. staeschei* and *I. isarcica* Zone). The median is taken from the available $\delta^{13}C_{carb}$ data for each interval and is subsequently taken as a representative value for the selected interval. Each interval includes the $\delta^{13}C_{carb}$ data from all sections combined together. I used the median $\delta^{13}C_{carb}$ value instead of the statistical mean value, because the median is less affected by outliers and skewed data. The stratigraphic median $\delta^{13}C_{carb}$ value is presented here using a Box-and-Whisker plot (Figs. 60, 61). It shows that after statistical treatment the ”first-order” negative $\delta^{13}C_{carb}$ trend is confirmed. The median $\delta^{13}C_{carb}$ value decreases from about +4 ‰ in the *C. subcarinata* interval (in which the maximum $\delta^{13}C_{carb}$ value is reported) across the P-Tr boundary to about 0.8 ‰ in the *H. parvus* interval and then increases again to more positive values in the *C. isarcica* interval. The largest scatter of the $\delta^{13}C_{carb}$ value occurs in the *H. praeparvus* interval (i.e., between the extinction horizon and the P-Tr boundary, where the median value is close to 0 ‰). This interval corresponds to the lithological interval of the Aras Member (=‘Boundary Clay’), for which a diagenetic impact on the $\delta^{13}C_{carb}$ values will be discussed in the Discussion chapter.

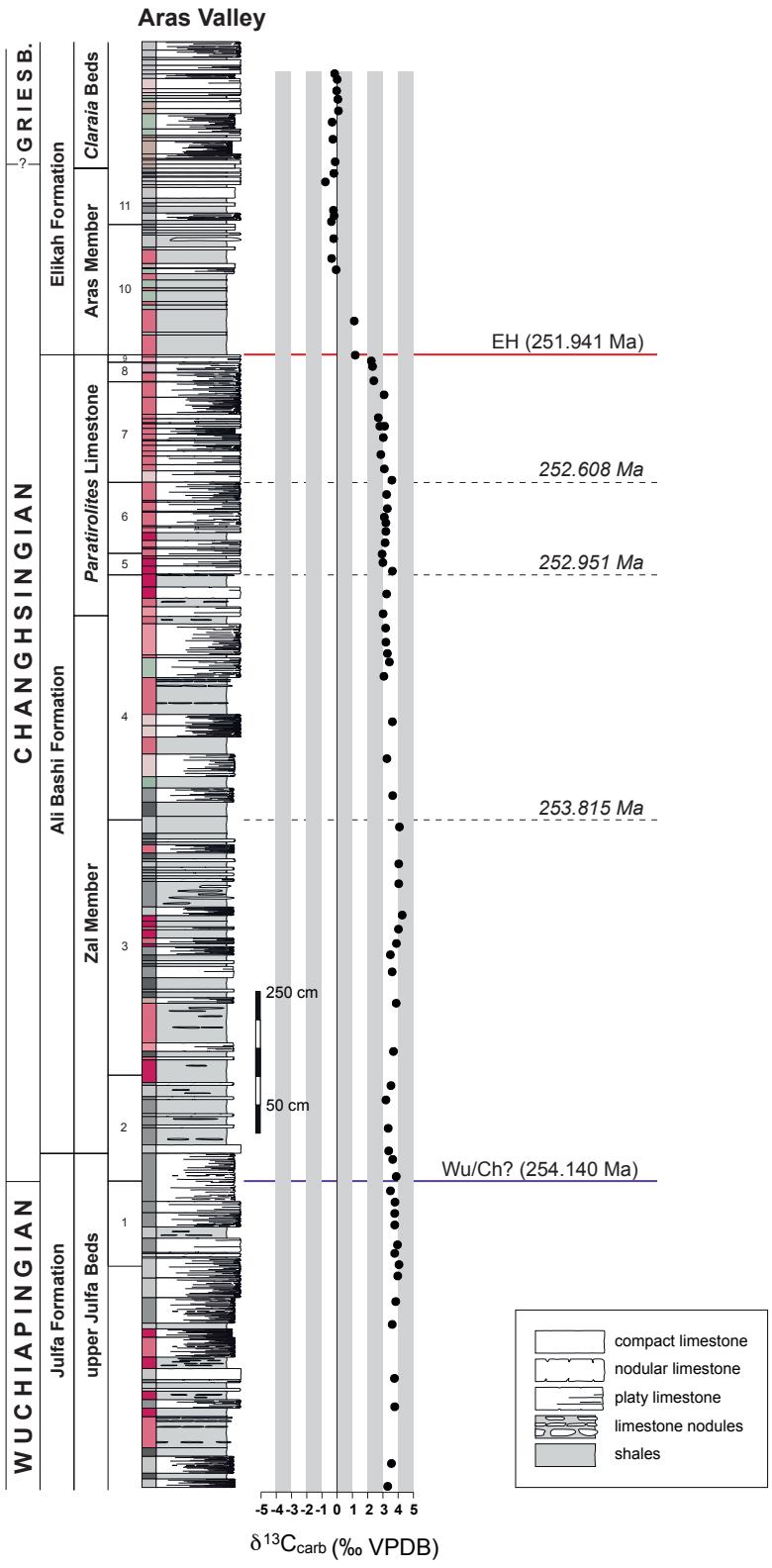

Figure 54 Lithology and bulk carbonate carbon isotope values of the P-Tr boundary sections at Aras Valley (20 m below, 5 m above the extinction horizon). Conodont zones are numbered according to conodont zonation after Ghaderi et al. (2014) in the Fig. 34.

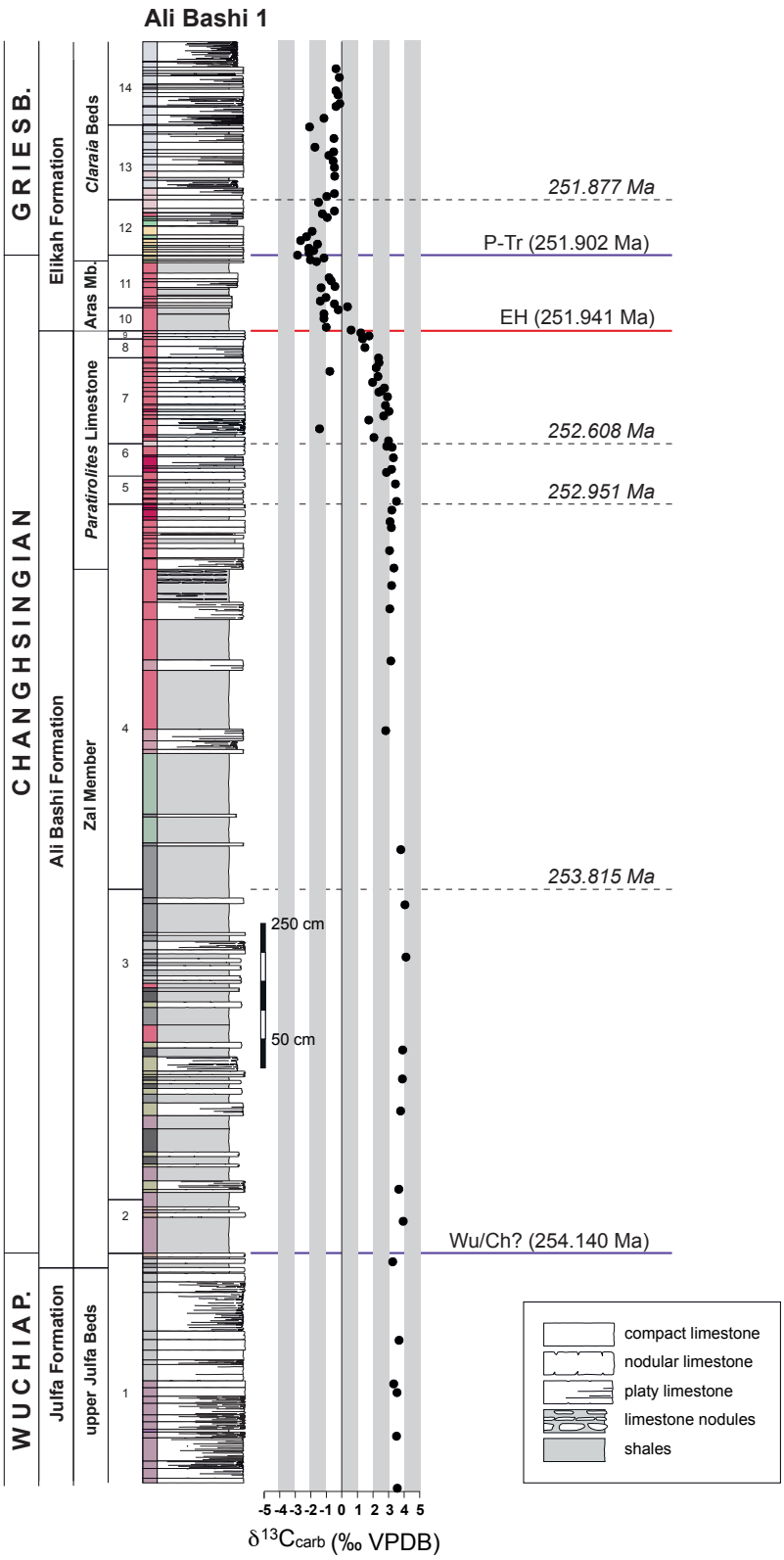

Figure 55 Lithology and bulk carbonate carbon isotope values of the P-Tr boundary sections at Ali Bashi 1 (20 m below, 5 m above the extinction horizon). Conodont zones are numbered according to conodont zonation after Ghaderi et al. (2014) in the Fig. 34.

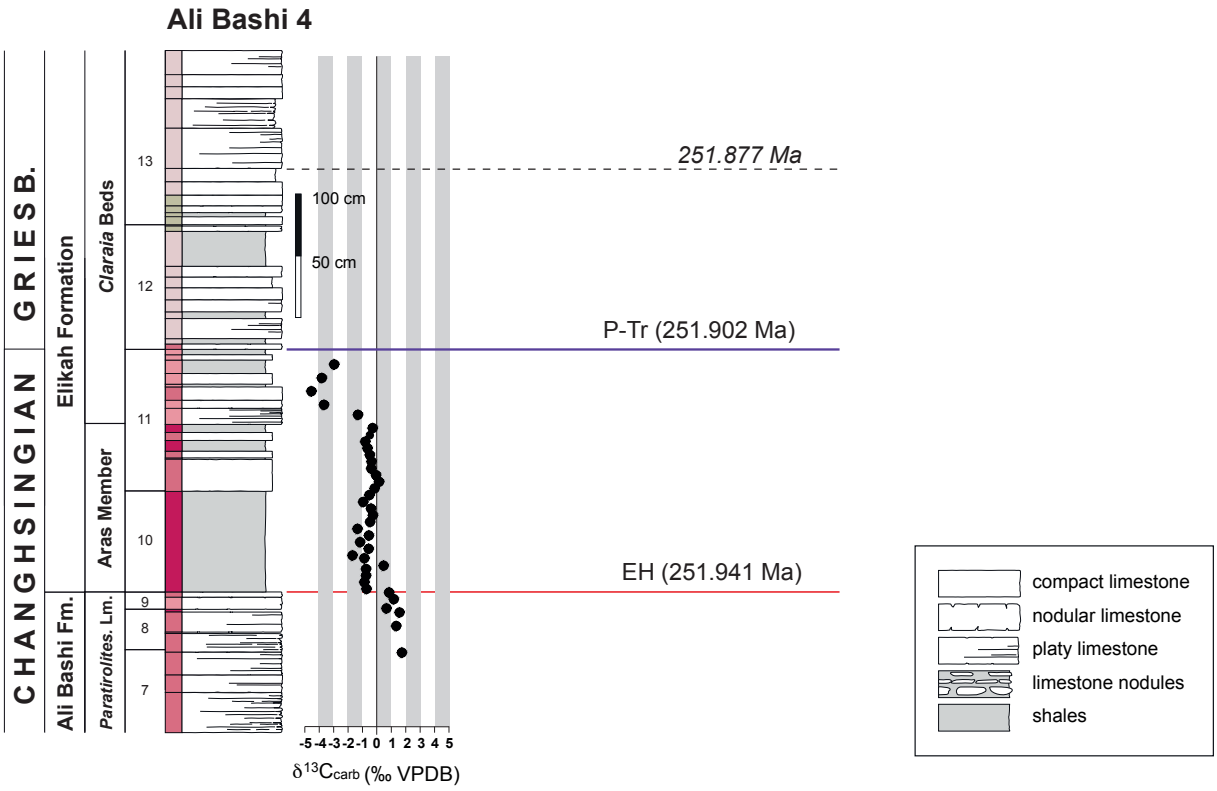

Figure 56 Lithology and bulk carbonate carbon isotope values of the P-Tr boundary sections at Ali Bashi 4 (20 m below, 5 m above the extinction horizon). Conodont zones are numbered according to conodont zonation after Ghaderi et al. (2014) in the Fig. 34.

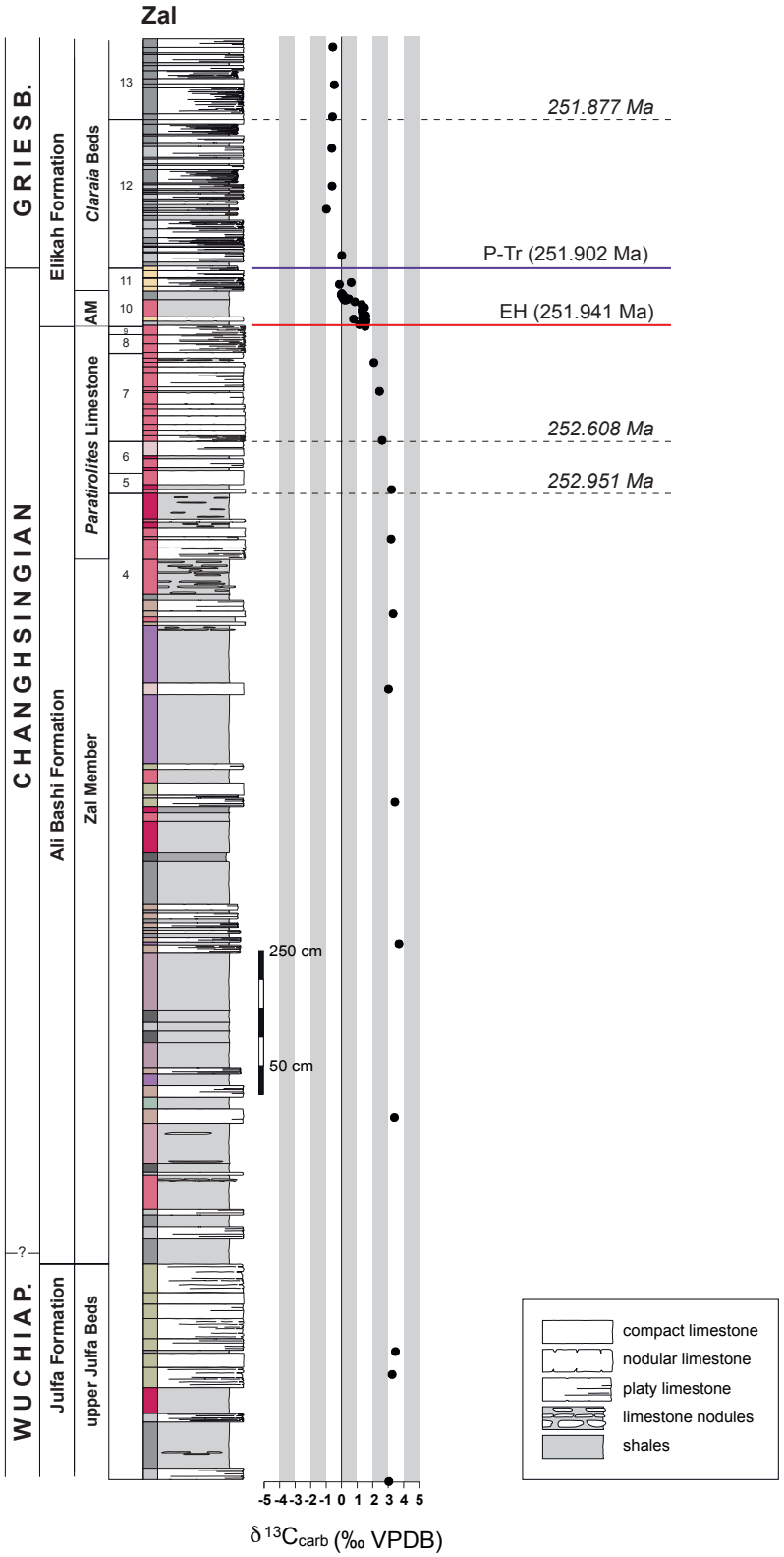

Figure 57 Lithology and bulk carbonate carbon isotope values of the P-Tr boundary sections at Zal (20 m below, 5 m above the extinction horizon). Conodont zones are numbered according to conodont zonation after Ghaderi et al. (2014) in the Fig. 34.

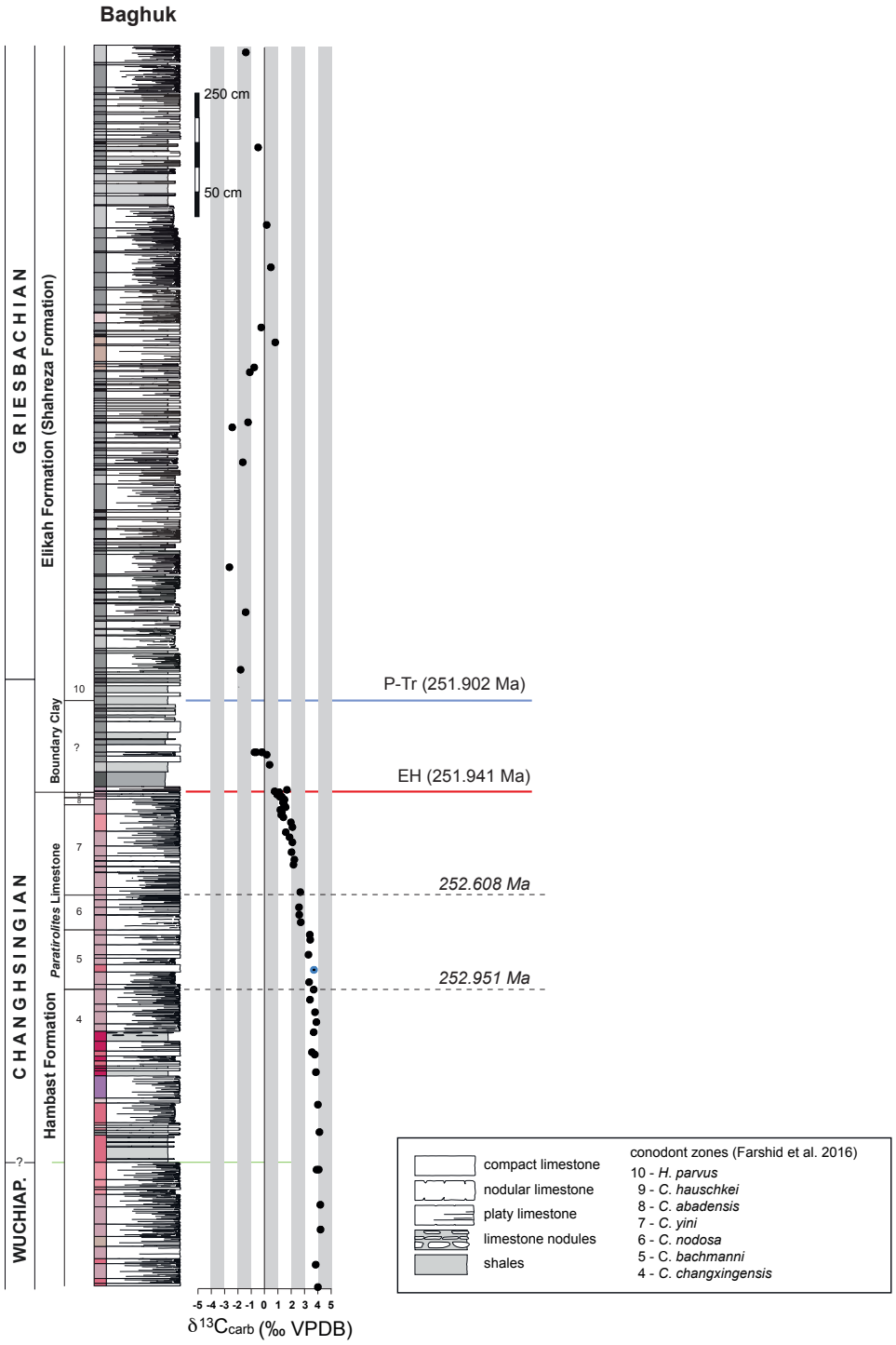

Figure 58 Lithology and bulk carbonate carbon isotope values of the P-Tr boundary sections in the Baghuk Mountain, composed of section 1 (10 m below the extinction horizon) and section C (15 m above the extinction horizon). Conodont zones are numbered according to conodont zonation after Ghaderi et al. (2014) in Fig. 34.

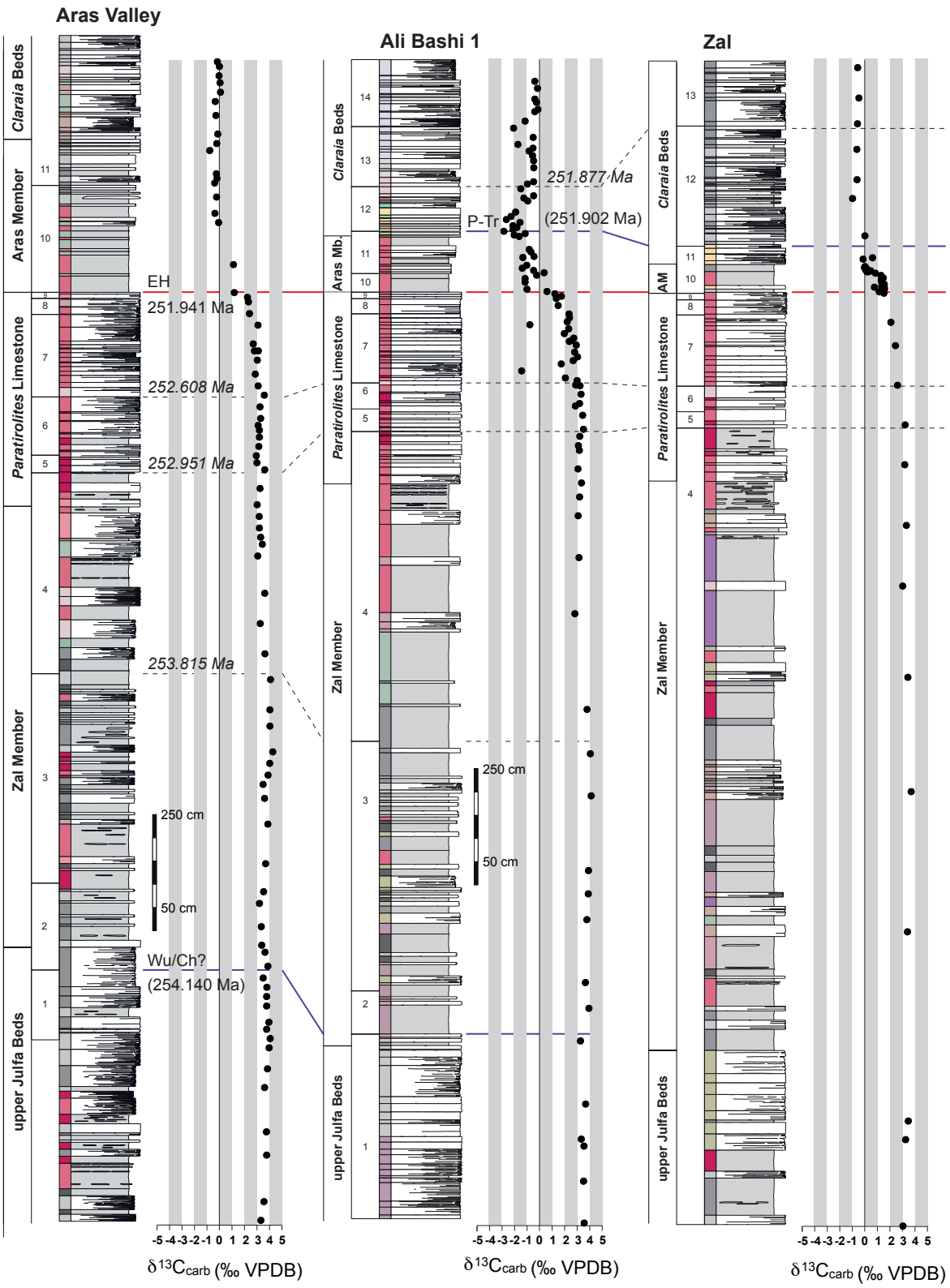

Figure 59 Lithology and bulk carbonate carbon isotope values of the P-Tr boundary sections at Aras Valley, Ali Bashi 1, and Zal (5 m below, 5 m above the extinction horizon). Conodont zones are numbered according to conodont zonation after Ghaderi et al. (2014) in the Fig. 34.

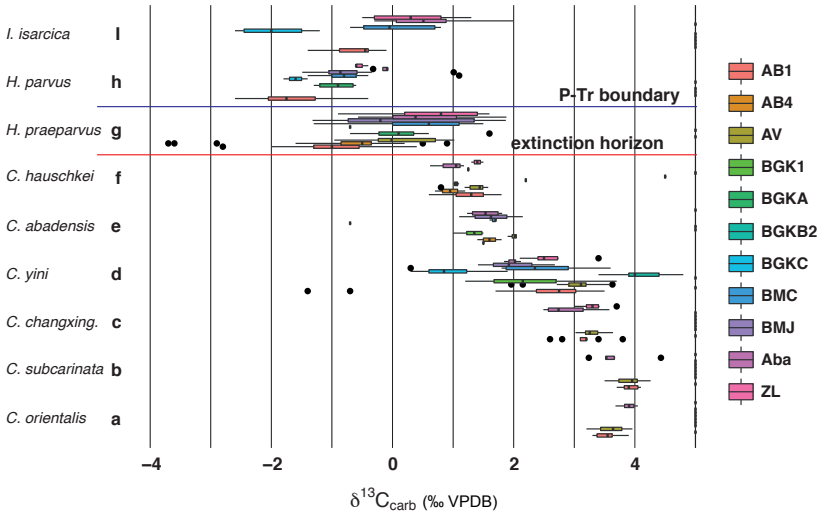

Figure 60 Box-and-Whiskers diagram of bulk carbonate carbon isotope values of the P-Tr boundary sections from NW and Central Iran subdivided into conodont-based stratigraphic intervals. AB1 (Ali Bashi 1), AB4 (Ali Bashi 4), AV (Aras Valley), BGK1 (Baghuk Mountain 1), BGKA (Baghuk Mountain A), BGKB2 (Baghuk Mountain B2), BMC (Baghuk Mountain C), BMJ (Baghuk Mountain J), Aba (Abadeh), ZL (Zal).

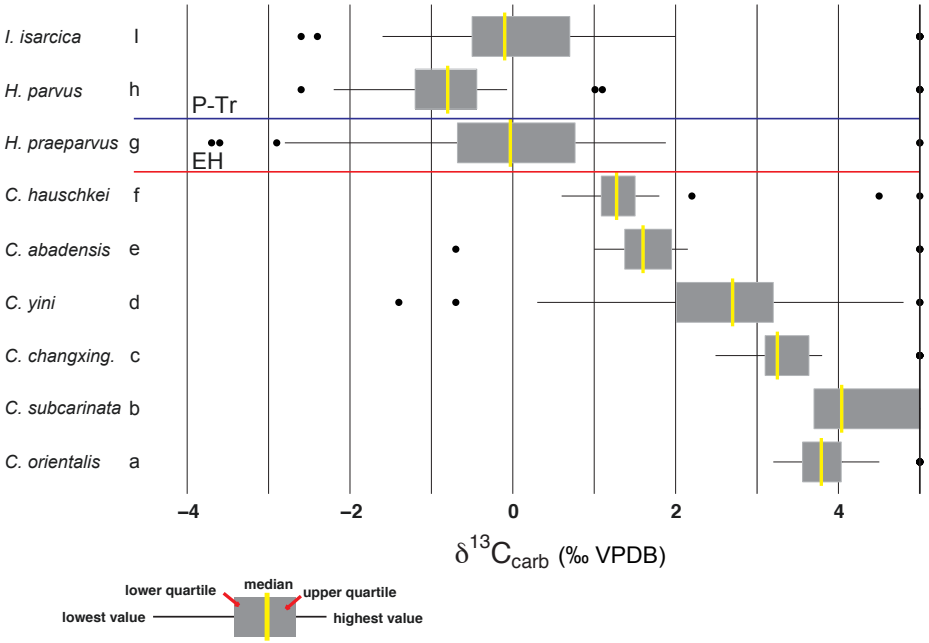

Figure 61 Stratigraphic median $\delta^{13}C_{carb}$ values of the P-Tr boundary sections from NW and Central Iran subdivided into conodont-based stratigraphic intervals.

8.2 Nitrogen isotope data for bulk samples

Bulk sediment nitrogen isotope values ($\delta^{15}N_{bulk}$), carbon isotope values for decalcified samples ($\delta^{13}C_{TOC}$), as well as total nitrogen (TN), total organic carbon (TOC) and TOC/TN atomic ratios were measured for the Ali Bashi 1 and Zal section (NW Iran) (Tables A.6 to A.9 (Appendix). Figures 62, 63, and 64 show chemostratigraphic profiles of $\delta^{15}N_{bulk}$ and $\delta^{13}C_{TOC}$ values, TOC and TN contents and TOC/TN atomic ratios for the analyzed P-Tr interval in NW Iran. Figures 65 and 66 show geochemical cross-plots for the analyzed samples. Nitrogen isotope values of bulk-carbonate rocks from the Ali Bashi 1 (69 samples) and Zal (22 samples) sections are -0.4 to +4.4 ‰ and +1.5 to +4.5 ‰ for $\delta^{15}N_{bulk}$ (AIR). $\delta^{15}N_{bulk}$ data are presented in relation to the conodont zonation of Ghaderi et al. (2014), Kozur (2007), and unpublished data from Ghaderi and Hairapetian (pers. commun.).

At Ali Bashi 1 the $\delta^{15}N_{bulk}$ values do not show any trend below the extinction horizon; the values are heterogenous and fluctuate between -0.4 ‰ and +4 ‰ (Fig. 62). There are significant changes of the $\delta^{15}N_{bulk}$ values between consecutive single beds; for example, at -0.65 m the $\delta^{15}N_{bulk}$ value is +4 ‰ and at -0.56 m the $\delta^{15}N_{bulk}$ value decreases to -0.2 ‰. Only directly below the EH, at -0.05 m and at -0.10 m, the $\delta^{15}N_{bulk}$ values are low (1.8 and 0.5 ‰, respectively). Within the lowermost 0.75 m of the Aras Member (in the *M. ultima* - *S.* ?*mostleri* and in the lowermost part of the *H. praeparvus* - *H. changxingensis* zones) the $\delta^{15}N_{bulk}$ values stabilize and oscillate between 3 and 4 ‰. From the middle part of the *H. praeparvus* - *H. changxingensis* Zone up to the top of the investigated sections the $\delta^{15}N_{bulk}$ values do not show any trend and scatter between -0.4 and 3.9 ‰ again. $\delta^{13}C_{TOC}$ values range mostly from -28 to -24 ‰ within the *Paratirolites* Limestone (Fig. 63). Around the extinction horizon (from -0. 05 m to +0.20 m) the $\delta^{13}C_{TOC}$ values are around -26 ‰. Within the Aras Member (in the *M. ultima* - *S.* ?*mostleri* and in the lowermost part of the *H. praeparvus* - *H. changxingensis* Zone) $\delta^{13}C_{TOC}$ values increase to -21 ‰ and then oscillate mostly between -28 and -24 ‰ in the *H. parvus*, *H. lobota* and *I. staeschei* zones, similar to the pre-extinction values.

At Zal, only two $\delta^{15}N_{bulk}$ values were measured before the extinction horizon: +2.4 ‰ at -2.85 m in the *C. chanxingensis* Zone and +3.0 ‰ at -1.15 m in the *C. yini* conodont Zone (Fig. 64). The most positive $\delta^{15}N_{bulk}$ value (+4.5 ‰) was found within the *C. hauschkei* Zone. Within the Aras Member the $\delta^{15}N_{bulk}$ values do not show any trend with data between +1.5 and +4.2 ‰. There are only two $\delta^{15}N_{bulk}$ values for samples from the *Claraia* Beds; +1.6 and +2.3 ‰ within the *H. parvus* Zone.

Evaluation of diagenetic alteration of organic C and N isotopic compositions

In Figures 65 and 66, $\delta^{15}N_{bulk}$, $\delta^{13}C_{TOC}$, $\delta^{13}C_{carb}$, TN, TOC and C/N ratio data are plotted to evaluate a possible diagenetic overprint and the origin (source) of nitrogen species in the sediments. For the Ali Bashi 1 section, C/N ratios of all samples are lower than 6.6, the Redfield value. Within the Aras Member (from +0.05 to 0.35 m) nitrogen is enriched and C/N ratios are exceptionally low (<1) (from +0.28 to 0.75 m). In these samples, their nitrogen enrichment

seems to be uneffected by TOC contents that are below 0.1%. Only at +0.05 m and at +0.20 m TOC contents are higher than in overall samples (0.06 and 0.11 %, respectively). The nitrogen enrichment in these marls and carbonates suggests addition of nitrogen from another source besides for organic matter, because C/N ratios of living marine organisms are generally around the Redfield value. The P-Tr boundary section at Ali Bashi 1 is marked by low values in the molar ratio of C_{org}/N_{tot} (<1), which corresponds to values measured for open ocean settings (e.g., Müller 1977; Waples and Sloan 1980) under low vertical flux of organic matter from the sea surface. Remarkably low C/N molar ratios (<6.6) were mentioned due to addition of nitrogen from clay minerals/micas.

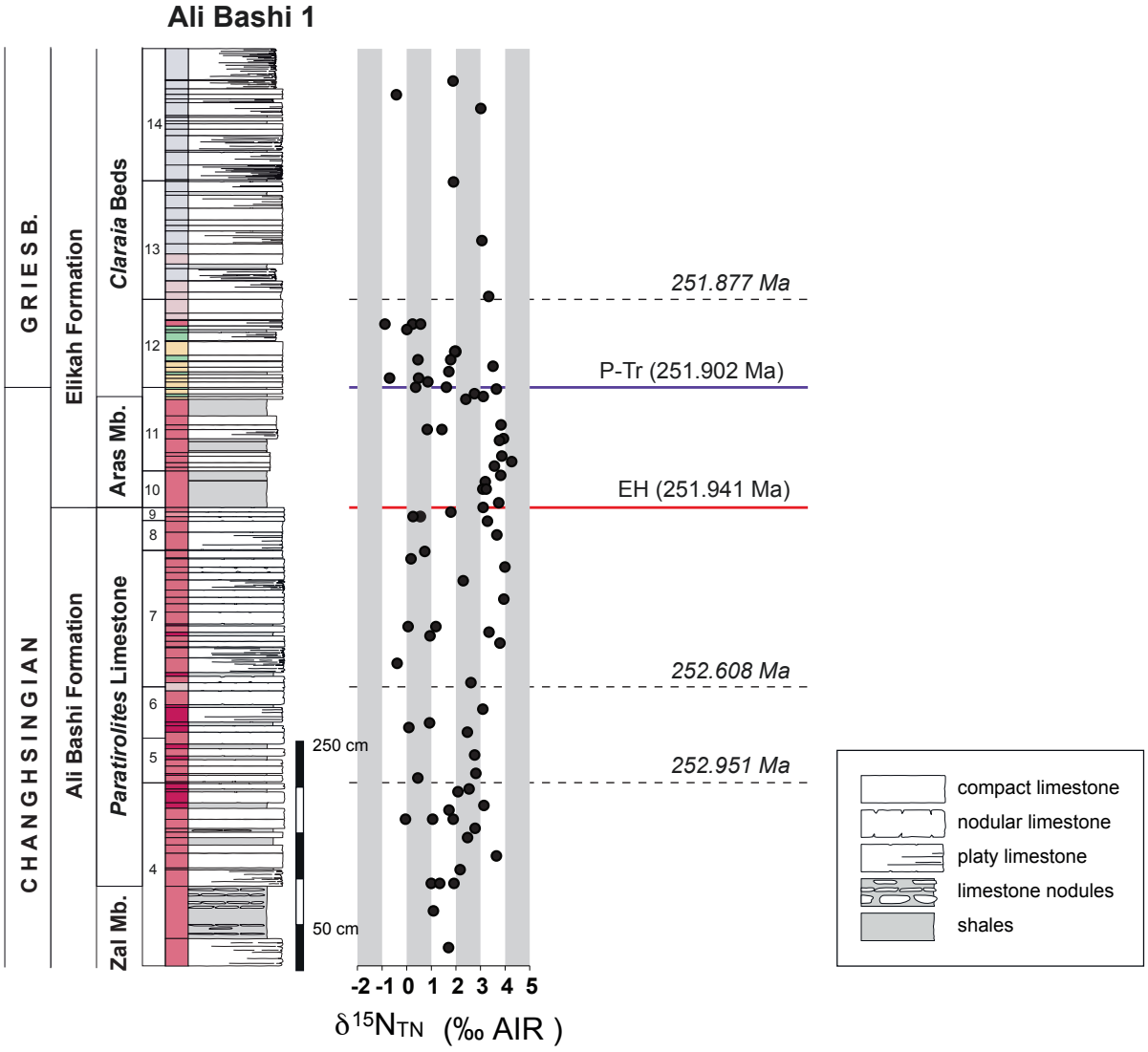

Figure 62 Lithology and bulk nitrogen isotope values of the P-Tr boundary sections at Ali Bashi 1 (20 m below, 5 m above the extinction horizon).

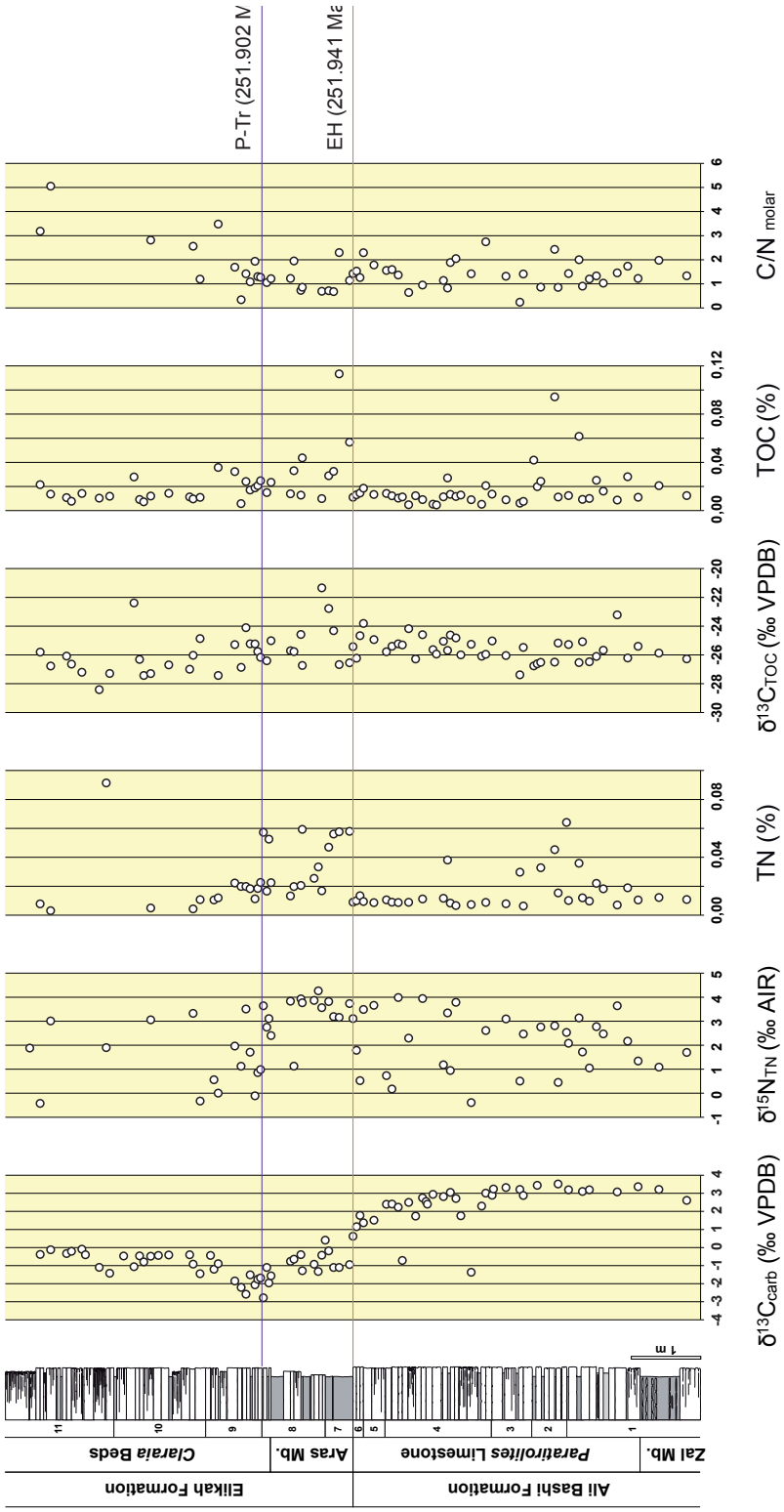

Figure 63. Chemostratigraphy of the P-Tr interval at Ali Bashi 1 section. TN (total nitrogen), TOC (total organic carbon). Conodont zones are numbered as follows: 1 - *C. changxingensis*, 2 - *C. bachmanni*, 3 - *C. nodosa*, 4 - *C. yini*, 5 - *C. abadehensis*, 6 - *C. hauschkei*, 7 - *Hindeodus praeparvus–H. changxingensis*, 8 - *Merrilina ultima–Stepanovites* ?*mostleri*, 9 - *Hindeodus parvus*, 10 - *H. lobota*, 11 - *Isarcica staeschei* zone.

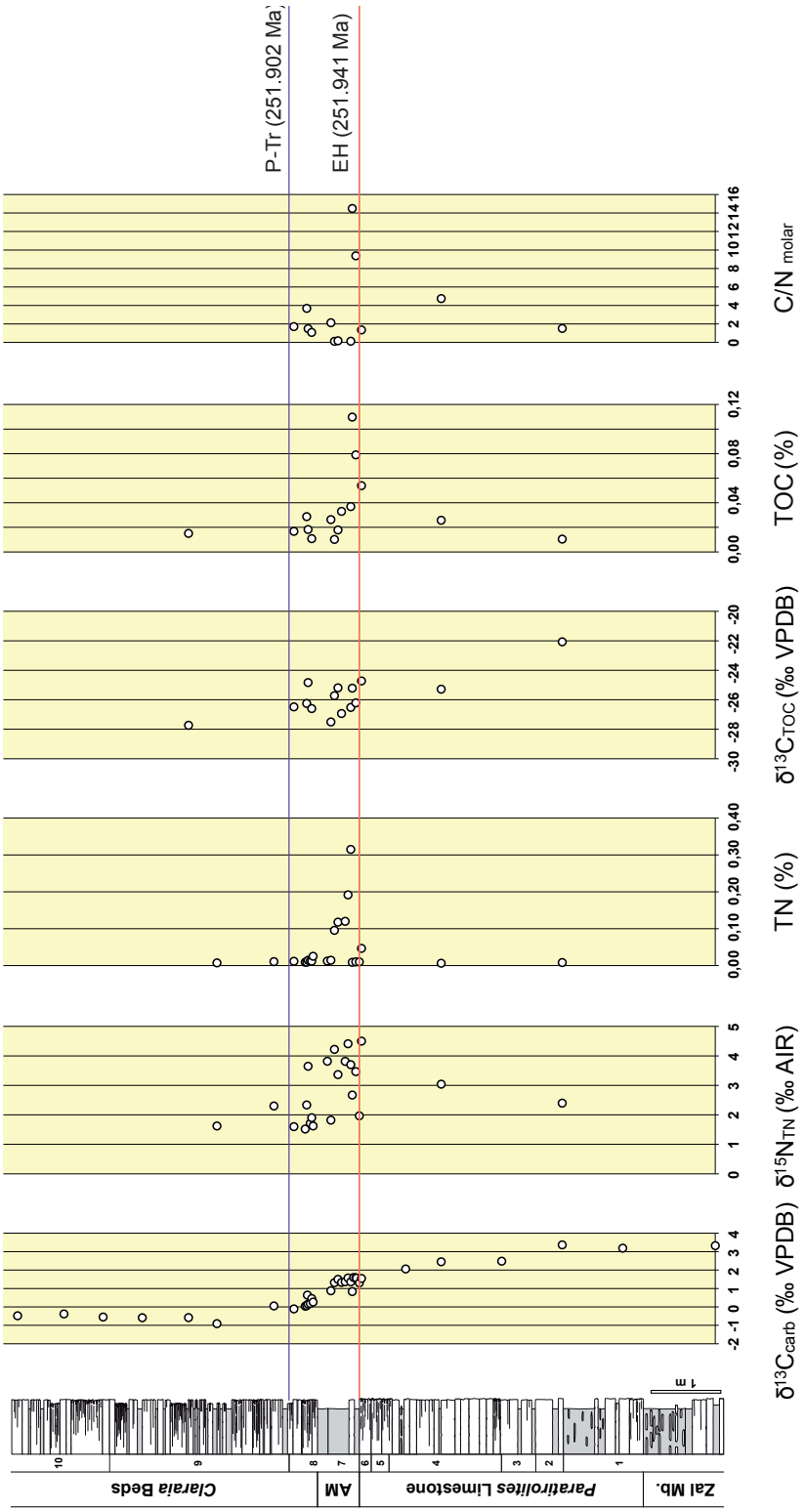

Figure 64. Chemostratigraphy of the P-Tr interval at Zal section. TN (total nitrogen), TOC (total organic carbon). Conodont zones are numbered as follows: 1 - *C. changxingensis*, 2 - *C. bachmanni*, 3 - *C. nodosa*, 4 - *C. yini*, 5 - *C. abadehensis*, 6 - *C. hauschkei*, 7 - *Hindeodus praeparvus–H. changxingensis*, 8 - *Merrilina ultima–Stepanovites* ?*mostleri*, 9 - *Hindeodus parvus*, 10 - *H. lobota* zones.

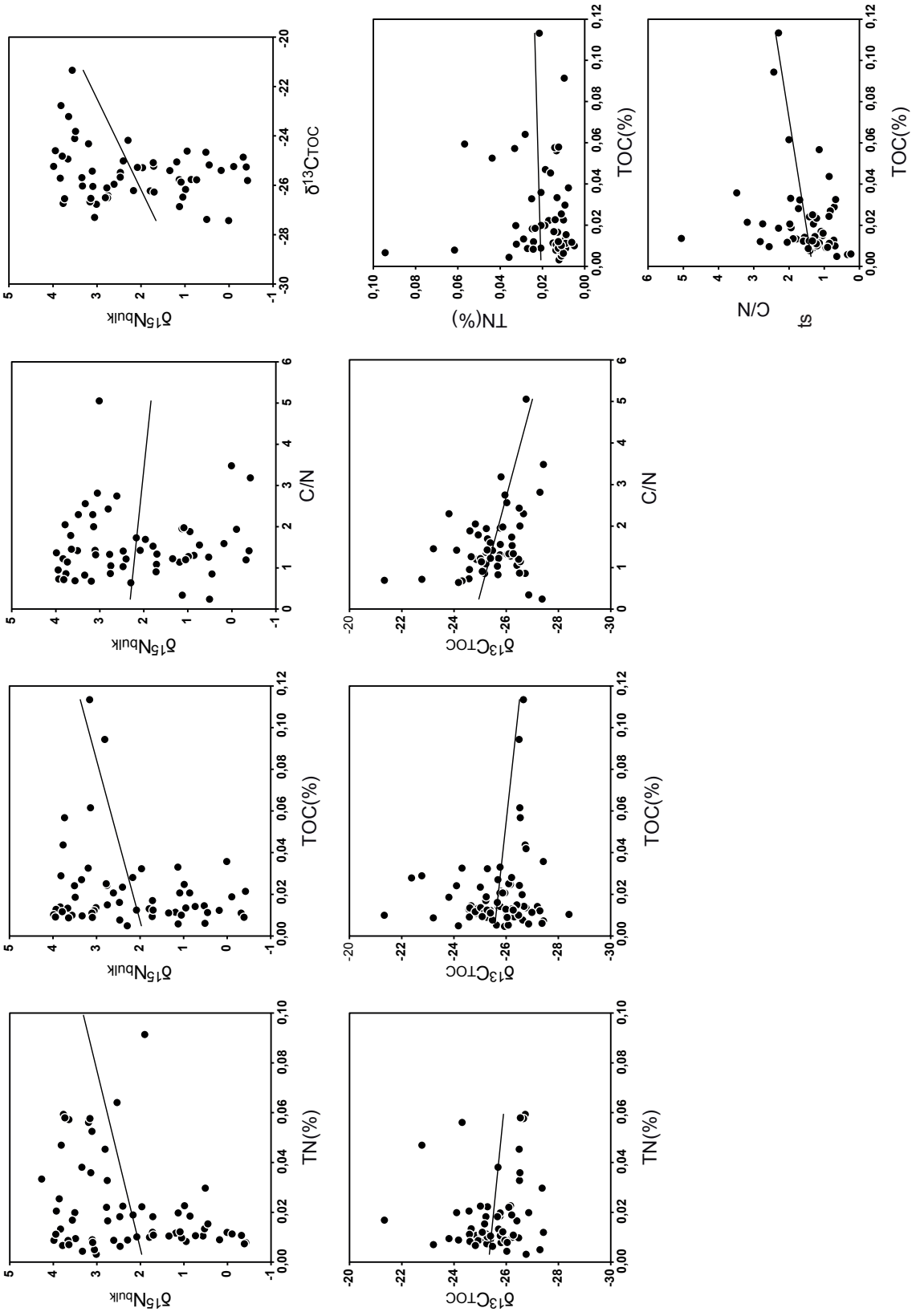

Figure 65. Nitrogen and bulk carbonate carbon isotopic compositions, and their relations to TN and TOC contents at Ali Bashi 1 section.

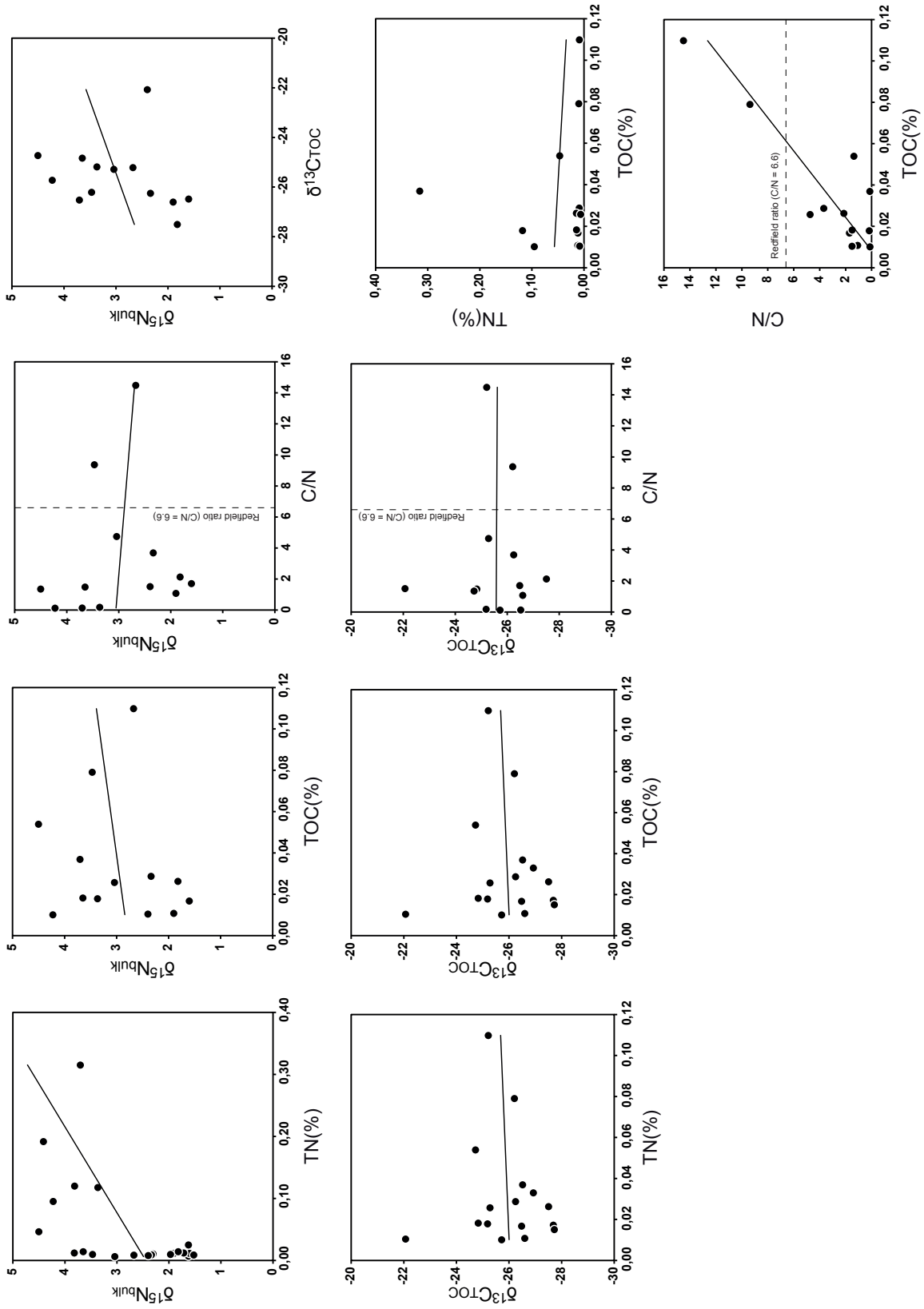

Figure 66. Nitrogen and bulk carbonate carbon isotopic compositions, and their relations to TN and TOC contents at Zal section. Dashed line represents a C/N ratio of 6.6 for original organic matter in sediments (Redfield value).

9 DISCUSSION

9.1 Microfacies correlation of the Julfa region with the Baghuk Mountain

The P-Tr boundary sections at Baghuk Mountain differ slightly in their microfacies characteristics and their lithological changes from the sections in the Julfa region (Figs. 12, 32). The nodular fabric of the *Paratirolites* Limestone is well-developed in the sections of the Julfa area; nodules are abundant and the boundaries between nodules and matrix are distinct and often marked by clay seams. Nodules are much rarer at Baghuk Mountain; the matrix is often recrystallized to microspar and the boundaries between nodules and matrix are inconspicuous. The *Paratirolites* Limestone of the sections at Baghuk Mountain appears rather uniform in its microfacies character. There is no significant change in abundance and fabric of biota throughout the entire unit. Also, there is no evidence for a reduction of carbonate accumulation in the upper part of the *Paratirolites* Limestone. There are no signs of condensed deposits or omission surfaces. Micrite clasts and biogenic encrustations occur only occasionally, and hardgrounds or ferruginous crusts are absent. Micro-cracks, fractures, and subtle calcite veins are abundant. The 'Boundary Clay' in the Baghuk Mountain sections differs from the sections in the Julfa area by the abundance of oxide/sulphide mineralization: dendrites of iron and manganese oxides or sulphides are common in the matrix.

Despite careful field examination of the sections in the Julfa region (Ali Bashi 1, Zal, Aras Valley; all the NW Iran) I did not find any in situ layers or mounds containing 'calcite fan' structures, as observed in the Baghuk Mountain. The recognition of 'calcite fan'-like structures in the Aras Valley section was possible because of microstructure recognized in the thin sections under the microscope. These enigmatic features occur in a strongly burrowed and fractured lime mudstone with abundant micrite-filled and calcite-filled burrows and with single sponge remains (Fig. 16e).

The microfacies of the carbonatic part of the Shahreza Formation of the sections at Baghuk Mountain are similar to those of the Julfa region. The Elikah Formation at Baghuk Mountain starts with deposition of densely laminated bindstone. There are though regional differences in architecture and microbialite types between the P-Tr sections in NW Iran (Ali Bashi 1 and Zal) and sections at Baghuk Mountian. In the sections in the Julfa region (NW Iran) the microbialite-dominated sequence starts in the Early Triassic *Claraia* Bed at +2.00 m in the Ali Bashi 1 section and at +2.40 m in the Zal section, and continues up to the end of the investigated section at +4.50 m at Ali Bashi 1 and at +12.00 m at Zal. Sections in the Julfa region lack large-scale microbial buildups as well as small-scale structures on the limestone bedding surfaces. The recognition of microbialite types was possible because of mesostructural elements visible with the naked eye and microstructure seen in thin sections under the microscope. In the sections of the Julfa region the most common microbialite type is poorly structured thrombolite and fine-grained agglutinated stromatolite (densely laminated bindstone). Densely laminated bindstone occurs within a 1 m thick horizon from +2.00 m to +3.12 m at Ali Bashi 1, within the uppermost

part of the *Hindeodus parvus* Zone and within the *H. lobota* Zone. In the Baghuk Mountain sections, similar to the sections at Ali Bashi and Zal, microbial deposits comprising laminated peloidal bindstone occur within an about 1.80 m thick interval within the *H. parvus* Zone. At Ali Bashi 1 and Zal densely laminated bindstone is followed by other microbially mediated deposits of the Early Triassic that comprise floatstone with sparry calcite spheres, aggregate grain grapestone and oncoid wackestone/floatstone (Leda et al., 2014, fig. 13c-h). These three microfacies types do not occur in the Shahreza Formation of Early Triassic sections at Baghuk Mountain. In the Shahreza Formation of Baghuk Mountain, microbialites are very abundant and occur as single large-scale buildups (conical and domal forms) or small-scale single and amalgamated forms on the bedding surfaces of platy limestones (Figs. 38, 41, 42, 43a). As stated above, no such biostromal or biohermal forms were found at Ali Bashi, Aras Valley and Zal. Reasons for the differences in microbialite types between the two regions (Julfa and Baghuk Mountain) may be related to local environmental conditions and/or sample resolution. Based on bed-by-bed sampling, only five metres of the Elikah Formation at Ali Bashi 1 were investigated. In the Zal section, twelve metres of the Elikah Formation were investigated with a resolution of only 0.5 m to 1 m. However, careful field examination was undertaken and no small-scale and large-scale microbial buildups were visible in the field. The sections in these two regions are today about 1000 km apart. The Julfa region had a position on the NNE part of the Sanandaj-Sirjan Terrane close to the Paleotethys, whereas the Baghuk Mountain region is situated on the SSW part of the Neotethyan shelf. However, there exist some other paleogeographic reconstructions, which represent a different division of the Cimmerian microcontinent (e.g., Şengör 1990; Ruban et al. 2007 a, b). According to Ruban et al. (2007a, 2007b), sections in the Julfa region belonged to the NW Iran Terrane, whereas sections in the Baghuk Mountain belonged to the Sanandaj-Sirjan Terrane. However, these two separate tectonic units (terranes) were apparently adjacent to each other throughout most of the Paleozoic (Ruban et al. 2007a, 2007b). Reasons for this geographic variation in morphology of microbialites have been little investigated. It is possible that a local variation in wave and current energy, sea-level change and/or local variation of sedimentation influenced the given microbial development at different sites. Thus, this regional difference in microbialite types is tentatively related to local environmental controls (e.g., different upwelling).

9.2 Microfacies and sea-level changes

As discussed by Richoz et al. (2010), there is no sedimentological evidence for large-scale sea-level changes around the P-Tr boundary, and there is no evidence for a shallowing-upward or subaerial exposure at that time in the sections near Julfa and at Baghuk Mountain. There are no vadose-meteoric cement types, no pedogenic structures, and no palaeokarst features seen across the P-Tr boundary beds in any of these sections. The occurrence of micrite clasts in the topmost 4-5 cm of the *Paratirolites* Limestone in the sections near Julfa does not prove subaerial exposure, but could be evidence for deep-water seafloor dissolution. The occurrence of a 1.5 cm thick horizon of marly matrix rich in crystal silt-filled and spar-filled interparticle cavities, between the micrite-clast wackestone and ‘sponge spike’ of the uppermost *Paratirolites* Lime-

stone, also does not support subaerial exposure. Abundant dissolution features, internal brecciation, and synsedimentary fissures within condensed pelagic limestone favour strong deep-water seafloor dissolution and reduced sedimentation.

The micritic matrix of the upper 5 cm of the *Paratirolites* Limestone contains abundant radiolaria and ammonoid conchs, which have been partially filled with remains of sponge skeletons as well as sparry cement. The co-occurrence of ammonoids, radiolaria, and sponges suggests a setting below the storm wave-base in a cratonic deep-water basin. There is also no change in sea level across the Aras Member (in the Julfa area) and the 'Boundary Clay' (at Baghuk Mountain). There are no pedogenic features, karst, soil or freshwater fabric that would imply subaerial exposure and dissolution. There is only evidence for continuation of a disruption in carbonate production together with mass extinction of biota. These investigations of the Shahreza Formation at Baghuk Mountain did not reveal any fabric diagnostic of subaerial exposure (e.g., ribbon rocks, water escape structures, pendant or meniscus cement, vugs, silt-filled dissolution voids, moldic pores). There is no supportive field and microfacies evidence of subareial exposure and/or freshwater dissolution at the Permian-Triassic transition in both areas – Julfa and Baghuk Mountain.

9.3 Reduction in carbonate production and its possible causes

Leda et al. (2014) showed that the upper 0.30 m of the *Paratirolites* Limestone display signs of stratigraphic condensation. This condensation is indicated by specific post-depositional and diagenetic features, by decreasing sedimentation rate as well as by decreasing thickness of limestone beds towards the top of the unit. These microfacies studies showed an increasing number of reworked hardground clasts, corrosion surfaces, bored and encrusted bio- and lithoclasts, ferruginous microstromatolite crusts, and impregnation of discontinuity surfaces with iron and manganese oxides (Fig. 17). The thickness of limestone horizons diminishes towards the top of the *Paratirolites* Limestone from about 0.3 m at the base of the *Paratirolites* Limestone to 0.05 m at the top of the member. Also clear separation between limestone beds and shale intercalations at the base of the *Paratirolites* Limestone diminishes towards the top of the member, but here an alternation of more compact limestone beds and horizons richer in clay (marls) has been recorded (Ghaderi et al. 2014). The reduction in the carbonate accumulation culminates at the transition from the *Paratirolites* Limestone into the Aras Member, where shales with only a few marly nodules replace the carbonate factory (Leda et al. 2014; Fig. 20). It appears that only carbonate sedimentation was disrupted at that time. The accumulation rate of clay possibly does not change in this interval. Furthermore, there is a remarkable drop in $CaCO_3$ content across the lithological boundary between the *Paratirolites* Limestone and the Aras Member (Figs. 67, 69).

In the Kuh-e-Ali Bashi 1 section, the vast majority of *Paratirolites* Limestone beds have a $CaCO_3$ content ranging from 80 to 96 wt% (determined by the weight loss-acid digestion method) (Ghaderi et al. 2014). At the transition from the *Paratirolites* Limestone to the Aras Member, the carbonate content falls off abruptly to 15-30 wt% (Fig. 68). High-spired gastropods

became medium in frequency in the *Claraia* Beds, about +1.41 m above the EH, being a constituent of bioclastic wackestone with diverse fossils. Bellerophontids are single at the EH. They are well preserved and partly filled with bioclastic matrix. Bellerophontids became abundant in the *Claraia* Beds in an interval between +1.27 m and +1.37 m, forming a bellerophontid wackestone and in the interval between +1.41 m and +1.91 m, being a constituent of bioclastic wackestone with diverse fossils. Siliceous sponge spicule remains are absent in most of the *Paratirolites* Limestone, became abundant in the topmost two centimetres of the *Paratirolites* Limestone, in some horizons within the Aras Member, and in the *Claraia* Beds. Radiolaria are becoming more common in the upper part of the *Paratirolites* Limestone and they became abundant in the uppermost 0.30 m of the *Paratirolites* Limestone. The radiolarians are poorly preserved and loosely packed; their original opaline silica has been replaced by calcite (mould preservation) and the margins of the tests appear ragged. Radiolaria detritus fills the pebbles at the EH. Foraminifera are very rare in the Aras Member, and in the entire Elikah Formation. They are abundant in the uppermost part of the *Paratirolites* Limestone where they encrust micrite clast and fossils. Some chambers of foraminiferal tests are filled with Fe–Mn oxides. In the *Claraia* Beds they are constituent of bellerophontid wackestone and reveal mould preservation. The amount of actinopterygian teeth found in the Ali Bashi Formation and the *Paratirolites* Limestone is within the range of 100 to almost 1000. In the uppermost 0.30 m of the *Paratirolites* Limestone fish teeth are scarce and up to 10 teeth were found (Fig. 68). Actinopterygian teeth are absent in the Aras Member and in the entire *Claraia* Beds. Notably, there is absence of organisms that built their skeletons with silica above the extinction horizon, and that is concordant with decrease of calcium carbonate content.

Consequently, it is here proposed that a deficit of the carbonate production and/or accumulation is responsible for this condensation (Fernandez-Lopez 1994). An interruption of carbonate sedimentation may indicate a rapid geochemical change towards carbonate undersaturation (Zachos et al. 2005). Either the carbonates were chemically dissolved at the sea-bottom or they were not produced in surface waters (primary productivity decrease and/or dissolution of calcareous skeletons). The disappearance of calcite above the extinction horizon may represent the extinction of some unknown algal producer of calcareous sediment. Enhanced carbonate carbon dissolution, and a biocalcification crisis are possible scenarios for a decrease in carbonate accumulation (e.g., Knoll et al. 1996, 2007; Fraiser and Bottjer 2007; Crne et al. 2011). Both scenarios are related to increasing acidity of the ocean and decrease in carbonate ion concentrations. Ocean acidification can be the result of increased fluxes of CO_2, SO_2, and CH_4, which could be related to basaltic Siberian Trap volcanism and explosive felsic volcanism in South China (Ganino and Arndt 2009; Retallack and Jahren 2008; Sobolev et al. 2011; Svensen et al. 2009). Volcanogenic CO_2 input into the ocean can slow carbonate precipitation and even favour dissolution of $CaCO_3$ (Caldeira and Wickett 2003; Feely et al. 2004, 2008; Knoll and Fisher 2011). Schobben et al. (2015) recognized a low Sr/Ca ratio of calcite in the nodular *Paratirolites* Limestone - a feature that could be related to longer exposure to seawater that is undersaturated with respect to carbonate. Partial dissolution of aragonite at the water-sediment interface, connected with periods of non-deposition and partial lithification of muddy infill prior to burial has been referred as a cause for specific preservation of the upper surface of ammonoid conchs

- truncation by dissolution (e.g., Preto et al. 2005; Leda et al. 2014; Fig. 69). The presence of hard substrates (hardgrounds, molluscan shells, etc.) allowing encrustation by sessile organisms may also support a decrease of carbonate production. Slow sedimentation is also considered to have been a critical factor for the formation of carbonate nodules (Hsü and Jenkyns 1974). The red colour of the nodular limestone unit is possibly related to authigenic iron accumulation and suggests a low rate of carbonate accumulation (Leda et al. 2014). Submarine dissolution (chemical corrosion) was postulated by Payne et al. (2007) as a cause for a rapid facies change between the latest Permian limestone and the base of Early Triassic microbialite.

Condensed horizons are interpreted as the markers of greatest water depths (Vail et al. 1984). Condensed sequences in the topmost *Paratirolites* Limestone were probably formed during the drowning phase of the carbonate platform, where carbonate growth potential was exceeded by relative sea-level rise. The platform growth crisis may have been explained also by strongly increased coastal runoff (for example, siliciclastics and nutrients) in combination with pronounced eustatic sea-level rises (Heldt et al. 2010).

The nature of the Aras Member might be related to temporarily increased influx of weathered terrestrial material causing the transition from carbonates and marls to clays (Algeo and Twitchett 2010; Algeo et al. 2011; Richoz et al. 2010; Leda et al. 2014). The Aras Member has been assigned to increased terrigenous input, based on the thickness of this unit (Richoz et al. 2010), expressing, possibly, high sediment accumulation rates (Kozur 2007). Concomitantly reduced carbonate production could have been equally important. Sediments deposited under high accumulation rate conditions are, e.g., tempestites (Gomez and Fernandez-Lopez 1994). There is a horizon with reworked ostracod shells in the Aras Member in the Kuh-e-Ali Bashi 1 section, which I interpret as a distal tempestite. Schobben et al. (2016) considered a sedimentation rate of 3 mm/kyr^{-1} for the *Paratirolites* Limestone unit. Based on radiometric ages of Burgess et al. (2014) and thickness of the unit in the Ali Bashi 1 section, a sedimentation rate for the Aras Member is 30 mm/kyr^{-1} (Schobben et al. 2016). This would mean that the sedimentation rate within the Aras Member is ten times greater in comparison to that for the deposition of the *Paratirolites* Limestone. However, the Iranian sites might have been isolated carbonate platforms far away from any large landmasses. So far no compound specific element (soil-derived biomarker) analysis has been undertaken for these sections, which might clarify relative proportion, distribution, and $\delta^{13}C$ of biomarkers assigned to vascular land plants, which means terrigenous input.

Song et al. (2015) reported a steep rise of $^{87}Sr/^{86}Sr$ ratios (based on single conodont albid crown analysis) in the Meishan section that began at the extinction horizon in Bed 25 (between the *C. yini* and *H. changxingensis* zones) and persisted through to the middle Spathian. They provided evidence that this rapid increase of $^{87}Sr/^{86}Sr$ ratios during the P-Tr transition is associated with a rapid increase in continental weathering. They calculated the ratio of riverine to mantle Sr flux based on a simple box model and figured out that weathering rates increased by >2.8 times during the P-Tr interval. From the Changhsingian (latest Permian) to the Griesbachian (earliest Triassic), sediment fluxes to marine depositional systems increased by, on average, ~700 % and

became more clay-rich globally (Algeo and Twitchett 2010). Schobben et al. (2015) suggested a 16 times increased weathering rate that stimulates a 16 times global marine organic carbon inventory, starting at the extinction horizon and lasting for a period of about 40 ka. Their sensitivity experiments suggest increased organic carbon degradation by microbial sulfate reduction. Intense weathering was likely a consequence of greenhouse warming and an enhanced hydrological cycle (Schobben et al. 2014) as well as land-vegetation destruction by acid rain (Black et al. 2014; Sephton et al. 2015; Visscher et al. 2004).

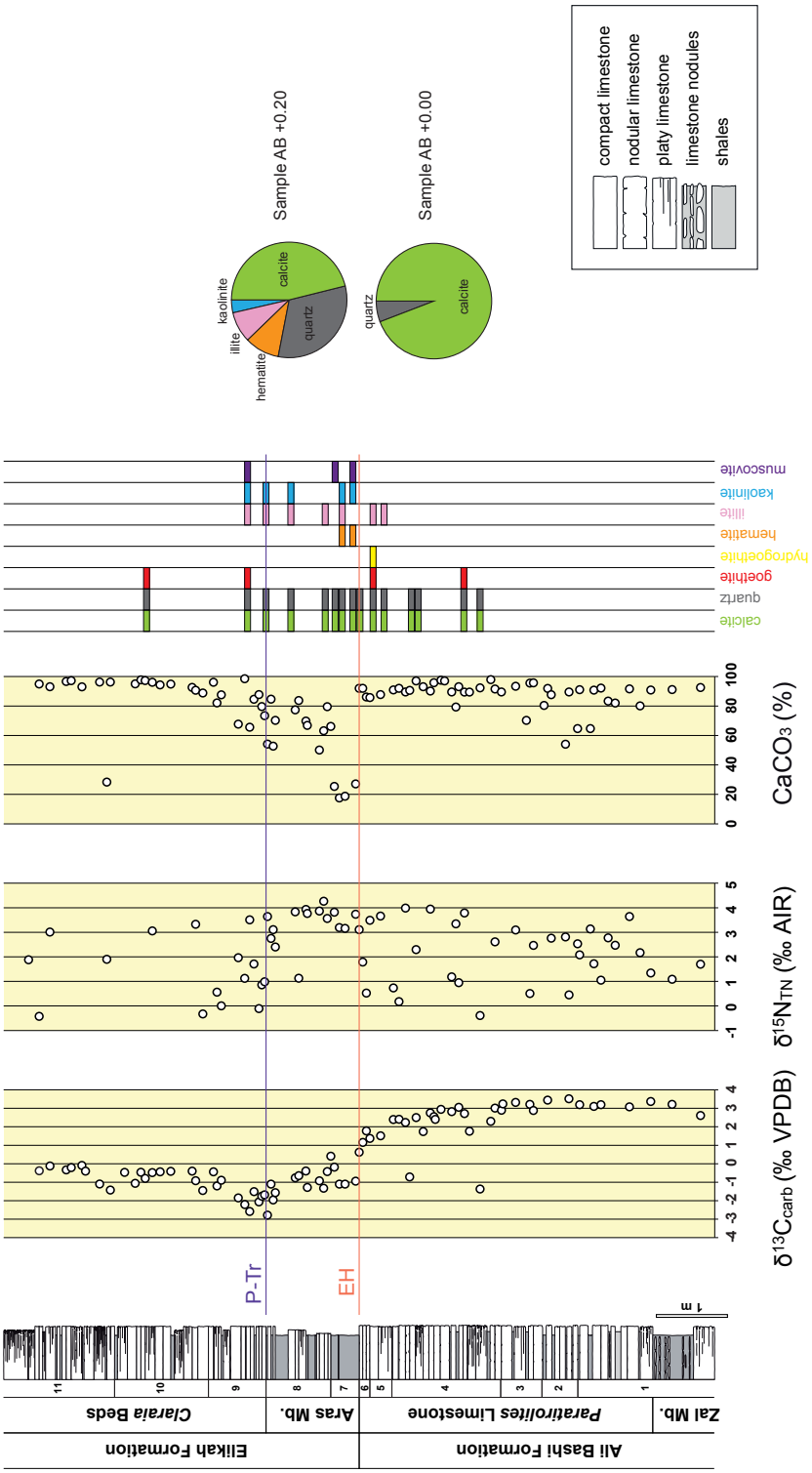

Figure 67. Bulk carbonate carbon, and bulk nitrogen isotopic compositions, and calcium carbonate content, and a diagram showing presence of clay minerals in marly/silty samples around the extinction horizon in the Ali Bashi 1 section. Conodont zones are numbered as follows: 1 - *C. changxingensis*, 2 - *C. bachmanni*, 3 - *C. nodosa*, 4 - *C. yini*, 5 - *C. abadehensis*, 6 - *C. hauschkei*, 7 - *Hindeodus praeparvus–H. changxingensis*, 8 - *Merrilina ultima–Stepanovites* ?*mostleri*, 9 - *Hindeodus parvus*, 10 - *H. lobota*, 11 - *Isarcica staeschei* zone.

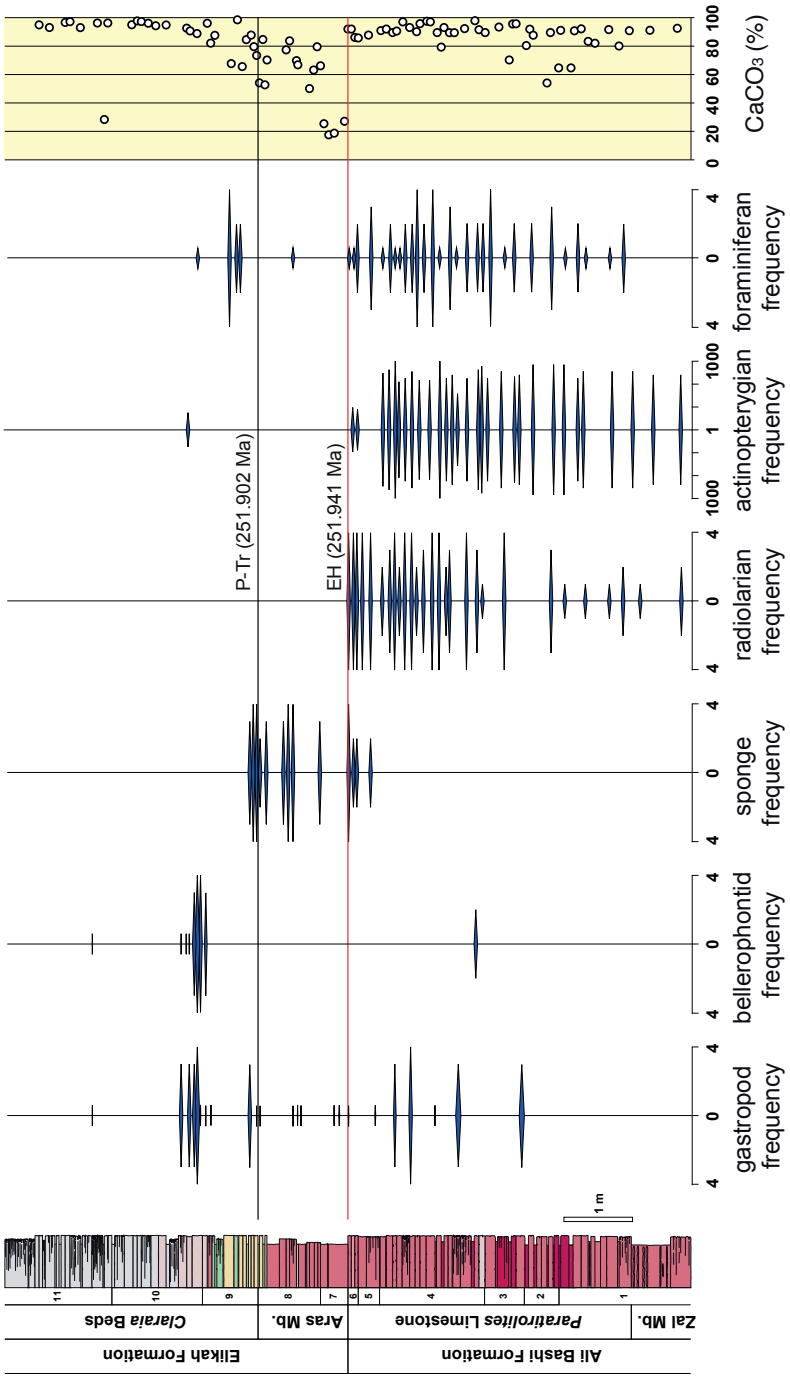

Figure 68. Fossil frequency changes around the extinction horizon coupled with calcium carbonate content at Ali Bashi 1. i. Conodont zones are numbered as follows: 1 - *C. changxingensis*, 2 - *C. bachmanni*, 3 - *C. nodosa*, 4 - *C. yini*, 5 - *C. abadehensis*, 6 - *C. hauschkei*, 7 - *Hindeodus praeparvus–H. changxingensis*, 8 - *Merrilina ultima–Stepanovites* ?*mostleri*, 9 - *Hindeodus parvus*, 10 - *H. lobota*, 11 - *Isarcica staeschei* zone.

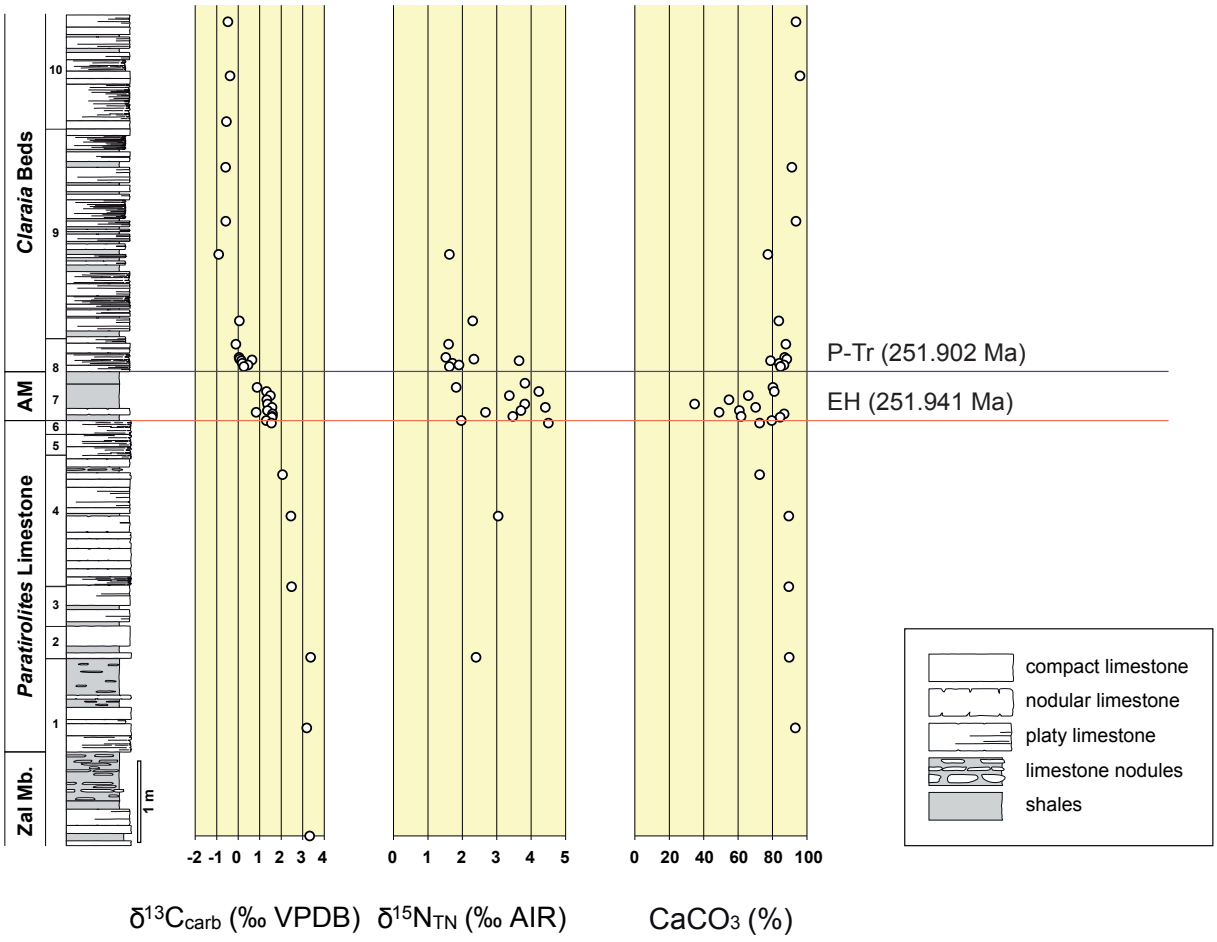

Figure 69 Bulk carbonate carbon, and bulk nitrogen isotopic compositions, and calcium carbonate content around the extinction horizon in the Zal section. Conodont zones are numbered as follow: 1 - *C. changxingensis*, 2 - *C. bachmanni*, 3 - *C. nodosa*, 4 - *C. yini*, 5 - *C. abadehensis*, 6 - *C. hauschkei,* 7 - *Hindeodus praeparvus–H. changxingensis*, 8 - *Merrilina ultima–Stepanovites* ?*mostleri*, 9 - *Hindeodus parvus*, 10 - *H. lobota* zone.

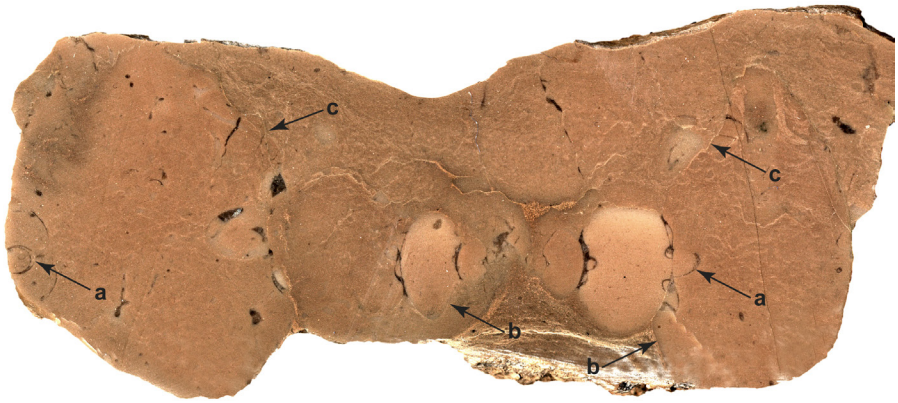

Figure 70 Cross section of a specimen of *Paratirolites* sp. from the Baghuk Mountain, MB.C.22215; 92.0. Note the different states of preservation of shell walls and septa: a -recrystallized but rather well preserved shell wall and septa preferably in the mid-dorsal portion of the ammonoid conch; b - dissolved shell wall but sharp demarcation of the ammonoid's internal mould from the sediment at the lower side of the ammonoid conch; c -dissolved shell wall and nearly continuous transition from the ammonoid's internal mould towards the sedimenton on the upper side of the ammonoid conch.

Table 12 Correlation coefficients for entire investigated sections (r value all), and for each lithostratigraphic unit. EF = Elikah Formation, BC = 'Boundary Clay', PL = *Paratirolites* Limestone, n = number of samples.

	Ali Bashi 1	Ali Bashi 4	Aras Valley	Zal	Baghuk Mt.
r value all	0.33 (n=96)	0.53 (n=37)	0.11 (n=78)	0.64 (n=43)	0.43 (n=88)
r value EF	0.57 (n=32)	-	-0.27 (n=14)	0.51 (n=7)	0.39 (n=25)
r value BC	0.43 (n=12)	0.26 (n=30)	0.64 (n=4)	0.62 (n=21)	0.23 (n=16)
r value PL	0.84 (n=34)	0.85 (n=7)	0.29 (n=25)	0.73 (n=8)	0.79 (n=37)

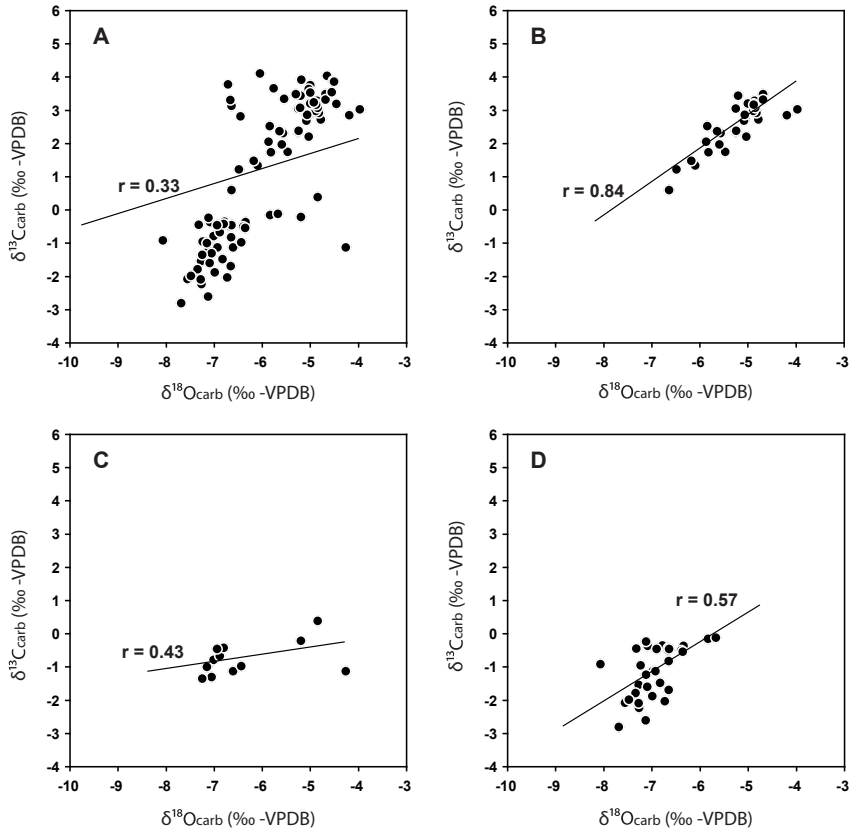

Figure 71 Cross-plots of δ^{13}Ccarb and δ^{18}Ocarb for Ali Bashi 1 section. a - for an interval of 25 m (20 m below, 5 m above the extinction horizon); b - for the *Paratirolites* Limestone; c - for the Aras Member, d - for the *Claraia* Beds; r - correlation coefficient.

9.4 Diagenesis and the $\delta^{13}C$/ $\delta^{18}O$ systematics

To utilize the carbonate carbon isotope values for detecting the primary geochemical signatures of the past and to delineate secular changes of the ocean/atmosphere system across the P-Tr boundary, the samples must be first evaluated in terms of alteration. Lithostratigraphic intervals of 25 metres, comprising 20 m below and 5 m above the extinction horizon, were investigated in detail in the Ali Bashi 1 and Aras Valley section. The high-resolution carbon isotope records of the investigated sections are all characterized by distinct oscillations; the excursions in the $\delta^{13}C_{carb}$ curves have high potential for regional chemostratigraphic correlation (Iranian sections) and also for correlations on a global scale (e.g., with China, Southern Alps), but potential secondary modifications must be evaluated first.

A correlation of the carbon and oxygen isotope ratios may be indicative of diagenetic alteration. But in the case that carbon and oxygen isotope ratios are not correlated, this does not necessarily imply that the carbon isotope ratios are well-preserved. Stabilisation and cementation in different diagenetic environments may result in different patterns. Meteoric diagenesis normally results in a J-inverted trend in a $\delta^{13}C_{carb}$/ $\delta^{18}O_{carb}$ diagram (Lohmann 1998), burial diagenesis normally results in lower $\delta^{18}O$ values whilst $\delta^{13}C$ remains unaltered. The alteration effect on the carbon isotope system is generally dependent on the diagenetic system and, for example, on the abundance of sedimentary organic carbon. Diagenesis in the mixing zone may result in a correlation of carbon and oxygen isotopes (Lohmann 1998). In order to identify effects of diagenesis, which might have modified the primary carbon isotope signals, $\delta^{13}C_{carb}$/ $\delta^{18}O_{carb}$ cross-plots from two sections have been produced and evaluated (Fig. 70). In addition, Pearson's correlation coefficients (r) (Taylor 1990) were applied to the individual rock units (*Paratirolites* Limestone, Aras Member and Elikah Formation) to identify potential alteration related to specific lithologies. This is important because different mineralogy and/or micro-structural character (e.g., porosity) – especially the latter - can affect the water/rock ratio crucially.

Pearson's correlation coefficients (r) were used to indicate how pronounced the $\delta^{13}C_{carb}$/$\delta^{18}O_{carb}$ correlations are. It has been explained earlier (chapter 7.1 Marine geochemistry of carbon (background)) that heavier oxygen and carbon isotopes will be depleted with progressive diagenesis. Strong correlations between $\delta^{13}C_{carb}$ and $\delta^{18}O_{carb}$ may indicate alteration (Brand and Veizer 1981; Veizer 1983; Marshall 1992). This is so because oxygen isotopes in bulk carbonates are usually altered because the $\delta^{18}O$ depends on temperature and the $\delta^{18}O$ of the fluid, and therefore reflects, at least in part, the temperature of the lithification/re-crystallization event. Moreover, pore water has much higher concentrations of O than C, and $\delta^{18}O$ values of carbonates are therefore more prone to post-sedimentary resetting than $\delta^{13}C$. Oxygen isotopes can serve consequently as a proxy for the diagenetic alteration degree affecting the C isotope ratio (Allan and Matthews 1982; James and Choquette 1990). The $\delta^{13}C_{carb}$/$\delta^{18}O_{carb}$ cross-plots for the Ali Bashi and Zal sections yield only weak correlations (Fig. 70; Table 12r). On the other hand, good correlations exist for the Ali Bashi, Zal and Baghuk Mountain sections, when regarding only the period of the negative $\delta^{13}C$ isotope trend within the *Paratirolites* Limestone (= upper part of the *Paratirolites* Limestone). For Ali Bashi 1, for example, only a very weak

correlation is observed for *Paratirolites* Limestone more than 2 m below the extinction horizon, for the Aras Member, and for the lower Elikah Formation. Better correlations, however, exist for the upper 2 m of the *Paratirolites* Limestone of the same section. It could be argued that a primary "background" signal indicates a primary warming trend of the ocean water coincident with the decrease of the carbon isotope values (indicating an increase in atmospheric/seawater carbon dioxide). However, this possible explanation is weakened by the fact that this correlation is not present for the same interval (i.e., the upper part of the *Paratirolites* Limestone) in the Aras Valley section. In addition, no correlation (r = 0.01) between $\delta^{13}C_{carb}$ and $\delta^{18}O_{carb}$ is observed for the period of the negative carbon isotope excursion at the Iranian P-Tr boundary succession at Abadeh (Korte et al. 2004a). All these observations strongly suggest that only parts of some sections were influenced by weak diagenetic overprint, because the general trends of the different sections are similar on the carbon isotope values (Brand and Veizer 1981; James and Choquette 1983; Veizer 1983).

Heydari et al. (2001) also found a negative correlation between $\delta^{13}C_{carb}$ and $\delta^{18}O_{carb}$ for their data for the Abadeh section. They concluded that the isotope signals reflected a secondary signal caused by meteoric diagenesis and that alteration took place before, during, and after the mass extinction, whereas the section was subaerially exposed during sedimentation. This view was refuted by Korte et al. (2004a), based on no correlation between the $\delta^{13}C_{carb}$ and $\delta^{18}O_{carb}$ in their data. Additionally, organic geochemistry of the lower part of the Abadeh section done by Korte et al. (2004a; fig. 4 and 5) suggests that the organic matter is derived from a marine source. The water depth was between 60 and 90 m at the time of interest; the sedimentation of all investigated sections took place on a carbonate platform that was not subaerially exposed during the Permian-Triassic transition (Leda et al. 2014). Alteration by meteoric water, which would also hold for the samples of the present study, could only have taken place during later diagenesis, but it is still enigmatic why this alteration should have affected solely the upper part of the *Paratirolites* Limestone.

Despite the large variation, the carbon isotopes of the different sections show clear trends with a general negative excursion ("first-order") trend, as determined by Schobben et al. (2016) interrupted by superimposed positive and negative shifts ("second-order" excursions according to Schobben et al. 2016). These "second-order" excursions (negative as well as positive) superimposed on the "first-order" $\delta^{13}C_{carb}$ trend are probably not useful as stratigraphic markers, because they might be influenced by diagenetic processes. Still, in some instances they may reflect original seawater isotopic composition of marine dissolved inorganic carbon (DIC) (Schobben et al. 2016). These authors evaluated the carbonate genesis and post-depositional alteration to isolate the primary versus secondary influences on bulk-rock $\delta^{13}C$ values from the Ali Bashi 1 and Zal sections. Schobben et al. (2016) reported a highly siginificant positive correlation between $\delta^{13}C_{carb}$ and $\delta^{18}O_{carb}$ (p-value < 0.001). Investigations by Schobben et al. (2016) imply a partial retention of primary carbon and oxygen isotope values in whole rock samples, in both cases expressed as a preservation of stratigraphic trends in isotope composition. In contrast, comparisons of different components (calcite brachiopod shells, conodont elements and bulk rock) from one horizon suggest an alteration of bulk rock $\delta^{13}C$ and $\delta^{18}O$. They stated, however,

that particularly the oxygen isotope values of bulk rock are skewed to lighter values, which is normally not observed for calcite formed in a marine environment. In addition, the carbon isotope values are generally more enriched in ^{13}C than would be expected for lithification under the influence of meteoric or phreatic water.

Preservation of the "first-order" $\delta^{13}C_{carb}$ trend is possibly governed by marine lithification of the micritic carbonate sediments in a relatively closed diagenetic environment with low water/rock ratios (Schobben et al. 2016). Comparison of oxygen-isotope profiles for bulk rock, and well-preserved fossils (both brachiopods and conodonts) shows that the former are offset by –2.1(±0.4) ‰. Diagenetic modeling suggests that these offsets were the product mainly of early diagenesis at burial temperatures of ~50-80°C and water/rock ratios of <10 (Schobben et al. 2016). Brachiopod shell calcite $\delta^{13}C$ and $\delta^{18}O$ values represent normal marine values (Schobben et al. 2014). Local diagenetic alteration was suggested for samples from calcareous clays that are susceptible to post-depositional recrystallization (Knauth and Kennedy 2009). The carbonate of the Aras Member in the Julfa area and 'Boundary Clay' in the Baghuk Mountain sections was suggested to be more prone to diagenesis than the bracketing limestone beds, due to a higher clastic content. The outstanding feature of bulk-rock element concentration is enrichment of Mg/Ca in calcite of the Aras Member and the occurrence of rhombic crystals of dolomite that suggest a localized late-stage dolomitization. In the present study sections, "second-order" $\delta^{13}C$ fluctuations, which are especially evident in the Aras Member, are likely to have been the product of late-stage diagenesis (Schobben et al. 2016).

9.5 Microfacies changes and the $\delta^{13}C_{carb}$ trend

To evaluate the impact of diagenesis on $\delta^{13}C_{carb}$, microfacies changes can be taken into account. In the upper part of the *Paratirolites* Limestone in sections near Julfa, there is a sharp decrease of the $\delta^{13}C_{carb}$ values that corresponds to the occurrence of features diagnostic for condensed sedimentation such as corrosion surfaces, reworked hardground clasts, bored and encrusted bioclasts and lithoclasts, ferruginous microstromatolite crusts, ferromanganese crusts (Leda et al. 2014). There occurs a reduction of overall carbonate content and calcite biogens in the sedimentary rocks across the extinction horizon (Ghaderi et al. 2014; Fig. 70). The decrease in carbonate accumulation occurred already in the upper part of the *Paratirolites* Limestone, about 0.48 m below the extinction horizon, with the carbonate factory finally being completely closed down by the time of deposition of the Aras Member (Leda et al. 2014). It is postulated here that a deficit in carbonate production and/or accumulation is responsible for this condensation, which consequently lead to a more rapid decrease in the $\delta^{13}C_{carb}$ values in the Ali Bashi 1 section in the uppermost part of the *Paratirolites* Limestone. In the Aras Valley section, features diagnostic for condensed sedimentation are also recognized in the uppermost part of the *Paratirolites* Limestone, but there is no acceleration of the $\delta^{13}C_{carb}$ decrease. This observation argues for a better preservation of the primary carbon isotope signal here (although the lithology is very similar to that of the Ali Bashi 1 section) and that the original decrease of the $\delta^{13}C$ values in this stratigraphic section was gradual. In the Baghuk Mountain sections, there is no

evidence for a reduction of carbonate accumulation in the upper part of the Hambast Formation. There is no indication of condensation of deposits or omission surfaces. The $\delta^{13}C_{carb}$ trend is continuous and shows a progressive decrease across the P-Tr boundary. The whole-rock $\delta^{13}C$ depletion begins in most sections in the middle part of the *Paratirolites* Limestone, within the *C. bachmanni* Zone, where there is no accompanying change in the microfacies (the interval from -2.67 to -0.75 m below the extinction horizon is nodular burrowed bioclastic lime mudstone and wackestone).

Two things must be considered when diagenesis could have impacted the carbonate carbon isotope values: (1) Alteration (generally expressed as negative trends of $\delta^{13}C_{carb}$ might not be (well) detectable at the P-Tr boundary because the primary negative carbonate carbon isotope excursion here is already pronounced. (2) A primary short-term positive $\delta^{13}C_{carb}$ trend might be mitigated by diagenetic impact. Therefore it is concluded that the carbonate carbon isotope values of the upper part of the *Paratirolites* Limestone are slightly overprinted by diagenesis in some localities in Iran (Ali Bashi, Zal and Baghuk Mountain), and that this could also be the case at other sections, such as in China and in the Alps. A diagenetic impact on the $\delta^{13}C_{carb}$ values below the marine extinction horizon might also explain, at least in part, the different amplitudes of the negative carbonate carbon isotope excursions (between 4 and 7 ‰) in the studied P-Tr boundary sections (also see discussion in Korte and Kozur 2010).

9.6 Possible causes of the $\delta^{13}C_{carb}$ trend

The Permian-Triassic boundary (PTB) sedimentary successions in Iran are marked by a prominent negative carbon isotope excursion. This excursion is found at many sites of the world in both fossil (e.g, brachiopod, conodont) and bulk carbonate, and is considered to be related to a global carbon cycle perturbation (e.g., Baud et al. 1989; Holser et al. 1989; for a review see Korte and Kozur 2010). Several mechanisms have been suggested to be responsible for this. The ultimate cause(s) is/are still debated (e.g., Shen et al. 2012a; Shen et al. 2012b; Song et al. 2013). This ‘‘first-order’’ $\delta^{13}C$ trend has been attributed, among others, to the effects of Siberian Traps volcanism, including effects of thermal metamorphism of organic-rich sediments (Ganino and Arndt 2009; Korte et al. 2010; Payne and Kump 2007; Retallack and Jahren 2008; Svensen et al. 2009; Sobolev et al. 2011), as well as to the erosion of continental organic matter (Holser and Magaritz 1987; Kraus et al. 2013; see also Sephton et al. 2005), and the reduction of marine primary productivity (Rampino and Caldeira 2005). However, basaltic, juvenile carbon dioxide has a $\delta^{13}C$ signature of about -5 ‰ (McLean 1985), so it is unlikely that this alone could produce an up to 7.4 ‰ negative excursion in the $\delta^{13}C_{carb}$ as reported from this study. This would only have produced a small $\delta^{13}C_{carb}$ change (Berner 2002; Kump and Arthur 1999; Wignall 2001). The amount of released volcanic CO_2 by flood basalt eruption is too low to produce such a big negative $\delta^{13}C_{carb}$ shift (Saunders and Reichow 2009). Additional source of more ^{13}C-depleted CO_2 might be carbon release by combustion due to Trap volcanism with lava flows, sills, dykes, and large sub-volcanic bodies burning organic-rich sediments and coals (Burgess et al. 2017).

In the present study, a gradual and continuous decrease of the $\delta^{13}C_{carb}$ values starts in the Aras Valley section in the *C. yini* Zone, i. e., 0.67 Ma before the extinction horizon. At Ali Bashi 1, Zal, and Baghuk Mountain decrease of the $\delta^{13}C_{carb}$ values starts already in the *C. bachmanni* Zone, about 1.01 Ma before the extinction horizon, based on interpolated ages by Schobben et al. (2016). My results and the literature data support the following: As the long-term (~0.5-1 Myr) negative carbonate carbon isotope trend is gradual, started in the latest Permian, and continued into the earliest Triassic, no short-term event has impacted the carbon isotope trend just before the extinction horizon. This suggests the action of a longer-lasting mechanism, such as thermal metamorphism of organic-rich sediments from lava flows and dykes of the Siberian Trap volcanism. Negative $\delta^{13}C_{carb}$ excursions are interpreted as a result of pronounced volcanic activity in Siberia (Kamo et al. 2003). The Siberian Trap volcanism with plateau basalts was the main phase of the volcanism, and was preceded by explosive volcanism (very thick tuffs) that commenced somewhat less than 400.000 years earlier (Korte et al. 2010).

The onset of the $\delta^{13}C_{carb}$ decrease in Iranian sections correlates with with the onset of of Siberian Trap volcanism with largely explosive volcanism with thick tuff deposition (Korte et al. 2010). The $\delta^{13}C_{carb}$ minimum at the P-Tr boundary mirrors the main phase of plateau basalt deposition of the Siberian Traps (Korte et al. 2010). During these volcanic period(s) a voluminous amount of ^{13}C-depleted CO_2 gases was released into the atmosphere. This intrusive phase of the sequence of Siberian Traps basalts would encompass sill emplacement in the sedimentary basins beneath the flood basalts. Such intrusions baked country rocks that included organic-rich, and carbonate-rich sediments, causing the escape of thermogenic methane (values of -40 ‰). These episodes could account for the negative $\delta^{13}C_{carb}$ trend as thermogenic methane was easily oxidised to CO_2 in the atmosphere (Payne et al. 2010; Retallack and Jahren 2008; Sobolev et al. 2011; Svensen et al. 2009). Products of the burning of the organic-rich strata may be distinctive charcoal and soot layers with pyrofusinite (charred plant remains). Widespread wildfire-derived products have been already recorded at several localities in North and South China (Shen et al. 2011), for Arctic Canada (Grasby et al. 2011), and for Western Australia (Thomas et al. 2004). Unfortunately, no combustion-derived particles were found in Iranian samples yet. Sobolev et al. (2011) provided geochemical and petrological evidence that the Siberian Large Igneous Province begun with a gigantic gaseous ''burp'', which preceded the main volcanic phase. Massive outgassing of the recycled crust in the plume head released voluminous amounts of carbon dioxide and hydrogen chloride into the atmosphere. In the model proposed by Sobolev and colleagues, deep-generated mantle plumes incorporated recycled, eroded oceanic crust. The $\delta^{13}C$ signature of CO_2 derived from oceanic crust shows more depleted values compared to that of pure mantle. The crust-derived CO_2 possesses a $\delta^{13}C$ signature of -12 ‰, whereas peridotite-derived CO_2 is characterized by $\delta^{13}C$ values of -5 ‰. Sobolev et al. (2011) considered the average carbon isotope composition of plume-release to be -9.9 ‰. They estimated that the $\delta^{13}C$ magnitude of all plume-released gases migrated to the surface was 4.9 ‰. This estimation agrees well with the $\delta^{13}C$ shift reported from Iranian sections, where for carbonate carbon as well as for the bulk organic matter carbon the magnitude of $\delta^{13}C$ ranges up to 6 ‰. These data fit well with the observed beginning of $\delta^{13}C_{carb}$ depletion in Iranian sections, below the extinction horizon. A massive release of ^{13}C-depleted carbon from, for example, methane, coal, and magma acified

the ocean, reducing carbonate sedimentation, and potentially lead to dissolution of carbonate sediments. Microfacies data (e.g., ammonoid truncation, stratigraphic condensation) confirm that ocean acidification could be responsible for reduction in the carbonate accumulation in the uppermost 0.48 m of the *Paratirolites* Limestone.

In addition or alternatively, enhanced weathering on the continents may have led to a higher supply of isotopically light organic matter to the ocean/atmosphere system (Fio et al. 2010; Kraus et al. 2013; Schwab and Spangenberg 2004; Sephton et al. 2001; Siegert et al. 2011; Watson et al. 2005). The nutrient-driven eutrophication of surface waters (due to high weathering rates) stimulated high (surface-water) bioproductivity in shelf settings followed by anoxic and sulfidic conditions as a consequence of increased (an)aerobic organic carbon remineralization (Meyer et al. 2008; Ozaki et al. 2011). Carbonate-associated sulfate (CAS) sulfur and CAS oxygen isotope studies by Schobben et al. (2015) suggest a flourishing of life within the Aras Member.

On the other hand, marine-productivity collapse (low organic matter accumulation) in connection with an input of light carbon (^{12}C) into the ocean-atmosphere system (e.g., Rampino and Caldeira 2005) may provide an explanation for the substantial $\delta^{13}C_{carb}$ shift. Simulations by Rampino and Caldeira (2005) showed that marine productivity reduction might have led only to a rapid, short-term increase in atmospheric pCO_2, which could produce a 3 ‰ negative shift in $\delta^{13}C$.

New studies by Schobben et al. (2015, 2017) pointed out that precipitation of ^{13}C-depleted secondary carbonate phases at the P-Tr boundary was considerable, and possibly influenced the global carbon cycle. A source of ^{13}C-depleted carbon is oxidation of sedimentary organic matter. Aerobic respiration of organic carbon (OC) generates CO_2 that can lead to carbonate dissolution, generating bicarbonate (HCO_3^-) that is markedly ^{13}C-depleted. Incorporation of such isotopically light carbon during precipitation of secondary carbonate phases causes a negative shift in bulk-rock $\delta^{13}C$. I postulate that the formation of a strongly ^{13}C-depleted pool of dissolved inorganic carbon (DIC) due to organic matter reminalization contributed to the post-extinction and post-PTB negative carbon isotopic trend.

In some terrestrial P-Tr sections, a similar pattern of carbon isotope data has been observed (Ward et al. 2005); however, this is not a ubiquitous observation. Analysis of the Kommandodrift Dam section in the southern Karoo basin by Coney et al. (2007) showed a pattern of cyclic change along the entire profile without specific change at the event bed. Where observed, the negative shift in the carbon isotopic ratio at the P–Tr boundary was attributed also to a global reduction of the level of atmospheric oxygen and an accompanying increase of the greenhouse gas CO_2 (Knoll et al. 1996; Benton and Twitchett 2003).

9.7 Possible causes of the $\delta^{15}N_{bulk}$ and $\delta^{13}C_{TOC}$ trends

The fluctuations of the $\delta^{15}N_{bulk}$ values within the *Paratirolites* Limestone at Ali Bashi 1 may represent a combination of two major processes occuring in the water: nitrogen fixation and an equilibrium state between nitrate assimilation, N_2 fixation and denitrification (the so-called 'normal marine production'). Low $\delta^{15}N_{bulk}$ values of ~2 ‰ describe a scenario where diazotrophic bacteria are responsible for the main input of bioavailable nitrogen to the ecosystem (Sachs and Repeta 1999). Higher $\delta^{15}N_{bulk}$ values within the range from +2 ‰ to +5 ‰ are consistent with values reported from modern marine sediments that are characterized by an average $\delta^{15}N$ value of +5 ‰ (Altabet and François 1994), which confirms essentially complete nitrate utilization as observed in the many open sea areas of the recent ocean, in so far as the $\delta^{15}N$ value of dissolved nitrate averages 4.8 ‰ (Sigman et al. 2000). The results suggest that the observed fluctuations of the $\delta^{15}N_{bulk}$ values within the *Paratirolites* Limestone and in the *Claraia* Beds can be best explained by a mixing of organic nitrogen and nitrogen from clay minerals/micas. The relatively high amount of total nitrogen in the Aras Member could be the result from absorption and retention of ammonium (NH_4^+) within clay minerals. Additionally Schubert and Calvert (2001) hypothesized that bound N is land derived, based on the high stability of the substitution of K^+ by NH_4^+ within clay minerals, especially in the high K^+ content of seawater. Potassium always occurs in relatively high concentrations in soil porewaters, so that there is no chemical gradient forcing the NH_4^+or K^+ out of the illite. It seems reasonable to assume, therefore, that once ammonium is bound in illites on land, there will be no leakage of this molecule out of the mineral once it is delivered (Schubert and Calvert 2001). In the same study, clay-bound $\delta^{15}N$ from modern ocean sediments are around 3‰ (+/-1.2) similar to our $\delta^{15}N_{bulk}$ values from the Aras Member that are between 3 and 4 ‰ in the *M. ultima* - *S.* ?*mostleri*, and in the lowermost part of the *H. praeparvus* - *H. changxingensis* zones. They argued that these low values are produced by the small fractionation of land plants from atmospheric $\delta^{15}N$ (~0‰) (Mariotti 1984). However, nitrogen fixation could be an additional mechanism for the $\delta^{15}N_{bulk}$ decrease, rather than stabilization of the $\delta^{15}N_{bulk}$ values within the lowermost Aras Member. Additionally, if there will be increase of nitrogen fixation by terrestrial plants or marine plankton, C/N ratios should be much higher (20-40 for land plants; Meyers 1994; 4-7 for marine plankton; Müller 1977) than those reported from my studies. Intriguingly, the $\delta^{15}N_{bulk}$ values within the Aras Member at Ali Bashi 1 are between values measured for a detrital organic matter in a river (+2.8 ‰) and soil organic matter (+4.1‰) (Wada et al. 1987).

The variance of the $\delta^{15}N_{bulk}$ values is dependent on lithology. This means that stabilization of the values occurred within marls and shales of the Aras Member, where also low $CaCO_3$ content was measured and increase in clay mineral content occurs (Figs. 67, 71). As the impact of early diagenesis and low-grade metamorphic reactions on the $\delta^{15}N$ signal is generally accepted to range between <1 and 3 ‰, it is probable that $\delta^{15}N_{bulk}$ values within the Aras Member may have been affected by early diagenesis. The $\delta^{15}N_{bulk}$ values within the Aras Member at Ali Bashi 1 are not in the range of $\delta^{15}N$ values for nitrogen fixation (see Table10; $\delta^{15}N$ ranges), but may reflect a domination of NO_3^- assimilation over other processes. Elevated $\delta^{15}N_{bulk}$ data within this shaly unit (between 3 and 4, up to 4.3 ‰) may indicate that nitrate became stable and available for bi-

oproductivity in surface waters, suggesting intensified nitrification-denitrification interactions during organic matter remineralization, rather than incorporation of land-derived nitrogen into the marine system. Another possibility to explain the observed positive nitrogen isotope shift and increase in total nitrogen (TN) content within this shaly unit is increase of denitrification within the sediment. This type of denitrification exhibits little isotope fractionation in contrast to denitrification within the water column, as the isotopic value of sedimentary denitrification is 3.5 (± 2) ‰ (Brandes and Devol 2002). Upwelling of denitrified ^{15}N-enriched waters from deep-waters would have contributed to the relatively high $\delta^{15}N_{bulk}$ values of nitrate in the surface oceans.

As stated above, the relatively high amount of total nitrogen in the Aras Member could be the result from absorption and retention of ammonium (NH_4^+) within clay minerals. I hypothesize that ammonium is not land-derived, but instead originated in marine sediment via anaerobic oxidation of organic carbon in a process called dissimilatory nitrate reduction to ammonium (DNRA) (Sigman et al. 2009). This process occurs where oxygen availability is low or absent within the sediment. The isotope fractionation (ε) associated with the breakdown of organic matter to NH_4^+ is usually small (up to 3 ‰) (Sigman et al. 2009).

In contrast to Ali Bashi 1, the $\delta^{15}N_{bulk}$ values within the shaly unit (Aras Member) at Zal do not show a plateau but oscillate between +1 and +5 ‰ and are within the range of the $\delta^{15}N_{bulk}$ values reported for the *Paratirolites* Limestone and *Claraia* Beds at Ali Bashi 1. This might imply that $\delta^{15}N_{bulk}$ values at Zal represent mixing of different processes (normal marine production plus nitrogen fixation) in the marine nitrogen cycle during deposition of the Aras Member sediments. More variable $\delta^{15}N_{bulk}$ values are expected in areas in proximity of land (along continental margins) rather than in oligotrophic, open-ocean settings with minor influence of continental input, where the $\delta^{15}N_{bulk}$ values are more stable. Both sections (Ali Bashi 1 and Zal) had similar palaeogeographic position during the Permian-Triassic transition, i.e, both on the NNE part of the Sanandaj-Sirjan Terrane of the Cimmerian microcontinent. However, sediments of the Aras Member at Ali Bashi 1 were deposited in deep shelf to basin settings, whereas at Zal in an open-marine interior platform setting. Also, the Aras Member comprises sediments of 1.18 m thickness at Ali Bashi 1, but only 0.60 m at Zal. These regional differences may speak for regional differences in relative sea level and need further investigation.

9.8 'Calcite Fans' – comparison with other structures and their origin

The term 'calcite fan' has been assigned by different authors to describe either microbial (Taraz et al. 1981, Heydari et al. 2000, 2001; Wignall and Twitchett 2002; Fang 2005) or abiotically produced features (Heydari et al. 2003, Heydari and Hassanzadeh 2003; Wignall et al. 2005). The 'calcite fan' of the Baghuk Mountain sections possesses the same texture as the elongated to cup-shaped microbial patches, made of branching, thinly laminated stromatolite, from the Hambast and Shahreza sections investigated by Baud et al. (2007, figs. 3e-f, 4) and as fans precipitated on the carbonate seafloor from the Shahreza section discussed by Richoz et al. (2010,

pl. 3A). Heydari et al. (2013, fig. 9) described a 0.20 m thick crystal fan layer from Early Triassic strata (Bed 4) at Shahreza that occurs above the P-Tr boundary (i.e., not in the 'Boundary Clay' as in the Baghuk Mountain sections). Microscopic examination by Heydari et al. (2013, fig. 9) indicated that crystal fans are highly recrystallized to the point of destruction of all original textures. As discussed by Heydari et al. (2003), the 'calcite fan' of the Hambast section shows characteristics consistent with inorganic, synsedimentary seafloor cement precipitation (bladed aragonite pseudomorphs neomorphosed to calcite). The cement layer at Hambast does not contain any lime mud and consists entirely of crystals, a feature that is in contrast to our findings in the Baghuk Mountain.

The 'calcite fan' of Baghuk Mountain reveals similarities to the dendroid-branching thrombolite from the Dongwan section of the Huaying area (South China), from where Ezaki et al. (2003, fig. 7A) described sparitic crystals with clearly visible growth banding. Longitudinal, polished surfaces of the 'calcite fan' from Baghuk Mountain reveal sparitic crystals that exhibit a macrostructure of subparallel, dendroid-branching, and coalesced forms with distinct growth banding.

Structures similar to the 'calcite fan' of Baghuk Mountain were described from the Smithian red ammonoid limestone of the Alwa Formation, Baid section in Oman (Baud et al. 2007) and from the Smithian-Spathian Union Wash Formation in south California, where large seafloor carbonate fans were described by Woods et al. (1999, 2007). The black calcium carbonate fans with elongated crystals of the Baid section grew in large cavities; they may thus represent abiotic precipitates. In fact, they differ from the Baghuk 'calcite fan' because there is no micritic material between the crystals, i.e., the crystals strictly adhere to each other forming botryoids. Seafloor carbonate fans from the Union Wash Formation in south California show intergrown hemispheres with radiating acicular to bladed crystals, in which the crystals radiate outward from a central nucleation location. The crystals also strictly adhere to each other forming botryoids. The branches of the 'calcite fan' at Baghuk Mountain do not radiate outward from a central nucleation location and the branches are separated by micritic matrix.

Calyx-shaped carbonate crystal fans were found in the Kuh-e-Dena section in SW Iran (north of the town of Shiraz) in late Dienerian to early Smithian sediments (Heindel et al. 2014). Heindel et al. (2014) showed that the calyx fans are banded perpendicular to crystal growth; there is no micritic material between the single fans. The calyxes consist of fibrous crystals being typically curved and reaching up to 2 cm in length. The calyxes are spaced in direct contact to each other, forming crusts. Curved, calyx-shaped crystals formed within the sediment by displacive growth. These structures differ from the 'calcite fan' at Baghuk Mountain, where crystals are not arranged in direct contact and do not form crusts, but are separated by a micritic and microsparitic matrix. Additionally, the crystals are straight and long and do not show displacive growth patterns. Crystal growth is unidirectional (upward).The 'calcite fan' layer from the Hambast and Shahreza sections has been interpreted in different ways, as a thrombolite (Taraz et al. 1981; Heydari et al. 2000, 2001), digitate or branching laminated stromatolite (Baud et al. 2005a, b; 2007), microbialite (Fang 2005), dendrolite (Richoz 2006), synsedimentary seafloor

carbonate cement (Heydari et al. 2003, 2008), or carbonate seafloor-precipitated fan (Richoz et al. 2010). Heindel et al. (2014) stated that the calyx-shaped crystals are biologically induced formations of diagenetic carbonate. The calyx-shaped crystal fans formed within soft sediment of the shallow subseafloor during early diagenesis, close to the sediment-water interface. Displacive growth of the calyx-shaped crystal fans during early diagenesis in soft sediment is evident from downward-facing crystal fans that deformed the lamination of the background sediment as a consequence of crystal growth.

Greene et al. (2012) investigated calcite fans of the Triassic-Jurassic boundary in Nevada and proposed that they are early diagenetic carbonate, i.e., carbonate formed soon after deposition. The crystals grew just below the sediment-water interface and protruded into the sediment. The fans appear to have incorporated a significant amount of siliciclastic material, which may indicate growth within, rather than on top, of the sediment. Additionally, fracture fills are generally pure carbonate and lack brecciation, which argues for crystal growth nearly concomitant with primary sediment deposition, precluding a late diagenetic origin. The 'calcite fan' branches at Baghuk Mountain show an internal lamination that may be interpreted as growth bands of inorganically precipitated calcite crystals that grew spontaneously directly on the seafloor. Encrustations by marine cement that occur along the branches may be interpreted as secondary, also laminated, generations of branches; they may have been aragonitic because of their acicular form. My study of the 'calcite fan' microstructure reveals, however, signs of bushy micrite with poorly defined margins that show locally a transition to microsparite that could be attributed to calcified cyanobacteria (Fig. 45b). Thus, this micrite is probably microbial in origin and points at a microbial influence during the growth of the 'calcite fan' branches. In my opinion, the 'calcite fan' formation was biologically induced. The 'calcite fan' at Baghuk Mountain does not occur in vugs and/or cracks. However, 'calcite fan'-like structures within the Aras Member in the Aras Valley section are embedded in the fractured lime mudstone. A presence of brecciation (common in veins opened by hydraulic pressure) may argue for a vein-infilling origin. I cannot provide any evidence to support whether these structures were formed within (diagenetic) or above (synsedimentary) the sediment.

There is vigorous debate whether calcite fan layers are biotic or abiotic in origin, and as to whether the conditions of formation were oxic or anoxic (e.g., Woods et al. 1999, 2007; Wignall and Twitchett 2002; Heydari et al. 2000, 2001, 2003, 2008; Wignall et al. 2005; Greene et al. 2012). The crystals were interpreted as calcite pseudomorphs after original aragonite (Richoz et al. 2010). The occurrence of inorganic calcite cements may be indicative of periods of unusual ocean chemistry (Baud et al. 1997; Woods et al. 1999; Heydari et al. 2003). Similar calcite fans have been found in other P-Tr sections around the world, across the deposits from early Triassic time: in the (1) USA (Woods et al. 1999; Woods and Bottjer 2000; Pruss et al. 2005; Woods et al. 2005), and (2) China (Kershaw et al. 1999), but they may have different origins from the calcite fan layer in Iran (Heydari 2005).

The development of seafloor calcite fans may be a result of CO_2 degassing from the upwelling of anoxic deep waters high in total alkalinity ($CaCO_3$ supersaturated) caused by bacterial sul-

phate reduction (Knoll et al. 1996; Kershaw et al. 1999; Woods et al. 1999, 2007; Heydari et al. 2003; Pruss and Bottjer 2004). Woods et al. (1999) interpreted the radiating sea-floor structures as calcium carbonate cement and postulated that the inorganic, synsedimentary carbonate precipitation took place at the interface between anoxic and oxygenated water masses. Kidder and Worsley (2004) published a model of the circulation of the Early Permian to the Early Triassic Tethys Ocean. They interpreted oceanic upwelling to have occurred along continental margins and in equatorial areas of ocean gyre divergence. Kiehl and Shields (2005) modelled the Tethys Ocean to have developed an extreme state of stratification due to limited connection with Panthalassa (Fig. 5). The Baghuk Mountain sections were located in the intertropical, equatorial zone during the Permian-Triassic transition, where the conceptual model by Kidder and Worsley (2004) indicates that upwelling would be focused. In the poorly circulated Tethys Ocean (as suggested by Kiehl and Shields 2005), patchy dysoxia may have developed in surface waters, as H_2S upwelled from the deep ocean towards the atmosphere (Kump et al. 2005). Frequent *Frutexites* within the 'Boundary Clay' may point to a poorly oxygenated environment, as calcified cyanobacteria were non-phototrophic and appear to have preferred an oxygen deficient, low-energy environment (Böhm and Brachert 1993).

More recent models of the conditions during formation of seafloor calcite crystals arouse from investigations of biomarker composition of the late Dienerian to early Smithian 'calcite fans' from the Dena section (Zagros Range, Iran) and the Triassic-Jurassic boundary 'calcite fans' at Muller Canyon (Nevada, USA) (Greene et al. 2012; Heindel et al. 2014). Greene et al. (2012) investigated $\delta^{13}C$ along a transect from base to top of a fan layer and showed that the $\delta^{13}C$ became progressively lighter as the fan grew. The concentration of carbonate associated sulphate (CAS, sulphate that substitutes for the carbonate ion molecule in the carbonate lattice) was measured along the same transect. The CAS decreases by ~50 % from the bottom to the top of the fan. This likely represents the consumption of SO_4^{2-} as the fans grew, consistent with growth in pore waters undergoing sulfate reduction. As $\delta^{13}C$ decreases, CAS generally decreases as well. This relationship was attributed by Greene et al. (2012) to sulfate reduction simultaneously removing sulfate from pore water and remineralizing organic matter. Heindel et al. (2014) described calyx-shaped carbonate crystal fans from the late Dienerian to early Smithian Dena section from southwestern Iran and figured that the calyx-shaped crystals precipitated from anoxic pore waters. Biomarker patterns of the carbonate beds investigated by Heindel et al. (2014) revealed major input of lipids from prokaryotes that typically occur within layered benthic microbial mats. Additionally, the presence of halophilic archaea was in accord with the lack of bioclasts and bioturbation within beds with calyx-shaped crystals, which likely reflects increased salinities and reducing conditions. Bergmann et al. (2013) related the occurrence of crystal fans to increase in anaerobic respiration, mainly through sulfate reduction and reduction in bioturbation on the seafloor, rather than a long-term change in the saturation state of global seawater. All these investigations imply that bacterial sulphate reduction at the sediment-water interface played a significant role in nucleation of aragonitic crystal fans.

A new high-resolution carbonate associated sulphate (CAS) and chromium-reducible sulphide (CRS) dataset for the Kuh-e-Ali Bashi 1 and Zal sections (both NW Iran) by Schobben et al.

(2015) suggests that: (1) the euxinic zones expanded suddenly at the extinction horizon implying a flourishing of life during this time, (2) a positive 5-7 ‰ excursion in carbonate-associated sulfate (CAS) oxygen isotopes across the extinction horizon (between the EH and the P-Tr boundary) is related to a higher local production of sulphide by microbial sulphate reduction (MSR). In this view, the post-depositional carbonate precipitation may be a direct result of increased pore water alkalinity due to sulphate reduction (Schrag et al. 2013). Lithological indices at the NW Iranian sites (Ali Bashi and Zal sections) for pervasive anoxia and euxinia, such as syngenetic framboidal pyrite or high organic carbon accumulation, are generally absent (Leda et al. 2014; Richoz et al. 2010; Schobben et al. 2015).

Besides the upwelling model described above, an increase of the seawater saturation state with respect to calcium carbonate may also be an effect of enhanced input of Ca^{2+} and HCO^{-} ions into the marine system caused by increased silicate weathering processes on land fuelled by elevated temperatures. Enhanced weathering brought down CO_2 and delivered excess alkalinity to the ocean, enhancing carbonate burial (Knoll and Fisher 2011; Schaller et al. 2012). Schobben et al. (2015) reported excursions in the records of sulphate-sulphur and oxygen isotopes from the sections in NW Iran, and their best model fit, based on sensitivity experiments, suggested a 16 times increased weathering rate starting directly at the extinction horizon and lasting for a period of 40 kyr (= the duration of Aras Member deposition). If the ‘calcite fan’ formed as cement, then supersaturation of the ocean water with respect to calcite promoted the recrystallization of the matrix and/or precipitation of the crystals. Pulses of high carbonate saturation may explain the precipitation of the upward-growing carbonate crystal fans. The internal lamination of the branches may reflect crystal growth bands, indicative of multiple precipitation events. Unfortunately, there is not yet any information about the water chemistry in terms of oxygenation and redox conditions from the layers containing ‘calcite fans’. Thus, the possibility that such production of sulphide by microbial sulphate reductive bacteria together with increased weathering rates can not be excluded to have contributed to an elevation of the saturation state of the seawater. Carbonate supersaturation of the oceans may have allowed nucleation of the ‘calcite fans’ within the ‘Boundary Clay’ at Baghuk Mountain. This needs further investigation.

9.9 Early Triassic microbialites – comparison with other structures and their origin

Microbialites of the Early Triassic sections at Baghuk Mountain are unique; they do not have any known counterparts worldwide. The club-shaped microbialites of morphotype 3 may be classified as hybrid microbialites, as there are at least two different types of microbialite textures in one specimen, i.e., stromatolite and leiolite (at +8.55 m) or stromatolite and dendrolite (Fig. 53b, c). Such heterogenous textures represent a unique structure that has not been described yet from other Early Triassic sections. Generally, leiolites have not been described from other P-Tr boundary sections. Dendrolites are very uncommon and are known from South China, in the Sichuan Province at Dongwan (Kershaw et al. 2007, figs. 4, 5). Hybrid microbial-inorganic structures have been described from shallow-shelf deposits in southern Turkey (Kershaw et al. 2011). They found several beds with mostly planar laminae, where stromatolitic, thrombolitic

and peloidal fabrics alternate with precipitated crystal fans. These structures differ from the inverted-conical, arborescent structures of Baghuk Mountain, where leiolites and dendrolites are preserved on the margins of the club-shaped specimens, and stromatolites are preserved in the central part.

Layers of sparite within hybrid stromatolite at +8.55 in section C are texturally similar to stromatolites from the Çürük Dag section (Kershaw et al. 2011, fig. 7). A dendrolite at +18.80 m reveals similar meso- and microstructure such as cements formed by elongated crystals growing in fringes and/or in fan arrays at the Çürük Dag section (Baud et al. 1997, pl.1, fig. 3). A dendrolite at +18.80 m exhibits a similar fabric to that of the carbonate crust at Tudiya reef (Sichuan, South China), where Kershaw et al. (2002, pl. 17, figs. 1, 3) described a microbialite of digitate architecture with radial fabric, showing also lobate and angular margins. Kershaw et al. (2002) pointed out that pervasive recrystallisation of calcified solenoporacean red algae can produce similar fabrics to that of the Sichuan crust from Dongwan (Sichuan, South Shina). A dendrolite at +18.80 m exhibits a fabric similar to red calcareous algae preserved in Carnian breccia clasts derived from the reef margin from the Anisian (earliest Middle Triassic) reef complex on the Great Bank of Guizhou, China (Payne et al. 2006; fig. 9a). Some of the microbialites described in our study (at +9.35 m) are similar to small domal stromatolites from the Elikah Valley in the Alborz Mountains of Iran (Kershaw et al. 2011, fig. 13d).

The microbialites from Baghuk Mountain described here are found in sediments above the *Hindeodus parvus* zone and do not belong to the Earliest Triassic stromatolites (ETMs) of Kershaw et al. (2007). As the first *Isarcicella isarcica* occurs at +3.71 m, the microbialites described here occur within and/or above the *I. isarcica* Zone, as the thickness of this conodont zone cannot be provided from the sampled material. Unfortunately, we do not have any complete biostratigraphic control above the *I. isarcica* Zone. Conodonts are absent at the beginning of an interval with conspicuous microbialites at +8.55 m and have not been found at the end of this interval at +18.85 m. However, this pulse of microbial activity took probably place during the latest Griesbachian/early Dienerian based on conodont zonation of the Hambast section by Kozur et al. (2007) and could serve as evidence for the second microbial pulse designated by Baud et al. (2007). Examples of the post-*Hindeodus parvus* microbialites are sporadic "*Renalcis*"- type bioherms in the southern China block, which were found up to ca. 200 m above the extinction horizon (Lehrmann 1999). In Italy, small stromatolites (0.25 m thick) occur at the Tesero Site (Wignall and Hallam 1992) in dysoxic settings (Wignall and Twitchett 2002).

In the Great Basin (Utah and Nevada), small microbialite mounds occur widespread in the late Early Triassic (Smithian and Spathian) Moenkopi Formation (Pruss et al. 2006). The morphology of the microbialites from Baghuk Mountain (Fig. 41d) reveals similarities to the lenticular to irregular sponge structures with centimetre-thick walls from the latest Smithian to early Spathian Thaynes Formation of the Mineral Mountains (Utah, USA) (Brayard et al. 2011, fig. 3i-k). Sponges from the Mineral Mountains are preserved as small and densely coalesced spheres up to 2 cm in diameter, showing a lenticular distribution and dermal (?) surface. Sponge encrustations on bivalve shells are visible in the Shahreza Formation of Baghuk Mountain at +8.70 m

and +8.80 m. Microphotographs of the spiculitic network of these samples show similarity to sponge bioaccumulations (boundstone) from the Pahvant Range (early Smithian, Utah), where encrusting, planar and branched sponges were described by Brayard et al. (2011). Filamentous and also coccoidal objects were found within the microbialites of Baghuk Mountain. Coccoid microfossils (*Renalcis*-like) occur within the densely laminated bindstone at +2.20 m. Calcified coccoid structures, typically 20-30 μm in size, are preserved along the margins of digitate microbialite branches between the dendrolite branches and on top of angular and lobate branches at +18.80 m. Aggregated spheroids occur also at +11.80 m and are interpreted here as remains of cyanobacteria. Densely growing tufts of filamentous porostromate microfossils (cyanobacteria or algae) occur at +18.65 m. Oval features that resemble oncoids at +9.30 m have probably been formed in situ and are interpreted here as microbial micrite oncoids. In my opinion, laminated peloidal bindstone (at +2.50 m), the burrowed microbial packstone (at +9.30 m), and the fenestral packstone/bindstone with porostromate microfossils (at +18.65 m) are microbial in origin and reflect the activity of benthic microbial communities. These microfacies represent microbially mediated calcareous structures (Burne and Moore 1987; Riding 2000). The lamination of the peloidal bindstone is related to the trapping and binding activity of microbes and algae and to autochthonous precipitation of calcium carbonate. Shell fragments of ammonoids and bivalves acted as a base for sediment deposition and the formation of microbially induced micrite crusts representing microcrystalline cement, i.e. a boundstone/bindstone at +8.70 m, +8.80 m and at +13.95 m. Isopachous radial fibrous crusts that grow on bivalve and/or ammonoid shells at +13.95 m and from float material in C section (Fig. 52a, b) may be regarded as early precipitates (abiogenically precipitated crust). In the same specimen (Fig. 52b), however, microstromatolites in form of encrusting calcified cyanobacteria occur on stylolite seams.

The matrix surrounding the microbialites is a burrowed, fine-grained micrite that occasionally possesses signs of recrystallization and neomorphism. Micritic matrix often contains small cuspate to vermiform microfenestrae, partially filled with internal sediment (clotted micrite and sparry calcite forming geopetal fabric) and small birdseye-type cavities, filled by sparitic cements. In my opinion, some fenestrae (Fig. 50h) originated from the decomposition of algae and cyanobacteria. Oxidation of the mat destroyed non-calcified cyanobacteria, leaving fenestrae within the mud- and grain-supported matrix. Irregular but pervasive fenestrae within the matrix may have been suitable for microbially induced precipitation of peloidal micrites. The micrite is interpreted to have formed as microbially induced precipitates. There is no red vadose silt within the fenestrae that could indicate intermittent subaerial exposure. Identification of the origin (microbial and/or inorganic) of the small-scale, in situ microbialites in section C at +8.55m (club-shaped hybrid stromatolite), at +13.85 m and +13.80 m (knobby, micropeloidal thrombolite) and at +18.80 m (dendrolite) is difficult and not clear. In my opinion, the dendrolite at +18.80 m might be considered a probably recrystallized colony of porostromate cyanobacteria and/or recrystallized algae that had branched and segmented growth habits and longitudinal sections that showed vertically divergent calcified filaments. Although branches of a dendrolite at +18.80 m have lobate margins and an internal structure of vertically erect crystals, an organic origin cannot be confirmed, because its fabric is largely recrystallized. Layers of sparite within hybrid stromatolite occur at +8.55 m that could be cloudy precipitated

cement (probably inorganic but possibly microbially mediated). Cloudy, thick, dense micrite laminae could be, however, microbial in origin. Knobby, micropeloidal thrombolite at +13.85 m and +13.80 m that is made of fan-like splays and botryoids of fibrous calcite crystals may represent marine cement crust. Sparitic, leiolitic walls of the mushroom-shaped microbialites at +8.55 m are morphologically similar to a sponge. However, pores or channels are not visible. Additionally, sponges do not develop any 'lid' structure that occurs in my samples. The internal lamination of the microbialite at +8.55 m (Fig. 51) may represent biosedimentological structures (e.g., animal 'escape structures'; personal commun. by A. Pisera, Polish Academy of Science, Warsaw). These unique structures are interpreted to result from escape behavior of an infaunal organism (e.g., sea anemone) moving upward through the sediment to maintain contact with the sediment-water interface. The sparitic 'holdfast' (basal disc) acted as an adhesive foot, which was used by the soft-body organism to attach to the substrate. The animal was forced to readjust its burrows to avoid burial. The lamination resulted from partial sediment infill during the upward movement of the animal and this lamination was possibly maintained by cyanobacterial/algal activity. Organic mucus may have cemented the walls. The 'lid' may represent the final stage of sediment cover (death of the organism). In some specimens (Fig. 53b) rod-like, fan-shaped crystals in the form of a rosette that occur on the edges of microbialites resemble gypsum crystals and may indicate replacement of gypsum crystals by calcite. According to these observations, the microbialites described here are possibly biologically mediated and/or induced.

The microbialite appearance in the aftermath of the end-Permian mass extinction event has been considered anomalous (Baud et al. 2005a, 2005b, 2007). Such microbialites are interpreted as a biotic response to periods of unusual ocean chemistry that may be related to the casual mechanism of both the biotic crisis and the delay of biotic recovery (Kershaw et al. 1999; Lehrmann 1999; Lehrmann et al. 2003; Ezaki et al 2003). Climate warming and consequential oceanographic changes have been implied in most scenarios to explain this apparently unusual chemical state of the latest Permian and Early Triassic ocean. Seawater warming across the P-Tr transition is recorded in conodont phosphate-oxygen isotope records at sites in South China and NW Iran (Joachimski et al. 2012; Schobben et al. 2014). Schobben et al. (2014, fig. 5) calculated the sea surface temperature (SST) for the Ali Bashi 1 and Zal sections based on oxygen isotopes from diagenetically resistant conodont apatite and from low Mg-calcite of well-preserved brachiopods. The $\delta^{18}O$ data from these two sections document a dramatic increase in SST of 7 and 10 °C for the sections at Ali Bashi and at Zal, respectively. The negative shift in $\delta^{18}O$ that started at the extinction horizon translated into an increase of SSTs to over 35 °C in the *Claraia* Beds. As the microbial deposits occur at Baghuk Mountain in an interval between 2 and 20 metres above the extinction horizon within the lowermost part of the Early Triassic Shahreza Formation (which is equivalent to the *Claraia* Beds of NW Iran), it can be postulated that such warming also occurred in the Baghuk Mountain during this time, as the sections in NW Iran and in the Abadeh-Shahreza area possess rather uniform lithological composition and were located paleogeographically in the same equatorial tropical area (Leda et al. 2014). The microfacies of the Shahreza Formation at Baghuk Mountain are similar to those of the *Claraia* Beds in the Julfa region. In both regions, the early Triassic succession starts with deposition of

peloidal bindstone that formed under quiet water conditions of the restricted platform interior.

Riding (2005) and Riding and Liang (2005) pointed out that the carbonate saturation state plays an important role in microbialite formation. An increase of the saturation state of the seawater may be caused (besides the upwelling model described above for the 'calcite fan') by increased weathering rates on land, fuelled by elevated pCO_2 and temperature. From the Changhsingian to the Griesbachian, sediment fluxes to marine depositional systems increased by an average of ~700 % and became more clay-rich globally (Algeo and Twitchett 2010). Song et al. (2015) reported a steep rise of $^{87}Sr/^{86}Sr$ ratios (based on single conodont albid crown analysis) along the Meishan section that began at the extinction horizon in Bed 25 (between the *C. yini* and *H. changxingensis* zones) and persisted up to the middle Spathian. They provided evidence that this rapid increase in $^{87}Sr/^{86}Sr$ ratios during the P-Tr transition is associated with a rapid increase in continental weathering. They calculated the ratio of riverine to mantle Sr flux based on a simple box model and figured out that weathering rates increased by >2.8 times during the P-Tr transition interval.

There is common agreement that many of the Early Triassic microbialites grew in poorly oxygenated conditions in shallow waters (Kershaw et al. 1999, 2007; Wignall and Twitchett 2002; Crasquin-Soleau and Kershaw 2005; Mu et al. 2009; Liao et al. 2010; Bond and Wignall 2010). The occurrence of pyrite framboids within both the microbialite branches and micritic matrix in Early Triassic sediments at the Laolongdong site (Chongqing Province, China) may speak for lowered oxygen levels within the sediments during the formation of the microbialites, suggesting the occurrence of anoxia (Liao et al. 2010). However, another hypothesis for the occurrence of pyrite framboids comes from geochemical studies of deep-water sediments across the P-Tr boundary in Japan by Algeo et al. (2010). They stated that the deep water was oxic but an oxygen-minimum zone (OMZ) was formed above the upwelling zone. Episodic upwelling from the OMZ drew anoxic, but normally saturated water across the shelf and may have led to anoxic conditions for microbialites to grow, without additional input from supersaturated water, as envisaged by the upwelling model by, e.g., Kershaw et al. (1999); Knoll et al. (1996); Woods et al. (1999, 2007) described above.

Recent studies by Collin et al. (2015) using redox-sensitive proxies (U, V, Mo, and REE) indicate that oxic conditions prevailed during the growth of microbialites. They investigated sections in Guizhou (Dawen, Dajiang and Rungbao), in Sichuan (Dongwan, Baizyhuyan, Laolongdong), in Hungary (Gerennovar), and in Turkey (Çürük Dag). They did not find any significant authigenic enrichment of U and Mo. This indicates that the shelf depositional conditions were neither durably suboxic nor anoxic nor even euxinic during the microbialite growth. Also REE patterns show shapes typical for oxygenated marine environments (Collin et al. (2015). Collin et al. (2015) investigated stromatolites and thrombolites that were formed in the immediate aftermath of the P-Tr mass extinction, but restricted their studies to the *H. parvus* Zone. The microbial deposits occurring in the Baghuk Mountain sections within the *H. parvus* Zone are a poorly structured thrombolite and a laminated fine-grained agglutinated stromatolite. However, no redox sensitive elements have been measured there yet.Moreover, the ostracod distribution

in the *H. parvus* Zone suggests that the shelf environment was well-oxygenated in several localities around the Tethys or on the Phantalassa margin (Forel et al. 2009, 2013a, 2013b). Ostracod assemblages (bairdiids, cytherocopids, kirkbyids) within the 'Boundary Clay' from the sections in the Abadeh, Shahreza and Julfa regions also indicate high oxygen content in the bottom waters (Kozur 2007). All these features may speak for oxygenated water conditions during formation of microbialites within both the 'Boundary Clay' and the *H. parvus* Zone, in the Baghuk Mountain sections. However, assemblages of gastropods together with abundant bivalve specimens (*Claraia*) and bioturbation may favour at least dysoxic conditions in the Iranian Early Triassic (Richoz et al. 2010). We do not have any obvious evidence for anoxia in the Shahreza Formation, but it is probable that anoxic carbon remineralization in the sediments could have elevated the saturation state to the point of microbial carbonate precipitation.

The Early Triassic microbialites may have been formed within periods of elevated primary productivity in surface water (Sephton et al. 2005). Recent geochemical research and modelling studies suggest enhanced productivity during the Early Triassic, perhaps from increased erosion and nutrient input from continents (Sephton et al. 2005; Algeo et al. 2010, Algeo and Twitchett 2010). Temperature-induced continental weathering and an enhanced nutrient availability may have caused eutrophication of the marine shelf - an expected climate feedback mechanism acting on a sub-million year timescale (Schobben et al. 2015). In modern oceans, phytoplankton growth is limited by the availability of iron and productivity increase dependent on efficient iron supply (Moore et al. 2013). Similarly, an enhanced iron supply could have stimulated the microbial bloom during the P-Tr interval. Schobben et al. (2017) investigated the S-Fe-TOC relations to reconstruct palaeoredox conditions during deposition of the NW Iranian (Ali Bashi 1 and Zal sections) P-Tr strata and indicated that these strata are marked by high amounts of iron. Additionally, they stated that microbial sulphate reduction (MSR) activity was high during the earliest Triassic, as evidenced by constant heavy $\delta^{18}O_{CAS}$ in strata at Ali Bashi and Zal. Elevated iron input could have become greatly enhanced under increased chemical and/or physical weathering that could be the result of greenhouse warming and an enhanced hydrological cycle (Schobben et al. 2014, 2016).

9.10 Hypotheses about the origin of the P-Tr boundary mass extinction

The emplacement of the Siberian Traps has been implicated as the root cause of this mega-extinction event (e.g., Reichow et al. 2009). Important contenders for the proximate causes of the marine ecosystem collapse are, e.g., oceanic anoxia (Wignall and Hallam 1992; Wignall and Twitchett 1996), sea water warming (Holser et al. 1989; Joachimski et al. 2012; Kidder and Worsley 2004), ocean acidification (Clarkson et al. 2015; Knoll et al. 1996; Payne et al. 2010), and enhanced productivity (Algeo et al. 2010; Algeo et al. 2011; Algeo et al. 2013; Georgiev et al. 2015; Schobben et al. 2015; Schoepfer et al. 2013) leading to asphyxia, hypercapnia and thermal stress at the organismal level (Knoll et al. 2007). Ultimately, it has been widely debated whether endogenic or exogenic agents triggered these principial mechanisms.

Basaltic outgassing, as well as contact metamorphism with organic-rich host rock, is thought to have released an estimated amount of 170,000 Gt CO_2 into the latest Permian atmosphere (Saunders and Reichow 2009; Svensen et al. 2009). Input of CO_2 from volcanogenic sources led to increase in dissolved inorganic carbon, but did not affect total alkalinity of the oceans. Even if more HCO_3^- and CO_3^{2-} ions became available by molecular diffusion of CO_2, the carbonate may not precipitate, because CO_2 uptake decreases alkalinity of the ocean (increase in H^+ ions). This process decreases the seawater saturation state, slows carbonate precipitation, and even favours dissolution of $CaCO_3$ (Caldeira and Wickett 2003; 2005; Feely et al. 2004, 2008; Knoll and Fisher 2011). Frequently occuring hardground features such as microbial encrustation, and ferromanganese crusts within the uppermost *Paratirolites* Limestone encompasses submarine carbonate dissolution, winnowing, and bio-erosion processes that are indicative of early sea-floor lithification and diagenesis (Flügel 2004; Melim et al. 2002). Sedimentary structures such as reworked hardground clasts, corrosion surfaces, bored and encrusted bioclasts and litho-clasts, ferruginous microstromatolite crusts, impregnation of discontinuity surfaces with iron and manganese oxides, and ammonoid truncation, etc.) were recognised in the sections near Julfa; they speak for a decrease in the carbonate accumulation already in the upper half metre of the *Paratirolites* Limestone, with the carbonate factory finally being completely closed down as indicated by features across the lithological boundary between the *Paratirolites* Limestone and the Aras Member. Those features are, e.g., absence of foraminifera, bivalves, brachiopods, radiolaria, a drop in $CaCO_3$ content from 80-96 wt% to 15-30wt%, and change in lithology from carbonates to poorly fossiliferous claystone and siltstone (Ghaderi et al. 2014; Figs. 12, 67, 68).

Recent studies have shown that elevated pCO_2 levels (hypercapnia) may affect calcification rates (via decreased $CaCO_3$ saturation) as well as physiology (via disturbance of metabolism) of organisms (Gatusso et al. 1998; Knoll et al. 1996, 2007; Melzner et al. 2009; Payne et al. 2010; Retallack et al. 2011). High pCO_2 levels induce cellular acid-base imbalances and may lead to a decrease in the capacity of respiratory pigments to oxygenate tissues and to disruption of the internal pH balance. In turn, this may affect the precipitation of skeletons (Dejours 1988). Stress due to hypercapnia, together with increased temperatures, reduces the oxygen efficiency, growth rate, and reproductive potential of marine biota (Guppy and Withers 1999; Pörtner 2001; Pörtner et al. 2004, 2005; Riebesell et al. 2000). Aragonite, in comparison to calcite, is the more soluble polymorph; its secretion requires higher metabolic cost, and it is less resistant against dissolution. Thus, secretion of aragonite instead of calcite may be a disadvantage in water undersaturated with respect to calcium carbonate. In such conditions, increased energy expenditure is needed for skeletal biomineralization, especially for organisms with thick aragonitic and high-magnesium calcite skeletons (Hautmann 2004). Decrease in saturation state weakens the skeletons' calcification potential (Gattuso et al. 1998; Riebesell et al. 2000).

Within the *Paratirolites* Limestone of both regions investigated in this study (Julfa and Baghuk), several morphological trends from bottom to top of Late Permian *Paratirolites* Limestone can be observed among ammonoids: a size decrease (with median sizes of first 80-100 mm to later 20 mm), a change in conch shape from trapezoidal to compressed whorls, increasing serration of the suture line, particularly in the external lobe (Korn et al. 2016). The uppermoste part oft he

Paratirolites Limestone is dominated by minute ammonoids (Korn et al. 2016; Kiessling et al. 2018). There is a significant reduction in the number of notches in the external, adventive, and lateral lobes up section toward the boundary clay (Kiessling et al. 2018). Miniaturization, often termed Lilliput Effect, has frequently been proposed for various organisms deposited at the PTB (e.g., Metcalfe et al. 2011; Twitchett 2007), and the size reduction was usually observed in the post-extinction interval. Studies by Korn et al. (2016) yielded a different picture, as the reduction of size occurs already below the extinction horizon. For ammonoids, two extinction pulses may exist at Julfa (1.4 and 2.5 m below the Aras Member), whereas only one pulse is evident at Baghuk (2.4 m below the 'Boundary Clay') (Kiessling et al. 2018). A pre-boundary extinction pulse in the regional *Paratirolites kittli* ammonoid zone is thought to be centered at ca. 252.6 Ma (Schobben et al. 2015); that is, ~700 kyr before the main extinction pulse recorded in China. This is also the time of onset of a long-term negative carbonate $\delta^{13}C$ excursion at a global scale (Korte and Kozur 2010; Schobben et al. 2017).

I hypothetize that morphological simplification, decreasing body size, and finally extinction among ammonoids are linked to environmental instability. Ammonoid miniaturization may be a physiological consequence of elevated levels of pCO_2 in internal fluids. Unfortunately, direct measurements of the ancient pCO_2 levels are impossible. Despite this, estimates of pCO_2 rely on models, based on geochemical proxy, e.g., stable isotope ratios of boron, the carbon isotope composition of organic matter biomarkers, soil carbonates (Berner and Kothavala 2001; Berner 2006).

Another possibility, besides hypercapnia, to explain miniaturization of the ammonoids is change of food availability. Warming of CO_2 enriched ocean water could cause a decrease in oxygen levels. In this case, the ammonoids may suffer from a deficit in oxygen, which is needed for active respiration. Unequivocal sedimentary signs of oxygen depletion before the extinction horizon (e.g., laminated sediments, black shales with abundant pyrite, the absence of a burrowing fauna) are absent in P-Tr successions in Iran. The mass extinction in the sections near Julfa took place within red sediments of the *Paratirolites* Limestone, which contains a rich and diverse benthos, consisting exclusively of faunal elements (such as a bairdiid-dominated ostracod fauna) of species that could only live in oxygen-rich bottom water. The sediments of the *Paratirolites* Limestone are highly bioturbated. Burrows are well-defined, bedding boundaries are indistinct.

A scenario of an enhanced productivity suggests that ocean fertilization fuelled increased production of organic matter, leading to increased oxygen demand, anoxia, and hydrogen sulfide production (Hotinski et al. 2001; Kump et al. 2005; Meyer et al. 2008; Winguth and Maier-Reimer 2005; Winguth and Winguth 2012). Changes in the isotopic composition of trace sulfate locked in marine carbonate rocks across the EPME reflect a secular change in the size of the global marine organic carbon inventory (Algeo et al. 2010; Schobben et al. 2017; Song et al. 2014). A positive 5-7‰ excursion in carbonate-associated sulfate (CAS)-oxygen isotopes across the extinction interval suggests increased microbial sulfate reduction (MSR) and increasing water column hydrogen sulfide production H_2S within the Aras Member at Ali Bashi

1 and Zal (Schobben et al. 2015). There is, however, no geochemical sign for an enhanced productivity before the extinction horizon.

Seawater warming across the P-Tr transition is recorded in oxygen isotope records of conodont phosphate at sites in NW Iran (Schobben et al. 2014). The $\delta^{18}O$ data from the Ali Bashi 1 and Zal sections document that the sea surface temperature (SST) was generally stable (in the range of 22-33°C) throughout most of the Changhsingian (Schobben et al. 2014, fig. 5), indicating a relatively stable tropical climate before the extinction horizon. Short term fluctuations of up to 5 °C (~1‰ $\delta^{18}O_{phos}$), however, do exist for the late Changhsingian *Paratirolites* Limestone of the Ali Bashi 1 section. At the 'extinction horizon', a dramatic increase in SST of, respectively, 7 and 10 °C was recorded for the sections at Kuh-e-Ali Bashi and Zal (Schobben et al. 2014).

I conclude that all changes reported in my studies before the extinction horizon can ultimately be related to extensive extrusion of basalt in the Siberian Traps. A disruption of carbonate production and accumulation at the end of the Permian was probably/possibly caused by synergistic effects of ocean water acidification and hypercapnia, which eventually lead to a biocalcification crisis. That these findings pertain to the stratigraphic interval deposited before the PTB and its associated mass extinction renders any process that would be coeval with the onset of the extinction unlikely. This includes a trigger by large bolide impact.

9.11 Recommendation for further work

In this thesis, bulk sediment nitrogen isotope values ($\delta^{15}N_{bulk}$) together with carbon isotope values for decalcified samples ($\delta^{13}C_{TOC}$) were measured for the first time for samples from the Ali Bashi 1 and Zal sections (NW Iran). The Ali Bashi 1 section was densely sampled on a bed-by-bed basis, whereas the Zal section was sampled at comparatively lower resolution. In order to clarify changes in the regional oceanic nitrogen cycle during the Changhsingian/Griesbachian transition (Late Permian/Early Triassic), it is recommended to resample the Zal section to attain a much higher resolution regarding nitrogen chemostratigraphy. The Aras Valley section was studied with the highest sample density and serves as the key section for defining the high-resolution carbonate-carbon chemostratigraphic scheme presented and interpreted here. The "first-order" $\delta^{13}C_{carb}$ isotope record of the Aras Valley section does not show any significant sudden variation and there is no acceleration of the $\delta^{13}C_{carb}$ decrease in the uppermost *Paratirolites* Limestone. This observation argues for a better preservation of the primary carbon isotope signal here, and only minor diagenetic influence on the bulk carbon isotope record. In my opinion, it is thus worth to produce high-stratigraphic-resolution carbonate/nitrogen isotope records for bulk rock samples. The Aras Valley section contains, for instance, extremely abundant ostracod assemblages in the Permian-Triassic boundary interval, and its inventory of cephalopods, both nautiloids and ammonoids, appears to be higher than in the other sections.

Quantitative X-ray diffraction analyses of bulk sediments from all shale horizons within the interval around the extinction horizon, from all sections from NW and Central Iran, will determine their mineralogical composition, help to identify ash layers, and will decipher changes

in the composition of the siliciclastic influx into the shallow- marine depositional environment. Additionally, XRD analyses of separated clay fractions (usually < 2 micrometer grain size) from these samples will help to decipher clay mineral associations. The change of clay mineral association type with sample depth may indicate the change of paleoclimate and paleoenvironment. For example, kaolinite usually forms under strongly leaching conditions, such as abundant rainfall, good drainage, and acid waters. Quantitative XRD bulk mineralogical determination should be achieved using the Rietveld refinement method, whereas quantitative XRD clay mineralogical determination of the clay-size fraction should be obtained using the reference intensity ratio method.

I recommend obtaining stable isotope ratios of boron, as boron isotopes in carbonates are important to test pH variations of seawater (Joachimski et al. 2005). Strong volcanic activity at the P-Tr transition could have produced high amounts of atmospheric CO_2, which then was transfered to the ocean and may have caused a rapid decrease in seawater pH. The concentration of atmospheric CO_2 and the amount of CO_2 drawn from the atmosphere to the ocean may strongly affect the carbonate equilibria in the ocean, which in turn controls the pH of the surface ocean. A promising proxy for seawater pH is the B-isotope ratio of marine carbonate. In seawater, boron occurs as $B(OH)_3$ and $B(OH)_4^-$ with a large isotope fractionation between the different co-ordinated species. The relative abundance of these species and, hence, the isotope ratio in the seawater are primarily controlled by pH (Kakihana et al. 1977). During the precipitation of marine carbonate from seawater, only $B(OH)_4^-$ is incorporated and hence the B-isotope composition of carbonates ($\delta^{11}B_{cc}$) reflects the pH of seawater (Hemming & Hanson 1992; Hemming et al. 1995) and can be used to estimate pCO_2 (Spivack et al. 1993).

Kasemann et al. (2005) demonstrated that robust estimates of seawater pH and variation of weathering rate can be obtained from Neoproterozoic marine bulk carbonates using B and Ca isotopes. Calcium isotopes in carbonates can be utilized to obtain information about continental (i.e., silicate) weathering in view of its role in the draw-down of CO_2 and in supplying a massive alkalinity flux to the ocean. Carbonate-ion concentration of the ocean and, hence, variations can be obtained from Neoproterozoic marine bulk carbonates using Ca-isotopes. Weathering rate can be inferred from the concentration of Ca^{2+}. A potential indicator of the magnitude and variability of Ca^{2+} is the Ca isotope composition of carbonates ($\delta^{44}Ca_{cc}$). Temporary fluctuations in Ca^{2+} reflect changes in input of calcium to the ocean from continental weathering by increased erosion. These changes will also affect the $\delta^{44}Ca$ of the seawater and, hence, that of the precipitated carbonates (Zhu and Macdougall 1998; De La Rocha and DePaolo 2000). Ca isotopes on drilled micritic bulk carbonate powder samples will help to discuss the role of alkalinity in the formation of Early Triassic microbialites from Baghuk Mountain.

10 DISCUSSION AND SYNTHESIS

Based on numerous lithological and petrographical investigations, there is no evidence for a shallowing-upward or subaerial exposure around the Permian-Triassic boundary in the sections near Julfa and at Baghuk Mountain. There are no pedogenic features, karst, soil or freshwater fabric that would imply subaerial exposure at the Permian-Triassic transition in both areas at Julfa and Baghuk Mountain. Deep-water dissolution of carbonates is indicated.

The microfacies reveal that the depositional regime began to change already at some distance below the extinction horizon. Within the uppermost 0.48 m of the red, nodular *Paratirolites* Limestone, a reduction in carbonate production and accumulation can be observed. This is evident in form of an increasing number of reworked hardground clasts, bored and encrusted bioclasts and lithoclasts, ferruginous crusts, and partially dissolved cephalopod shells. Reduction in the carbonate accumulation culminated at the transition from the *Paratirolites* Limestone into the Aras Member, where shales with only a few marly nodules replace the carbonate factory. At this transition also a significant reduction of biogenic components occurs. A deficit of the carbonate production and/or accumulation is responsible for this condensation. The Aras Member has been assigned to temporarily increased influx of weathered terrestrial material, i.e., expressing high sediment accumulation rates. The skeletal carbonate factory was restored in sections near Julfa with the deposition of platy, micritic limestone at the base of the Elikah Formation. In the sections of the Julfa region the most common microbialite type is poorly structured thrombolite and fine-grained agglutinated stromatolite (densely laminated bindstone) followed by floatstone with sparry calcite spheres, aggregate grain grapestone and oncoid wackestone/floatstone.

Detailed carbonate petrography investigations show a conspicuous accumulation of sponge remains at the uppermost part of the topmost 4- to 5-cm-thick bed of the *Paratirolites* Limestone, marking the extinction horizon in all sections between the Aras Valley, and the Ali Bashi Mountains. Irregularly distributed spicules without any arrangement at the extinction horizon, as well as accumulation of reworked ostracod shells within the Aras Member, suggest reworking before final deposition, and may speak for storm-flow processes. At Baghuk Mountain, many small ammonoids can be found within marly limestone nodules directly above the extinction horizon. They could also have been transported prior to deposition.

Microbialites from Baghuk Mountain are found in sediments of the Shahreza Formation, below (the ‘calcite fan’) as well as above the *Hindeodus parvus* zone. In the transition from the ‘Boundary Clay’ to the overlying grey, platy limestone beds of the Shahreza Formation in Baghuk Mountain sections enigmatic layers with dome-shaped, upward-branching ‘calcite fan’ branches occurs. The ‘calcite fan’ formation was biologically induced. Production of sulphide by microbial sulphate reductive bacteria together with increased weathering rates can not be excluded to have contributed to an elevation of the saturation state of the seawater that allowed the precipitation of the upward-growing carbonate crystal fans. In section C, in the interval between +8.55 m and +18.85 m, microbialites are most abundant and diverse, and occur in situ in most bedding planes. Three microbialite types are preserved as small-scale individual forms:

a hybrid microbialite, a knobby micropeloidal thrombolite, and a dendrolite. Hybrid microbialites are unique structures, as there are at least two different types of microbialite textures in one specimen, i.e., stromatolite and leiolite or stromatolite and dendrolite. Such structures have not been described yet from other Early Triassic sections. Other microbialites are: a laminated peloidal bindstone, a burrowed microbial packstone, and a fenestral packstone/bindstone with porostromate microfossils. Additional forms of microbialite are sparry calcite and micritic crusts that were found on the skeletal elements of bivalves and ammonoids. Sections near Julfa lack large-scale microbial buildups as well as small-scale structures on the limestone bedding surfaces. The microbialites from the interval between +8.55 m and +18.85 m grew under relatively low-energy conditions, possibly below the fair-weather wave base, and above but near the storm-wave base in the photic zone. The microbialites described here are biologically mediated and/or induced.

Stable carbon isotope results presented in my work show that the whole-rock $\delta^{13}C$ depletion begins in most sections in the middle part of the *Paratirolites* Limestone, within the *C. bachmanni* Zone, already about 1 Ma before the extinction horizon. The $\delta^{13}C_{carb}$ trend is continuous, and shows a progressive decrease across the P-Tr boundary. Only at Ali Bashi 1 there is a sharp decrease of the $\delta^{13}C_{carb}$ values that corresponds to the occurrence of features diagnostic for condensed sedimentation described above. I postulate that no short-term event has impacted the carbon isotope trend just before the extinction. The negative carbon isotope excursion at the P-Tr boundary was mainly triggered by a longer-lasting mechanism, such as thermal metamorphism of organic-rich sediments from lava flows and dykes of the Siberian Trap volcanism or by enhanced continental weathering supplying isotopically light organic matter to the ocean/atmosphere system. It is therefore most likely that a short-term event – like methane release or upward rise of anoxia – has not played an important role in constraining the isotope trend. On a timescale over 1 Ma, the $\delta^{13}C_{carb}$ values are a function of the relative proportion of inorganic to organic carbon, so two processes, namely aerobic respiration of organic carbon and volcanism were sources of ^{13}C-depleted carbon (CO_2). Ocean acidification due to CO_2 input from volcanism and related processes was, according to my investigations, responsible for carbonate carbon dissolution well before the mass extinction event. Stable nitrogen isotope data show, however, no trend before the extinction horizon. The observed fluctuations of the $\delta^{15}N_{bulk}$ values within the *Paratirolites* Limestone, and in the *Claraia* Beds may speak for the so-called 'normal marine production', where a mixing of organic nitrogen and nitrogen from clay minerals/micas occurs. In the Aras Member, a high amount of total nitrogen and stabilization of the $\delta^{15}N_{bulk}$ values may speak for enhanced sediment denitrification, and intensified nitrification-denitrification interactions during organic matter remineralization. This is contrary to the knowledge about $\delta^{15}N$ values from other sections around the world, where a negative shift across the extinction horizon occurs; it is discussed to be a result of an increase in nitrogen fixation. Schobben et al. (2015) suggested that the euxinic zones expanded suddenly at the extinction horizon, implying a flourishing of life (eutrophication), and local production of sulphide by microbial sulphate reduction within the Aras Member. Additionally, a 16 times increased weathering rate is simulated during the Aras Member by those authors. These processes may have led to an elevation of the saturation state of the seawater, allowing nucleation and growth of a plethora of microbial

carbonate within both units, the Shahreza Formation at Baghuk Mountain, and *Claraia* Beds at Julfa. Degradation of organic substrates on the seafloor by sulphate-reducing microbes facilitate a sustained large marine organic carbon (OC) pool. However, lithological indices at the NW Iranian sites (Ali Bashi and Zal sections) for pervasive anoxia and euxinia, such as syngenetic framboidal pyrite or high organic carbon accumulation, are absent. However, assemblages of ostracods together with abundant bivalve specimens (*Claraia*) might indicate slight or episodic dysoxic bottom water conditions. On the other hand, frequent *Frutexites* within the 'Boundary Clay' may point to a poorly oxygenated environment during the 'calcite fan' formation at Baghuk Mountain. Low molar C_{org}/N_{tot} ratio, low concentration levels of organic carbon would speak rather for lowered oceanic primary productivity during the Aras Member at Julfa.

11 SUMMARY / CONCLUSIONS

1. A succession of three major sedimentation types can be observed across the Permian-Triassic boundary in sections of NW and Central Iran: (1) A skeletal-dominated carbonate factory documented by the Late Permian *Paratirolites* Limestone and Hambast Formation, which was closed down at the top of this rock unit (= the extinction horizon), (2) Clay/silt sedimentation with few marly intercalations of the Aras Member (=‘Boundary Clay’), (3) A microbial-dominated carbonate factory of the Early Triassic Elikah Formation.

2. The P-Tr boundary sections in the Julfa area and Central Iran were deposited on a carbonate shelf (platform) in near-equatorial latitudes. There is no evidence of a pronounced sea-level drop around the P-Tr boundary in these sections.

3. There is evidence for stratigraphic condensation in the uppermost 0.48 m of the red, nodular *Paratirolites* Limestone. Enhanced carbonate carbon dissolution, and a biocalcification crisis related to acidic, volcanogenic CO_2 inputs are probably responsible for decrease in carbonate accumulation in the uppermost part of the *Paratirolites* Limestone.

4. A conspicuous sponge packstone of two centimetre thickness occurs, in the sections of the Aras Valley and Ali Bashi Mountains, at the top of the *Paratirolites* Limestone immediately below the extinction horizon.

5. Microbialites from Baghuk Mountain were found in sediments of the Shahreza Formation above the horizon marking the end-Permian mass extinction event (the ‘calcite fan’) as well as above the *Hindeodus parvus* zone. Microbialites are diverse including large- and small-scale, arborescent microbialite buildups with conspicuous external morphology and various internal structures. They comprise, e.g., heart-shaped, flower-shaped, isolated and amalgamated forms that are classified in this thesis into three macrostructure morphotypes. Most of the microbialites have a club-shaped and digitate form and their internal structure is strongly recrystallized. The most common mesostructure types of microbialites at Baghuk Mountain are dendrolites, stromatolites, thrombolites, hybrid microbialites and isopachous crusts on bivalve and ammonoid shells.

6. The Early Triassic microbialites and inorganic precipitates from Baghuk Mountain were formed in a low-energy, shallow subtidal environment, during a regressive episode. They may have been formed within periods of elevated primary productivity in surface water, perhaps from increased erosion and nutrient input from continents.

7. A gradual and continuous decrease of the $\delta^{13}C_{carb}$ values starts in Ali Bashi 1, Zal, and Baghuk Mountain sections about 1 Ma before the extinction horizon. A sharp decrease of the $\delta^{13}C_{carb}$ values in the upper part of the *Paratirolites* Limestone in sections near Julfa is accompanied by features diagnostic for condensed sedimentation.

8. Aerobic respiration of organic carbon, and volcanism were probably sources of ^{13}C-depleted

carbon (CO_2), incorporated into marine carbonates and thus responsible for the $\delta^{13}C_{carb}$ decrease.

9. The fluctuations of the $\delta^{15}N_{bulk}$ within the *Paratirolites* Limestone and *Claraia* Beds at Ali Bashi 1 may represent a combination of two major processes occuring in the water: nitrogen fixation and an equilibrium state between nitrate assimilation, N_2 fixation and denitrification (the so-called 'normal marine production'), where nitrogen comes from two sources: organic and clay-bond.

10. The recognised molar C_{org}/N_{tot} ratio over the Aras Member interval is probably a consequence of lowered oceanic primary productivity (as seen in low concentration levels of organic carbon), and the complete absence of calcium carbonate causing an increased clay content. The relatively high amount of total nitrogen in the Aras Member could be the result of absorption and retention of ammonium (NH_4^+) within clay minerals. This scenario supports the idea that the oceanic biota have gone through a general productivity crisis ending in a phase of mass extinction of marine life.

11. It is probable that $\delta^{15}N_{bulk}$ values within the Aras Member may have been affected by early diagenesis. Two processes could explain the observed positive nitrogen isotope shift and increase in TN content within the Aras Member: (1) intensified nitrification-denitrification interactions during organic matter remineralization, and (2) increase of denitrification within the sediment.

12 REFERENCES

Abich H (1878) Geologische Forschungen in den kaukasischen Ländern. Teil I. Eine Bergkalkfauna aus der Araxesenge bei Djoulfa in Armenien. Hölder, Wien, 126 p.

Abrajano T, Aksu AE, Hiscott RN, Mudie PJ (2002) Aspects of carbon isotope biogeochemistry of late Quaternary sediments from the Marmara Sea and Black Sea: Mar Geol 190(1-2):151–164

Ader M, Cartigny P, Boudou J-P, Oh J-H, Petit E, Javoy M (2006) Nitrogen isotopic evolution of carbonaceous matter during metamorphism: Methodology and preliminary results. Chem Geol 232:152–169

Ader M, Macouin M, Trindade RIF, Hadrien MH, Yang Z, Sun Z, Besse J (2009) A multilayered water column in the Ediacaran Yangtze platform? Insights from carbonate and organic matter paired $\delta^{13}C$. Earth Planet Sci Lett 288(1-2):213–222

Aghai PM, Vachard D, Krainer K (2009) Transported foraminifera in Palaeozoic deep red nodular limestones exemplied by latest Permian Neoendothyra in the Zal section (Julfa area, NW Iran). Rev Españ Micropaléontol 41(1-2):197–213

Algeo TJ, Twitchett RJ (2010) Anomalous Early Triassic sediment fluxes due to elevated weathering rates and their biological consequences. Geology 38(11):1023–1026

Algeo TJ, Ellwood B, Nguyen TKT, Rowe H, Maynard JB (2007) The Permian-Triassic boundary at Nhi Tao, Vietnam: Evidence for recurrent influx of sulfidic watermasses to a shallow-marine carbonate platform. Palaeogeogr Palaeoclimatol Palaeoecol 252:304–327

Algeo TJ, Shen Y, Zhang T, Lyons TW, Bates SM, Rowe H, Nguyen TKT (2008) Association of ^{34}S-depleted pyrite layers with negative carbonate $\delta^{13}C$ excursions at the Permian/Triassic boundary: Evidence for upwelling of sulfidic deepocean watermasses. Geochem Geophy Geosyst 9(4),10 p

Algeo TJ, Chen ZQ, Fraiser ML, Twitchett RJ (2011a) Terrestrial-marine teleconnections in the collapse and rebuilding of Early Triassic marine ecosystems. Palaeogeogr Palaeoclimatol Palaeoecol 308(1-2):1–11

Algeo TJ, Kuwahara K, Sano H, Bates S, Lyons T, Elswick E, Hinnov L, Ellwood BB, Moser J, Maynard JB (2011b) Spatial variation in sediment fluxes, redox conditions, and productivity in the Permian–Triassic Panthalassic Ocean. Palaeogeogr Palaeocl 308:65–83

Algeo T, Henderson CM, Ellwood B, Rowe H, Elswick E, Bates S, Lyons T, Hower JC, Smith C, Maynard B, Hays LE, Summons RE, Fulton J, Freeman KH (2012) Evidence for a diachronous Late Permian marine crisis from the Canadian Arctic region. Geol Soc Am Bull 124:1424–1448

Algeo TJ, Henderson CM, Tong J, Feng Q, Yin H, Tyson RV (2013) Plankton and productivity during the Permian–Triassic boundary crisis: An analysis of organic carbon fluxes. Global Planet Change 105:52–67

Allan JR, Matthews RK (1982) Isotope signatures associated with early meteoric diagenesis. Sedimentology 29:797–817

Altabet MA (2007) Constraints on oceanic N balance/imbalance from sedimentary ^{15}N records. Biogeosciences 4:75–86

Altabet MA, François R (1994) Sedimentary nitrogen isotopic ratio as a recorder for surface ocean nitrate utilization. Global Biogeochem Cycles 8:103–116

Altabet MA, Deuser W (1985) Seasonal variations in natural abundance of ^{15}N in particles sinking to the deep Sargasso Sea. Nature 315:218–219

Altabet MA, Higginson MJ, Murray DW (2002) The effect of millennial-scale changes in Arabian Sea denitrification on atmospheric CO_2. Nature 415:159–162

Anderson TF, Arthur MA (1983) Stable isotopes of oxygen and carbon and their application to sedimentologic and paleoenvironmental problems. In: Arthur MA, Anderson TF, Kaplan IR, Veizer J, Land LS (eds) Stable isotopes in sedimentary geology. Columbia, SEPM Short Course:1–151

Arakelyan RA, Grunt TA, Shevyrev AA (1965) Kratkiy stratigraficheskiy ocherk. Tr Paleontol Inst Akad Nauk SSSR 108:20–25

Arnaboldi M, Meyers PA (2006) Patterns of organic carbon and nitrogen isotopic compositions of latest Pliocene sapropels from six locations across the Mediterranean Sea. Palaeogeogr Palaeoclimatol Palaeoecol 235(1–3):149–167

Attendorn H-G, Bowen RNC (1997) Radioactive and Stable Isotope Geology. Chapman & Hall, London, 519 p

Baccelle L, Bosellini A (1965) Diagrammi per la sistima visiva della composizione percentuale nelle rocce sedimentarie. Ann Univ Ferrara Sez IX Sci Geol Paleontol 1:59–62

Baghbani D (1993) The Permian Sequence in the Abadeh Region, Central Iran. Occasional Publications ESRI New Series 9B:7–22

Bambach RK, Knoll AH, Sepkoski JJ (2002) Anatomical and ecological constraints on Phanerozoic animal diversity in the marine realm. Proc Natl Acad Sci USA 99:6854–6859

Bando Y (1979) Upper Permian and Lower Triassic ammonoids from Abadeh, Central Iran. Mem Fac Educ Kagawa Univ 29:103–128

Bando Y (1981) Discovery of Lower Triassic ammonites in the Abadeh region of Central Iran. Geol Surv Iran Rep 49:73–103

Baud A, Magaritz M, Holser W (1989) Permian-Triassic of the Tethys: Carbon isotope studies. Geol Rundsch 78:649–677

Baud A, Cirilli S, Marcoux J (1997) Biotic response to mass extinction: the lowermost Triassic

microbialites. Facies 36:238–242

Baud A, Atudorei V, Richoz S (2005a) Sea-floor carbonate fans and calcimicrobial mound in the lower Triassic red limestone of the Alwa Formation, Baid Exotic, Eastern Oman Mountains. In: IAS (ed) 24th IAS meeting of Sedimentology, Muscat (Oman), 31 p.

Baud A, Richoz S, and Marcoux J (2005b) Calcimicrobial cap rocks from the basal Triassic units: western Taurus occurrences (SW Turkey). CR Palevol 4:569–582

Baud A, Richoz S, Pruss S (2007) The lower Triassic anachronistic carbonate facies in space and time. Global Planet Change 55:81–89

Baud A (2008) Correlation of Upper Permian localities in the Kuh-e-Ali Bashi area, NW Iran: old collections, old and new data. Permophiles 52:6–11

Baud A, Brönnimann P, Zaninetti L, Addendum (1972) In: Zaninetti L, Brönnimann P, Bozorgnia F, Huber H (eds) Étude lithologique et micropaléontologique de la formation d'Elika dans la coupe d'Aruh, Alborz Central, Iran septentrional, Arch Sci Genève 25:248–254

Bebout GE, Fogel ML (1992) Nitrogen isotope compositions of metasedimentary rocks in the Catalina Schist, California: Implications for metamorphic devolatilization history. Geochim Cosmochim Acta 56:2839–2849

Becker L, Porada RJ, Basu AR, Pope KO, Harrison TM, Nicholson C, Iasky R (2004) Bedout: A possible End-Permian impact crater offshore of northwestern Australia. Science 304:1469–1476

Benton MJ, Twitchett RJ (2003) How to kill (almost) all life: the end-Permian extinction event. Trends Ecol Evol 18:358–365

Bergmann KD, Grotzinger JP, Fischer WW (2013) Biological influences on seafloor carbonate precipitation. Palaios 28:99–115

Berner RA (2002) Examination of hypotheses for the Permo-Triassic boundary extinction by carbon cycle modeling. P Natl Acad Sci USA 99:4172–4177

Berner RA, Kothavala Z (2001) Geocarb III: A Revised Model of Atmospheric CO_2 over Phanerozoic Time. Am J Sci 301(2)182–204

Berner RA (2006) GEOCARBSULF: A combined model for Phanerozoic atmospheric O_2 and CO_2. Geochim Cosmochin Acta 70(23) 5653-5664

Besse J, Torcq F, Gallet Y, Ricou LE, Krystyn L, Saidi A (1998) Late Permian to Late Triassic palaeomagnetic data from Iran:constraints on the migration of the Iranian block through the Tethyan Ocean and initial destruction of Pangaea. Geophys J Int 135:77–92

Bijma J, Pörtner Ho, Yesson C, Rogers AD (2013) Climate change and the oceans - What does the future hold? Mar Poll Bull 74(495-505):436

Black BA, Lamarque J-F, Shields CA, Elkins-Tanton LT, Kiehl JT (2014) Acid rain and ozone depletion from pulsed Siberian Traps magmatism. Geology 42(1):67–70

Bond DPG,Wignall PB (2010) Pyrite framboid study of marine Permian–Triassic boundary sections: A complex anoxic event and its relationship to contemporaneous mass extinction. Geol Soc Am Bull 122(7-8):1265–1279

Bottrell SH, Newton RJ (2006) Reconstruction of changes in global sulfur cycling from marine sulfate isotopes. Earth-Sci Rev 75:59–83

Boyd SR, Philippot P (1998) Precambrian ammonium biogeochemistry: a study of the Moine metasediments, Scotland. Chem Geol 144: 257–268

Böhm F, Brachert TC (1993) Deep-water stromatolites and Frutexites Maslov from the Early and Middle Jurassic of S-Germany and Austria. Facies 28(1):145–168

Brand U, Veizer J (1980) Chemical diagenesis of a multicomponent carbonate system. 1. Trace elements. J Sed Petrol 50:1219–1236

Brand U, Veizer J (1981) Chemical diagenesis of a multicomponent carbonate system. 2. Stable Isotopes. J Sed Petrol 50: 987–997

Brandes J, Devol AH (2002) A global marine-fixed nitrogen isotopic budget: Implications for Holocene nitrogen cycling. Glob Biogeochem Cycle 16(4):1–14

Brayard A, Vennin E, Olivier N, Bylund K, Jenks J, Stephen AD, Bucher H, Hofmann R, Goudemand N, Escarguel G (2011). Transient metazoan reefs in the aftermath of the end-Permian mass extinction. Nat Geosci 4:693–697

Brennecka GA, Herrmann AD, Algeo TJ, Anbar AD (2011) Rapid expansion of oceanic anoxia immediately before the end-Permian mass extinction. P Natl Acad Sci USA 108(43):17631–17634

Brussate SL, Benton MJ, Desojo JB, Langer MC (2010) The higher-level phylogeny of Archosauria (Tetrapoda: Diapsida). J Sys Pal 8(1):3–47

Burchette TP, Wrigh VP (1992) Carbonate ramp depositional systems. Sediment Geol 79:3–57

Burgess SD, Bowring S, Shen S-z (2014) High-precision timeline for Earth's most severe extinction. Proc Natl Acad Sci USA 111:3316–3321

Burgess SD, Muirhead JD, Bowring SA (2017) Initial pulse of Siberian Traps sills as the trigger of the end-Permian mass extinction. Nat Commun 8:164

Burne RV, Moore IS (1987) Microbialites: organosedimentary deposits of benthic microbial communities. Palaios 2:241–254

Caldeira K, Wickett ME (2003) Anthropogenic carbon and ocean pH. Nature 425:365

Caldeira K, Wickett ME (2005) Ocean model predictions of chemistry changes from carbon dioxide emissions to the atmosphere and ocean. J Geophys Res 110:C09S04

Cao CQ, Wang W, Jin YG (2002) Carbon isotope excursions across the Permian-Triassic boundary in the Meishan section, Zhejiang Province, China. Chinese Sci Bull 47:1125–1129

Cao CQ, Love GD, Hays LE, Wang W, Shen SZ, Summons RE (2009) Biogeochemical evidence for euxinic oceans and ecological disturbance presaging the end-Permian mass extinction event. Earth Planet Sci Lett 281:188–201

Cao C, Colonero CLK, Shen S, Summons RE (2010) Pattern of $\delta^{13}C_{carb}$ and Implications for Geological Events during the Permian-Triassic Transition in South China. J Earth Sci 21:118–120

Carpenter E, Harvey H, Fry B, Capone D (1997) Biogeochemical tracers of the marine cyanobacterium Trichodesmium: Deep Sea Res 44(I) 27–38

Cecca F, Fourcade E, Azema J (1992) The disappearance of the 'Ammonitico Rosso'. Palaeogeogr Palaeoclimatol Palaeoecol 99:55–70

Chapman CR (2005) Were Permian-Triassic extinctions sudden and caused by impact? Meteorit Planet Sci 40 (Suppl). A28

Chen J-S, Shao M-R, Huo W-G, Yao Y-Y (1984) Carbon isotope of carbonate strata at Permian–Triassic boundary in Changxing, Zhejiang. Sci Geol Sinica 19:88–93

Chen Z-Q, Benton MJ (2012) The timing and pattern of biotic recovery following the end-Permian mass extinction. Nat Geosci 5:375–383 Chen Z-Q, Tong J, Liao ZT, Song H (2010) Structural changes of marine communities over the Permian-Triassic transition: Ecologically assessing the end-Permian mass extinction and its aftermath. Global Planet Change 73:123–140

Chevalier N, Bouloubassi I, Birgel D, Taphanel MH, López-García P (2013) Microbial methane turnover at Marmara Sea cold seeps: a combined 16S rRNA and lipid biomarker investigation. Geobiology 11(1):55–71

Clapham ME, Payne JL (2011) Acidification, anoxia, and extinction: A multiple logistic regression analysis of extinction selectivity during the Middle and Late Permian. Geology 39:1059–1062

Clarkson MO, Kasemann SA, Wood RA, Lenton TM, Daines SJ, Richoz S, Ohnemueller F,Meixner A, Poulton SW, Tipper ET (2015) Ocean acidification and the Permo-Triassic mass extinction. Science 348:229–232

Collin P-Y, Kershaw S, Tribovillard N,. Forel M-B, Crasquin S (2015) Geochemistry of post-extinction microbialites as a powerful tool to assess the oxygenation of shallow marine water in the immediate aftermath of the end-Permian mass extinction. Int J Earth Sci 104 (4):1025–1037

Coney L, Reimold WU, Koeberl C, Hancox PJ, Mader D, McDonald I, Struck U, Vajda V, Kamo SL (2007) Geochemical and mineralogical investigation of the Permian–Triassic bound-

ary in the continental realm of the southern Karoo Basin, South Africa. Palaeoworld 16:67–104

Craig H (1957) Isotopic standards for carbon and oxygen and correction factors for mass-spectrometric analysis of carbon dioxide. Geochim Cosmochim Acta 12:133–149

Crasquin-Soleau S, Kershaw S (2005) Ostracod fauna from the Permian-Triassic Boundary Interval of South China (Huaying Mountains, eastern Sichuan Province): palaeoenvironmental significance. Palaeogeogr Palaeoclimatol Palaeoecol 217:131–141

Cremonese L, Shields-Zhou G, Struck U, Ling HF, Och L, Chen X, Li D (2013) Marine biogeochemical cycling during the early Cambrian constrained by a nitrogen and organic carbon isotope study of the Xiaotan section, South China. Precambrian Res 225:148–165

Crne AE, Weissert H, Gorican S, Bernasconi SM (2011) A biocalcification crisis at the Triassic–Jurassic boundary recorded in the Budva Basin (Dinarides, Montenegro). Geol Soc Am Bull 123:40–50

Deines P (1980) The isotopic composition of reduced organic carbon. In: Fritz P, Fontes J Ch (eds) Handbook of Envoironmental Isotope Geochemistry 1:329–398

Dejours P (1988) Respiration in water and air:adaptations, regulation and evolution. Elsevier, Amsterdam, 179 p

Derry LA (2010) A burial diagenesis origin for the Ediacaran Shuram–Wonoka carbon isotope anomaly. Earth Planet Sci Lett 294(1-2):152–162

De La Rocha CL, DePaolo DJ (2000) Isotopic evidence for variations in the marine calcium cycle over the Cenozoic. Science 289:1176–1178

De Pol-Holz R, Ulloa O, Dezileau L, Kaiser J, Lamy F, Hebbeln D (2006) Melting of the PatagonianIce Sheet and deglacial perturbations of the nitrogen cycle in the eastern South Pacific. Geophys Res Lett 33(4):L04704

De Wit MJ, Ghosh JG, de Villiers S, Rakotosolofo N, Alexander J, Tripathi A, Looy C (2002) Multiple organic carbon isotope reversals across the Permo-Triassic boundary of terrestrial Gondwana sequences: Clues to extinction patterns and delayed ecosystem recovery. J Geol 110:227–246

Dolenec T, Lojen S, Ramovs A (2001) The Permian-Triassic boundary in Western Slovenia (Idrijca Valley section): magnetostratigraphy, stable isotopes, and elemental variations. Chem Geol 17:175–190

Dumitrescu M, Brassel SC (2006) Compositional and isotopic characteristics of organic matter for the early Aptian Oceanic Anoxic Event at Shatsky Rise, ODP Leg 198. Palaeogeogr Palaeoclimatol Palaeoecol 235(1-3):168–191

Emeis K-C (1987) Cretaceous black shales of the South Atlantic Ocean: the role and origin of recycled organic matter. In: Degens ET, Und IE, Honjo S (eds) Particle flux in the Ocean. Mitt.

Geol.-Paläont. Inst, Univ. Hamburg, Hamburg:209–232

Emeis K-C, Struck U, Leipe T, Pollehne F, Kunzendorf H, Christiansen C (2000) Changes in the burialrates and C:N:P ratios in Baltic Sea sediments over the last 150 years – relevance to P regeneration rates and phosphorus cycle. Mar Geol 167(1–2):43–59

Emeis K-C, Struck U, Leipe T, Ferdelmann TG (2009) Variability in upwelling intensity and nutrientregime in the coastal upwelling system offshore Namibia: results from sediment archives. Int J Earth Sci 89:309–326

Erwin DH (1993) The Great Paleozoic Crisis. Life and Death in the Permian. Columbia University Press, New York, 327 p.

Erwin DH (1994) The Permo-Triassic extinction. Nature 367:231–236

Erwin DH(2001) Extinction: End-Permian Mass Extinction. Encyclopedia of Life Sciences: 1-5

Erwin DH (2006) Extinction - How life on Earth nearly ended 250 million years ago. Princeton University Press, Princeton and Oxford, 264 p.

Ezaki Y, Liu J, Nagano T, Adachi N (2008) Geobiological spects of the earliest Triassic microbialites along the southern periphery of the tropical Yangtze Platform: initiation and cessationof a microbial regime. Palaios 23:356–369

Ezaki Y, Liu J, Adachi N (2003) Earliest Triassic Microbialite Micro- to Megastructures in the Huaying Area of Sichuan Province, South China: Implications for the Nature of Oceanic Conditions after the End-Permian Extinction. Palaios 18(4):388–402

Faith DP, Minchin PR, Belbin L (1987) Compositional dissimilarity as a robust measure of ecological distance. Vegetatio 69(1-3): 57–68

Falk M (2011) Physico-chemical stratification and stability of the meromictic Lake Alat. - BSc thesis Geosciences, Freie Universität, Berlin, Supervisor: M. Schneider, 27 p.

Fang ZJ (2005) Comment on Heydari, E., Hassanzadeh, J., Wade, W. J., Ghazi, A.M., 2003. Permian–Triassic boundary interval in the Abadeh section of Iran with implications for mass extinction: part 1. Sedimentology. Palaeogeogr Palaeoclimatol Palaeoecol 217:311–313

Farshid E, Hamdi B, Hairapetian V, Aghanabati S (2016). Conodont biostratigraphy of the Permian-Triassic boundary in the Baghuk Mountain section, Northwest of Abadeh. Geosciences 25:285–294

Feely RA, Sabine CL, Lee K, Berelson W, Kleypas J, Fabry VJ, Millero FJ (2004) Impact of Anthropogenic CO_2 on the $CaCO_3$ System in the Oceans. Science 305(5682):362–366

Feely RA, Sabine CL, Hernandez-Ayon JM, Ianson D, Hales B (2008) Evidence for upwelling of corrosive “acidified” water onto the Continental Shelf. Science 320(5882): 1490–1492

Fenton S, Grice K, Twitchett RJ, Bottcher ME, Looy CV, Nabbefeld B (2007) Changes in biomarker abundances and sulfur isotopes of pyrite across the Permian-Triassic (P/Tr) Schuchert Dal section (East Greenland). Earth Planet Sci Lett 262:230–239

Fernandez-Lopez S, Melendez G (1994) Abrasion surfaces on internal moulds of ammonites as palaeobathymetric indicators. Palaeogeogr Palaeoclimatol Palaeoecol 110:29–42

Fio K, Spangenberg JE, Vlahovic I, Sremac J, Velic I, Mrinjek E (2010) Stable isotope and trace element stratigraphy across the Permian-Triassic transition: A redefinition of the boundary in the Velebit Mountain, Croatia. Chem Geol 278:38–57

Fisher AG, Garrison RE (1967) Carbonate Lithification on the Sea Floor. J Geol 75(4):488–496

Flügel E (2004) Microfacies of carbonate rocks. Springer, Berlin, 976 p

Forel M-B, Crasquin S, Kershaw S, Feng Q, Collin PY(2009) Ostracods (Crustacea) and water oxygenation in earliest Triassic of South China: implications for oceanic events of the end-Permian mass extinction. Aust J Earth Sci 56:815–823

Forel M-B, Crasquin S, Kershaw, S, Collin PY (2013a) In the aftermath of the end−Permian extinction: the microbialite refuge. Terra Nova 25(2):137–143

Forel M-B, Crasquin S, Hips K, Kershaw S, Collin P-Y, Haas J (2013b) Biodiversity evolution through the Permian-Triassic boundary event: Ostracods from the Bükk Mountains, Hungary. Ac Geol Pol 58(1):195–219

Foster WJ, Twitchett RJ (2014) Functional diversity of marine ecosystems after the Late Permian mass extinction event. Nat Geosci 7(3):233–238

Fraiser ML, Bottjer DJ (2007) The non-actualistic Early Triassic gastropod fauna: a case study of the Lower Triassic Sinbad Limestone Member. Palaios 19:259–275

François R, Altabet MA, Burkle LH (1992) Glacial to interglacial changes in surface nitrate utilization in the Indian sector of the Southern Ocean as recorded by sediment $\delta^{15}N$. Paleoceanography 7:589–606

Frech F, von Arthaber G (1900) Über das Paläozoicum in Hocharmenien und Persien. Mit einem Anhang über die Kreide von Sirab in Persien. Beitr Paläont Geol Österr Ungarn Orient12:161–308

Freudenthal T, Wagner T, Wenzhofer F, Zabel M, Wefer G (2001) Early diagenesis of organic matter from sediments of the eastern subtropical Atlantic: Evidence from stable nitrogen and carbon isotopes: Geochim Cosmochim Acta 65(11):1795–1808

Fry B, Jannasch HW, Molyneaux SJ, Wirsen CO, Muramoto JA, King S (1991) Stable isotope studies of the carbon, nitrogen and sulfur cycles in the Black Sea and the Cariaco Trench. Deep Sea Res 38(2):S1003–S1019

Fuchsman CA, Murray JW, Konovalov SK (2008) Concentration and natural stable isotope profiles of nitrogen species in the Black Sea. Marine Chem 111:90–105

Galbraith E, Kienast M, Pedersen T, Calvert S (2004) Glacial-interglacial modulation of the marine nitrogen cycle by high-latitude O2 supply to the global thermocline. Paleoceanography 19(4):1–12

Gallet Y, Krystyn L, Besse J, Saidi A, Ricou L (2000) New constraints on the Upper Permian and Lower Triassic geomagnetic polarity timescale from the Abadeh section (central Iran).J Geophys Res 105:2805–2815

Ganeshram RS, Pedersen TF, Calvert SE, Murray JW (1995) Large changes in oceanic nutrient inventories from glacial to interglacial periods. Nature 376:755–758

Ganino C, Arndt NT (2009) Climate changes caused by degassing of sediments during the emplacement of large igneous provinces. Geology 37:323–326

Gatusso JP, Frankignoulle M, Bourge I, Romaine S, Buddemeier RW (1998) Effect of calcium carbonate saturation of seawater on coral calcification. Global Planet Change 18(1-2):37–46

Gaye-Haake BT, Lahajnar N, Emeis KCh, Unger D, Rixen T, Suthhof A, Ramaswamy V, Schulz H, Paropkari AL, Guptha MVS, Ittekkot V (2005) Stable nitrogen isotopic ratios of sinking particles and sediments from the northern Indian Ocean. Marine Chem 96:243–255

Georgiev SV, Stein HJ, Hannah JL, Henderson CM, Algeo TJ (2015) Enhanced recycling of organic matter and Os-isotopic evidence for multiple magmatic or meteoritic inputs to the Late Permian Panthalassic Ocean, Opal Creek, Canada. Geochim Cosmochim Acta 150:192–210

Ghaderi A, Garbelli C, Angiolini L, Ashouri AR, Korn D, Rettori R Gharaie MHM (2014a) Faunal change near the end-Permian extinction: the brachiopods of the Ali Bashi Mountains, NW Iran. Riv Ital Paleontol S 120:27–59

Ghaderi A, Leda L, Schobben M, Korn D, Ashouri AR (2014b) High-resolution stratigraphy of the Changhsingian (Late Permian) successions of NW Iran and the Transcaucasus based on lithological features, conodonts, and ammonoids. Foss Rec 15:41–57

Glikson AY (2004) Comment on “Bedout: A possible End-Permian impact crater offshore of northwestern Australia”. Science 306:613b

Golonka J (2000) Cambrian-Neogene plate tectonic maps. Wydawnictwa Uniwersytetu Jagiellońskiego, Kraków, 125 p

Gomez JJ, Fernandez-Lopez S (1994) Condensation processes in shallow platforms. Sed Geol 92:147–159

Granger J, Sigman DM, Rohde MM, Maldonado MT, Tortell PD (2010) N and O isotope effects during nitrate assimilation by unicellular prokaryotic and eukaryotic plankton cultures. Geochim Cosmochim Acta 74(3):1030–1040

Grasby SE, Beauchamp B (2008) Intrabasin variability of the carbon-isotope record across the Permian–Triassic transition, Sverdrup Basin, Arctic Canada. Chem Geol 253:41–250

Grasby SE, Sanei H, Beauchamp B (2011) Catastrophic dispersion of coal fly ash into oceans during the latest Permian extinction: Nat Geosci 4:104–107

Greene SE, Bottjer DJ, Corsetti FA, Berelson WM, Zonneveld J-P (2012) A subseafloor carbonate factory across the Triassic–Jurassic transition. Geology 40:1043–1046

Grice K, Cao C, Love GD, Böttcher ME, Twitchett RJ, Grosjean R, Summons RE, Turgeon SC, Dunning W, Jin Y (2005) Photic zone euxinia during the Permian–Triassic superanoxic event. Science 307:706–709

Grice K, Nabbefeld B, Maslen E (2007) Source and significance of selected polycyclic aromatic hydrocarbons in sediments (Hovea-3 well, Perth Basin, Western Australia) spanning the Permian-Triassic boundary. Org Geochem 38:1795–1803

Gross MG (1964) Variations in the $^{18}O/^{16}O$ and $^{13}C/^{12}C$ ratios of diagenetically altered limestones in the Bermuda islands. J Geol 72:172–193

Grossman EL, Ku TL (1986) Oxygen and carbon isotope fractionation in biogenic aragonite: Temperature effects. Chem Geol 59(1):59–74

Grotzinger JP, Knoll AH (1995) Anomalous carbonate precipitates: Is the Precambrian the key to the Permian? Palaios 10:578–596

Guppa M, Withers P (1999) Metabolic depression in animals: physiological perspectives and biochemical generalisations. Biol Rev 74:1–40

Halm H, Musat N, Lam P, Langlois R, Musat F, Peduzzi S, Lavik G, Schubert CJ, Sinha B, LaRoche J, Kuypers MMM (2009) Co-occurrence of denitrifi cation and nitrogen fixation in a meromicticlake, Lake Cadagno (Switzerland). Env Microbiol 11:1945–1958

Hampe O, Hairapetian V, Dorka M, Witzmann F, Akbari AM, Korn D (2013) A first Late Permian fish fauna from Baghuk Mountain (Neo-Tethyan shelf, central Iran). Bull Geosci 88(1):1–20

Hansen HJ. Lojen S. Toft, P, Dolenec T, Tong J-n, Michaelsen P, Sarkar A (2000) Magnetic susceptibility and organic carbon isotopes of sediments across some marine and terrestrial Permo–Triassic boundaries, In: Hongfu Y, Dickins JM, Shi GR, Tong Jinnan E (eds) Permian–Triassic evolution of Tethys and Western circum-Pacific. Elsevier, Amsterdam, pp 271–289

Hallam A, Wignall PB (1997) Mass Extinctions and their Aftermath. Oxford University Press, Oxford, 320 p.

Haug GH, Pedersen TF, Sigman DM, Calvert SE, Nielsen B, Peterson L (1998) Glacial/interglacial variations in production and nitrogen fixation in the Cariaco Basin during the last 580 ka. Paleoceanography 13(5):427–432

Hautmann M (2004) Effect of End-Triassic CO_2 maximum on carbonate sedimentation and marine mass extinction. Facies 50(2):257–261

Hayes JM, Strauss H, Kaufman AJ (1999) The abundance of ^{13}C in marine organicmatter and isotopic fractionation in the global biogeochemical cycle of carbon during the past 800 Ma. Chem Geol 161(1-3):103–125

Heindel K, Richoz S, Birgel D, Brandner R, Klügel A, Krystyn L, Baud A, Horacek M, Mohtat T, Peckmann J (2014) Biogeochemical formation of calyx-shaped carbonate crystal fans in the subsurface of the Early Triassic seafloor. Gondwana Res 27(2):840–861

Heldt M, Lehmann J, Bachmann M, Hedi Negra ME, Kuss J (2010) Increased terrigenous influx but no drowning: Paleoenvironmental evolution of the Tunisian carbonate platform margin during the Late Aptian. Sedimentology 57(2):1–25

Henderson CM, Mei SL, Shen SZ, Wardlaw BR (2008) Resolution of the reported Upper Permian conodont occurrences from northwestern Iran. Permophiles 51:2–9

Hemming NG, Hanson GN (1992) Boron isotope composition and concentration in modern marine carbonates. Geochim Cosmochim Acta 56:537– 543

Hemming NG, Reeder RJ, Hanson GN (1995) Mineral–fluid partitioning and isotopic fractionation of boron in synthetic calcium carbonate. Geochim Cosmochim Acta 59:371– 379

Hermann E, Hochuli PA, Bucher H, Vigran JO, Weissert H, Bernasconi SM (2010) A close-up view of the Permian-Triassic boundary based on expanded organic carbon isotope records from Norway (Trondelag and Finnmark Platform). Global Planet Change 74:156–167

Hermann E, Hochuli PA, Bucher H, Bruehwiler T, Hautmann M, Ware D, Roohi G (2011) Terrestrial ecosystems on North Gondwana following the end-Permian mass extinction. Gondwana Res 20:630–637

Heydari E (1997) The role of burial diagenesis in hydrocarbon destruction and H_2S accumulation, Upper Jurassic Smackover Formation, Black Creek Field, Mississippi. Geol Soc Am Bull 81:26–45

Heydari E (2005) Reply to the comments on Permian–Triassic boundary interval in the Abadeh section of Iran with implications for mass extinction: part 1—sedimentology. Palaeogeogr Palaeoclimatol Palaeoecol 217:319

Heydari E, Hassanzadeh J (2003) Deev Jahi Model of the Permian–Triassic boundary mass extinction: a case for gas hydrates as the main cause of biological crisis on Earth. Sediment Geol 163(1-2):147–163

Heydari E, Arzani N, Hassanzadeh J (2008) Mantle plume: The invisible serial killer — Application to the Permian–Triassic boundary mass extinction. Palaeogeogr Palaeoclimatol Palaeoecol 264:147–162

Heydari E, Arzani N, Safaei M, Hassanzadeh J (2013) Ocean's response to a changing climate: Clues from variations in carbonate mineralogy across the Permian–Triassic boundary of the Shareza Section, Iran. Global Planet Change 105:79–90

Heydari E, Hassandzadeh J, Wade WJ (2000) Geochemistry of central Tethyan Upper Permian and Lower Triassic strata, Abadeh region, Iran. Sediment Geol 137:85–99

Heydari E, Hassanzadeh J, Wade WJ, Ghazi AM (2003) Permian–Triassic boundary interval in the Abadeh section of Iran with implications for mass extinction: Part 1 – Sedimentology. Palaeogeogr Palaeoclimatol Palaeoecol 193:405–423

Heydari E, Wade WJ, Hassanzadeh J (2001) Diagenetic origin of carbon and oxygen isotope compositions of Permian–Triassic boundary strata. Sediment Geol 143:191–197

Higgins MB, Robinson RS, Husson JM, Carter SJ, Pearson A (2012) Dominant eukaryotic export production during ocean anoxic events reflects the importance of recycled NH_4^+. Proc Natl Acad Sci USA 109(7):2269–2274

Higgins MB, Robinson RS, Carter SJ, Pearson A (2010) Evidence from chlorin nitrogen isotopes for alternating nutrient regimes in the Eastern Mediterranean Sea. Earth Planet Sci Lett 290(1–2):102–107

Holmes B, Eichner C, Struck U, Wefer G (1999) Reconstructions of surface ocean nitrate utilization using stable nitrogen isotopes in sinking particles and sediments. In: Fischer G, Wefer G (eds) Use of proxies in paleoceanography: examples from the South Atlantic. Springer, Berlin pp 447–468

Holser WT, Magaritz M (1987) Events near the Permian–Triassic boundary. Modern Geology 11:155–180

Holser WT, Magaritz M (1992) Cretaceous/Tertiary and Permian/Triassic boundary events compared. Geochim Cosmochim Acta 56:3297–3309

Holser WT, Schönlaub H-P, Attrep M, Boeckelmann K, Klein P, Magaritz M, Orth CJ, Fenninger A, Jenny C, Kralik M, Mauritsch H, Pak E, Schramm J-M, Stattegger K, Schmoller R (1989) A unique geochemical record at the Permian/Triassic boundary. Nature 337:39–44

Horacek M, Richoz S, Brandner R, Krystyn L, Spötl C (2007) Evidence for recurrent changes in Lower Triassic oceanic circulation of the Tethys: the $d^{13}C$ record from marine section in Iran. Palaeogeogr Palaeoclimatol Palaeoecol 252:355–369

Hotinski RM, Bice KL, Kump LR, Najjar RG, Arthur MA (2001) Ocean stagnation and end-Permian anoxia. Geology 29:7–10

Hsü KJ, Jenkyns HC (1974) Pelagic sediments: on land and under the sea. Spec Publ Int Ass Sedimentol 1:1–447

Irwin H, Curtis CD, Coleman M (1977) Isotopic evidence for source of diagenetic carbonates

formed during burial of organic-rich sediments. Nature 269:209–213

Jaccard SL, Galbraith ED (2012) Large climate-driven changes of oceanic oxygen concentrations during the last deglaciation. Nature Geosci 5 (2):151–156

James NP, Choquette PW (1983) Diagenesis-5. Limestones. Geoscience Canada 10:159–161

Jin YG, Wang Y, Wang W, Shang QH, Cao CQ, Erwin DH (2000) Pattern of marine mass extinction near the Permian-Triassic boundary in South China. Science 289:432–436

Jin Y, Wang Y, Henderson C, Wardlaw BR, Shen S, Cao C (2006) The Global Boundary Stratotype Section and Point (GSSP) for the base of Changhsingian Stage (Upper Permian). Episodes 29(3):175–182

Jenkyns HC (1971) The genesis of condensed sequences in the Tethyan Jurassic. Lethaia 4(3):3279–352

Jenkyns HC (1974) Origin of red nodular limestones (Ammonitico Rosso, Knollenkalke) in the Mediterranean Jurassic: a diagenetic model. In: Hsü KJ, Jenkyns HC (eds) Pelagic sediments: on land and under the sea. Int Assoc Sediment Spec Publ 1:249–271

Jenkyns HC, Gröcke DR, Hesselbo SP (2001) Nitrogen isotope evidence for water mass denitrification during the early Toarcian (Jurassic) oceanic anoxic event. Paleoceanography 16(6):593–603

Joachimski MM, Simon L, van Geldern R, Lecuyer C (2005) Boron isotope geochemistry of Paleozoic brachiopod calcite: Implications for a secular change in the boron isotope geochemistry of seawater over the Phanerozoic. Geochim Cosmochim Acta 69(16):4035–4044

Joachimski MM, Lai XL, Shen SZ, Jiang H S, Luo GM, Chen B, Chen J, Sun YD (2012) Climate warming in the latest Permian and the Permian-Triassic mass extinction. Geology 40 (3):195–198

Junium CK, Arthur MA (2007) Nitrogen cycling during the Cretaceous, Cenomanian-Turonian Oceanic Anoxic Event II. Geochem Geophy Geosy 8(3):1–18

Kaiho K, Kajiwara Y, Nakano T, Miura Y, Kawahata H, Tazaki K, Ueshima M, Chen Z, Shi GR (2001) End-Permian catastrophe by a bolide impact: Evidence of a gigantic release of sulfur from the mantle. Geology 29(9):815–818

Kaiho K, Kajiwara Y, Chen Zhong-qiang, Gorjan P (2006a): A sulfur isotope event at the end of the Permian. Chem Geol 235:33–47

Kaiho K, Chen Zhong-qiang, Kawahata H. Kajiwara Y, Sato H (2006b): Close-up of the end-Permian mass extinction horizon recorded in the Meishan section, South China: Sedimentary, elemental, and biotic characterization and a negative shift of sulfate sulfur isotope ratio. Palaeogeogr Palaeoclimatol Palaeoecol 239:396–405

Kajiwara Y, Imai A, Ishida K, Ishiga H, Yamakita S (1994) Development of a largely anoxic stratified ocean and its temporary massive mixing at the Permian/Triassic boundary supported by the sulfur isotopic record. Palaeogeogr Palaeoclimatol Palaeoecol 111(3-4):367–379

Kakihana H, Kotaka M, Satoh S, Nomura M, Okamoto M (1977) Fundamental studies on the ion exchange separation of boron isotopes. Bull Chem Soc Jap 50:158–163

Kakuwa Y, Matsumoto R (2006) Cerium negative anomaly just before the Permian and Triassic boundary event – the upward expansion of anoxia in the water column. Palaeogeogr Palaeoclimatol Palaeoecol 229:335–344

Kamo SL, Czamanske GK, Amelin Y, Fedorenko VA, Davis DW, Trofimov VR (2003) Rapid eruption of Siberian flood-volcanic rocks and evidence for coincidence with the Permian–Triassic boundary and mass extinction at 251 Ma. Earth Planet Sci Lett 214:1–2:75–91

Kasemann SA, Hawkesworth CJ, Prave AR, Fallick AE, Pearson PN (2005) Boron and calcium isotope composition in Neoproterozoic carbonate rocks from Namibia: evidence for extreme environmental change. Earth Planet Sci Lett 231(1-2):73–86

Kershaw S (2015) Modern Black Sea oceanography applied to the end-Permain extinction event. J Palaeogeogr 4(1):52–62

Kershaw S, Guo L, Swift A, Fan J (2002) ?Microbialites in the Permian-Triassic boundary interval in central China: structure, age and distribution. Facies 47:83–90

Kershaw S, Crasquin S, Forel M-B, Randon C, Collin P-Y, Kosun E, Richoz S, Baud A (2011) Earliest Triassic microbialites in Çürük Dag, southern Turkey; composition, sequences and controls on formation. Sedimentology 58, 739–755

Kershaw S, Crasquin S, Li Y, Collin PY, Forel MB, Mu X, Baud A, Wang Y, Xie S, Maurer F, Guo L (2012) Microbialites and global environmental change across the Permian-Triassic boundary: a synthesis. Geobiology 10:25–47

Kershaw S, Li Y, Crasquin-Soleau S, Feng Q, Mu X, Collin P-Y, Reynolds A, Guo L (2007) Earliest Triassic microbialites in the South China block and other areas: controls on their growth and distribution. Facies 53:409–425

Kessler AJ, Bristow LA, Cardenas MB, Glud RN, Thamdrup B, Cook PLM (2014) The isotope effect of denitrification in permeable sediments. Geochim Cosmochim Acta 133(0):156–167

Kidder DL, Worsley TR (2004) Causes and consequences of extreme Permo-Triassic warming to globally equable climate and relation to the Permo-Triassic extinction and recovery. Palaeogeogr Palaeoclimatol Palaeoecol 203(3-4):207–237

Kiehl JT, Shields CA (2005) Climate simulation of the latest Permian: Implications for massextinction. Geology 33:757–760

Kienast M, Higginson MJ, Mollenhauer G, Eglinton T, Chen Min-Te, Calvert S (2005) On the

sedimentological origin of down-core variations of bulk sedimentary nitrogen isotope ratios. Paleoceanography 20(2):PA2009

Kiessling W, Simpson C (2011) On the potential for ocean acidification to be a general cause of ancient reef crises. Glob Chang Biol 17:56–67

Kiessling W, Schobben M, Ghaderi A, Hairapetian V, Leda L, Korn D (2018) Pre–mass extinction decline of latest Permian ammonoids. Geology 46 (3):283–286

Knauth LP, Kennedy MJ (2009) The late Precambrian greening of the Earth. Nature 460:728–732

Knies J, Grasby SE, Beauchamp B, Schubert CJ (2013) Water mass denitrification during the latest Permian extinction in the Sverdrup Basin, Arctic Canada. Geology 41:167–170

Knoll AH, Fischer WW (2011) Skeletons and ocean chemistry: The long view. In: Gattuso JP, Hansson L (eds) Ocean Acidification. Oxford, UK, Oxford University Press, p. 67–82

Knoll AH, Bambach RK, Canfield DE, Grotzinger JP (1996) Comparative earth history and Late Permian mass extinction. Science 273:452–457

Knoll AH, Barnbach RK, Payne JL, Pruss S, Fischer WW (2007) Paleophysiology and end-Permian mass extinction. Earth Planet Sci Lett 256:295–313

Koeberl C, Gilmour I, Reimold WU, Claeys P, Ivanov B (2002) End-Permian catastrophe by bolide impact: Evidence of a gigantic release of sulfur from the mantle: Geology 30(9):855–856

Koeberl C, Farley KA, Peucker-Ehrenbrink B, Sephton MA (2004) End-Permian catastrophe by bolide impact: Evidence of a gigantic release of sulfur from the mantle: Comment and Reply: Comment. Geology 32(12):1053–1056

Korn D, Ghaderi A, Leda L, Schobben M, Ashouri AR (2016) The ammonoids from the Late Permian *Paratirolites* Limestone of Julfa (East Azerbaijan, Iran). J Sys Paleontol 14(10):841–890

Korte C, Kozur HW (2005a) Carbon isotope stratigraphy across the Permian/Triassic boundary at Jolfa (NW-Iran), Peitlerkofel (Sas de Pütia, Sass de Putia), Pufels (Bula, Bulla), Tesero (all three Southern Alps, Italy) and Gerennavár (Bükk Mts., Hungary). J Alpine Geol 47:119–135

Korte C, Kozur HW (2005b) Carbon isotope trends in continental lake deposits of uppermost Permian to Lower Olenekian: Germanic lower Buntsandstein (Calvorde and Bernburg Formation). Halle Jb Geowiss B Beih 19:87–94

Korte C, Kozur HW (2010) Carbon-isotope stratigraphy across the Permian-Triassic boundary: A review. J Asian Earth Sci 39:215–235

Korte C, Kozur HW, Joachimski MM, Strauss H, Veizer J, Schwark L (2004a) Carbon, sulfur, oxygen and strontium isotope records, organic geochemistry and biostratigraphy across the

Permian/Triassic boundary in Abadeh, Iran. Int J Earth Sci 93: 565–581

Korte C, Kozur HW, Mohtat-Aghai P (2004b) Dzhulfian to lowermost Triassic $\delta^{13}C$ record at the Permian/Triassic boundary section at Shahreza, Central Iran. Halle Jb Geowiss B Beih 18:73–78

Korte C, Kozur HW, Partoazar H (2004c) Negative carbon isotope excursion at the Permian/Triassic boundary section at Zal, NW Iran. Halle Jb Geowiss B Beih 18:69–71

Korte C, Pande P, Kalia P, Kozur HW, Joachimski MM, Oberhänsli H (2010) Massive volcanism at the Permian-Triassic boundary and its impact on the isotopic composition of the ocean and atmosphere. J Asian Earth Sci 37:293–311

Kotlyar GV, Zakharov YD, Koczyrkevicz BV, Kropatcheva GS, Rostovcev KO, Chedija IO, Vuks GP, Guseva EA (1983) Pozdnepermskiy etap evolyutsii organicheskogo mira. Dzul'fichеskiy i dorashamskiy yarusy SSSR. In: Gramm MN, Rostovcev KO (eds) Proekt No 106 (''Permo-Triasovaya stadiya geologicheskoy evolyutsii'') mezhdunarodnoy programmy geologicheskoy korrelatsii, 70p.

Kozur HW (1998) Some aspects of the Permian–Triassic boundary (PTB) and of the possible causes for the biotic crisis around this boundary. Palaeogeogr Palaeoclimatol Palaeoecol 143:227–272

Kozur HW (2004) Pelagic uppermost Permian and the Permian–Triassic boundary conodonts of Iran, Part I: Taxonomy. Halle Jb Geowiss B Beih 18:39–68

Kozur HW (2005) Pelagic uppermost Permian and the Permian– Triassic boundary conodonts of Iran. Part II: investigated sections and evaluation of the conodont faunas. Halle J Geowiss B Beih 19:49–86

Kozur HW (2007) Biostratigraphy and event stratigraphy in Iran around the Permian–Triassic Boundary (PTB): Implications for the causes of the PTB biotic crisis. Global Planet Change 55:155–176

Kozur HW, Leven EY, Lozovskiy VR, Pyatakova MV (1980) Subdivision of Permian–Triassic Boundary beds in Transcaucasia on the basis of conodonts. Int Geol Rev 22:361–368

Kraus SH, Brandner R, Heubeck C, Kozur HW, Struck U, Korte C (2013) Carbon isotope signatures of latest Permian marine successions of the Southern Alps suggest a continental runoff pulse enriched in land plant material. Foss Rec 16:97–109

Krull ES, Retallack GJ (2000) $\delta^{13}C$ depth profiles from paleosols across the Permian-Triassic boundary: Evidence for methane release. Geol Soc Am Bull 112:1459–1472

Krull ES, Retallack GJ, Campbell HJ, Lyon GL (2000) $\delta^{13}C_{org}$ chemostratigraphy of the Permian-Triassic boundary in the Maitai Group, New Zealand: evidence for high-latitudinal methane release. New Zeal J Geol Geop 43:21–32

Kump LR, Arthur MA (1999) Interpreting carbon-isotope excursions: Carbonates and organic matter. Chem Geol 161(1-3):181–198

Kump LR, Pavlov A, Arthur Ma (2005) Massive release of hydrogen sulfide to the surface ocean and atmosphere during intervals of oceanic anoxia. Geology 33(5):397–400

Kuypers MMM, Lavik G, Woebken D, Schmid M, Fuchs BM, Amann R, Barker Jørgensen B, Jetten MSM (2005) Massive nitrogen loss from the Benguela upwelling system through anaerobic ammonium oxidation. Proc Natl Acad Sci USA 102:6478–6483

Langenhorst F, Kyte FT, Retallack GR (2005) Reexamination of quartz grains from the Permian-Triassic boundary section at Graphite Peak, Antarctica. Lunar Planet Sci XXXVI, abstr. # 2358, 2p.

Leda L, Korn D, Ghaderi A, Hairapetian V, Struck U, Reimold WU (2014) Lithostratigraphy and carbonate microfacies across the Permian-Triassic boundary near Julfa (NW Iran) and in the Baghuk Mountain (Central Iran). Facies 60:295–325

Lehrmann DJ (1999) Early Triassic calcimicrobial mounds and biostromes of the Nanpanjiang Basin, South China. Geology 27:359–362

Lehrmann DJ, Wei Jiayong, Enos Paul (1998) Controls on facies architecture of a large Triassic carbonate platform: The Great Bank of Guizhou, Nanpanjiang Basin, South China. J Sediment Res 68:311–326

Lehrmann DJ, Yang Wan, Wei Jiayong, Yu Youyi, Xiao Jiafei (2001) Lower Triassic peritidal cyclic limestone: an example of anachronistic carbonate facies from the Great Bank of Guizhou, Nanpanjiang Basin, Guizhou province, South China. Palaeogeogr Palaeoclimatol Palaeoecol 173: 103–123

Lehrmann DL, Payne JL, Felix SV, Dillett PM, Wang H, Yu Y, Wei J (2003) Permian–Triassic boundary sections from shallow-marine carbonate platforms of the Nanpanjiang Basin, South China: implications for oceanic conditions associated with the end-Permianextinction and its aftermath. Palaios 18:138–152

Leven EJa (1998) Permian Fusulinid assemblages and stratigraphy of the Transcaucasia. Riv Ital Paleontol S 104(3):299–328

Li D, Ling H-F, Shields-Zhou GA, Chen X, Cremonese L, Och L, Thirlwall M, Manning C J (2013) Carbon and strontium isotope evolution of seawater across the Ediacaran–Cambrian transition: Evidence from the Xiaotan section, NE Yunnan, South China. Precambrian Res 225(0):128–147

Liao W, Wang Y, Kershaw S, Weng Z, Yang H (2010) Shallow marine dysoxia across the Permian-Triassic boundary; evidence frompyrite framboids in the microbialite in South China. Sediment Geol 232:77–83

Liu KK, Kaplan IR (1988) Variation of nitrogen isotope fractionation during denitrification and nitrogen isotope balance in the ocean. EOS 69:1098

Liu KK, Kao SJ, Hu HC, Chou WC, Hung GW, Tseng CM (2007) Carbon isotopic composition of suspended and sinking particulate organic matter in the northern South China Sea-From production to deposition: Deep Sea Res Part II. Top Stud Oceanogr 54(14-15):1504–1527

Liu X-C, Wang W, Shen S-Z, Gorgij MN, Ye F-C, Zhang Y-C, Furuyama S, Kano A, Chen X-Z (2013) Late Guadalupian to Lopingian (Permian) carbon and strontium isotopic chemostratigraphy in the Abadeh section, central Iran. Gondwana Res 24:222–232

Logan BW, Rezak R, Ginsburg RN (1964) Classification and environmental significance of algal stromatolites. J Geol 72:68–83

Lohman KC (1987) Geochemical patterns of meteoric diagenetic systems and their applications to studies of palekarst. In: James NP, Choquette PW (eds) Soc Econ Paleontol Mineral, Special Publication, Tulsa, pp 58–80

Looy CV, Brugman WA, Dilcher DL, Visscher H (1999) The delayed resurgence of equatorial forests after the Permian–Triassic cologic crisis. Proc Natl Acad Sci USA 96:13857–13862

Luo G, Wang Y, Yang H, Algeo TJ, Kump LR, Huang J, Xie S (2011) Stepwise and large-magnitude negative shift in delta C-13(carb) preceded the main marine mass extinction of the Permian-Triassic crisis interval. Palaeogeogr Palaeoclimatol Palaeoecol 299:70–82

Luo G, Wang Y, Grice K, Kershaw S, Ruan X, Algeo TJ, Yang H, Jia C, Xie S (2013) Microbial-algal community changes during the latest Permian ecological crisis: evidence from lipid biomarkers at Cili, South China. Global Planet Change 105:36–51

Luo G, Algeo TJ, Zhan R, Yan D, Huang J, Liu J, Xie S (2016) Perturbation of the marine nitrogen cycle during the Late Ordovician glaciation and mass extinction. Palaeogeogr Palaeoclimatol Palaeoecol 448:339–348

Macko SA, Fogel ML, Hare PE, Hoering TC (1987) Isotopic fractionation of nitrogen and carbon in the synthesis of amino acids by microorganisms. Chem Geol Isot Geosci 65:79–92

Magaritz M, Bart R, Baud A, Holser WT (1988) The carbon-isotope shift at the Permian/Triassic boundary in the southern Alps is gradual. Nature 331:337–339

Malkowski K, Gruszczyński M, Hoffman A, Halas S (1989) Oceanic stable isotope composition and a scenario for the Permo-Triassic crisis. Hist Biol 2:289–309

Mamet B, Préat A (2003) Sur l'origine bactérienne et fongique de la pigmentation de l'Ammonitico Rosso (Jurassique, région de Vérone, Italie du nord). Rev Micropaléontol 46:35–46

Mamet B, Préat A (2005) Why is red marble red? Rev Espanñ Micropaléontol 37:13–21Mariotti A (1983) Atmospheric nitrogen as a reliable standard for natural ^{15}N abundance measurements. Nature 303:685–687

Mamet B, Préat A (2006a) Iron-bacterial mediation in Phanerozoic red limestones: state of the art. Sediment Geol 185:147–157

Mamet B, Préat A (2006b) Jurassic microfacies, Rosso Ammonitico Limestone, Subbetic Cordillera, Spain. Rev Españ Micropaléontol 38:219–228

Mariotti A, Pierre D, Vedy JC, Bruckert S, Guillemot J (1980) The abundance of natural nitrogen 15 in the organic matter of soils along an altitudinal gradient (Chablais, Haute Savoie, France). Catena 7(4):293–300

Marshall JD (1992) Climatic and oceanographic isotopic signals from the carbonate rock record and their preservation. Geol Mag 129:143–160

Maurer F, Martini R, Rettori R, Hillgärtner H, Cirilli S (2009) The geology of Khuff outcrop analogues in the Musandam Peninsula, United Arab Emirates and Oman. GeoArabia 14:125–158

McConnaughey TA (1989a) ^{13}C and ^{18}O isotope disequilibria in biological carbonates. 1. Patterns. Geochim Cosmochim Acta 53:151–162

McConnaughey TA (1989b) ^{13}C and ^{18}O isotope disequilibria in biological carbonates. 2. In vitro simulation of kinetic isotope effects. Geochim Cosmochim Acta 53:163–171

McLean DM (1985) Deccan Traps mantle degassing in the terminal Cretaceous marine extinctions. Cretaceous Res 6(3):235–259

Melim LA, Westphal H, Swart PK, Eberli GP, Munnecke A (2002) Questioning carbonate diagenetic paradigms: evidence from the Neogene of the Bahamas. Marine Geol 185(1-2):27–53

Melzner F, Gutowska MA, Langenbuch M, Dupont S, Lucassen M, Thorndyke MC, Bleich M, Pörtner H-O (2009) Physiological basis for high CO_2 tolerance in marine ectothermic animals: pre-adaptation through lifestyle and ontogeny? Biogeosciences 6:2313–2331

Metcalfe B, Twitchett RJ, Price-Lloyd N (2011) Size and growth rate of 'Lilliput' animals in the earliest Triassic. 308(1-2):171–b180

Mette W, Mohtat-Aghai P (2004) Late Permian and Early Triassic microfossil assemblages of Iran. Ber. Inst. Erdwiss. K.-F. Univ. Graz, 9:263–265

Meyer KM, Kump LR, Ridgwell A (2008) Biogeochemical controls on photic-zone euxinia during the end-Permian mass extinction. Geology 36(9):747–750

Meyers PA (1994) Preservation of elemental and isotopic source identification of sedimentary organic matter. Chem Geol 114:289–302

Milder JC, Montoya JP, Altabet MA (1999) Carbon and nitrogen stable isotope ratios at Sites 969 and 974: interpreting spatial gradients in sapropel properties. In: Zahn R, Comas MC, Klaus A (eds) Proceedings of the Ocean Drilling Program, Scientific Results 161:401–411

Mohtat Aghai P, Vachard D, Krainer K (2009) Transported Foraminifera in the Palaeozoic deep

red nodular Limestones; exemplified by Latest Permian Neoendothyra in the Zal section (Julfa area, NW Iran). Rev Españ Micropaléontol 41:197–213

Montoya JP (2008) Chapter 29 - Nitrogen Stable Isotopes in Marine Environments. In: Capone DG, Bronk DA, Mulholland MR, Carpenter EJ (eds) Nitrogen in the Marine Environment (2nd Edition). San Diego, Academic Press:1277–1302

Montoya JP, Carpenter EJ, Capone DG (2002) Nitrogen-fixation and nitrogen isotope abundances in zooplankton of the oligotrophic North Atlantic. Limnol Oceanogr 47:1617–1628

Moore CM, Mills MM, Arrigo KR, Berman-Frank I, Bopp L, Boyd PW, Galbraith ED, Geider RJ, Guieu C, Jaccard SL, Jickells TD, La Roche J, Lenton TM, Mahowald NM, Marañón E, Marinov I, Moore JK, Nakatsuka T, Oschlies A, Saito MA, Thingstad TF, Tsuda A, Ulloa O (2013) Processes and patterns of oceanic nutrient limitation. Nat Geosci 6:701–710

Mu X, Kershaw S, Li Y, Guo L, Qi Y, Reynolds A (2009) High-resolution carbon isotope changes in the Permian–Triassic boundary interval, Chongqing, South China; implications for control andgrowth of earliest Triassic microbialites. J Asian Earth Sci 36:434–441

Musashi M, Isozaki Y, Koike T, Kreulen R (2001) Stable carbon isotope signature in mid-Panthalassa shallow-water carbonates across the Permo-Triassic boundary: evidence for C-13-depleted superocean. Earth Planet Sci Lett 191:9–20

Muttoni G, Gaetani M, Kent D, Sciunnach D, Angiolini L, Berra F, Garzanti E, Mattei M, Zanchi A(2009a) Opening of the Neo-tethys ocean and the pangea B to pangea A transformation during the permian. GeoArabia 14(4):17–48

Muttoni G, Mattei M, Balini M, Zanchi A, Gaetani M, Berra F (2009b) The drift historyof Iran from the Ordovician to the Triassic. In: Brunet M-F, Wilmsen M, Granath J (eds)South Caspian to Central Iran Basins. Geol Soc London Spec Publ 312:7–29

Müller PJ (1977) C/N ratios in Pacific deep-sea sediments: effect of inorganic ammonium and organic nitrogen compounds sorbed by clays. Geochim Cosmochim Acta 41:549–553

Newton RJ, Pevitt EL, Wignall PB, Bottrell SH (2004): Large shifts in the isotopic composition of seawater sulphate across the Permo–Triassic boundary in northern Italy. Earth Planet Sci Lett 218:331–345

Nier AO (1950) A redetermination of the relative abundances of the isotopes of carbon, nitrogen, oxygen, argon, and potassium. Phys Rev 77:789

Oberhänsli H, Hsü KJ, Piasecki S, Weissert H (1989) Permian–Triassic carbon isotope anomaly in Greenland and in the Southern Alps. Hist Biol 2:37–49

Ohkouchi N, Nakajima Y, Okada H, Ogawa NO, Suga H, Oguri K and Kitazato H (2005) Biogeochemical processes in the saline meromictic Lake Kaiike, Japan: implications from molecular isotopic evidences of photosynthetic pigments. Environ Microbiol 7(7):1009–1016

Ohkouchi N, Kashiyama Y, Kuroda J, Ogawa NO, Kitazato H (2006) The importance of diazotrophic cyanobacteria as primary producers during Cretaceous Oceanic Anoxic Event 2. Biogeosciences 3(4):467–478

O'Leary MH (1981) Carbon isotope fractionation in plants. Phytochemistry 20:553–567

Ozaki K, Tajima S, Tajika E (2011) Conditions required for oceanic anoxia/euxinia: Constraints from a one-dimensional ocean biogeochemical cycle model. Earth Planet Sci Lett 304(1-2):270–279

Pancost RD, Crawford N, Magness S, Turner A, Jenkyns HC, Maxwell JR (2004) Further evidence for the development of photic-zone euxinic conditions during Mesozoic oceanic anoxic events. J Geol Soc 161:353–364

Partoazar H (2002) Permian–Triassic boundary conodonts from Julfa-Abadeh Belt along Northwest and Central Iran. Permophiles 41:34–40

Payne JL, Kump LR (2007) Evidence for recurrent Early Triassic massive volcanism from quantitative interpretation of carbon isotope fluctuations. Earth Planet Sci Lett 256:264–277

Payne JL, Lehrmann DJ, Wei J, Knoll AH (2006) The pattern and timing of biotic recovery from the end-Permian extinction on the Great Bank of Guizhou, Guizhou Province, China. Palaios 21:63–85

Payne JL, Turchyn AV, Paytan A, DePaolo DJ, Lehrmann DJ, Yu M, Wei J (2010) Calcium isotope constraints on the end-Permian mass extinction. Proc Natl Acad Sci USA 107(19):8543–8548

Pietsch C, Petsios E, Bottjer DJ (2016) Sudden and extreme hyperthermals, low-oxygen, and sediment influx drove community phase shifts following the end-Permian mass extinction. Palaeogeogr Palaeoclimatol Palaeoecol 451:183–196

Peng YQ, Zhang SX, Yu TX, Yang FQ, Gao YQ. Shi GR (2005) High-resolution terrestrial Pennian-Triassic eventostratigraphic boundary in western Guizhou and eastern Yunnan, southwestern China. Palaeogeogr Palaeoclimatol Palaeoecol 215:285–295

Pörtner H-O (2001) Climate change and temperature-dependent biogeography: Oxygen limitation of thermal tolerance in animals. The Science of Nature 88(4):137–46

Pörtner H-O, Langenbuch M, Reipschläger A (2004) Biological Impact of Elevated Ocean CO2 Concentrations: Lessons from Animal Physiology and Earth History. J Oceanogr 60(4):705–718

Pörtner H-O, Langenbuch M, Michaelidis B (2005a) Synergistic effects of temperature extremes, hypoxia, and increases in CO_2 on marine animals: From Earth history to global change. J Geophys Res-Oceans (1978–2012): 110(C9)

Pörtner H-O, Langenbuch M, Michaelidis B (2005b) Synergistic effects of temperature extremes, hypoxia, and increases in CO2 on marine animals: From Earth history to global change.

J Geophys Res 110: C09S10

Préat A, Mamet B, Bernard A, Gillan D (1999) Bacterial modification, red matrices diagenesis, Devonian, Montagne Noire (southern France). Sediment Geol 126:223–242

Préat A, Mamet B, De Ridder C, Boulvain F, Gillan D (2000) Iron bacterial and fungal mats, Bajocian stratotype (Mid-Jurassic, northern Normandy, France). Sediment Geol 137:107–126

Préat A, Loreau JP, Durlet C, Mamet B (2006) Petrography and biosedimentology of the Rosso Ammonitico Veronese (Middle–Upper Jurassic, Northeastern Italy). Facies 52:265–278

Préat A, Mattielli NL, De Jong J, Mamet B (2008) Stable iron isotopes confirm microbial mediation in red pigmentation of the Rosso Ammonitico (Mid-Late Jurassic, Verona Area, Italy). Astrobiology 8:841–857

Pride C, Thunell R, Sigman D, Keigwin L, Altabet M, Tappa E (1999) Nitrogen isotopic variations inthe Gulf of California since the last deglaciation: Response to global climate change. Paleoceanography 4(3):397–409

Preto N, Spötl C, Mietto P, Gianolla P, Riva A, Manfrin S (2005) Aragonite dissolution, sedimentation rates and carbon isotopes in deep-water hemipelagites (Livinallongo Formation, Middle Triassic, northern Italy). Sediment Geol 181:173–194

Pruss SB, Bottjer DJ (2004) Early Triassic trace fossils of the western United States and their implications for prolonged environmental stress from the end-Permian mass extinction. Palaios 19:551–564

Pruss SB, Corsetti FA, Bottjer DJ (2005) The unusual sedimentary rock record of the Early Triassic: a case study from the southwestern United States. Palaeogeogr Palaeoclimatol Palaeoecol 222:33–52

Pruss SB, Bottjer DJ, Corsetti FA, Baud A (2006) A global marine sedimentary response to the end-Permian mass extinction: Examples from southern Turkey and the western United States. Earth-Sci Rev 78:193–206

Racki G (1999) Kontrowersje wokół przyczyn wielkich katastrof ekologicznych w historii Ziemi: podsumowanie debaty. Przegl Geol 47:343–348

Rampino MR, Caldeira K (2005) Major perturbation of ocean chemistry and a ‘Strangelove Ocean’ after the end-Permian mass extinction. Terra Nova 17:554–559

Rao CP (1996) Modern carbonates. Tropical, temperate, polar. Howrah (Carbonates), 206 p.

Raven JA (1997) Inorganic carbon acquisition by marine autotrophs. Adv Bot Res 27:85–209

Reichow MK, Pringle MS, Al’Mukhamedov AI, Allen MB, Andreichev VL, Buslov MM, Davies CE, Fedoseev GS, Fitton JG, Inger S, Medvedev AY, Mitchell C, Puchkov VN, Safonova IY, Scott RA, Saunders AD (2009) The timing and extent of the eruption of the Siberian

Traps large igneous province: Implications for the end-Permian environmental crisis. Earth Planet Sci Lett 277:9–20

Renne PR, Melosh HJ, Farley KA, Reimold WU, Koeberl C, Rampino MR, Kelly SP, Ivanov BA (2004) Is bedout an impact Crater? Take 2. Science 306(5696):611–612

Renne PR, Zichao Z, Richards MA, Black MT, Basu AR (1995) Synchrony and causal relations between Permian–Triassic boundary crisis and Siberian flood volcanism. Science 269:1414–1416

Repeta DJ, Simpson DJ, Jørgensen BB, Jannasch HW (1989) Evidence for anoxygenic photosynthesis from the distribution of bacteriochlorophylls in the Black Sea. Nature 342:69–72

Retallack GJ, Jahren AH (2008) Methane release from igneous intrusion of coal during late permian extinction events. J Geol 116:1–20

Retallack GJ, Krull ES (2006) Carbon isotopic evidence for terminal-Permian methane outbursts and their role in extinctions of animals, plants, coral reefs, and peat swamps. Geol Soc Spec Pap 399:249–268

Retallack GJ, Seyedolali A, Krull ES, Holser WT, Ambers CP, Kyte FT (1998) Search for evidence of impact at the Permian-Triassic boundary in Antarctica and Australia. Geology 26:979–982

Retallack GJ, Jahren AH, Sheldon ND, Chakrabarti R, Metzger CA, Smith RMH (2005) The Permian-Triassic boundary in Antarctica. Antarc Sci 17:241–258

Retallack GJ, Sheldon ND, Carr PF, Fanning M, Thompson, CA, Williams ML, Jones BG, Hutton A (2011) Multiple Early Triassic greenhouse crises impeded recovery from Late Permian mass extinction. Palaeogeogr Palaeoclimatol Palaeoecol 308:233–251

Riebesell U, Zondervan I, Rost B, Tortell PD, Zeebe RE, Morel FM (2000) Reduced calcification of marine plankton in response to increased atmospheric CO_2. Nature 407(6802):364–7

Riedinger N, Brunner B, Lin YS, Voßmeyer A, Ferdelman TG, Jørgensen BB (2010) Methane at the sediment–water transition in Black Sea sediments. Chem Geol 274(1-2):29–37

Riccardi AL, Arthur MA, Kump LR (2006) Sulfur isotopic evidence for chemocline upward excursions during the end-Permian mass extinction. Geochim Cosmochim Acta 70: 5740–5752

Riccardi A, Kump LR, Arthur MA, D'Hondt S (2007) Carbon isotopic evidence for chemocline upward excursions during the end-Permian event. Palaeogeogr Palaeoclimatol Palaeoecol 248:73–81

Richoz S (2006) Stratigraphie et variations isotopiques du carbone dans le Permien supérieur et le Trias inférieur de la Neéotéhys (Turquie, Oman et Iran). Mem Géol Lausanne 46:1–251

Richoz S, Krystyn L, Baud A, Brandner R, Horacek M, Mohtat-Aghai P (2010) Permian-Tri-

assic boundary interval in Middle East (Iran and N. Oman): progressive environmental change from detailed carbonate carbon isotope marine curve and sedimentary evolution. J Asian Earth Sci 39:236–253

Riding R (1997) Stromatolite decline: a brief reassessment. In: Neuweiler F, Reitner J, Monty C (eds) Biosedimentology of Microbial Buildups. Facies 36:227–230

Riding R (2000) Microbial carbonates: the geological record of calcified bacterial-algal mats and biofilms. Sedimentology 47(1):179–214

Riding R (2005) Phanerozoic reefal microbial carbonate abundance: comparisons with metazoan diversity, mass extinction events, and seawater saturation state. Rev Españ Micropaléontol 37(1):23–39

Riding R (2008) Abiogenic, microbial and hybrid authigenic carbonate crusts: components of Precambrian stromatolites. Geol Croat 61(2–3):73–103

Riding R (2011) The nature of stromatolites: 3,500 million years of history and a century of research. In: Reitner J, Quéric N-V, G. Arp G (eds) Advances in Stromatolite Geobiology, Springer, Heidelberg, Lecture Notes in Earth Sciences 131: 29–74

Riding R, Liang L (2005) Geobiology of microbial carbonates: metazoan and seawater saturation state influences on secular trends during the Phanerozoic. Palaeogeogr Palaeoclimatol Palaeoecol 219:101–115

Robinson RS, Kienast M, Luiza Albuquerque A, Altabet M, Contreras S, De Pol Holz R, Dubois N, Francois R, Galbraith E, Hsu T-C, Ivanochko T, Jaccard S, Kao S-J, Kiefer T, Kienast S, Lehmann M, Martinez P, McCarthy M, Möbius J, Pedersen T, Quan TM, Ryabenko E, Schmittner A, Schneider R, Schneider-Mor A, Shigemitsu M, Sinclair D, Somes C, Studer A, Thunell R, Yang J-Y (2012) A review of nitrogen isotopic alteration in marine sediments. Paleoceanography 27(4):PA4203

Rothman DH, Fournier GP, French KL, Alm EJ, Boyle EA, Cao C, Summons RE (2014) Methanogenic burst in the end- Permian carbon cycle. Proc Natl Acad Sci USA 111:5462–5467

Rostovtsev KO, Azaryan NR (1973) The Permian-Triassic Boundary in Transcaucasia, Can Soc Petrol Geol Memoir 2:89–99

Ruban DA, Al-Husseini MI, Iwasaki Y (2007a) Review of Middle East Paleozoic plate tectonics. GeoArabia 12:35–56

Ruban DA, Zerfass H, Yang W (2007b) A new hypothesis on theposition of the Greater Caucasus Terrane in the Late Palaeozoic–Early Mesozoic based on palaeontologic and lithologic data. Trab Geol 27:19–27

Ruzhencev VE, Sarycheva TG (1965) (eds) Razvitie i smena morskikh organizmov na Rubezhe Paleozoya i Mezozoya. Trudy Paleont Inst Akad Nauk SSSR 108 Ruzhencev VE, Sarycheva

TG, Shevyrev, AA (1965) Biostratigraficheskie vyvody. Trudy Paleont Inst Akad Nauk SSSR 108:93–116

Sachs JP, Repeta DJ (1999) Oligotrophy and Nitrogen Fixation During Eastern Mediterranean Sapropel Events. Science 286(5449):2485–2488

Saitoh M, Ueno Y, Nishizawa M, Isozaki Y, Takai K, Yao J, Ji Z (2014) Nitrogen isotope chemostratigraphy across the Permian–Triassic boundary at Chaotian, Sichuan, South China. J Asian Earth Sci 93:113–128

Saltzman MR, Thomas E (2012). Chapter 11 - Carbon Isotope Stratigraphy. In: Gradstein F M, Ogg JG, Schmitz MD, Ogg GM (eds) The Geologic Time Scale. Boston, Elsevier, 207–232

Sandler A, Eshet Y, Schilman B (2006) Evidence for a fungal event, methane-hydrate release and soil erosion at the Permian-Triassic boundary in southern Israel. Palaeogeogr Palaeoclimatol Palaeoecol 242:68–89

Sano H, Nakashima K (1997) Lowermost Triassic (Griesbachian) microbial bindstone-cementstone facies, southwest Japan. Facies 36:1–24

Sarkar A, Yoshioka H, Ebihara M, Naraoka H (2003) Geochemical and organic carbon isotope studies across the continental Permo–Triassic boundary of Raniganj Basin, eastern India. Palaeogeogr Palaeoclimatol Palaeoecol 191:1–14

Saunders A, Reichow M (2009) The Siberian Traps and the End-Permian mass extinction: a critical review. Chinese Sci Bull 54(1):20–37

Schaller M, Wright J, Kent D, Olsen P (2012) Rapid emplacement of the Central Atlantic Magmatic Province as a net sink for CO_2. Earth Planet Sci Lett 323–324:27–39

Scheffer F, Schachtschabel P (1970) Lehrbuch der Bodenkunde. Enke Verlag, Stuttgart, 448 p.

Schlager W (1974) Preservation of cephalopod skeletons and carbonate dissolution on ancient Tethyan sea floors. Spec Publ Intern Assoc Sediment 1:49–70

Schlager W (2002) Sedimentology and sequence stratigraphy of carbonate rocks. Frije Universiteit, Amsterdam, 146 p.

Schobben M, Joachimski MM, Korn D, Leda L, Korte C (2014) Palaeotethys seawater temperature rise and an intensified hydrological cycle following the end-Permian mass extinction. Gondwana Res 26:675–683

Schobben M, Stebbins A, Ghaderi A, Strauss H, Korn D, Korte C (2015) Flourishing ocean drives the end-Permian marine mass extinction. Proc Natl Acad Sci USA 112:10298–10303

Schobben M, Ullmann CV, Leda L, Korn D, Struck U, Reimold WU, Ghaderi A, Algeo TJ, Korte C (2016) Discerning primary versus diagenetic signals in carbonate carbon and oxygen stable isotope records: An example from the Permian-Triassic boundary of Iran. Chem Geol

422:94–107

Schobben M, van de Velde S, Gliwa J, Leda L, Korn D, Struck U, Ullmann CV, Hairapetian V, Ghaderi A, Korte C, Newton RJ, Poulton SW, Wignal PB (2017) Latest Permian carbonate-carbon isotope variability traces heterogeneous organic carbon accumulation and authigenic carbonate formation. Clim Past 13:1635–1659

Schoepfer SD, Henderson CM, Garrison GH, Foriel J, Ward PD, Selby D, Hower JC, AlgeoTJ, Shen Y (2013a) Termination of a continent-margin upwelling system at the Permian carbonate-carbon isotope variability traces heterogeneous organic carbon accumulation and authigenic carbonate formation. Clim Past 13:1635–1659

Schoepfer SD, Henderson CM, Garrison GH, Foriel J, Ward PD, Selby D, Hower JC, AlgeoTJ, Shen Y (2013b) Termination of a continent-margin upwelling system at the Permian–Triassic boundary (Opal Creek, Alberta, Canada). Global Planet Change 105:21–35

Scholle P, Arthur MA (1980) Carbon isotope fluctuations in Cretaceous pelagic limestones: potential stratigraphic and petroleum exploration tool. Bull. Amer Assoc Petrol Geol 64:67–87

Schrag DP, Higgins JA, Macdonald FA, Johnston DT (2013) Authigenic Carbonate and the History of the Global Carbon Cycle. Science 339(6119):540–543

Schubert JK, Bottjer DJ (1992) Early Triassic stromatolites as post-mass extinction disaster forms. Geology 20(10):883–886

Schubert CJ, Calvert SE (2001) Nitrogen and carbon isotopic composition of marine and terrestrial organic matter in Arctic Ocean sediments: implications for nutrient utilization and organic matter composition. Deep Sea Res Part I. Oceanogr Res Pap 48(3): 789–810

Scholten SO (1991) The distribution of nitrogen isotopes in sediments. Geol Ultraiect 81:101

Schwab V, Spangenberg JE (2004) Organic geochemistry across the Permian-Triassic transition at the Idrijca Valley, Western Slovenia. Appl Geochem 19:55–72

Scotese CR, Langford RP (1995) Pangea and the paleogeography of the Permian. In: Scholle PA, Peryt TM, Ulmer-Scholle DS (eds) The Permian of northern Pangea. Springer, Berlin, pp 3–19

Sephton MA, Veefkind RJ, Looy CV, Visscher H, Brinkhuis H, de Leeuw JW (2001) Lateral variations in end-Permian organic matter. In: Buffetaut E, Koeberl C (eds) Geological and biological effects of impact events. Springer, Berlin, 11–24

Sephton MA, Jiao D, Engel MH, Looy CV Visscher H (2015) Terrestrial acidification during the end-Permian biosphere crisis? Geology 43(2):159–162

Sengör AMC (1990) A new model for the late Palaeozoic–Mesozoictectonic evolution of Iran and implications for Oman. Geol Soc London Spec Publ 49:797–831

Shapiro RS (2000) A comment on the systematic confusionof thrombolites. Palaios 15:166–169

Sharp Z (2007) Principles of Stable Isotope Geochemistry. New Jersey, Pearson Prentice Hall, 355 p.

Shen S-Z, Mei SL (2010) Lopingian (Late Permian) high-resolution conodont biostratigraphy in Iran with comparison to South China zonation. Geol J 45:135–161

Shen S-Z, Crowley JL, Wang Y, Bowring SA, Erwin DH, Sadler PM (2011) Calibrating the End-Permian Mass Extinction. Science 334(6061):1367–1372

Shen J, Algeo TJ, Hu Q, Zhang N, Zhou L, Xia WC, Xie SC, Feng QL (2012a) Negative C-isotope excursions at the Permian-Triassic boundary linked to volcanism. Geology 40:963–966

Shen J, Algeo TJ, Zhou L, Feng Q, Yu J, Ellwood B (2012b) Volcanic perturbations of the marine environment in South China preceding the latest Permian mass extinction and their biotic effects. Geobiology 10:82–103

Shen J, Schoepfer SD, Feng Q, Zhou L, Yu J, Song H, Wei H, Algeo TJ (2015) Marine productivity changes during the end-Permian crisis and Early Triassic recovery. Earth-Sci Rev 149:136–162

Siegert S, Kraus SH, Mette W, Struck U, Korte C (2011) Organic carbon isotope values from the Late Permian Seis/Siusi succession (Dolomites, Italy): Implications for palaeoenvironmental changes. Fossil Rec 14:207–217

Sigman DM, Altabet MA, McCorkle DC, François R, Fischer G (2000) The $\delta^{15}N$ of nitrate in the Southern Ocean: Nitrogen cycling and circulation in the ocean interior. J Geophys Res-Oceans 105(C8):19599–19614

Sigman DM, Karsh KL, Casciotti KL (2009) Nitrogen Isotopes in the Ocean. In: Steele JH, (eds) Encyclopedia of Ocean Sciences (2nd Edition): Oxford, Academic Press, 40–54

Sobolev SV, Sobolev AV, Kuzmin DV, Krivolutskaya NA, Petrunin AG, Arndt NT, Radko VA, Vasiliev YR (2011) Linking mantle plumes, large igneous provinces and environmental catastrophes. Nature 477:312–316

Song H, Tong J, Algeo TJ, Song H, Qiu H, Zhu Y, Tian L, Bates S, Lyons TW, Luo G, Kump LR (2014) Early Triassic seawater sulfate drawdown. Geochim Cosmochim Acta 128:95–113

Song HJ, Wignall PB, Tong J, Yin H (2013) Two pulses of extinction during the Permian-Triassic crisis. Nature Geosci 6(1):52–56

Song HJ, Wignall PB, Tong J, Song HY, Chen J, Chu DL, Tian L, Luo M, Zong KQ, Chen YL, Lai XL, Zhang KX, Wang HM (2015) Integrated Sr isotope variations and global environmental changes through the Late Permian to early Late Triassic. Earth Planet Sci Lett 424:140–147

Spivack AJ, You CF, Smith HJ (1993) Foraminiferal boron isotope ratios as a proxy for surface

ocean pH over the past 21 Myr. Nature 363:149–151

Stampfli GM, Borel GD (2002) A plate tectonic model for the Paleozoic and Mesozoic constrained by dynamic plate boundaries and restored synthetic oceanic isochrons. Earth Planet Sci Lett 196:17–33

Stampfli GM, Borel GD (2004) The TRANSMED transects in space and time. Constraints on the paleotectonic evolution of the Mediterranean Domain. In: Cavazza W, Roure F, Spakman W, Stampfli GM, Ziegler P (eds) The TRANSMED Atlas: the Mediterranean region from crust to mantle. Springer, Berlin. p. 53–80

Stampfli G, Zaninetti L, Brönimann P, Jenny-Deshusses C, Stampfli-Vuille B (1976) Trias de l'Elburz oriental, Iran. Stratigraphie, sédimentologie, micropaléontologie, Riv It Paleontol Stratigr 82: 467–500

Stepanov DL, Golshani F, Stöcklin J (1969) Upper Permian and Permian–Triassic Boundary in North Iran. Geol Surv Iran Rep 12:1–72

Stoyanow AA (1910) On the character of the boundary of Palaeozoic and Mesozoic near Djulfa. Zap Imp Sankt-Peterburgskago Miner Obshch Nov Ser 47:61–135

Struck U (2012) On the use of stable Nitrogen isotopes in present and past anoxic environments. In: Altenbach AV, Bernhard JM, Seckbach J (eds). Anoxia. Springer, Netherlands, 497–513

Struck U, Voss M, Mumm N, Bodungen VB (1998) Stable isotopes of nitrogen in fossil cladoceran exoskeletons: implications for nitrogen sources in the Baltic Sea during the last century. Naturwissenschaften 85:597–603

Struck U, Emeis KC, Voss M, Christiansen CC, Kunzendorf H (2000) Records of southern and central Baltic Sea eutrophication in $\delta^{13}C$ and $\delta^{15}N$ of sedimentary organic matter. Mar Geol 164(3–4):157–171

Struck U, Emeis KC, Voss M, Krom MD, Rau GH (2001) Biological productivity during sapropel S5 formation in the eastern Mediterranean Sea. Evidence from a stable isotopes of nitrogen and carbon. Geochim Cosmochim Acta 65(19):3249–3266

Struck U, Pollehne F, Bauerfeind E, Bodungen VB (2004) Sources of nitrogen for the vertical particle flux in the Gotland Sea (Baltic Proper) – results from sediment trap studies. J Mar Syst 45:91–101

Struck U, Falk M, Altenbach AV, Pollehne F, Schneider M (2009) Nitrogen and carbon isotope ratios in suspended matter and dissolved inorganic carbon in a meromictic lake of the northern Alps (Bavaria, Germany). In: ASLO Aquatic Sciences Meeting 2009, Nice, France, 25–30 Jan 2009

Struck U, Emeis K-C, Alheit J, Schneider R, Eichner C, Altenbach A-V (2002) Changes of the upwelling rate of nitrate preserved in the d15N-signature of sediments and fish scales from the

diatomaceous mud belt off Namibia: GeoBios 35:3–11

Svensen H, Planke S, Polozov AG, Schmidbauer N, Corfu F, Podladchikov YY, Jamtveit B (2009) Siberian gas venting and the end-Permian environmental crisis. Earth Planet Sci Lett 277:490–500

Swart PK, Kennedy MJ (2011) Does the global stratigraphic reproducibility of $\delta^{13}C$ in Neoproterozoic carbonates require a marine origin? A Pliocene- Pleistocene comparison. Geology 40:87–90

Sweet WC, Mei SL (1999) The Permian Lopingian and basal Triassic sequence in Northwest Iran. Permophiles 33:14–18

Taraz H (1969) Permo-Triassic section in central Iran. Amer Ass Petrol Geol Bull 53:688–693

Taraz H (1971) Uppermost Permian and Permo-Triassic transition beds in central Iran. Amer Assoc Petrol Geol Bull 5355:1280–1294

Taraz H (1973) Correlation of Uppermost Permian in Iran, Central Asia, and South China. Amer Assoc Petrol Geol Bull 5357:1117–1133

Taraz H, Golshani F, Nakazawa K, Shimizu D, Bando Y, Ishii K-I, Murata M, Okimura Y, Sakagami S, Nakamura K, Tukuoka T (1981) The Permian and the Lower Triassic systems in Abadeh region, central Iran. Mem Fac Sci Kyoto Univ Ser Geol Miner 47:62–133

Taylor R (1990) Interpretation of the correlation coefficient: A Basic Review. J Diagn Med Sonog 6(1):35–39

Teichert C, Kummel B, Sweet WC (1973) Permian-Triassic strata, Kuh-e-Ali Bashi, northwestern Iran. Bull Mus Comp Zool 145:359–472

Thomas BM, Willink RJ, Grice K, Twitchett RJ, Purcell RR, Archbold NW, George AD, Tye S, Alexander R, Foster CB, Barber CJ (2004) Unique marine Permian-Triassic boundary section from Western Australia. Aust J Earth Sci 51:423–430

Torsvik TH, Cocks LRM (2004) Earth geography from 400 to 250 Ma: a palaeomagnetic, faunal and facies review. J Geol Soc 161:555–572

Turekian KK (2001) Stable carbon isotope variations in the ocean. In: Steele J, Thorpe S, Turekian K (eds) A Derivative of Encyclopedia of Ocean Sciences (2nd Edition, 2010). Oxford, Academic Press, 566 p.

Twitchett RJ (2007) The Late Permian mass extinction event and recovery: biological catastrophe in a greenhouse world. In: Sammonds PR, Thompson JMT (eds) Advances in Earth Science - from earthquakes to global warming. Royal Society Series on Advances in Science, Imperial College Press, London, pp 69–90

Twitchett RJ, Looy CV, Morante R, Visscher H, Wignall PB (2001) Rapid and synchronous

collapse of marine and terrestrial ecosystems during the end-Permian biotic crisis. Geology 29: 351–354

Vail PR, Hardenbol J, Todd RG (1984) Jurassic unconformities, chronostratigraphy, and sea-level changes from seismic stratigraphy and biostratigraphy. In: Schlee JS (ed) Interregional Unconformities and Hydrocarbon Accumulation. Amer Assoc Petrol Geol Mem 36, 184 p.

Veizer J (1992) Depositional and diagenetic history of limestones: Stable and radiogenic isotopes. In: Clauer N, Chaudhuri S (eds) Isotopic Signatures and Sedimentary Records. Springer-Verlag, Berlin, 13–48

Veizer J (1983) Chemical diagenesis of carbonates: theory and application of trace element techniques. In: Arthur MA, Anderson TF, Kaplan IR, Veizer J, Land LS (eds) Stable isotopes in sedimentary geology. Soc Econom Paleont Miner, Short Course 10:3.1–3.10

Verma HC, UpadhyayC, TripathiRP, Shukla AD, Bhandari N (2002) Evidence of Impact at the Permian/Triassic Boundary from Mössbauer Spectroscopy. Hyperfine Interact 141(1-4): 357–360

Vermeij GJ (1977) The Mesozoic Marine Revolution: Evidence from Snails, Predators and Grazers. Paleobiology 3(3):245–258

Visscher H, Looy CV, Collinson ME, Brinkhuis H, Cittert J, Kürschner WM, Sephton MA (2004) Environmental mutagenesis during the end-Permian ecological crisis. Proc Natl Acad Sci USA 101:12952–12956

Voss M, Dippner JW, Montoya JP (2001) Nitrogen isotope patterns in the oxygen deficient waters of the Eastern Tropical North Pacific Ocean. Deep Sea Res Part I 48(8):1905–1921

Wada E, Hattori A (1991) Nitrogen in the sea: forms, abundances & rate processes. CRC Press, Florida, USA, 213 p.

Wada E, Kadonaga T, Matsuo S (1975) ^{15}N abundance in nitrogen of naturally occurring substances and global assessment of denitrification from isotopic viewpoint. Geochem J 9: 139–148

Wada E, Terezaki M, Kabaya Y, Nemoto T (1987) ^{15}N and ^{13}C abundances in the Antartic Ocean with emphasis on the biogeochemical structure of the food web. Deep Sea Res Part I.Oceanogr Res Pap 34(5-6):829–841

Wang K, Geldsetzer HHJ, Krouse HR (1994) Permian-Triassic extinction: Organic delta ^{13}C evidence from British Columbia, Canada. Geology 22:580–584

Waples D, Sloan JR (1980) Carbon and nitrogen diagenesis in deep sea sediments (DSDP). Geochim Cosmochim Acta 44(10):1463–1470

Ward PD, Montgomery DR, Smith R (2000) Altered river morphology in South Africa related to the Permian-Triassic extinction. Science 289:1740–1743

Ward PD, Botha J, Buick R, De Kock MO, Erwin DH, Garrison GH, Kirschvink J, Smith R (2005) Abrupt and gradual extinction among Late Permian land vertebrates in the Karoo Basin, South Africa. Science 307:709–714

Watson JS, Sephton MA, Looy CV, Gilmour I (2005) Novel oxygencontaining aromatic compounds in Permian sediment. Org Geochem 36:371–384

Westerhausen L, Poynter J, Eglinton G, Erlenkeuser H, Sarnthein M (1993) Marine and terrigenous origin of organic matter in modern sediments of the equatorial East Atlantic: the $\delta^{13}C$ and molecular record: Deep Sea Res Part I. Oceanogr Res Pap 40(5):1087–1121

Westphal H, Munnecke A (2003) Limestone-marl alternations: a warm-water phenomenon? Geology 31:263–266

Westphal H, Munnecke A, Brandano M (2008) Effects of diagenesis on the astrochronological approach of defining stratigraphic boundaries in calcareous rhythmites: The Tortonian GSSP. Lethaia 41:461–476

Wignall PB (2001) Large igneous provinces and mass extinctions. Earth Sci Rev 53:1–33

Wignall PB, Hallam A (1992) Anoxia as a cause of the Permian/Triassic mass extinction: facies evidence from northern Italy and the western United States. Palaeogeogr Palaeoclimatol Palaeoecol 93:21–46

Wignall PB, Twitchett RJ (1996) Oceanic anoxia and the end Permian mass extinction. Science 272:1155–1158

Wignall PB, Twitchett RJ (2002) Extent, duration, and nature of the Permian–Triassic superanoxic event. Geol Soc Spec Pap 356:395–413

Wignall PB, Morante R, Newton R (1998) The Permo-Triassic transition in Spitsbergen: delta(13)C(org) chemostratigraphy, Fe and S geochemistry, facies, fauna and trace fossils. Geol Mag 135:47–62

Wignall PB, Newton R, Brookfield ME (2005) Pyrite framboid evidence for oxygen-poor deposition during the Permian–Triassic crisis in Kashmir. Palaeogeogr Palaeoclimatol Palaeoecol 216:183–188

Wilson JL (1975) Carbonate facies in geologic history. Springer, Berlin. 471 pp.

Winguth AME, Maier-Reimer E (2005) Causes of the marine productivity and oxygen changes associated with the Permian–Triassic boundary: A reevaluation with ocean general circulation models. Mar Geol 217:283–304

Winguth C, Winguth AME (2012) Simulating Permian–Triassic oceanic anoxia distribution: Implications for species extinction and recovery. Geology 40:127–130

Woods AD, Bottjer DJ (2000) Distribution of ammonoids in the Lower Triassic Union Wash

Formation (eastern California): evidence for paleoceanographic conditions during recovery from the end-Permian mass extinction. Palaios 15:535–545

Woods AD, Bottjer DJ, Corsetti FA (2005) Lower Triassic seafloor precipitates from east-central California: sedimentology and paleobiological significance. Albertiana 33:90–93

Woods AD, Bottjer DJ, Corsetti FA (2007) Calciumcarbonate seafloor precipitates fromthe outer shelf to slope facies of the Lower Triassic (Smithian–Spathian) Union WashFormation, California, U.S.A.: sedimentology and palaeobiologic significance. Palaeogeogr Palaeoclimatol Palaeoecol 252:281–290

Woods AD, Bottjer DJ, Mutti M, Morrison J (1999) Lower Triassic large sea-floorcarbonate cements: their origin and a mechanism for the prolonged biotic recoveryfrom the end-Permian mass extinction. Geology 27:645–648

Xie S, Pancost RD, Yin H, Wang H, Evershed RP (2005) Two episodes of microbial change coupled with Permo/Triassic faunal mass extinction. Nature 434:494–497

Xie S, Pancost RD, Huang JH, Wignall PB, Yu J, Tang X, Chen L, Huang X, Lai X (2007a) Molecular and isotopic evidence for episodic environmental change across the Permo/Triassic boundary at Meishan in South China. Global Planet Change 55:56–65

Xie S, Pancost RD, Huang J, Wignall PB, Yu J, Tang X, Chen L, Huang X, Lai X (2007b) Changes in the global carbon cycle occurred as two episodes during the Permian–Triassic crisis. Geology 35:1083–1083

Xie S, Pancost RD, Wang Y, Yang H, Wignall PB, Luo G, Jia C, Chen L (2010) Cyanobacterial blooms tied to volcanism during the 5 m.y. Permo–Triassic biotic crisis. Geology 38(5):447–450

Yang H, Chen ZQ, Wang Y, Tong J, Song H, Chen J (2011) Composition and structure of microbialite ecosystems following the end- Permian mass extinction in South China. Palaeogeogr Palaeoclimatol Palaeoecol 308:111–128

Yazdi M, Shirani M (2002) First research on marine and nonmarine sedimentary sequences and micropaleontologic significance across Permian/Triassic boundary in Iran (Isfahan and Abadeh). J China Univ Geosci 13:172–176

Yin HF, Zhang KX, Tong JN, Yang ZY, Wu SB (2001) The Global Stratotype Section and Point (GSSP) of the Permian-Triassic Boundary. Episodes 24:102–114

Yin H, Xie S, Luo G, Algeo TJ, Zhang K (2012) Two episodes of environmental change at the Permian–Triassic boundary of the GSSP section Meishan. Earth-Sci Rev 115:163–172

Yuan D-X, Shen S-Z, Henderson CM, Chen J, Zhang H, Feng H-Z (2014) Revised conodont-based integrated high-resolution timescale for the Changhsingian Stage and end-Permian extinction interval at the Meishan sections, South China. Lithos 204:220–245

Zachos JC, Rühl U, Schellenberg SA, Sluijs A, Hodell DA, Kelly DC, Thomas E, Nicolo M, Raffi I, Lourens LJ (2005) Rapid acidification of the ocean during the Paleocene–Eocene thermal maximum. Science 308:1611–1615

Zakharov YD (1992) The Permo–Triassic boundary in the southern and eastern USSR and its intercontinental correlation. In: Sweet WC, Yang Z, Dickins JM, Yin H (eds) Permo–Triassic events in the eastern Tethys. Cambridge University Press, Cambridge, 46–55

Zhu P, MacDougall JD (1998) Calcium isotopes in the marine environment and the oceanic calcium cycle. Geochim Cosmochim Acta 62:1691–1698

13 APPENDIX

Table A.1 Bulk carbonate carbon isotope values ($\delta^{13}C_{carb}$) and bulk carbonate oxygen isotope values ($\delta^{18}O_{carb}$) for the Ali Bashi 1 section. Sample height of 0 cm = the end-Permian mass extinction horizon.

Sample number	Sample height (cm)	$\delta^{13}C_{carb}$	$\delta^{18}O_{carb}$
AB +450	+450	-0.33	-6.80
AB +435	+435	-0.12	-5.86
AB +412	+412	-0.33	-7.10
AB +405	+405	-0.21	-7.14
AB +390	+390	-0.09	-5.69
AB +385	+385	-0.34	-6.36
AB +365	+365	-1.10	-7.00
AB +350	+350	-2.01	-6.75
AB +330	+330	-0.47	-6.69
AB +315	+315	-1.67	-6.67
AB +307	+307	-0.48	-6.41
AB +301	+301	-0.80	-6.67
AB +291	+291	-0.51	-6.38
AB +280	+280	-0.44	-6.93
AB +265	+265	-0.41	-6.67
AB +235	+235	-0.42	-7.34
AB +230	+230	-0.92	-7.26
AB +220	+220	-1.45	-6.84
AB +205	+205	-0.44	-6.66
AB +200	+200	-1.20	-7.14
AB +194	+194	-0.89	-8.09
AB +170	+170	-1.85	-7.01
AB +161	+161	-2.21	-7.29
AB +154	+154	-2.58	-7.15
AB +148	+148	-1.51	-7.29
AB +141	+141	-2.07	-7.30
AB +137	+137	-1.76	-7.36
AB +131	+133	-2.05	-7.58
AB +129	+129	-2.78	-7.71
AB +124	+124	-1.10	-6.95
AB+121	+121	-1.96	-7.50
AB +118	+118	-1.57	-7.11
AB +90	+90	-0.77	-7.03
AB +85	+85	-0.65	-6.90
AB +75	+75	-0.40	-6.82
AB +73	+73	-1.28	-7.07
AB+56	+56	-0.97	-7.17
AB+50	+50	-1.32	-7.27

AB+45	+45	-0.43	-6.96
AB+40	+40	0.41	-4.87
AB +35	+35	-0.18	-5.22
AB +28	+28	-1.11	-6.62
AB +20	+20	-1.11	-4.28
AB +5	+5	-0.94	-6.46
AB-0	0	0.62	-6.66
AB-5	-5	1.25	-6.51
AB-10	-10	1.78	-5.49
AB-15	-15	1.37	-6.11
AB-30	-30	1.51	-6.19
AB-48	-48	2.38	-5.28
AB-56	-56	2.40	-5.27
AB-65	-65	2.23	-5.05
AB-71	-71	-0.72	-6.22
AB-80	-80	2.34	-5.59
AB-90	-90	2.00	-5.61
AB-100	-100	2.75	-4.80
AB-105	-105	2.55	-5.86
AB-105	-107	2.40	-5.66
AB-115	-115	2.95	-4.84
AB-130	-130	2.82	-5.07
AB-140	-140	3.05	-3.99
AB-148	-148	2.71	-5.10
AB-155	-155	1.76	-5.84
AB-170	-170	-1.37	-6.12
AB-185	-185	2.08	-5.89
AB-191	-191	3.01	-4.90
AB-200	-200	2.89	-5.09
AB-200	-202	3.24	-4.87
AB-220	-220	3.32	-4.88
AB-240	-240	3.22	-4.90
AB-245	-245	2.88	-4.21
AB-265	-265	3.46	-5.22
AB-295	-295	3.51	-4.70
AB-310	-310	3.23	-5.02
AB-330	-330	3.11	-4.86
AB-340	-340	3.20	-4.90
AB-380	-380	3.08	-5.27
AB-410	-410	3.35	-4.70
AB-440	-440	3.21	-4.48
AB-480	-480	3.10	-5.23
AB-570	-570	3.15	-6.66
AB-690	-690	2.84	-6.47
AB-895	-895	3.80	-6.73

AB-990	-990	4.06	-4.67
AB-1080	-1080	4.13	-6.07
AB-1240	-1240	3.92	-4.54
AB-1290	-1290	3.89	-4.53
AB-1345	-1345	3.78	-5.02
AB-1480	-1480	3.67	-5.05
AB-1535	-1535	3.95	-5.21
AB-1605	-1605	3.27	-4.95
AB-1740	-1740	3.69	-5.78
AB-1815	-1815	3.33	-6.68
AB-1830	-1830	3.56	-5.02
AB-1905	-1905	3.52	-5.32
AB-1995	-1995	3.57	-4.58

Table A.2 Bulk carbonate carbon isotope values ($\delta^{13}C_{carb}$) and bulk carbonate oxygen isotope values ($\delta^{18}O_{carb}$) for the Ali Bashi 4 section. Sample height of 0 m = the end-Permian mass extinction horizon.

Sample number	**Sample height (cm)**	**$\delta^{13}C_{carb}$**	**$\delta^{18}O_{carb}$**
AB4 +170	+170	-2.90	-6.95
AB4 +160	+160	-3.74	-6.90
AB4 +150	+150	-4.45	-7.03
AB4 +140	+140	-3.60	-6.51
AB4 +130-135	+132,5	-1.26	-6.77
AB4 +120-125	+122.5	-0.25	-7.05
AB4 +115-120	+117.5	-0.46	-6.76
AB4 +110-115	+112.5	-0.75	-7.00
AB4 +105-110	+107.5	-0.61	-7.00
AB4 +100-105	+102.5	-0.45	-7.06
AB4 +95-100	+97.5	-0.32	-6.71
AB4 +90-95	+92.5	-0.35	-6.87
AB4 +85-90	+87.5	-0.01	-6.68
AB4 +80-85	+82.5	0.20	-6.64
AB4 +75-80	+77.5	-0.12	-6.68
AB4 +70-75	+72.5	-0.47	-6.87
AB4 +65-70	+67.5	-0.91	-6.83
AB4 +60-65	+62.5	-0.36	-6.82
AB4 + 55-60	+57.5	-0.23	-6.46
AB4 +50-55	+52.5	-0.43	-6.65
AB4 +45-50	+47.5	-1.29	-7.36
AB4 +40-45	+42.5	-0.51	-7.11
AB4 +35-40	+37.5	-1.12	-7.42
AB4 +30-35	+32.5	-0.52	-7.00

AB4 +25-30	+27.5	-1.63	-8.15
AB4 +20-25	+25.5	-0.81	-7.31
AB4 +20	+20	0.51	-4.40
AB4 +15-20	+17.5	-0.70	-6.99
AB4 +10-15	+12.5	-0.70	-6.98
AB4 +5-10	+7.5	-0.82	-7.48
AB4 -0	0	0.87	-6.51
AB4 +0-5	2.5	-0.68	-7.25
AB4 -5	-5	1.21	-6.31
AB4 -12	-12	0.70	-5.64
AB4 -15	-15	1.59	-5.30
AB4 -25	-25	1.36	-5.72
AB4 -45	-45	1.76	-5.51

Table A.3 Bulk carbonate carbon isotope values ($\delta^{13}C_{carb}$) and bulk carbonate oxygen isotope values ($\delta^{18}O_{carb}$) for the Aras Valley section. Sample height of 0 m = the end-Permian mass extinction horizon.

Sample number	**Sample height (cm)**	**$\delta^{13}C_{carb}$**	**$\delta^{18}O_{carb}$**
AV216	+495	-0.13	-6.31
AV215	+485	0.04	-5.96
AV214	+465	0.00	-5.98
AV213	+450	0.08	-5.87
AV212	+430	0.11	-6.30
AV211	+410	-0.30	-5.93
AV210	+380	-0.24	-6.52
AV209	+340	-0.09	-6.28
AV208	+320	-0.18	-6.07
AV207	+305	-0.74	-5.45
AV206	+255	-0.21	-4.45
AV205	+245	-0.16	-4.55
AV204	+235	-0.35	-5.84
AV203	+205	-0.19	-3.50
AV202	+170	-0.33	-5.59
AV201	+150	-0.03	-3.50
AV+60	+60	1.14	-3.01
AV200	0	1.20	-5.71
AV199	-10	2.25	-5.07
AV198	-20	2.34	-5.54
AV197	-45	2.41	-5.47
AV196	-70	3.09	-4.84
AV195	-110	2.71	-4.83
AV194	-125	3.12	-3.42

AV195	-125	2.80	-4.85
AV193	-145	3.03	-4.95
AV192	-175	2.87	-4.68
AV191	-200	3.11	-4.89
AV190	-220	3.59	-5.61
AV189	-245	3.25	-5.24
AV188	-270	3.30	-4.99
AV187	-285	3.11	-5.38
AV186	-295	3.20	-5.23
AV185	-310	3.19	-5.23
AV184	-330	3.15	-4.68
AV183	-350	2.95	-5.06
AV182	-365	3.00	-4.83
AV181	-380	3.63	-5.18
AV180	-420	3.24	-4.92
AV179	-455	3.02	-5.24
AV178	-480	3.18	-4.75
AV177	-505	3.20	-4.64
AV176	-525	3.29	-4.29
AV175	-540	3.42	-5.05
AV174	-565	3.08	-5.03
AV173	-645	3.63	-5.36
AV172	-710	3.27	-5.55
AV171	-775	3.64	-5.84
AV170	-830	4.09	-6.31
AV169	-895	4.04	-6.13
AV168	-930	4.04	-5.70
AV167	-985	4.26	-5.16
AV166	-1010	4.02	-5.01
AV165	-1035	3.89	-4.65
AV164	-1055	3.50	-4.02
AV163	-1085	3.60	-4.66
AV162	-1140	3.87	-5.76
AV161	-1225	3.69	-5.40
AV160	-1285	3.52	-5.42
AV159	-1310	3.20	-5.83
AV158	-1360	3.34	-6.03
AV157	-1400	3.37	-4.82
AV156	-1415	3.64	-5.62
AV155	-1445	3.87	-5.68
AV154	-1470	3.50	-5.20
AV153	-1490	3.79	-5.05
AV152	-1510	3.77	-5.15
AV151	-1530	3.78	-5.76
AV150	-1565	3.96	-5.08

AV149	-1580	3.77	-5.07
AV148	-1600	4.06	-5.58
AV147	-1620	3.96	-5.18
AV146	-1665	3.85	-4.95
AV145	-1705	3.60	-5.18
AV144	-1800	3.76	-5.56
AV143	-1850	3.78	-5.66
AV142	-1950	3.57	-5.16
AV141	-1990	3.31	-4.12

Table A.4 Bulk carbonate carbon isotope values ($\delta^{13}C_{carb}$) and bulk carbonate oxygen isotope values ($\delta^{18}O_{carb}$) for the Zal section. Sample height of 0 m = the end-Permian mass extinction horizon.

Sample number	**Sample height (cm)**	**$\delta^{13}C_{carb}$**	**$\delta^{18}O_{carb}$**
ZL25	+360	-0.55	-7.84
Zl24	+305	-0.59	-6.67
Zl 23	+240	-0.58	-6.71
Zl 22II	+200	-0.94	-6.17
Zl 21	+120	0.05	-8.25
Zl+73	+73	0.64	-3.04
Zl19	+70	-0.11	-7.22
Zl18e	+54	0.04	-7.01
ZL18d	+52	0.01	-9.26
Zl18d	+52	0.11	-7.36
Zl 18c	+50	0.15	-7.02
Zl 18bI	+47	0.11	-7.53
Zl18b2	+47	0.26	-6.99
Zl 18a2	+45	0.51	-6.91
Zl 18aI	+45	0.41	-6.61
Zl 17I	+43	0.32	-6.57
Zl17II	+43	0.21	-6.91
Zl+40	+40	0.88	-7.41
Zl+35	+35	1.32	-6.33
Zl+30	+30	1.50	-6.06
Zl+25	+25	1.33	-6.40
Zl+20	+20	1.37	-7.17
Zl+16	+16	1.57	-6.08
Zl+12	+12	1.36	-6.37
ZL20	+10	0.79	-7.04
Zl+8	+8	1.59	-6.14
Zl+5	+5	1.59	-6.89
Zl+4	+4	1.56	-6.43

ZL16	0	1.17	-9.22
Zl0-3	-3	1.55	-5.46
Zl 15I	-65	2.10	-5.56
Zl 14	-115	2.45	-5.46
Zl 13II	-200	2.62	-5.22
ZL 12b	-285	3.22	-4.93
ZL 11	-370	3.19	-5.33
ZL 10	-500	3.32	-4.99
ZL 09II	-630	3.03	-6.16
ZL 08	-825	3.45	-5.28
ZL 07	-1070	3.70	-5.75
ZL 06	-1370	3.41	-4.00
ZL 04I	-1775	3.48	-4.81
ZL 03	-1815	3.25	-5.24
ZL 02	-2000	3.05	-4.44

Table A.5 Bulk carbonate carbon isotope values ($\delta^{13}C_{carb}$) and bulk carbonate oxygen isotope values ($\delta^{18}O_{carb}$) for the Baghuk Mountain sections. Sample height of 0 m = the end-Permian mass extinction horizon.

Sample number	**Sample height (cm)**	**$\delta^{13}C_{carb}$**	**$\delta^{18}O_{carb}$**
BGKC+1885	+1885	-0.41	-9.01
BGKC+1865	+1865	-1.44	-10.02
BGKC+1795	+1795	0.32	-8.28
BGKC+1725	+1725	1.46	-6.24
BGKC+1640	+1640	-1.07	-9.18
BGKC+1560	+1560	-1.51	-9.67
BGKC+1480	+1480	-1.35	-10.22
BGKC+1290	+1290	-0.44	-8.74
BGKC+1135II	+1135	0.19	-8.10
BGKC+1050	+1050	0.51	-7.35
BGKC+930	+930	-0.22	-9.45
BGKC+900	+900	0.83	-6.99
BGKC+850	+850	-0.74	-8.63
BGKC+840	+840	-1.06	-9.44
BGKC+740	+740	-1.19	-8.80
BGKC+730	+730	-2.37	-9.32
BGKC+660	+660	-1.58	-8.86
BGKC+450	+450	-2.58	-9.13
BGKC+360	+360	-1.37	-7.08
BGKA+247	+247	-0.55	-7.49
BGKC+245	+245	-1.75	-8.96
BGKA+243	+243	-0.65	-8.21

BGKA+235	+235	-0.57	-6.97
BGKA+230	+230	-0.71	-7.76
BGKA+228	+228	-1.05	-7.52
BGKA+220	+220	-0.93	-7.33
BGKA+213	+213	-0.72	-7.47
BGKA+205	+205	-1.23	-7.38
BGKA+197	+197	-1.17	-7.66
BGKA+192	+192	-1.33	-7.18
BGKA+190	+190	-1.17	-6.99
BGKA+123	+123	-0.27	-4.77
BGKA+107	+107	-0.22	-5.03
BGKA+104	+104	0.12	-4.33
BGKA+96	+96	-0.49	-8.14
BGKA+91	+91	0.10	-4.67
BGKA+85	+85	-0.71	-8.68
BGKC+75	+75	0.19	-7.67
BGKA+57	+57	0.62	-4.72
BGKC+55	+55	0.40	-8.24
BGKA+40	+40	1.57	-0.36
BGKA+25	+25	0.20	-2.58
BGKA+10	+10	0.00	-8.43
BGKC+5	+5	1.69	-7.98
BGKC+2	+2	0.78	-9.62
BGKA+2	+2	0.35	-7.19
BGKA+0	+1	0.50	-7.13
BGKA-0	0	2.20	-8.27
BGK1-0base	-2	1.12	-7.02
BGK1-0top	-3	0.99	-7.27
BGK1-5	-5	0.99	-7.01
BGK1-9a	-9	1.33	-6.87
BGK1-9b	-9	1.18	-7.05
BGK1-15	-15	1.52	-7.28
BGK1-20	-20	1.40	-6.92
BGK1-25	-25	1.48	-6.95
BGK1-30	-30	1.60	-6.82
BGK1-35	-35	1.21	-7.02
BGK1-40	-40	1.33	-6.90
BGK1-45	-45	1.27	-7.14
BGK1-50	-50	1.44	-6.83
BGK1-60	-60	1.99	-6.82
BGK1-70	-70	2.11	-6.69
BGK1-80	-80	1.62	-6.98
BGK1-90	-90	1.90	-7.18
BGK1-100	-100	2.11	-6.74
BGK1-120	-120	2.05	-6.70

BGK1-135	-135	2.25	-6.46
BGK1-145	-145	2.19	-6.48
BGK1-200	-200	2.69	-6.32
BGK1-230	-230	2.59	-6.40
BGK1-245	-245	2.61	-6.60
BGK1-260	-260	2.72	-6.13
BGK1-285	-285	3.39	-6.30
BGK1-295	-295	3.44	-6.40
BGK1-325	-325	3.30	-6.51
BGK1-355	-355	3.70	-3.96
BGK1-380	-380	3.34	-6.09
BGK1-395	-395	3.69	-6.44
BGK1-415	-415	3.42	-5.97
BGK1-440	-440	3.79	-5.88
BGK1-460	-460	3.89	-5.89
BGK1-480	-480	3.69	-5.49
BGK1-520	-520	3.55	-5.96
BGK1-525	-525	3.78	-6.49
BGK1b-560	-560	3.85	-7.18
BGK1b-625	-625	4.00	-6.88
BGK1b-680	-680	4.11	-6.01
BGK1b-755	-755	3.90	-6.97
BGK1b-755	-755	4.06	-5.98
BGK1b-825	-825	4.18	-6.23
BGK1b-875	-875	4.20	-7.13
BGK1b-945	-945	3.84	-7.44
BGK1b-990	-990	4.00	-6.93

Table A.6 Bulk sediment nitrogen isotope values ($\delta^{15}N_{TN}$) and total nitrogen concentration (TN) for the Ali Bashi 1 section. Sample height of 0 cm = the end-Permian mass extinction horizon.

Sample number	**Sample height (cm)**	**$\delta^{15}N_{TN}$ (%VPDB)**	**TN (%)**
AB +465	+465	1.88	0.113
AB +450	+450	-0.42	0.008
AB +435	+435	3.01	0.003
AB +355	+350	1.90	0.091
AB +291	+291	3.06	0.005
AB +230	+230	3.33	0.004
AB +220	+220	-0.32	0.011
AB +200	+200	0.56	0.011
AB +194	+194	0.01	0.012

AB +170	+170	1.96	0.022
AB +161	+161	1.12	0.020
AB +154	+154	3.51	0.020
AB +148	+148	1.71	0.018
AB +141	+141	-0.11	0.011
AB +137	+137	0.86	0.018
AB +131	+133	0.99	0.023
AB +129	+129	3.64	0.057
AB +124	+124	2.75	0.017
AB +121	+121	3.11	0.053
AB +118	+118	2.40	0.023
AB +90	+90	3.83	0.013
AB +85	+85	1.13	0.020
AB +75	+75	3.93	0.021
AB +73	+73	3.77	0.059
AB +56	+56	3.86	0.025
AB +50	+50	4.27	0.033
AB +45	+45	3.56	0.017
AB +35	+35	3.82	0.047
AB +28	+28	3.19	0.056
AB +20	+20	3.16	0.058
AB +5	+5	3.74	0.058
AB-0	0	3.11	0.009
AB-5	-5	1.79	0.010
AB-10	-10	0.52	0.013
AB-15	-15	3.49	0.009
AB-30	-30	3.66	0.009
AB-48	-48	0.73	0.011
AB-56	-56	0.18	0.009
AB-65	-65	3.99	0.009
AB-80	-80	2.29	0.009
AB-100	-100	3.94	0.011
AB-130	-130	1.19	0.012
AB-136	-136	3.34	0.038
AB-140	-140	0.95	0.008
AB-148	-148	3.79	0.007
AB-170	-170	-0.39	0.007
AB-191	-191	2.61	0.009
AB-220	-220	3.09	0.008
AB-240	-240	0.51	0.030
AB-245	-245	2.47	0.006
AB-270	-270	2.76	0.033
AB-290	-290	2.81	0.045
AB-295	-295	0.45	0.015
AB-307	-307	2.53	0.064

AB-310	-310	2.08	0.010
AB-325	-325	3.14	0.036
AB-330	-330	1.72	0.012
AB-340	-340	1.05	0.010
AB-350	-350	2.78	0.022
AB-360	-360	2.47	0.018
AB-380	-380	3.64	0.007
AB-395	-395	2.17	0.019
AB-410	-410	1.34	0.011
AB-440	-440	1.09	0.012
AB-480	-480	1.70	0.011
AB-570	-570	4.35	0.013
AB-895	-895	3.82	0.010
AB-1740	-1740	2.99	0.007
AB-1995	-1995	2.16	0.003

Table A.7 Total organic carbon isotope values ($\delta^{13}C_{TOC}$ values), total organic carbon concentration (TOC), and TOC/TN atomic ratios for the Ali Bashi 1 section. Sample height of 0 cm = the end-Permian mass extinction horizon.

Sample number	**Sample height (cm)**	**$\delta^{13}C_{TOC}$ (%VPBD)**	**TOC (%)**	**C/N molar**
AB +465	+465	1.88	0.113	-
AB +450	+450	-25.80	0.021	3.19
AB +435	+435	-26.77	0.014	5.05
AB +412	+412	-26.08	0.011	-
AB +405	+405	-26.64	0.008	-
AB +390	+390	-27.20	0.014	-
AB +365	+365	-28.41	0.010	-
AB +350	+350	-27.29	0.012	-
AB +315	+315	-22.38	0.028	-
AB +307	+307	-26.31	0.009	-
AB +301	+301	-27.43	0.007	-
AB +291	+291	-27.30	0.012	2.81
AB +265	+265	-26.69	0.014	-
AB+235	+235	-26.99	0.011	-
AB +230	+230	-26.03	0.010	2.56
AB +220	+220	-24.86	0.011	1.19
AB +194	+194	-27.43	0.036	3.48
AB +170	+170	-25.29	0.032	1.69
AB +161	+161	-26.86	0.006	0.34
AB +154	+154	-24.11	0.024	1.42

AB +148	+148	-25.23	0.017	1.09
AB +141	+141	-25.24	0.019	1.94
AB +137	+137	-25.76	0.021	1.30
AB +131	+131	-26.17	0.025	1.28
AB +124	+124	-26.41	0.015	1.05
AB +118	+118	-25.01	0.023	1.22
AB +90	+90	-25.71	0.014	1.22
AB +85	+85	-25.77	0.033	1.95
AB +75	+75	-24.58	0.013	0.73
AB +73	+73	-26.73	0.044	0.86
AB +45	+45	-21.34	0.010	0.69
AB +35	+35	-22.77	0.029	0.72
AB +28	+28	-24.32	0.033	0.68
AB +20	+20	-26.67	0.113	2.30
AB +5	+5	-26.54	0.057	1.14
AB-0	0	-25.42	0.011	1.43
AB-5	-5	-26.23	0.013	1.53
AB-10	-10	-24.66	0.015	1.26
AB-15	-15	-23.81	0.019	2.29
AB-30	-30	-24.93	0.013	1.79
AB-48	-48	-25.78	0.014	1.56
AB-56	-56	-25.40	0.012	1.59
AB-65	-65	-25.23	0.010	1.37
AB-71	-71	-25.31	0.011	-
AB-80	-80	-24.18	0.005	0.64
AB-90	-90	-26.29	0.012	-
AB-100	-100	-24.59	0.009	0.95
AB-115	-115	-25.63	0.005	-
AB-120	-120	-25.94	0.005	-
AB-130	-130	-25.05	0.011	1.14
AB-136	-136	-25.69	0.027	0.83
AB-140	-140	-24.61	0.013	1.88
AB-148	-148	-24.82	0.012	2.05
AB-155	-155	-25.99	0.013	-
AB-170	-170	-25.26	0.009	1.42
AB-185	-185	-26.09	0.005	-
AB-191	-191	-25.96	0.021	2.75
AB-200	-200	-25.03	0.014	-
AB-220	-220	-26.04	0.009	1.32
AB-240	-240	-27.38	0.006	0.24
AB-245	-245	-25.48	0.008	1.41
AB-260	-260	-26.76	0.042	-
AB-265	-265	-26.62	0.020	-
AB-270	-270	-26.51	0.024	0.86
AB-290	-290	-26.50	0.094	2.43

AB-295	-295	-25.18	0.011	0.85
AB-310	-310	-25.28	0.012	1.43
AB-325	-325	-26.53	0.062	2.00
AB-330	-330	-25.08	0.009	0.91
AB-340	-340	-26.48	0.010	1.20
AB-350	-350	-26.10	0.025	1.33
AB-360	-360	-25.67	0.016	1.03
AB-380	-380	-23.21	0.009	1.45
AB-395	-395	-26.21	0.028	1.73
AB-410	-410	-25.40	0.011	1.22
AB-440	-440	-25.87	0.021	1.98
AB-480	-480	-26.27	0.012	1.33
AB-570	-570	-21.18	-	-
AB-895	-895	-24.24	-	-
AB-1240	-1240	-25.17	-	-
AB-1740	-1740	-23.81	-	-
AB-1995	-1995	-24.63	-	-

Table A.8 Bulk sediment nitrogen isotope values ($\delta^{15}N_{TN}$) and total nitrogen concentration (TN) for the Zal section. Sample height of 0 cm = the end-Permian mass extinction horizon.

Sample number	Sample height (cm)	$\delta^{15}N_{TN}$ (%AIR)	TN (%)
Zl 22II	+200	1.62	0.007
Zl 21	+120	2.30	0.011
Zl19	+70	1.60	0.011
Zl18e	+54	1.52	0.009
ZL18d	+52	2.37	0.009
Zl 18c	+50	3.64	0.014
Zl 18bI	+47	1.71	0.012
Zl 18aI	+45	1.90	0.012
Zl 17I	+43	1.62	0.025
Zl+45	+45	3.82	0.012
Zl+40	+40	1.82	0.014
Zl+35	+35	4.22	0.095
Zl+30	+30	3.37	0.118
Zl+20	+20	3 .81	0.120
Zl+16	+16	4.41	0.192
Zl+12	+12	3.70	0.315
ZL20	+10	2.67	0.009
Zl+5	+5	3.47	0.010
ZL16	0	1.97	0.010

Zl0-3	-3	4.50	0.046
Zl 14	-115	3.04	0.006
ZL 12b	-285	2.37	0.008

Table A.9 Total organic carbon isotope values ($\delta^{13}C_{TOC}$ values), total organic carbon concentration (TOC), and TOC/TN atomic ratios for the Zal section. Sample height of 0 cm = the end-Permian mass extinction horizon.

Sample number	**Sample height (cm)**	**$\delta^{13}C_{TOC}$ (%VPBD)**	**TOC (%)**	**C/N molar**
Zl 28	+530	-27.69	0.017	-
Zl 23	+240	-27.73	0.015	-
Zl 19	+92	-26.48	0.017	1.70
ZL18d	+74	-26.25	0.029	3.68
Zl 18c	+72	-24.83	0.018	1.49
Zl 18a	+67	-26.60	0.011	1.08
Zl+40	+40	-27.51	0.026	2.13
Zl+35	+35	-25.73	0.010	0.12
Zl+30	+30	-25.19	0.018	0.18
Zl+25	+25	-26.93	0.033	-
Zl+12	+12	-26.52	0.037	0.14
ZL20	+10	-25.21	0.110	14.49
Zl+5	+5	-26.21	0.079	9.37
Zl0-3	-3	-24.73	0.054	1.36
Zl 14	-115	-25.28	0.026	4.74
ZL 12b	-285	-22.07	0.010	1.51

A.10 X-Ray diffraction patterns for bulk samples from the Ali Bashi 1 section. The positions of samples are either prefixed with a - sign (beginning at the top of the sample) or a + sign (beginning at the base of the sample), depending on the distance (in cm) below or above the reference horizon.

Sample AB +291

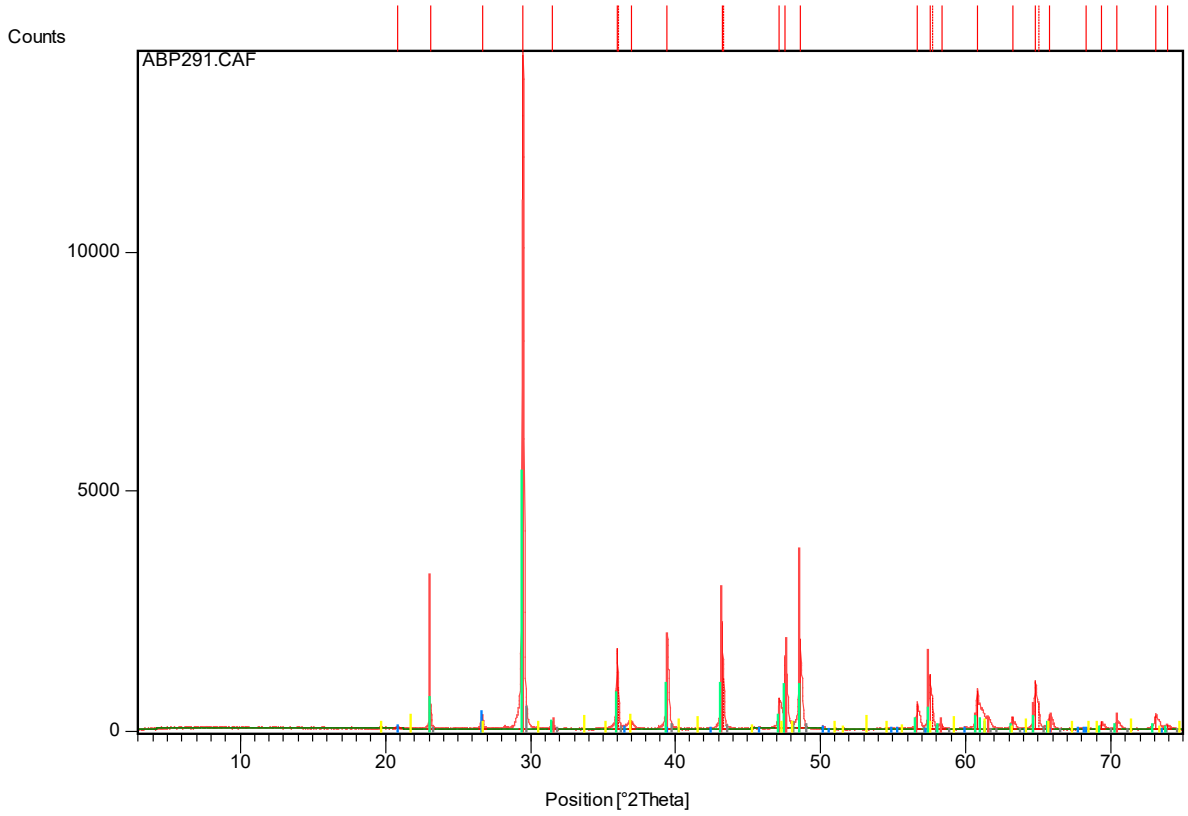

Qualitative pattern list:

Ref. Code	Score	Compound Name	Displace-ment [°2Th.]	Scale Factor	Chemical Formula
24-0027	64	Calcite	0	0.776	$CaCO_3$
46-1045	52	Quartz, syn	0	0.026	SiO_2
05-0586	57	Calcite, syn	0	0.377	$CaCO_3$
02-0281	Unmatched Strong	Goethite	0	0.020	$Fe_2O_3 \times H_2O$

Sample AB +155

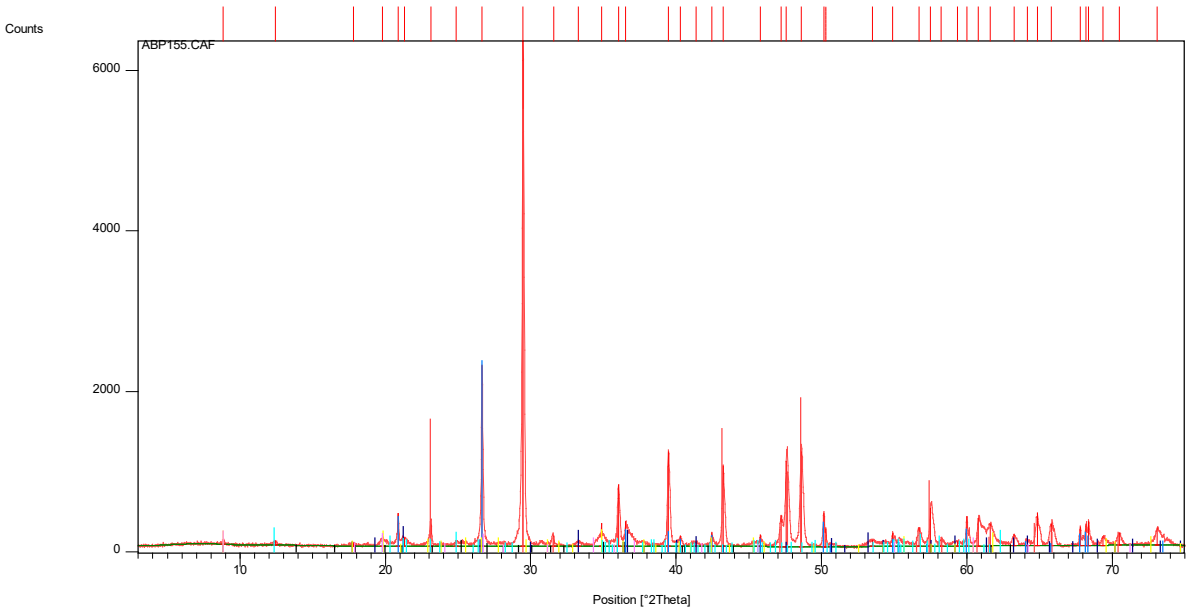

Qualitative pattern list:

Ref. Code	Score	Compound Name	Displacement [°2Th.]	Scale Factor	Chemical Formula
24-0027	61	Calcite	0	0.854	$CaCO_3$
46-1045	69	Quartz, syn	0	0.362	SiO_2
02-0272	37	Goethite	0	0.038	$Fe_2O_3 \times H_2O$
03-0849	36	Muscovite	0	0.032	$H_4K_2 (Al, Fe)_6 Si_6O_{24}$
14-0164	38	Kaolinite-1\ ITA\RG	0	0.033	$Al_2Si_2O_5 (OH)_4$
09-0343	34	Illite, trioctahe-dral	0	0.026	$K_{0.5}(Al, Fe, Mg)_3 (Si, Al)_4O_{10} (OH_2)$

Sample AB +129

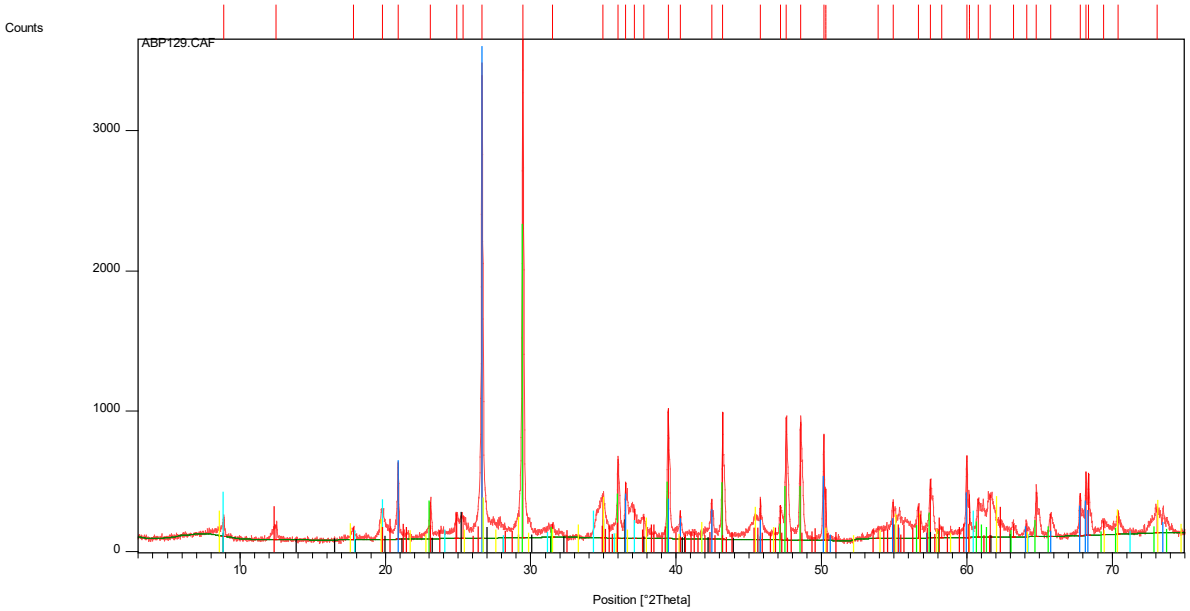

Qualitative pattern list:

Ref. Code	Score	Compound Name	Displacement [°2Th.]	Scale Factor	Chemical Formula
46-1045	69	Quartz, syn	0	0.957	SiO_2
05-0586	59	Calcite, syn	0	0.610	$CaCO_3$
09-0343	38	Illite, trioctahedral	0	0.085	$K_{0.5}(Al, Fe, Mg)_3 (Si, Al)_4 O_{10} (OH)_2$
15-0603	40	Illite	0	0.079	$K(AlFe)_2 AlSi_3O_{10} (OH)_2 \times H_2O$
14-0164	35	Kaolinite-1\ ITA\RG	0	0.064	$Al_2Si2O_5 (OH)_4$

Sample AB + 90

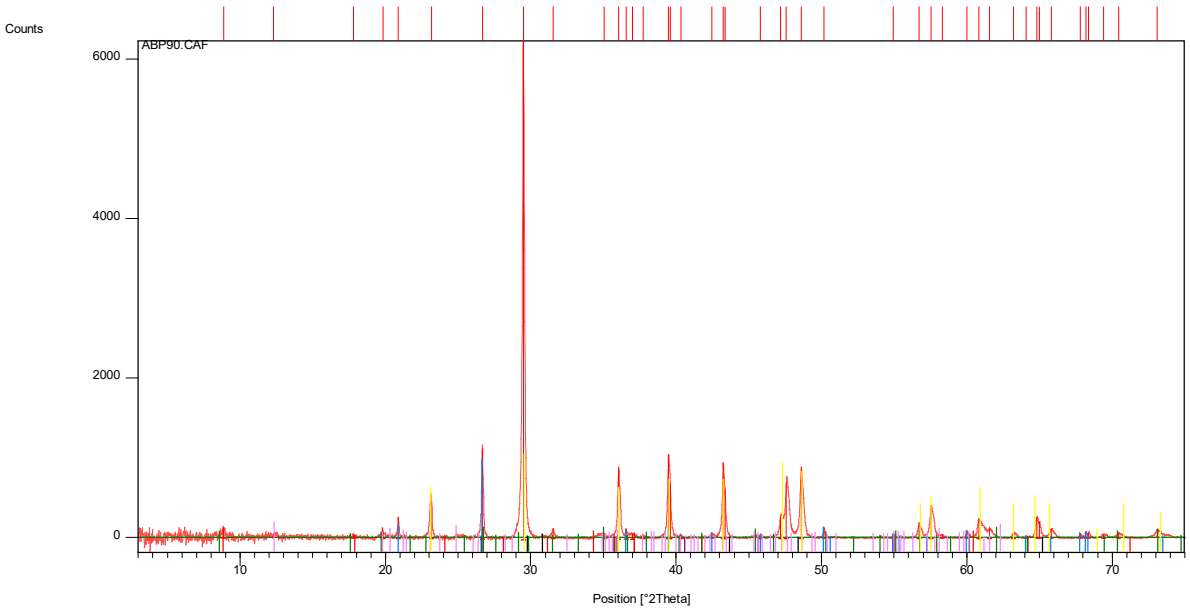

Qualitative pattern list:

Ref. Code	Score	Compound Name	Displacement [°2Th.]	Scale Factor	Chemical Formula
46-1045	58	Quartz, syn	0	0.158	SiO_2
09-0343	19	Illite, trioctahedral	0	0.022	$K_{0.5}(Al, Fe, Mg)_3 (Si, Al)_4 O_{10} (OH)_2$
15-0603	20	Illite	0	0.021	$K(AlFe)_2 AlSi_3O_{10}(OH)_2 \times H_2O$
14-0164	16	Kaolinite-1\ ITA\RG	0	0.031	$Al_2Si_2O_5 (OH)_4$
02-0629	43	Calcite	0	0.167	$CaCO_3$

Sample AB +45

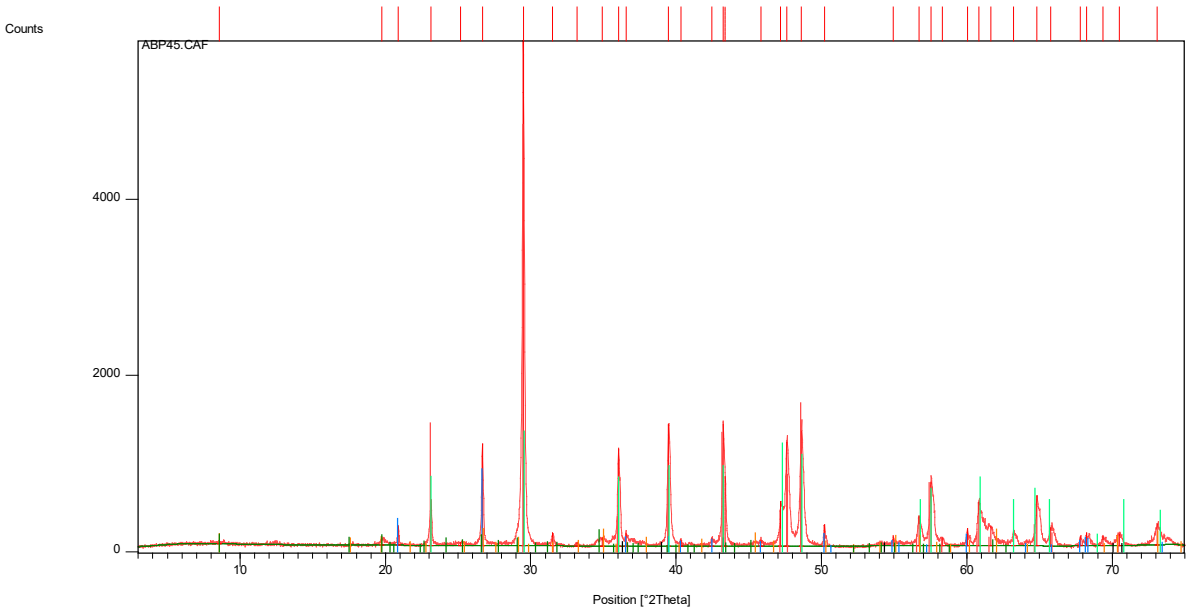

Qualitative pattern list:

Ref. Code	Score	Compound Name	Displacement [°2Th.]	Scale Factor	Chemical Formula
24-0027	62	Calcite	0	0.823	$CaCO_3$
05-0490	60	Quartz, low	0	0.150	SiO_2
02-0629	49	Calcite	0	0.224	$CaCO_3$
15-0603	32	Illite	0	0.033	$K(Al\ Fe)_2\ AlSi_3O_{10}\ (OH)_2\ x\ H_2O$
24-0495	28	Illite-2\ITM#2\ RG	0	0.032	$K0_{.7}Al_{2.1}\ (Si,\ Al)_4\ O_{10}\ (OH)_2$

Sample AB +30

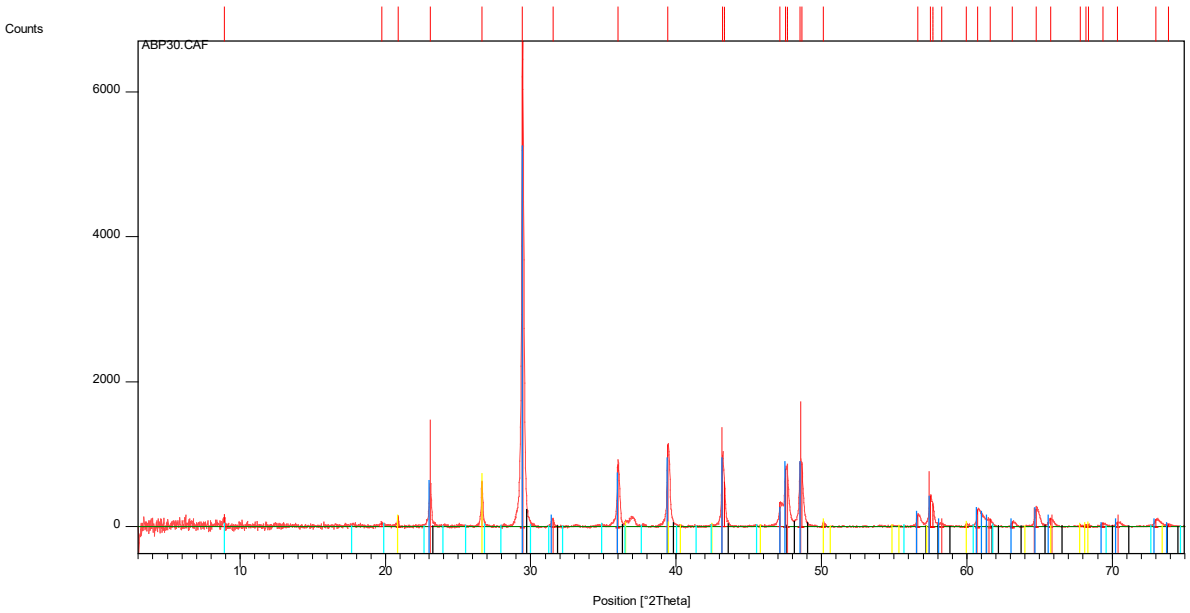

Qualitative pattern list:

Ref. Code	Score	Compound Name	Displacement [°2Th.]	Scale Factor	Chemical Formula
24-0027	64	Calcite	0	0.754	$CaCO_3$
05-0586	55	Calcite, syn	0	0.781	$CaCO_3$
33-1161	55	silica	0	0.108	SiO_2
02-0058	21	Muscovite	0	0.007	$H_2KAl_3Si_3O_{12}$

Sample AB +20

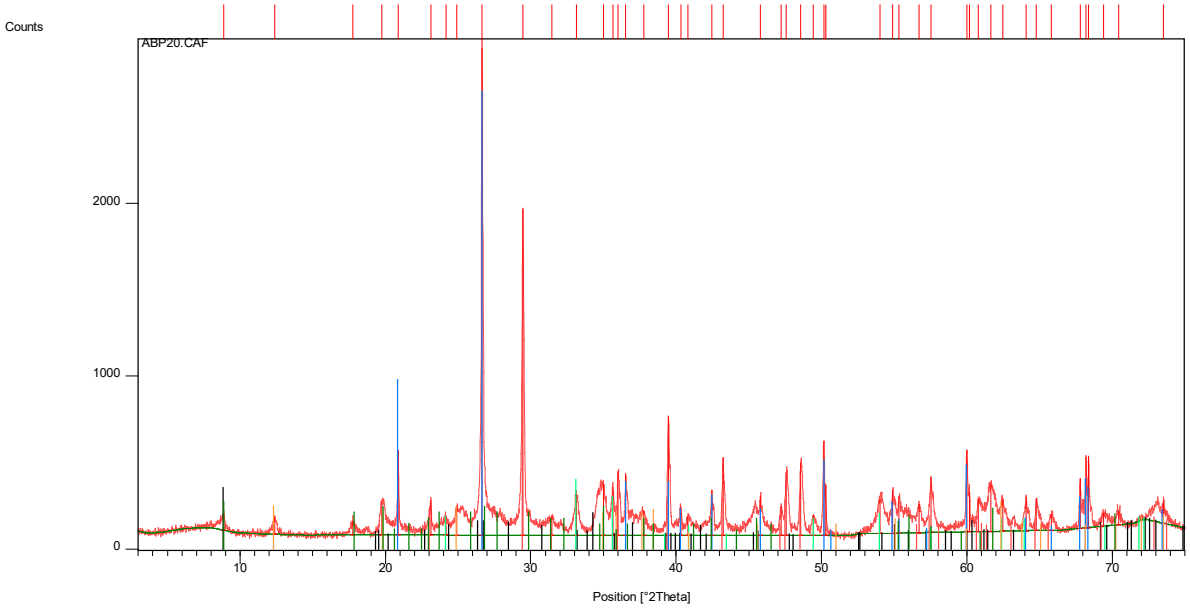

Qualitative pattern list:

Ref. Code	Score	Compound Name	Displacement [°2Th.]	Scale Factor	Chemical Formula
05-0586	51	Calcite, syn	0	0.408	$CaCO_3$
05-0490	66	Quartz, low	0	0.869	SiO_2
24-0072	49	Hematite	0	0.109	Fe_2O_3
06-0221	38	Kaolinite 1Md	0	0.055	$Al_2Si_2O_5(OH)_4$
02-0056	41	Illite	0	0.056	$KA_{l2}Si_3AlO_{10}(OH)_2$

Semi-quantitative pattern list:

Mineral	°2 Theta	Peak height	Factor	Result	%
Calcite	29.406	1793.37	1.65	2959.0605	41.5
Quartz	26.644	2764	1	2764	38.8
Hematite	33.115	191.66	3.33	638.2278	8.9
Illite	8.8506	91.6	6	549.6	7.7
Kaolinite	12.3832	98.45	2.25	221.5125	3.1

Sample AB +5

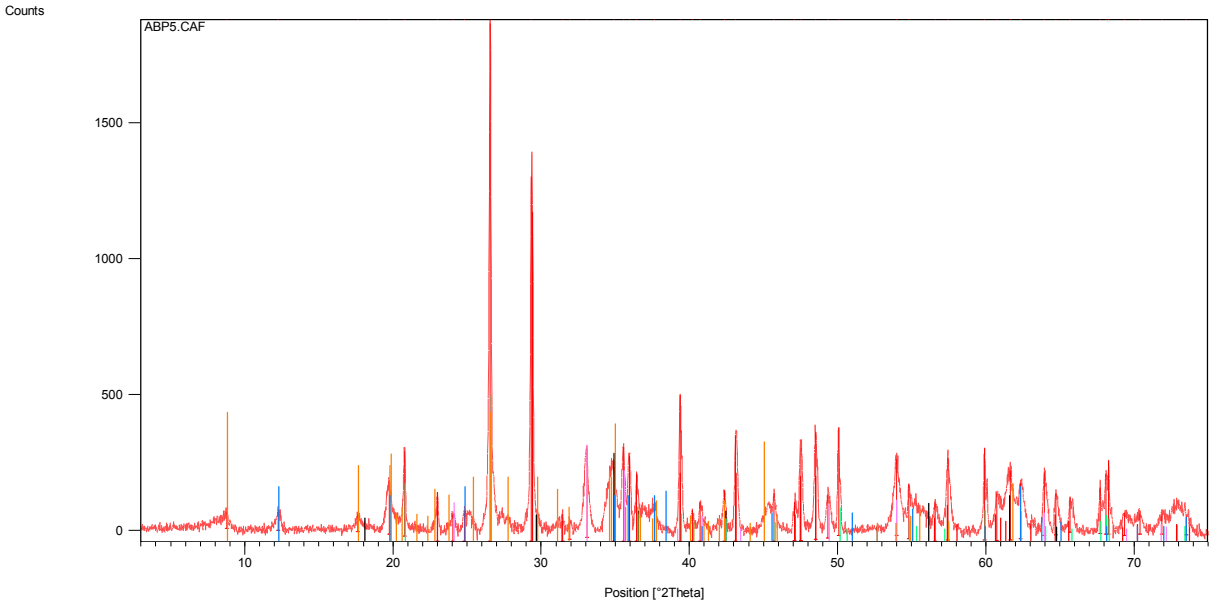

Qualitative pattern list:

Ref. Code	Score	Compound Name	Displacement [°2Th.]	Scale Factor	Chemical Formula
05-0586	55	Calcite, syn	0	0.622	$CaCO_3$
05-0490	40	Quartz, low	0	0.265	SiO_2
24-0072	41	Hematite	0	0.167	Fe_2O_3
07-0032	39	Muscovite 2M1, syn	0	0.231	$KA_{l2}Si_3AlO_{10}(OH)_2$
06-0221	41	Kaolinite 1Md	0	0.085	$Al_2SiO_5(OH)_4$

Sample AB -0 m

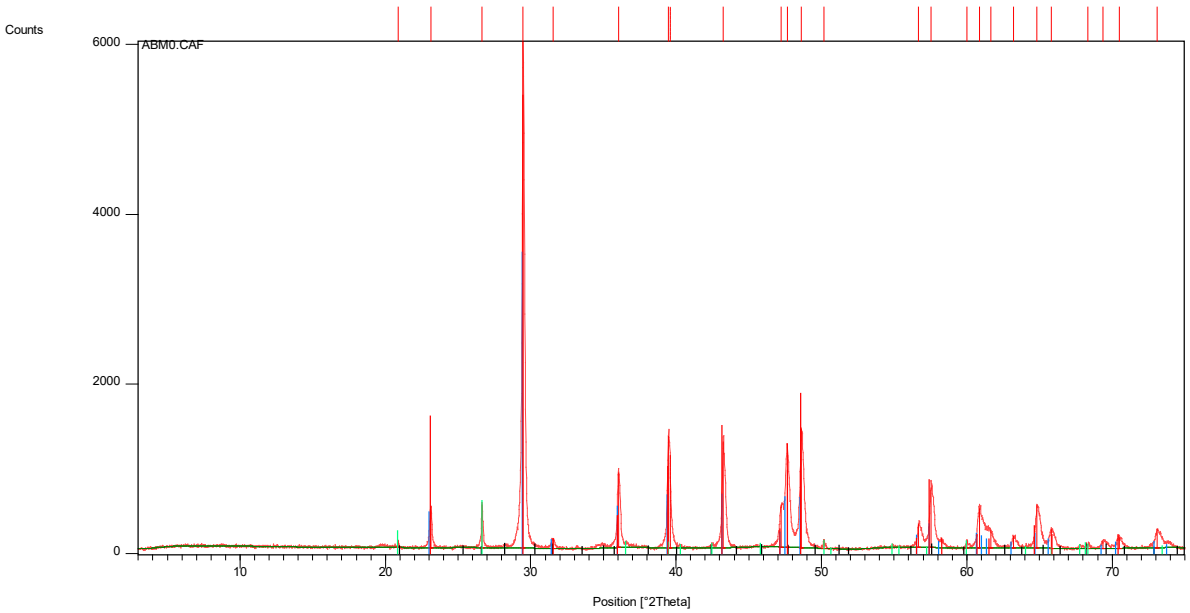

Qualitative pattern list:

Ref. Code	Score	Compound Name	Displacement [°2Th.]	Scale Factor	Chemical Formula
05-0586	64	Calcite, syn	0	0.576	$CaCO_3$
05-0490	52	Quartz, low	0	0.091	SiO_2
24-0027	71	Calcite	0	0.882	$CaCO_3$

Semi-quantitative pattern list:

Mineral	°2 Theta	Peak height	Factor	Result	%
Calcite	29.48	5859.26	1.65	9667.779	94.4
Quartz	26.657	572.97	1	572.97	5.6

Sample AB -15

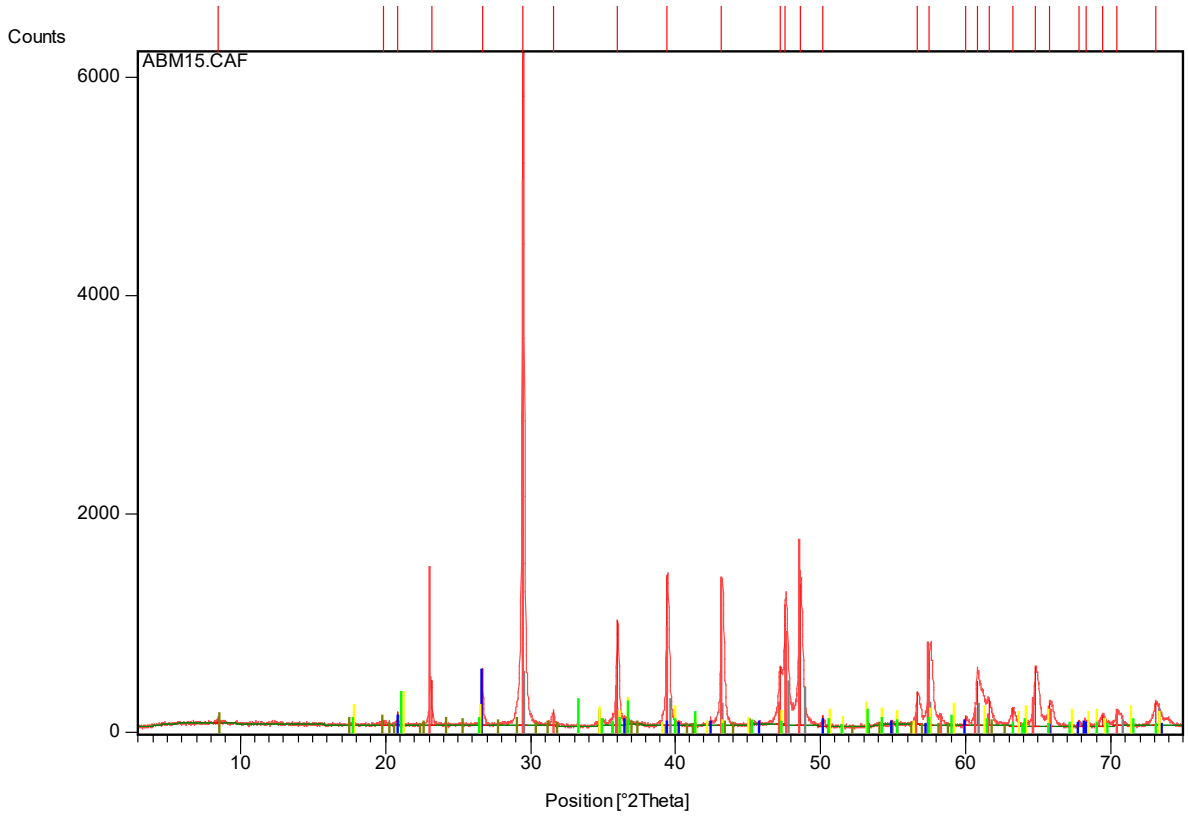

Qualitative pattern list:

Ref. Code	Score	Compound Name	Displace-ment [°2Th.]	Scale Factor	Chemical Formula
24-0027	63	Calcite	0	0.799	$CaCO_3$
24-0495	15	I l l i t e - 2 \ ITM#2\RG	0	0.022	$K_{0.7}Al_{2.1}(Si, Al)_4O_{10}(OH)_2$
46-1045	52	Quartz, syn	0	0.081	SiO_2
03-0249	Unmatched Strong	Goethite, syn	0	0.048	FeO (OH)
08-0097	7	hydrogoethite	0	0.048	$Fe_2O_3 \times H_2O$

Sample AB -30

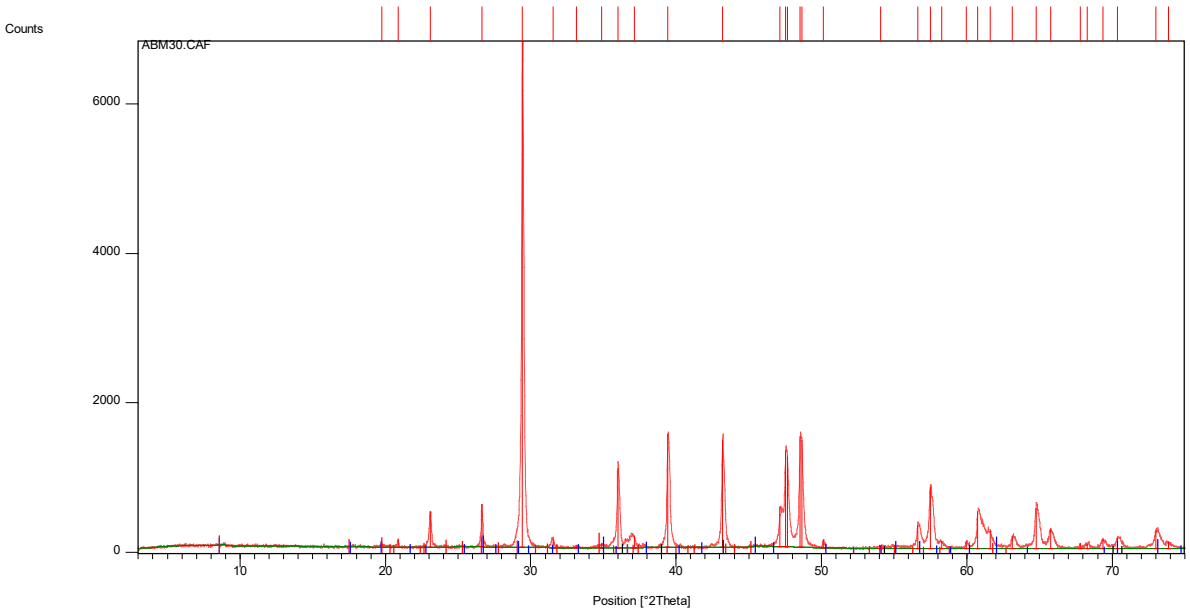

Qualitative pattern list:

Ref. Code	Score	Compound Name	Displacement [°2Th.]	Scale Factor	Chemical Formula
05-0586	73	Calcite, syn	0	0.820	$CaCO_3$
46-1045	60	Quartz, syn	0	0.109	SiO_2
15-0603	24	Illite	0	0.021	$K(Al\ Fe)_2\ AlSi_3O_{10}\ (OH)_2\ x\ H_2O$
24-0495	21	Illite-2\ITM#2\RG	0	0.029	$K_{0.7}\ Al_{2.1}\ (Si,\ Al)_4\ O_{10}\ (OH)_2$

Sample AB -71

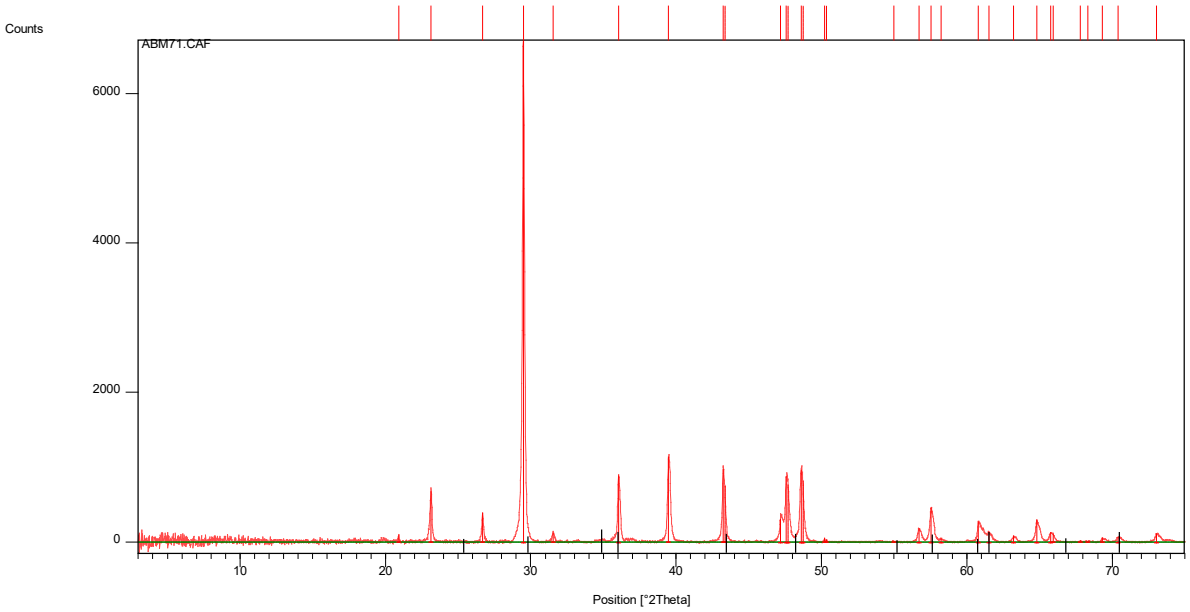

Qualitative pattern list:

Ref. Code	Score	Compound Name	Displacement [°2Th.]	Scale Factor	Chemical Formula
46-1045	37	Quartz, syn	0	0.044	SiO_2
05-0586	48	Calcite, syn	0	0.442	$CaCO_3$

Sample AB -80

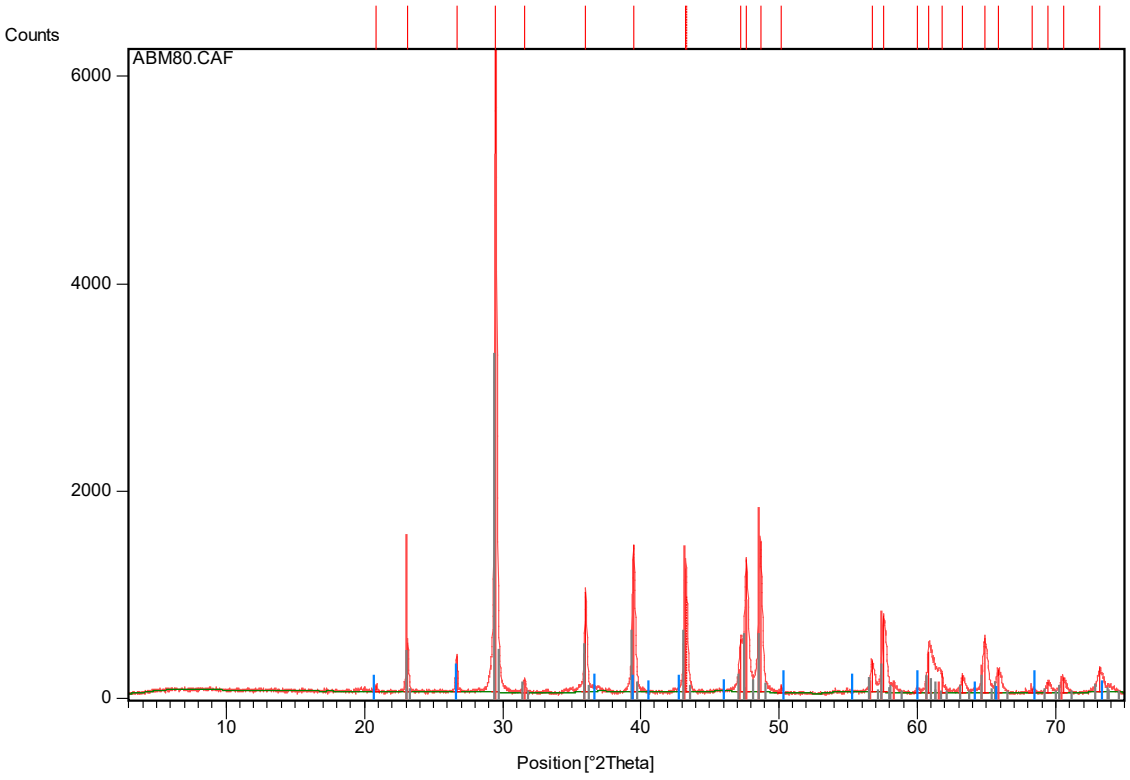

Qualitative pattern list:

Ref. Code	Score	Compound Name	Displacement [°2Th.]	Scale Factor	Chemical Formula
24-0027	66	Calcite	0	0.826	$CaCO_3$
05-0586	59	Calcite, syn	0	0.520	$CaCO_3$
02-0458	18	Quartz	0	0.041	SiO_2

Sample AB -148

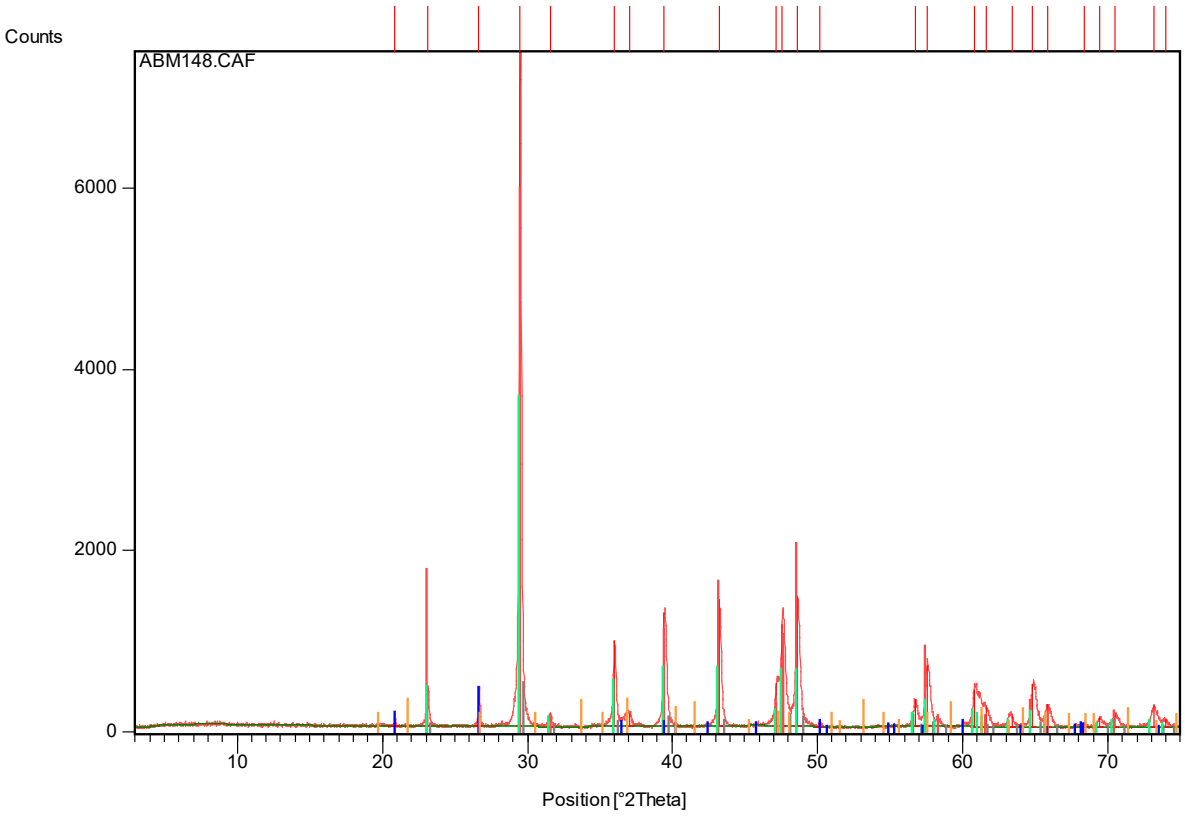

Qualitative pattern list:

Ref. Code	Score	Compound Name	Displace-ment [°2Th.]	Scale Factor	Chemical Formula
24-0027	65	Calcite	0	0.791	$CaCO_3$
05-0586	58	Calcite, syn	0	0.486	$CaCO_3$
05-0490	48	Quartz, low	0	0.058	SiO_2
02-0281	Unmatched Strong	Goethite	0	0.039	$Fe_2O_3 \times H_2O$

Sample AB -170

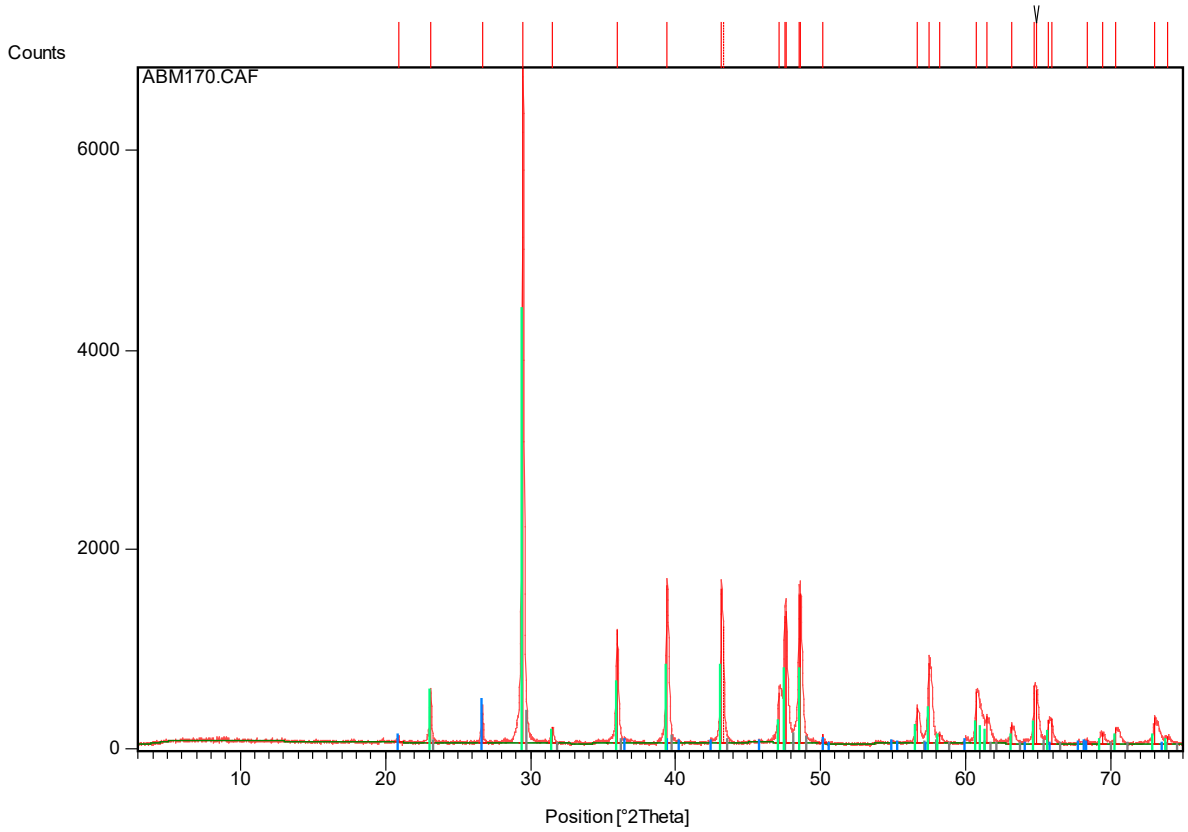

Qualitative pattern list:

Ref. Code	Score	Compound Name	Displacement [°2Th.]	Scale Factor	Chemical Formula
46-1045	53	Quartz, syn	0	0.064	SiO_2
05-0586	66	Calcite, syn	0	0.638	$CaCO_3$